Optimization of Porous Metal Oxides and Metal-Organic Frameworks for High Temperature Catalysis

A DISSERTATION
SUBMITTED TO THE FACULTY OF
UNIVERSITY OF MINNESOTA
BY

Camille Malonzo May

IN PARTIAL FULFILLMENT OF THE REQUIREMENTS
FOR THE DEGREE OF
DOCTOR OF PHILOSOPHY

Andreas Stein, Advisor

September 2017

Acknowledgements

I owe many thanks to everyone who made the past five years a very enriching and memorable experience. First, to my adviser, Prof. Andreas Stein, thank you for your guidance and support. Thank you for challenging me, for helping me hone my skills as a researcher. I am truly grateful for the time I spent as part of the Stein Group. And to my other committee members, Prof. Lee Penn, Prof. Alon McCormick and Prof. Ian Tonks, thank you for your kindness, time and invaluable feedback for this dissertation.

I had the pleasure to work with great collaborators who I also want to thank, including Prof. Jane Davidson and Robert de Smith of the Solar Energy Laboratory here at UMN, and everyone in the Inorganometallic Catalyst Design Center. Learning from these great minds has indeed been a wonderful opportunity for me.

I am indebted to Jiaxin Duan, Steven Prinslow and Sammy Shaker, the undergraduate students who I worked with. I thank them for all their contributions to this work. Thank you too, to the rest of the Stein group, especially to my seniors, Dr. Stephen Rudisill and Dr. Nick Petkovich for being my mentors when I was just starting in the group.

Lastly, I want to thank my family and friends for their support. They kept me moving forward and kept me sane, and I could not have made it without them. Special thanks to my life/career coaches, Maria Victoria Punay and Stacey Saba, for all the help and encouragement during this final stage of graduate school. And to Jeremy, thank you. Thank you for always being there, and for being my home.

Dedication

To the people who lifted me up

Abstract

The structural integrity of porous materials is critical to their application as heterogeneous catalysts. For high temperature catalysis, sintering and decomposition are common routes to structural destabilization and ultimately to irreversible deactivation of porous catalysts. This thesis describes the optimization of two types of porous catalysts, namely, porous metal oxides and metal-organic frameworks, for application in solar thermochemical fuel production and high temperature natural gas conversion.

Thermochemical cycles can use the heat generated from solar thermal power to split H_2O and CO_2 into H_2 and CO, both of which are valuable fuel and chemical feedstocks. These cycles can be catalyzed by metal oxides. In the first part of this thesis, wood-templating is demonstrated as an approach to generate a macroporous oxide structure that balances high thermal stability and accessible porosity for enhanced thermochemical cycling kinetics.

The other part of this thesis describes the development of a silica nanocasting method for the thermal stabilization of metal-organic framework (MOF)-based catalytic metal sites. Nanocasting incorporates a thermally stable silica layer in the MOF pores, which serves as a scaffold for the metal active sites in the MOF after the organic linkers are removed at high temperatures. The work described here shows the applicability of the nanocasting method to MOFs with different pore sizes and compositions, and demonstrates that the method is capable of producing MOF-derived materials that retain their catalytic properties after exposure to high temperatures.

Table of Contents

List of Tables

List of Figures

Abbreviations and Symbols

3-D	three-dimensional
3DOM	three-dimensionally ordered macroporous
A	ampere, SI unit of electrical current
Å	angstroms
AIM	atomic layer deposition in MOFs
ALD	atomic layer deposition
atm	atmospheres
BDC	benzene-1,4-dicarboxylate
BET	Brunauer−Emmett−Teller
BPDC	biphenyl-4,4'-dicarboxylate
BTB	benzene-1,3,5-tribenzoate
c (prefix)	centi ($\times 10^{-2}$)
°C	degrees Celsius
CSP	concentrated solar power
DED	difference envelope density analysis
DEF	diethylformamide
DFT	density functional theory
DMF	dimethylformamide
DMSO	dimethylsulfoxide
dPDF	differential pair distribution function

DSC	differential scanning calorimetry
EDS	energy dispersive spectroscopy
EDTA	ethylenediaminetetraacetic acid
eV	electron volt
EXAFS	extended X-ray absorption fine structure
FT-IR	Fourier-transform infrared spectroscopy
g	grams, SI unit of mass
h	hour
ΔH^{o}	standard enthalpy of reaction
HAADF	high-angle annular dark field
HPLC	high performance liquid chromatogrphy
Hz	Hertz, SI unit of frequency
ICP-MS	inductively coupled plasma – mass spectrometry
ICP-OES	inductively coupled plasma – optical emission spectrometry
J	Joule, SI unit of energy
k (prefix)	kilo ($\times 10^{3}$)
K	Kelvin
L	liter
L:B	Lewis to Brønsted acid ratio
m	meter
m (prefix)	milli ($\times 10^{-3}$)
M (prefix)	mega ($\times 10^{6}$)

M	molarity (moles L^{-1})
min	minute
MOF	metal-organic framework
mol	moles
MTG	methanol-to-gasoline
MTO	methanol-to-olefin
n (prefix)	nano ($\times 10^{-9}$)
NGL	natural gas liquid
NMR	nuclear magnetic resonance
P123	$HO(CH_2CH_2O)_{20}(CH_2CHCH_3O)_{70}(CH_2CH_2O)_{20}H$
P/P_0	relative pressure
Pa	Pascal, SI unit of pressure
PDF	pair distribution function
PDF#	powder diffraction file number
pO_2	oxygen partial pressure
PTFE	polytetrafluoroethylene
rad	radians
RLGA	Raman laser gas analyzer
RPC	reticulated porous ceramic
ΔS^o	standard entropy of reaction
SAED	small area electron diffraction
sc-CO_2	supercritical CO_2

sccm	standard cubic centimeter
SEM	scanning-electron microscopy
SIM	solution deposition in MOFs
STP	standard temperature and pressure (0 °C, 1 atm)
STEM	scanning transmission electron microscopy
t	time
T	temperature
T_{mp}	melting point
T_{ox}	oxidation tempreature
T_{red}	reduction temperature
TBAPy	1,3,6,8-tetrakis(*p*-benzoate)pyrene
TBHP	*t*-butyl hydroperoxide
TEM	transmission electron microscopy
TGA	thermogravimetric analysis
THF	tetrahydrofuran
TMOS	tetramethylorthosilicate
TON	turnover number
UV	ultraviolet
$\dot{V}'_{CO}$	volumetric CO production rate
vis	visible
WT	wood-templated
XANES	X-ray absorption near-edge spectroscopy

XPS	X-ray photoelectron spectroscopy
XRD	X-ray diffraction
γ	surface tension
δ	oxygen nonstoichiometry
η_{STF}	solar-to-fuel efficiency
η_{STH}	solar-to-hydrogen efficiency
μ (prefix)	micro ($\times 10^{-6}$)
$\Delta\mu^o$	change in chemical potential
υ	wavenumber
χ	electronegativity
Ω	Ohm, SI unit of electrical resistance

Chapter 1

Introduction to Porous Materials for High Temperature Catalysis

1.1 Porous Materials in Catalysis

Heterogeneous catalysts are catalysts whose phase differs from that of the reactants. The term is typically associated with solids catalyzing the reaction between gaseous, liquid, or solution-phase reactants, though it also applies to the case where the catalyst and reactants are dissolved separately in two immiscible liquids. Catalysis occurs at the interface of the two phases. For solid catalysts, the catalytic reaction begins with the adsorption of reactants on the surface of the solid, which then undergo a surface reaction to form the products. Desorption of the products makes the surface available again for the next catalytic reaction. Because of this nature of reaction, solids with high surface areas are desirable as catalysts. Heterogeneous catalysts offer easy catalyst separation, and can be operated in a wider range of reaction conditions than homogeneous catalysts.

Porous solids have long been used in heterogeneous catalysis either as active material or as catalyst support.[1-4] Compared to a bulk material, the porous structure affords more exposed surface for interaction with reactants or, as a support, for the installation of a higher loading of active sites onto the structure. Depending on the pore size, porous solids can be classified as microporous (< 2 nm), mesoporous (2 - 50 nm) or macroporous (> 50 nm), where micropores typically provide the highest surface area.[5] Some materials incorporate more than one type of pores in their structure, a so-called hierarchical porosity.[6] The hierarchical pore structure serves to combine the advantage of optimal diffusion rates in the larger pores, and the selectivity and high surface areas for reactivity in the smaller pores.[7]

Zeolites are among the widely used porous catalytic materials especially in the oil and gas industry.[8-11] Zeolites have tunable Lewis and Brønsted acidity used for acid catalysis, and they are also used as catalyst supports.[12] The porosity in zeolites arises from different arrangements of the tetrahedral SiO_4 or AlO_4 building blocks forming different microporous crystalline structures.[11] This microporosity has been shown to afford shape selectivity in the products of zeolite-catalyzed reactions.[13,14] Methods to introduce mesoporosity in zeolites have also been developed to facilitate diffusion of reactants and products through the material, which is otherwise rate-limiting in a purely microporous structure.[15-17]

Apart from zeolites, advances in materials synthesis have afforded the preparation of other porous structures of different compositions and tailorable structures, making it possible to tap a wide range of reactivities for carrying out various transformations.[17-25] In this thesis, particular focus is given on two types of porous catalysts: porous metal oxides and metal-organic frameworks. Research on heterogeneous catalysts is still thriving, with a consistent goal of identifying more active, highly selective, and stable catalysts.

1.1.1 Porous Metal oxides

Like zeolites, there is an extensive literature on the synthesis and catalytic applications of porous metal oxides.[2,26-32] A rich variety of chemistries is possible not just with different oxide compositions, but also with different polymorphs of a given oxide. Manganese oxide for example, has 30 different polymorphs,[33] and studies comparing

some of these phases show that they have different activities in chemical, photochemical and electrochemical oxidation reactions.[34,35] Transition metal oxides are particularly interesting for catalysis because of their ability to change valence states, enabling them to exchange electrons, protons and oxide ions for acid-base and redox catalysis.[36,37] Oxides like Al_2O_3, MgO, and ZrO_2 that have metals that exist in only one oxidation state can still have acidic or basic properties[38] and are usually used as catalyst support (**Table 1.1**).

Table 1.1. Examples of Commercial Heterogeneous Catalyst Compositions with Metal Oxide Active Phase and/or Support[32,39,40]

process	catalyst
Hydroprocessing	CoO-MoO_3-P/Al_2O_3; NiO-MoO_3-P/Al_2O_3
Polymerization (polyolefins)	CrO_x/SiO_2
Oxidation	
Butane to maleic anhydride	V_2O_5-P_2O_5/Al_2O_3
Propene to acrolein	Bi_2MoO_6/SiO_2
Ammonia synthesis	Fe_3O_4; Fe_3O_4-CoO_x
Methanol synthesis	CuO-ZnO-Al_2O_3
Phenol hydrogenation	CuO-ZnO
Dehydrogenation of lower alkanes	Cr_2O_3/Al_2O_3
Dehydrogenation of alcohols	CuO/Al_2O_3; ZnO; CuO/ZnO

Porous oxides can be synthesized with control of composition, structural features (e.g., pore size, wall thickness), phase, and crystallinity. Template-assisted synthesis is the most common route to prepare porous oxides. Briefly, templating involves forming the metal oxide in the voids of a template structure, followed by the removal of that

template. If these voids are completely filled – referred to as volume templating, the porous oxide will be a negative replica of the template. If the voids are not filled and the oxide is formed by surface templating, the resulting structure will be a hollow positive replica of the template (**Figure 1.1**).

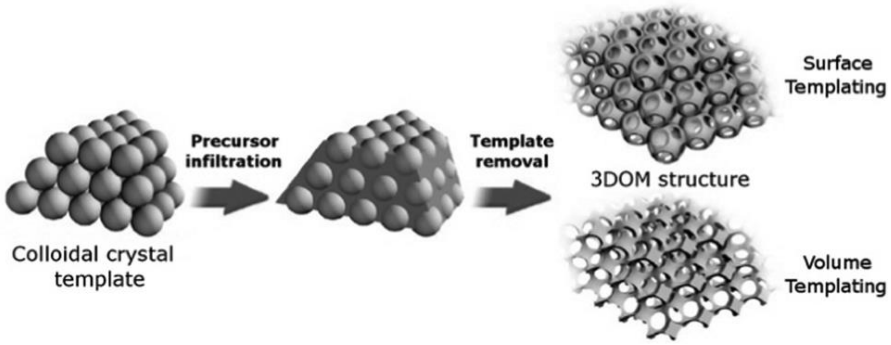

Figure 1.1. Comparison of structures formed by surface and volume templating of a colloidal crystal. Reproduced with permission from Reference [6].

Both hard and soft templates have been used to make mesoporous, macroporous, and hierarchically porous oxide structures. In soft-templating, supramolecular assemblies of amphiphilic block copolymers or surfactants (micelles) are used as templates, which are co-assembled with the metal precursors in solution. As with any self-assembly process, favorable interactions between the template and the metal precursors (e.g., electrostatic, hydrogen bonding) are essential.[41] The co-assembly can be carried out in aqueous or non-aqueous solvents, with the latter allowing the use of non-ionic surfactants as templates.[42,43] Controlled hydrolysis/condensation of the metal precursors (e.g., alkoxides) followed by template removal by calcination or dissolution yields the porous oxide. Soft templating generates mesoporous structures with pore sizes typically of a few nanometers for micellar templates, and from several to a few tens of nanometers for

block copolymer templates.[26] Gu et al. summarized unary metal oxide compositions made via soft-templating, ranging from those of light metals such as Al to rare earth elements such as La, Ce and Dy.[26]

Hard templating, also called nanocasting, uses pre-formed rigid structures such as mesoporous silica as template.[44,45] The process involves infiltration of the template with the metal precursor that can be in the vapor or solution phase. The metal precursor within the template is then converted to the target oxide, e.g., by heating, and afterwards, the template is removed by calcination or etching. Hard templating allows the synthesis of mesoporous and macroporous structures alike, controlled by the type of template used. For example, colloidal crystal templates made up of close-packed polymer or silica spheres have been used as template to make porous structures made of metal oxides, carbon and other inorganic materials.[46,47] The morphology (e.g., pore size) can be tuned by the choice of spheres and the processing conditions.[46] Biological templates have also been used to generate porous materials. The pore structure varies from species to species. Examples of bio-based templates that have been used to make porous structures of metal oxides are wood,[48-50] insect wings[51] and eggshell membranes.[52,53] An example of a porous template with 10-15 μm pores is the sea urchin skeletal plate made of $CaCO_3$, which has been used as template for gold.[54] A limitation encountered with bio-based templates is that the pore properties cannot be controlled and are dependent on the sample used. Variability can be expected even within the same species as a result of the age of the sample and other environmental conditions under which these structures have developed. Thus, the performance in applications such as catalysis that rely on the structure of the

material could have some uncontrollable variability. However, they can be accounted for through correlation of the observed activity with surface area, pore size distribution, and pore connectivity of the solid. Hard templating can be combined with soft templating to produce hierarchical porous structures.

Sol-gel chemistry provides a convenient way to synthesize templated oxides with tunable composition from metal alkoxide or chloride precursors. Sol-gel refers to the various synthesis method of forming a homogeneous precursor solution that can be turned to a gel via polycondensation (**Figure 1.2**). The gelled metal precursors can be converted to the target oxide by calcination. Sol-gel techniques allow the formation of compositionally homogeneous metal oxide materials, particularly important for multi-metallic oxide preparations. As an example, the Pechini method, also called the polymerizable complex method, is a sol-gel technique that has been used to prepare multicomponent metal oxides from simple unary[55,56] and binary oxides[57-59] to more complex compositions like doped perovskites.[60-62] The method was named after its inventor, Maggio Pechini who used the method to prepare lead and alkaline earth titanates as capacitor materials.[63] The method relies on polydentate ligands such as citric acid and EDTA to form complexes with metal ions. These complexes are then polymerized in the presence of a polyol, usually ethylene glycol. The polymerization takes place at about 100 to 130 °C, forming a resin with well-distributed metal ions. In a last step, the resulting resin is calcined, removing the organic components and yielding the compositionally homogeneous metal oxide. The Pechini precursor solution composed

of the metal-citrate complex and ethylene glycol, as well as other "sols", can be infiltrated into a template to make porous oxide structures.[64]

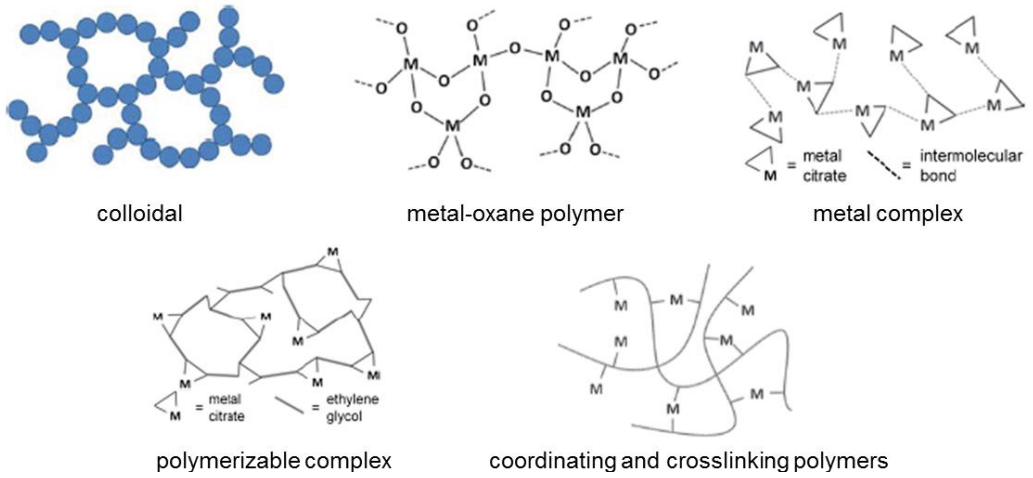

Figure 1.2. Types of gels formed during sol-gel synthesis. Gels could be (a) colloidal particles connected by van der Waals forces or hydrogen bonding, (b) metal-oxane polymers formed by hydrolysis and condensation of alkoxide precursors, (c) weakly interconnected metal complexes in a concentrated solution, (d) polyesters formed between metal carboxylate complexes (e.g., metal citrate) and a polyhydroxyalcohol (e.g., ethylene glycol) and (e) complexation of metal ions by a coordinating polymer (e.g., alginate). Adapted from Reference [65]. Published by The Royal Society of Chemistry.

1.1.2 Metal-Organic Frameworks

Metal-organic frameworks (MOFs) are an emerging class of porous materials for catalytic applications.[24,66-75] MOFs are coordination polymers made up of metal ions or clusters that are interconnected by multidentate organic ligands called linkers. They form a three-dimensional crystalline network (**Figure 1.3**), and the pores in the material directly result from this assembly. MOFs are compositionally abundant. There is an extensive library of MOF nodes and linkers to choose from, building on both coordination and cluster chemistry libraries. The choice of node and linkers gives rise to

different MOF structures and consequently, properties that can be tuned to different applications. **Table 1.2** lists the MOFs discussed in this section along with their constituent nodes and linkers for reference.

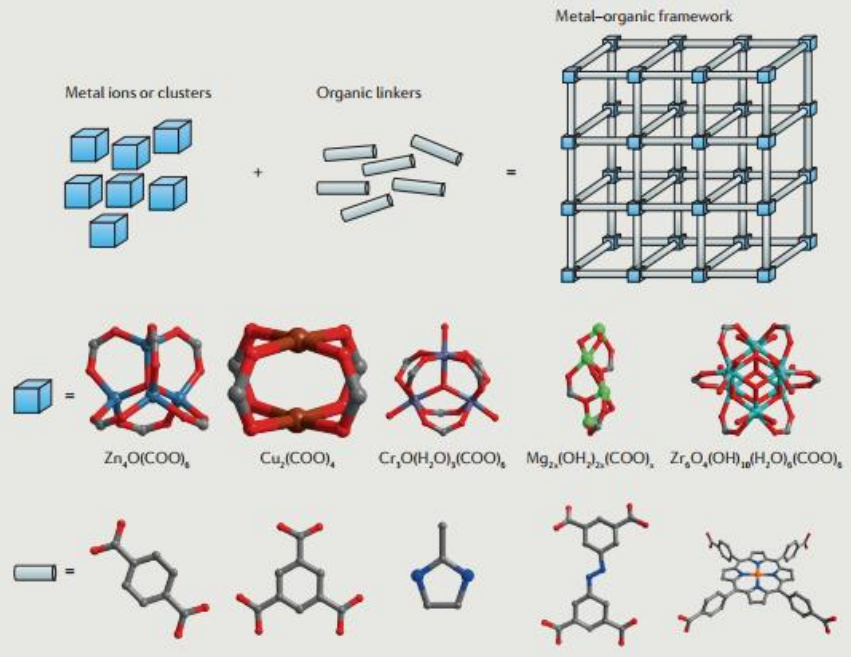

Figure 1.3. Construction of MOFs from metal-based nodes and organic linkers. Some examples of node and linker structures are also shown. Element colors: C (gray), O (red), and N (blue). Figure reproduced with permission from Reference [76].

MOFs have a number of properties of interest for catalytic materials. For one, their synthesis is typically simple. The conventional synthesis is based on the self-assembly of metal precursors (e.g., metal chlorides and nitrates) and organic linkers in solution at temperatures from room temperature to about 250 °C.[77] Polar aprotic solvents such as dimethylformamide (DMF), diethylformamide (DEF), and dimethylsulfoxide (DMSO) that can dissolve both the bulky organic linker and the metal precursor, are used as reaction medium. Nanometer-sized to millimeter-sized single crystals can be produced

by controlling synthesis conditions, e.g., temperature, pH, and reactant concentration.[78] One technique that has been used for the size-controlled synthesis of highly crystalline MOFs with narrow particle distribution is the use of modulators – monocarboxylic acids – that generate an equilibrium that slows down the crystallization of the metal nodes with the multitopic carboxylic acid linkers.[79-81] Alternative synthesis methods have been explored as well. These include electrochemical, mechanochemical, sonochemical, and microwave-assisted syntheses, and using different precursors such as metals, and metal oxides, hydroxides and carbonates.[77,82,83] A key to the industrial application of MOFs is their large-scale synthesis, and gram to kilogram-scale syntheses have been achieved with some MOFs through continuous flow reactor systems.[84-86] BASF claimed the first industrial, ton-scale MOF synthesis in 2010, and more companies are now producing MOFs commercially.[87-89]

Table 1.2. List of selected MOFs and their secondary building units.

MOF	node	linker	ref
UiO-66	$[Zr_6(\mu_3\text{-}O)_4(\mu_3\text{-}OH)_4]^{12+}$	benzene-1,4-dicarboxylate, bdc^{2-}	90
UiO-67	$[Zr_6(\mu_3\text{-}O)_4(\mu_3\text{-}OH)_4]^{12+}$	biphenyl-4,4'-dicarboxylate, $bpdc^{2-}$	90
IRMOF-74-I	$(M^{2+})_\infty$, M = Mg or Zn	2,5-dioxido-1,4-benzenedicarboxylate, $dobdc^{4-}$	91
IRMOF-74-II	$(M^{2+})_\infty$, M = Mg or Zn	4,4′-dioxido-3,3′-biphenyldicarboxylate, $dobpdc^{4-}$	91
NU-1000	$[Zr_6(\mu_3\text{-}O)_4(\mu_3\text{-}OH)_4(H_2O)_4(OH)_4]^{8+}$	1,3,6,8-tetrakis(*p*-benzoate)pyrene, $tbapy^{4-}$	92
MIL-140A	$([ZrO]^{2+})_\infty$	benzene-1,4-dicarboxylate, bdc^{2-}	93
DUT-9	$[Ni_5(\mu_3\text{-}O)_2]^{6+}$	benzene-1,3,5-tribenzoate, btb^{3-}	94

Aside from the ease and scalability of their synthesis, MOFs are particularly interesting for catalysis because of the abundance of the types and composition of catalytic sites that can be generated in their structure. The catalytic sites in MOFs could be the framework itself, they can be active sites that are installed onto the framework by post-synthetic modification, or they can be some catalytically active guest species in the MOF pores.[68,95,96] The metal nodes of MOFs can themselves be catalytic, especially if the metals are coordinatively unsaturated, leaving sites available for interaction with reactant molecules.[97,98] The unsaturated metal sites are usually generated by the removal of solvent molecules attached to the node by heating[99-101] and may be accompanied by structural changes in the node[102] and the framework.[103] Because of how they are constructed, MOFs have high loadings of these site-isolated, uniform metal nodes which can serve as catalytic single-sites.[73,74,104] There is potential for product selectivity from these uniform, well-defined metal nodes having similar interactions with reactants.[105,106] These metal nodes are also highly tunable, first through the choice of metal used in the synthesis, and additionally by post-synthetic modification. Both solution-phase and atomic layer deposition have been used to install additional metal atoms onto the nodes or linkers of MOFs.[107,108] Metal exchange has also been reported, for example in the exchange of the zirconium atoms in the nodes of the MOF UiO-66 with titanium.[109] This compositional tunability could give rise to different catalytic properties in MOFs. For some MOFs, the active metal sites are present in the organic linker, e.g., coordinated metals in linkers with porphyrin,[110,111] salen,[112-115] and catechol[116] moieties. MOFs have

also been studied as hosts for active catalyst species, including noble metal nanoparticles[117-119] and polyoxometalates.[120,121]

MOFs have high internal surface areas and tunable porosities, which also aid in their application as catalysts. Some MOFs are mesoporous, making them applicable for the conversion of larger molecules and making mass transport in these catalysts more favorable than in microporous systems like zeolites. Pore sizes of up to 98 Å have been achieved.[91] MOFs with bigger pores can be obtained by using longer linkers, as in the case of the UiO MOFs[90] and the IRMOF[91] series.

The crystalline nature of the MOF structure allows the application of structural characterization techniques like X-ray crystallography, extended X-ray absorption fine structure (EXAFS), pair distribution function (PDF) analysis, and solid-state nuclear magnetic resonance (NMR) spectroscopy to determine the structure of the metal active sites.[122-125] This can also apply to post-synthetically modified MOFs, especially since single-crystal to single-crystal metal modification is possible.[105,126] The crystallinity of MOFs makes them amenable to computational modeling for the design of new MOFs, and to understand and predict desirable morphologies and properties for specific applications.[127-131] Computational methods have been used to rationalize the reactivity of MOF metal sites and to predict suitable node compositions to catalyze specific reactions.[132-137] MOFs have been studied as photocatalysts and electrocatalysts,[138-140] and as catalysts for asymmetric conversion, hydrogenation, oxidation and isomerization of organics.[141,142] Computational methods have been used to rationalize the reactivity of MOF metal sites and to predict suitable node compositions to catalyze specific reactions.

MOFs have been studied as photocatalysts and electrocatalysts, and as catalysts for asymmetric conversion, hydrogenation, oxidation and isomerization of organics.

Stability is presumably the primary challenge in the industrial application of MOFs as catalysts. MOFs vary in their chemical, mechanical and thermal stabilities arising from differences in the nature of metal nodes and linkers, and the framework architecture. The lability of the metal-linker bond accounts for the chemical stability limitations in MOFs, especially for aqueous phase catalysis. First, water itself can attack the MOF framework by binding to the metal nodes and displacing the linkers. MOFs can be designed to have high water stability however, by matching metals and linkers for favorable hard acid-hard base or soft acid-soft base interactions, and by incorporating hydrophobic groups in the linkers.[143,144] Water-stable ones include MOFs of benzoate linkers with high valence metals such as Zr^{4+} (e.g., UiO-66 and NU-1000), and MOFs of softer linkers such as imidazolate with divalent metals.[145] MOFs with linkers that are fluorinated or have organic substituents are hydrophobic and are water-stable.[146-148] There is also a pH dependence of the stability, related to the protonation of linkers at high H^+ concentrations and the displacement of linkers by hydroxo ligands at high OH^- concentrations.

MOFs have inherent mechanical instability that comes with having a porous, low density structure. Among MOFs, mechanical stability varies with framework architecture as well as the strength of the metal-linker coordination. Denser MOFs like UiO-66 and MIL-140A can have higher shear stability, approaching that of zeolites.[149,150] Important to the preparation of MOFs and their application to solution-phase catalysis is their

stability against capillary forces. Some MOFs collapse when dried from solvents with high surface tension (γ) like DMF (γ = 34 dynes cm^{-1}), a solvent commonly used for MOF synthesis. Exchanging with a solvent with lower γ, like acetone (γ = 23 dynes cm^{-1}), is usually done to prevent the structural collapse when drying MOFs.[76,78] MOFs like DUT-9 that have very low mechanical stability may require supercritical CO_2 drying (γ = 0.6 dynes cm^{-1}) to retain their structure.[94]

The thermal stability is dictated largely by the organic linkers in the MOF and their tendency to decompose at high temperatures. When the linkers decompose, the MOF structure is lost and the metal sites in the MOF aggregate. For catalysis, this results in loss of catalytic activity due to loss of the single-site character of the MOF-based metal sites. Thermal stabilities of MOFs are usually determined by thermogravimetric analysis (TGA), which can detect the onset of linker decomposition. Most MOFs can only be heated to 150-350 °C in air without undergoing framework collapse.[151-153] Zr MOFs such as UiO-66 and NU-1000 are among the most stable and can be heated up to 500 °C under nitrogen. Zr MOFs such as UiO-66 and NU-1000 are among the most stable and can be heated up to 500 °C under nitrogen without linker decomposition.[154-157] However, significant loss of crystallinity in these MOFs is already observed at 350 °C.[102] At temperatures below the decomposition temperature of the linker, other modes of thermal degradation may still occur, including amorphization and melting,[76,158,159] which can be detected by differential scanning calorimetry (DSC) and X-ray diffraction (XRD).[102]

1.1.3 High Temperature Deactivation of Porous Catalysts

The structural integrity of porous materials is critical for their function in most applications. However, factors such as heat, chemical attack, and mechanical stress can cause destabilization of a porous structure.[160] These factors can be inherent to the application and are therefore unavoidable.

Stability is an important property that dictates a catalyst's lifetime in chemical reactors. For high temperature catalysis, sintering and decomposition are common routes to structural destabilization and ultimately to irreversible deactivation of porous catalysts. Decomposition is particularly prominent for organic-based catalysts, including MOFs. Heating under inert or reducing atmospheres (pyrolysis) leads to carbonization of organic components while oxidizing atmospheres (calcination) lead to loss of the organics as CO or CO_2. Calcination of MOFs, as described in the previous section, leads to linker decomposition accompanied by the loss of the MOF structure and aggregation of the catalytic metal sites. MOF pyrolysis, although it causes loss of the original MOF structure, can been used to make derivative catalytic materials including metal-, metal oxide-, and metal carbide-decorated porous carbon materials.[161,162] It is important to note that the metal sites of the original MOF are converted into larger nanoparticles in these derivatives and would therefore give different catalytic properties.

Sintering, on the other hand, can cause structural collapse when grains grow at high temperatures to sizes larger than the dimensions of the structure, e.g., pore walls, in which they are contained.[160,163-166] This leads to loss of active surface area and loss of pore openings, concomitant with loss of catalytic activity.[167] Aboav quantitatively

described the relationship between temperature and the distribution of grain sizes in a material: small grains are stable until a certain temperature is reached, above which the minimum stable grain size increases parabolically with temperature.[164] Sintering is a thermally-activated physical process and is driven by the tendency to reduce a particle's surface energy by forming more spherical structures. There are several modes of material transport that can happen during sintering that lead to the effective coalescence of grains (**Figure 1.4**). The extent and rate of sintering at a given temperature differ among different materials and also depend on factors such as initial grain size and distribution, the presence of additives and the environment.[168,169] The presence of water vapor, for example, is known to promote sintering of metal oxides through formation of surface hydroxyls that are condensed into oxygen bridges between neighboring grains, initiating coalescence.[170-172] The effects of sintering on the destabilization of a porous structure can also be compounded by phase transformations. Macroporous TiO_2, for instance, showed significant morphological changes at 800 °C that came with the onset of the conversion of the anatase phase to rutile.[173]

High reaction temperatures are beneficial, if not necessary, for some chemical transformations. Faster kinetics is attainable with increasing reaction temperatures, and there are reactions that are thermodynamically favored only at high temperatures. Thus, the optimization of catalytic materials to make them stable at high temperatures is desirable. The conversion of small molecules such as H_2O, CO_2, and light alkanes to higher value commodity chemicals such as syngas and olefins is a type of reaction that requires high temperatures to be thermodynamically favored.[174,175] This is because these

conversions involve the enthalpically disfavored breaking of rather inert chemical bonds and the entropically driven formation of gaseous splitting products. The splitting of CO_2 to CO and H_2 for instance, requires reaction temperatures of at least 3000 °C, while the conversion of light alkanes to olefins occurs above 500 °C.[174,176] Despite the high temperature requirements, these conversions are of interest not only because they produce useful chemical feedstocks, but also because they can be coupled to renewable energy storage and the utilization of cheap, abundant resources.

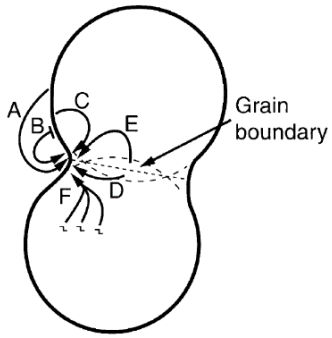

Figure 1.4. Paths for the transport of matter during sintering. Grains coalesce when more material are brought to the "neck" adjoining them. A source of material is the grain surface, and transport to the neck could occur by paths A (vapor transport), B (surface diffusion), and C (lattice diffusion). Matter from the grain boundary can transported to the neck via paths D (diffusion along the grain boundary) and E (lattice diffusion). Lastly, material can come from the lattice and delivered to the neck through path F (lattice diffusion). Figure reproduced with permission from Reference [177]

This dissertation describes work on the development of catalysts for application in solar fuel production and natural gas conversion, both of which involve high temperature reactions. The focus is on strategies for addressing the stability issues in porous materials to make them suitable for high temperature catalysis.

1.2 Solar Fuel Production

Solar energy is abundant and practically inexhaustible. The sun supplies an average annual energy of 170 W/m^2, more than enough to cover 7500 times of the world's current energy consumption per year.[178] Only a small part of this energy is tapped by today's solar energy systems. However, with the current movement towards using renewable forms of energy to replace fossil fuels, the larger and efficient utilization of solar energy has a promising potential. The intermittent nature of solar radiation makes it necessary to devise methods for energy storage. One storage method, which could allow wider distribution and extended storage time of solar energy is through the production of solar fuels such as H_2 and other energy carriers.[179,180]

1.2.1 Concentrated Solar Energy Generation and Storage

Capturing solar energy can be done in two ways: using photovoltaic systems and concentrated solar power (CSP) collectors. Photovoltaic systems directly convert solar energy to electricity while CSP systems collect solar energy as heat. Both technologies have experienced advancements over time, concurrent with decreasing cost and increasing installed capacity.

The advantage of CSP systems is that they utilize the entire solar spectrum, which makes solar conversion efficiency, in principle, higher compared to photovoltaic systems that utilize only a rather narrow band of solar energies. CSP systems use an array of reflective surfaces that concentrates the sun's radiation on either a line or a point focus. A few configurations of CSP systems are shown in **Figure 1.5**. Solar troughs and linear

fresnels are linear focus systems that use mirrors to track the sun in one axis and concentrate sunlight onto receiver tubes. The main difference between the two is that linear fresnels use flat or slightly curved mirrors to focus the sunlight onto a stationary receiver tube, whereas in solar troughs the receiver tube moves with the parabolic mirror. Point focus systems include solar towers and solar dishes. Solar towers use heliostats to track the sun and focus incident solar radiation to a central receiver mounted at the top of a tower. Solar dishes are parabolic dish-shaped reflectors that also track the sun and have a receiver at their focal point. Higher temperatures are generally achieved with a point focus as compared to a line focus.[181] Solar towers and dishes, for example, can achieve temperatures well over 1000 °C.[182] The efficiency of the conversion of solar energy to work (e.g., electricity) is dependent on the temperature achieved by the CSP system. Carnot's principle predicts that higher temperatures would lead to higher solar to work conversion efficiency. However, the efficiency at which a solar receiver converts solar radiation to heat decreases with temperature. Thus for each CSP system, there is a temperature at which solar to work efficiency is maximum, which depends in part on the solar receiver's properties such as its collecting area, curvature, and absorptivity.[183]

The high temperatures generated by CSP systems can be used as industrial process heat or in utility scale electricity generation. When the thermal energy from CSP is converted to electricity using heat engines, the electrical energy produced can be stored in capacitors, batteries and fuel cells. Heat could also be stored directly, using materials such as concrete, graphite and even water as storage media.[184] Lastly, the high temperatures from CSP systems can be used to make solar thermochemical fuels.

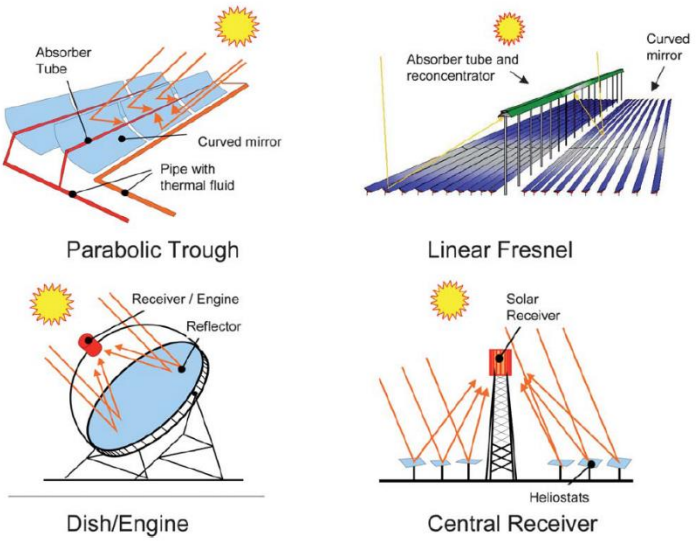

Figure 1.5. Schematic of concentrated solar power systems. The point focus systems (dishes and central receivers) generate higher temperatures than the linear focus systems (troughs and linear fresnels). Reproduced with permission from Reference 181.

1.2.2 Solar Thermochemical Fuel Production

The thermal energy from CSP can be stored in chemical bonds in fuels. Some thermochemical routes to fuel production are shown in **Figure 1.6**. Feedstocks including CO_2, H_2O, and biomass can be converted directly to H_2 and CO. A mixture of CO and H_2 is called syngas, which is used to make liquid hydrocarbon fuels via the industrial Fischer-Tropsch process.[185,186] Methanol can also be produced from syngas over catalysts such as ZnO/Cr_2O_3.[187] Of the fuel products, there is still the preference for liquid hydrocarbon fuels as energy carriers because of their high specific and volumetric energy density, along with ease of storage and transportation, compared to H_2 or CH_3OH on which future energy economies have been proposed. For H_2, its gaseous nature translates to low volumetric energy density and the need for extreme temperatures and pressures,

and expensive cylinders to achieve storage.[188] CH_3OH is a liquid and can be more easily stored than H_2 but is known to be corrosive towards metals such as aluminum, a common engine material.[50] Its energy density is also only half of the energy density of gasoline.[189]

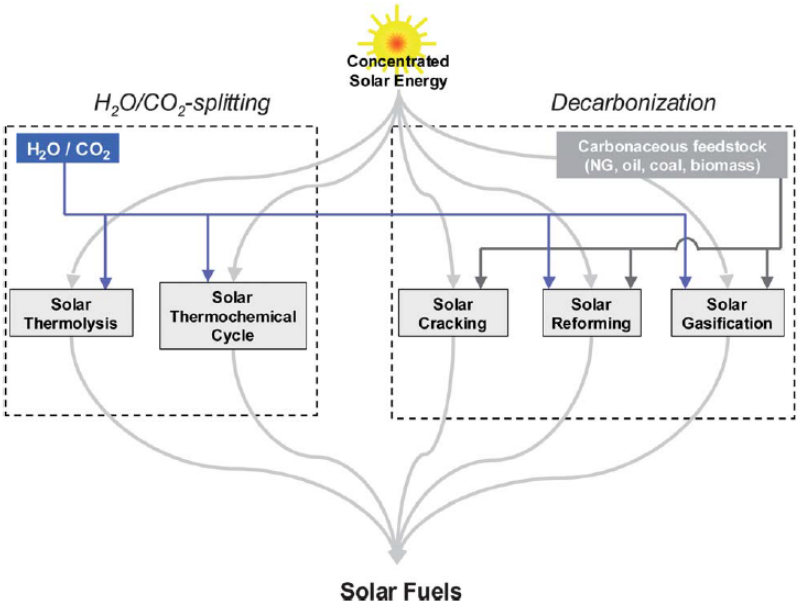

Figure 1.6. Solar thermochemical routes to fuel production. Using CO_2 and H_2O as starting materials, however, gives a carbon-neutral route to fuel production. Reproduced with permission from Reference 181.

1.2.3 Thermochemical CO Production from CO_2

A green route towards liquid hydrocarbon fuel production would use H_2O and atmospheric CO_2 as feedstocks. The initial steps in this process involve the splitting of H_2O and CO_2, which are the steps with the highest energy requirements:

$$H_2O_{(g)} \rightarrow H_{2(g)} + 0.5\ O_{2(g)} \qquad \Delta H^\circ = 286\ \text{kJ/mol}$$

$$CO_{2(g)} \rightarrow CO_{(g)} + 0.5\ O_{2(g)} \qquad \Delta H^\circ = 283\ \text{kJ/mol}$$

The splitting of H_2O and CO_2 can be achieved either by solar thermolysis or through a solar thermochemical cycle. Thermolysis appears to be the simpler method, which involves direct splitting of H_2O or CO_2 at high temperatures. However, thermodynamics predicts that the temperature requirement for full dissociation of CO_2 is at least 3000 °C, while that for H_2O is at least 4000 °C.[176] This creates the need to use secondary concentrators to re-focus the already concentrated solar radiation by refraction and achieve this high temperature requirement.[190] Mechanical and thermal stability problems for solar reactor materials exist, and apart from this, the product gases are obtained as a mixture, and therefore require separation methods suitable for high temperatures.[191] Product recombination could occur, which would lower the fuel yield from the process.[192]

Thermochemical cycles, on the other hand, split H_2O and CO_2 in multiple steps. The simplest cycles are two-step processes involving metal oxides, as shown below for CO_2 splitting:

$$M_xO_y \rightarrow M_xO_{y-\delta} + \frac{\delta}{2}O_2 \quad (1)$$

$$M_xO_{y-\delta} + \delta CO_2 \rightarrow M_xO_y + \delta CO \quad (2)$$

$$\delta CO_2 \rightarrow \delta CO + \frac{\delta}{2}O_2 \quad (3)$$

A similar cycle can be written for H_2O splitting. The first step involves the reduction of a metal oxide, M_xO_y, introducing vacancies – also called oxygen defects, into its lattice and releasing the oxygen as O_2. Some oxides can undergo complete reduction in this step, e.g., ZnO to Zn.[193-196] The deviation in the oxygen content of the

resulting reduced metal oxide from the stoichiometric value, *y*, is called the oxygen nonstoichiometry, δ. This reduction step is the endothermic step in the thermochemical cycle, which can be driven by the heat generated in CSP systems. Metal oxides usually release their oxygen at a lower temperature range than do CO_2 or H_2O. For this reason, thermochemical cycling can be performed at a lower temperature (below 2000 °C) than direct thermolysis. The second step is an exothermic oxidation reaction between the reduced metal oxide, and CO_2 or H_2O. This step regenerates the metal oxide and converts CO_2 to CO (or H_2O to H_2). The metal oxide is then recycled to the first step. In a thermochemical cycle, O_2 is produced in a separate step from CO or H_2, which eliminates the recombination and separation problem encountered in direct thermolysis.

1.2.4 Oxygen Nonstoichiometry in Metal Oxides

Oxygen vacancies are among the most prevalent defects in metal oxides. The formation of vacancies has various effects on the electronic, magnetic, and optical properties of metal oxides both in the bulk[197] and in the nanoscale materials.[198] As such, these vacancies play a major role in metal oxide applications.[199] Because of this, understanding the oxygen defect chemistry in metal oxides – their formation, the defect structure and interactions, has been central to studies relating to the applications of metal oxides. For thermochemical cycling applications, the thermodynamic driving forces of oxygen vacancy formation are of interest since they allow prediction of nonstoichiometric states of metal oxides under different conditions.

For a given metal oxide, the nonstoichiometry depends on the temperature and the oxygen partial pressure, pO_2, of the gas phase in equilibrium with the oxide material:

$$M_xO_y \rightleftharpoons M_xO_{y-\delta} + \frac{\delta}{2}O_2 \quad (4)$$

Knowledge of how the nonstoichiometry varies with pO_2 and temperature is important in thermochemical cycling as this would allow selection of values of these two parameters at which the metal oxide should be exposed to get to a certain reduced state and thereby maximizing fuel yield. Methods such as high temperature gravimetry, volumetric measurements, neutron diffraction, and coulometric titration are being used to measure this dependence, based on the change in mass of a metal oxide sample or in gas phase pressure and composition that result from controlled changes in pO_2 and temperature.[200] Data from these methods are commonly presented as pO_2–T–δ diagrams and are available for a great number of oxides. Analysis of a pO_2–T–δ diagram for a given metal oxide allows the determination of its nonstoichiometry at a given pO_2 and T. From these diagrams, suitable oxide compositions that can have high δ values to generate high CO and H_2 yield (Equation 3) can be identified.

In most cases, the pO_2–T–δ diagram is limited to a few to several experimental isotherms (**Figure 1.7a**). However, using these isotherms, thermodynamic quantities associated with the defect formation equilibrium for the oxide can be extracted and used to calculate additional isotherms.[201] For a given metal oxide, the change in chemical potential of oxygen as it is brought from the gas phase into the oxide lattice is a function of temperature, oxygen partial pressure, and the initial nonstoichiometric state of the oxide[200]:

$$\Delta\mu^{\circ}(\delta) = \mu^{\circ}_{M_xO_{y-\delta}} - \mu^{\circ}_{O_2} = RT \ln (pO_2) \quad (5)$$

Since the chemical potential is also related to the enthalpy and entropy for a given nonstoichiometric state by $\Delta\mu^{\circ}(\delta) = \Delta H^{\circ}(\delta) - T\Delta S^{\circ}(\delta)$, Equation 6 can be written. Thus, $\Delta H^{\circ}(\delta)$ and $\Delta S^{\circ}(\delta)$ can be evaluated from the slopes from the variation of $\Delta\mu^{\circ}$ with $1/T$ and T, respectively (Equation 7).

$$\Delta\mu^{\circ}(\delta) = \Delta H^{\circ}(\delta) - T\Delta S^{\circ}(\delta) = RT \ln (pO_2) \quad (6)$$

$$\Delta H^{\circ}(\delta) = \frac{d(\Delta\mu^{\circ}(\delta))}{d(1/T)} \quad \text{and} \quad \Delta S^{\circ}(\delta) = \frac{d(\Delta\mu^{\circ}(\delta))}{dT} \quad (7)$$

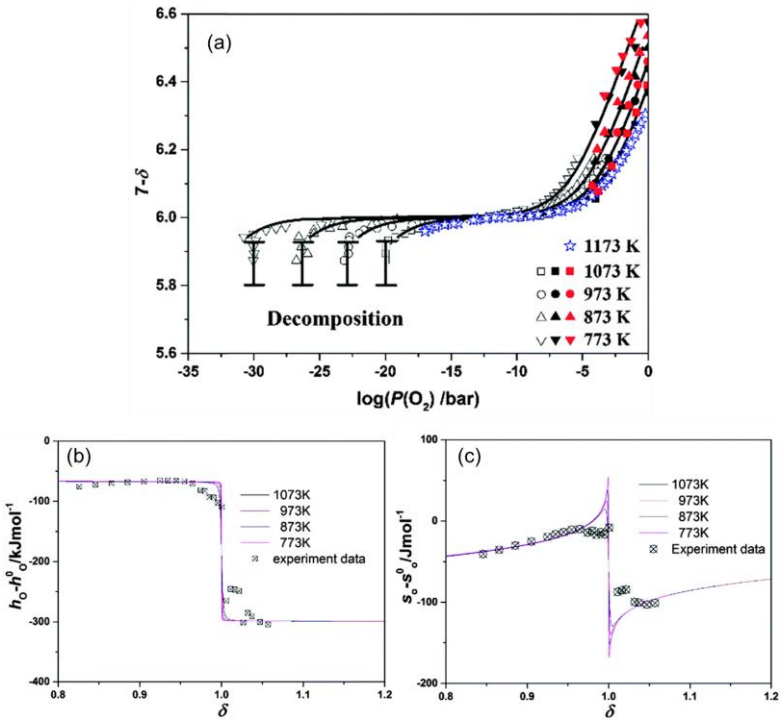

Figure 1.7. Experimental pO_2–T–δ diagram for the oxide, $Sr_3Fe_2O_7$ (a) and the calculated values of ΔH°(b) and ΔS° (c) at different oxygen nonstoichiometries, δ. Reproduced with permission from Reference 202.

Shown in **Figure 1.7b and 1.7c** are the calculated values of ΔH° and ΔS° for each nonstoichiometric state of $Sr_3Fe_2O_7$ as an example. Once this variation in ΔH° and ΔS° with δ is known, the values can be substituted in Equation 6 to generate additional δ versus pO_2 isotherms. Thus, δ can be evaluated even at temperatures and oxygen partial pressures not measured experimentally. In the following section, metal oxides of interest for thermochemical cycling are discussed.

1.2.4.1. CeO_2

CeO_2, a rare earth oxide, has been one of the most studied redox materials for solar thermochemical fuel production.[203-208] The cycle was first reported by Abanades and Flamant[209] for splitting H_2O. CeO_2 is an attractive material for thermochemical CO_2 splitting because of its ability to accommodate substantial oxygen vacancies while still maintaining a stable fluorite structure, extremely high melting temperature (2400 °C) and high catalytic activity towards carbon-containing gases.[204] The performance of CeO_2 in thermochemical cycling has been used as standard for comparing new materials for this application.[210-212]

The thermodynamic data for the oxygen vacancy formation in CeO_2 forming the nonstoichiometric oxide, $CeO_{2-\delta}$, was reported by Panlener[213] in 1975 (**Figure 1.8**). Nonstoichiometries up to $\delta = 0.3$ can be achieved under high temperatures and very low oxygen partial pressures. For instance, heating CeO_2 at 1500 °C under an atmosphere of high purity Ar (pO_2 of about 10^{-6} atm), a nonstoichiometry of 0.1 can be achieved. This corresponds to a production of 13 mL CO (at STP) per gram of CeO_2 in a single

thermochemical cycle. A large temperature dependence of the nonstoichiometry can be observed, making cycling at high reduction temperatures necessary for considerable fuel yield.

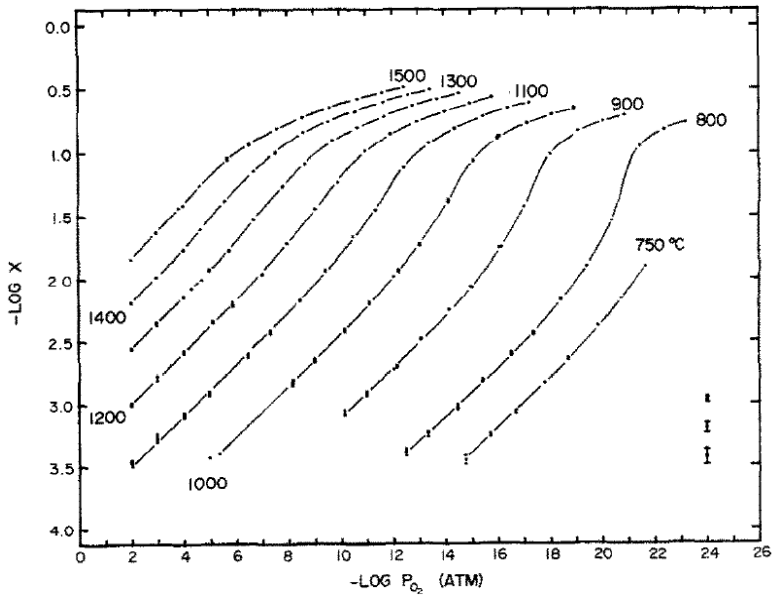

Figure 1.8. Isothermal plots of the negative log of oxygen nonstoichiometry, herein denoted as x instead of δ, versus the negative log of oxygen partial pressure. Reproduced with permission from Reference 213.

To maximize fuel production from CeO_2, doping has been used as a means to improve lattice stability towards accommodating large oxygen vacancy concentrations. In general, doping with a cation of a different ionic radius or lower charge than Ce^{4+} can cause lattice strain and charge imbalance in the CeO_2 lattice, which is compensated through the formation of oxygen vacancies.[214-217] Doping with Zr was shown to enhance the CO yield of CeO_2 albeit under slower kinetics than pure CeO_2.[218] In a study on H_2O splitting by CeO_2, doping with the trivalent lanthanides, La, Sm and Gd, however,

showed no improvement in fuel productivity.[219] In a study on H_2O splitting by CeO_2, doping with the trivalent lanthanides, La, Sm and Gd, however, showed no improvement in fuel productivity.

1.2.4.2. Perovskites

More recent work on solar thermochemical cycles has also used more complex metal oxides like the perovskites with high H_2 and CO yield.[211,212,220,221] Perovskite oxides are a class of compounds with the general formula, ABO_3, where A is usually a rare earth, alkaline earth, or alkali metal ion and B is a rare earth or transition metal. They are known to maintain a stable structure under a high degree of oxygen nonstoichiometry, with both oxygen vacancy and oxygen excess possible.[222] Oxygen nonstoichiometry of perovskites has been studied extensively by Mizusaki and coworkers who have reported thermodynamic plots for a number of perovskites[223-227] and other related structures.[228-230]

Similarly to CeO_2, perovskites have also been doped to enhance oxygen vacancy formation in these materials. A commonly used dopant, particularly for perovskites containing La^{3+} at the A site, is Sr^{2+}. Here, oxygen vacancy formation is enhanced through the charge imbalance that result from the replacement of La^{3+} with lower valent cation. In $La_{1-x}Sr_xMnO_3$ for example, increasing Sr^{2+} content result to higher stability towards oxygen nonstoichiometry.[231]

A perovskite that has been studied for thermochemical H_2O and CO_2 splitting is $La_{0.7}Sr_{0.3}MnO_3$.[212] The thermodynamic data available is limited with the highest temperature isotherm at 1273 K.[225] Thus, extrapolation of thermodynamic quantities was done to determine higher temperature isotherms and identify the reduction temperature

necessary to achieve nonstoichiometry under oxygen partial pressures achievable in the experiment (**Figure 1.9**). A problem that has been observed is the less favorable oxidation as compared to CeO_2. Nonetheless, the potential of these types of oxides has been shown, particularly in producing higher amounts of fuel than CeO_2.

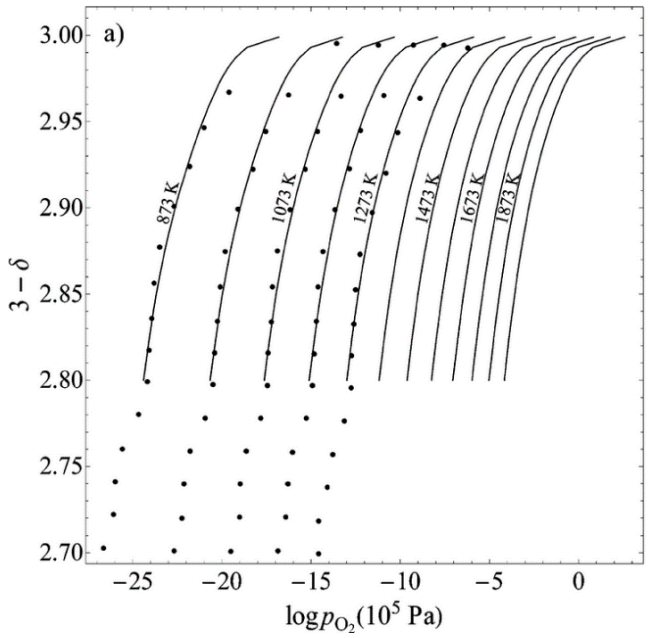

Figure 1.9. Oxygen nonstoichiometry in $La_{0.7}Sr_{0.3}MnO_3$. Shown are extrapolated lines for the higher temperature isotherms based on the original equilibrium data (black dots) from Mizusaki. The higher temperature isotherms were obtained by thermodynamic calculations using Equations 6-7. Reprinted with permission from Reference 212. Copyright © 2013 American Chemical Society.

1.2.5 Material and Process Considerations in Thermochemical Cycling

The amount of CO or H_2 produced from a thermochemical cycle is limited by the degree of nonstoichiometry of the metal oxide (Equation 3). Thus, metal oxides that can be reduced to higher δ values are desirable since they can, in principle, yield a greater amount of CO in the oxidation step. While this is true, there are other important factors,

both material and process-related, that determine the feasibility of a metal oxide thermochemical cycle as a mode of solar energy storage.

The so-called solar-to-fuel efficiency, η_{STF}, has been used as metric for the comparative evaluation of potential solar energy-based fuel generation methods. It is the ratio of the chemical energy of the fuel produced to the solar energy incident on the collector.[232] It is usually expressed in terms of H_2 as the fuel product, η_{STH}. The η_{STH} for H_2 generation using solar driven electrolysis is 18%,[233] which reflects the combined efficiencies of solar energy collection as heat, the conversion of heat to electricity, and finally the conversion of electricity to fuel. For solar thermochemical metal oxide cycles, heat is directly converted to fuel, and the estimated achievable η_{STH} is 25%.[232,234]

The all-inclusiveness of η_{STH} imposes process compatibility and material requirements on the metal oxide used for thermochemical cycling (**Figure 1.10**). Siegel et al.,[232] Allendorf et al.,[235,236] and Perret[237] summarized these guidelines as follows. First, the reduction temperature, T_{red}, of the oxide must be below 1500 °C to minimize radiation losses at increased temperatures and for operating temperatures to be close to the highest optimal temperature of a CSP (1125 °C for a dish solar collector). Second, the reduction must occur at $pO_2 = 10^{-4}$ atm as a lower practical limit, accounting for the additional work needed when using a pump. Third, the difference between T_{red} and T_{ox} (oxidation temperature) should be less than 500 °C. This favors reaction kinetics, optimal heat recuperation when cycling between the two temperatures. Fourth, the oxide should be non-volatile under the cycling conditions to minimize mass losses, e.g., volatile hydroxides in the presence of H_2O. Fifth, the oxide should have a high melting

temperature since sintering can be significant at about $0.4T_{mp}$ (T_{mp} is the melting point of the oxide). This means that oxides with T_{mp} < 3300 °C would sinter when cycled at T_{red} = 1500 °C. Because only a few materials have such a high T_{mp}, any porosity introduced in a metal oxide to improve kinetics will have a definite lifetime but could still be designed to withstand as many thermochemical cycles as possible. Lastly, the kinetics of reduction and oxidation must match the heat flux from CSP. The rate of the oxidation step in particular, could be increased by the introduction of porosity in the metal oxide.

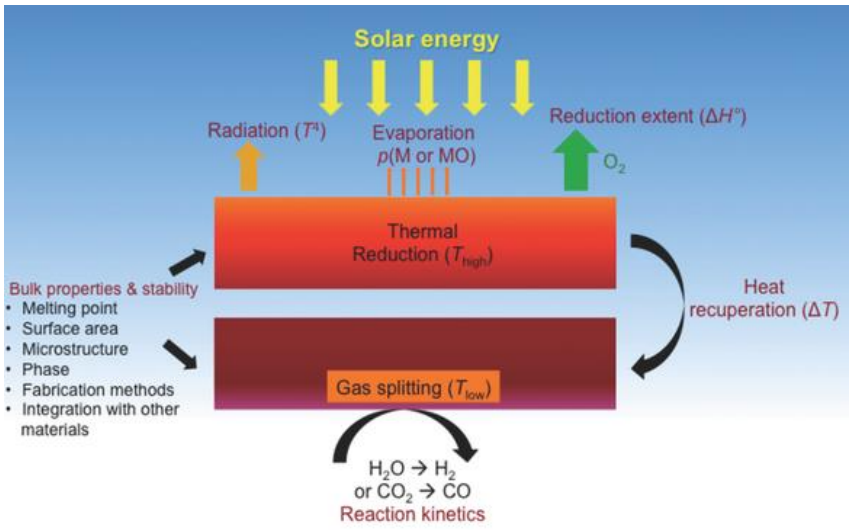

Figure 1.10. Process and material-related factors that affect the efficiency of a metal oxide thermochemical cycle. Reproduced with permission from Reference 235.

1.3 Natural Gas Conversion

The variety and quantity of petroleum-based products, which include fuels, commodity chemicals, and materials, reflect our heavy reliance on petroleum. The global demand for petroleum has increased steadily over the years. In the United States, an

average of 19.9 million barrels of petroleum were consumed per day in 2017, about 1.6% higher than the consumption rate in 2016.[238] Demand is predicted to grow further by 1.8% in 2018.[238] Being a finite resource, however, the need to develop processes to make petroleum products from alternative feedstocks is certain. In the US, the recent boom in natural gas production makes it advantageous as an energy source and as feedstock for chemicals and materials production. The US is projected to be a net exporter of natural gas through 2040, at which point natural gas would account for 40% of the country's total energy production, while remaining as a net petroleum importer.[239]

1.3.1 Light Alkanes in Natural Gas as Feedstock

Natural gas consists of primarily of methane (over 80%, varies from source to source) along with other light alkanes such as ethane, propane and butane. The latter three are often referred to as natural gas liquids (NGLs) because they can be easily condensed and separated from methane on extraction from natural gas deposits.[240]

The light alkanes in natural gas are useful for on-purpose product synthesis, in comparison to the cracking of petroleum, which is not product selective. Routes for the conversion of the light alkanes in natural gas to useful chemical intermediates are shown in **Figure 1.11**. These intermediates are syngas (a mixture of H_2 and CO), methanol, and light olefins such as ethylene (C_2H_4) and propylene (C_3H_6). Commercial technology for these conversions exists, and in some cases indirect conversions (e.g., methanol synthesis via syngas) are more economical than direct ones (e.g., methanol from partial oxidation of methane).[201] Syngas, methanol and olefins are then used to make a wide range of

commodities.[241] Syngas is a precursor to gasoline, diesel, olefins, and oxygenates (e.g., acetic acid, ethanol) through the well-establish Fischer-Tropsch process.[185,186] It is also used in the Haber-Bosch process to make ammonia,[242] and in the oxo process for the production of aldehydes.[243] Methanol can be used as fuel[244] or it can be used to make other fuels and chemicals via processes such as catalytic oxidation to fomaldehyde,[245] carbonylation to acetic acid,[246] methanol-to-gasoline (MTG),[247] and methanol-to-olefins (MTO).[248] Light olefins are important precursors for industrially important polymers such as polyethylene and polypropylene. They can also be converted to gasoline and distillates via oligomerization, also known as catalytic condensation.[249] These routes show the versatility of natural gas as feedstock and in all these conversions, there are opportunities for catalytic chemistry to improve process efficiency, selectivity, and economy.

Catalysis is necessary in natural gas conversion because of the simplicity and chemical inertness of the molecules that are being transformed. All of the bonds in light alkanes are C–H and C–C bonds. The bond energies are high (420.5 $kJ \cdot mol^{-1}$ for C–H and 377.4 $kJ \cdot mol^{-1}$ for C–C in ethane). These bonds are also non-polar due to the similar electronegativities, χ, of carbon (χ = 2.5) and hydrogen (χ = 2.1). This makes bond cleavage highly unfavorable and conversion processes energetically demanding. Aiding and controlling bond cleavage is key to the selective transformation of light alkanes to different chemicals.

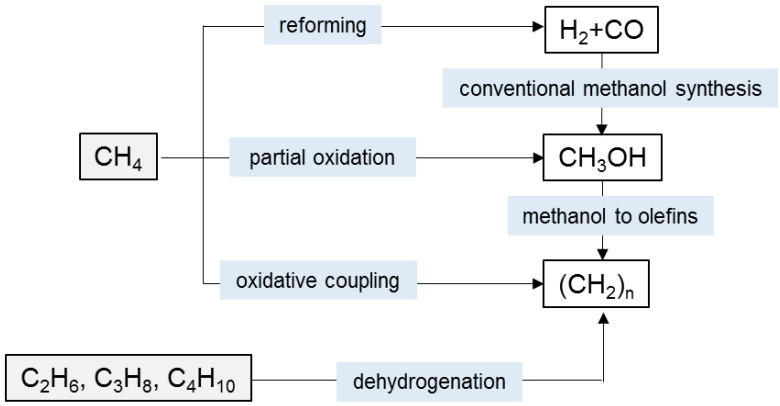

Figure 1.11. Production routes of important chemical intermediates from light alkanes.

1.3.2 C-H Bond Activation

The cleavage of the C–H bond can be facilitated by metal-based catalysts. Modes of activation are shown in **Figure 1.12**. Some of the mechanisms involve direct interaction of the alkane with the metal while others involve interaction of the alkane with just the atoms (e.g., ligands, counter-ions) surrounding the metal. Lewis acid/base pairs can promote heterolytic C–H bond cleavage: the Lewis acidic metal, M, can stabilize the carbanion (formation of M–C bond), while the base site, X, stabilizes the proton (X–H bond formation). This mode involves electron-deficient metals. An example of a Lewis acid/base pair catalyst applied to C–H activation is Li-doped MgO used in the oxidative coupling of methane. For this catalyst, the active sites are the Mg^{2+} and O^{2-} ions on the morphological defect sites (step and corners) of the catalyst surface.[250] Electrophilic activation and oxidative addition are more commonly observed in homogeneous catalysts.[251] Electrophilic activation involves complexes of late or post-transition metals such as Pd^{2+}, Pt^{2+} and Pt^{4+}.[252] The name is due to the displacement of a proton in the alkane by the electron-deficient metal (electrophile) yielding M-alkyl

species. Oxidative addition, on the other hand, occurs for catalysts with electron-rich metal centers, typically complexes of late transition metals that are coordinatively unsaturated.[253] The metal center coordinates to the C–H bond in a similar way that metals can coordinate dihydrogen. Metal back donation to the non-bonding orbitals of the alkane leads to bond cleavage and formation of M-alkyl and M–H bonds. The metal center is oxidized by 2 e^- in the process.[254] In some C–H activation mechanisms, the metal does not directly interact with the alkane. Activation is carried out by ligands such as O atoms which abstract the H from the alkane, as seen in metal oxides.[255]

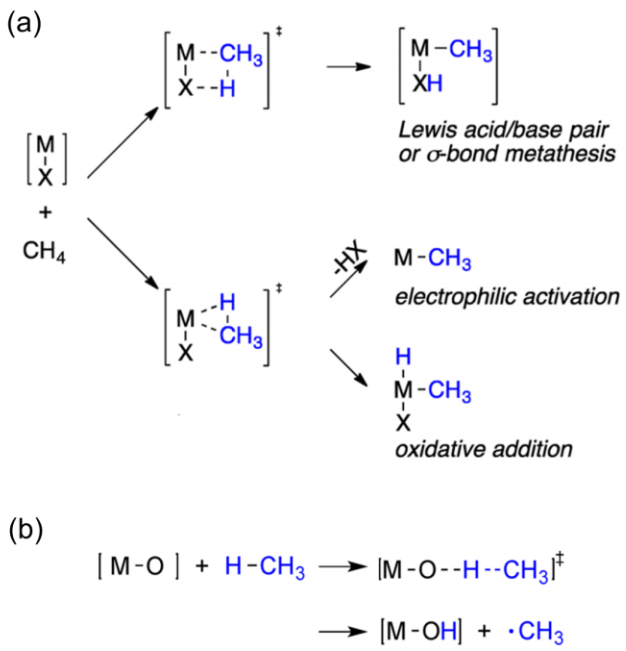

Figure 1.12. Activation of the C–H bond by metal-based catalysis. The alkane can interact directly with the metal (a) or to atoms bonded to the metal (b). Reprinted with permission from Reference 255. Copyright © 2016 American Chemical Society.

1.3.3 Catalytic Processes for the Conversion of Natural Gas

The reactions for the initial conversion of the light alkanes in natural gas are equilibrium reactions and are affected by pressure and temperature following Le Chatelier's principle. The following outlines the reactions involved and the relevant reaction conditions, catalyst systems and product yields in these conversions.

1.3.3.1. Methane reforming to syngas

Reforming is the primary route for the conversion of natural gas to value-added chemicals. Syngas is produced from methane via reforming using either H_2O (steam reforming) or CO_2 (dry reforming) as oxidant. Both reactions are endothermic, and the oxidant dictates the ratio of CO to H_2 produced from the conversion:[256]

$$CH_4 + H_2O \rightleftharpoons CO + 3H_2 \text{ (steam reforming)} \qquad \Delta H^0_{298K} = 206 \text{ kJ·mol}^{-1}$$

$$CH_4 + CO_2 \rightleftharpoons 2CO + 2H_2 \text{ (dry reforming)} \qquad \Delta H^0_{298K} = 247 \text{ kJ·mol}^{-1}$$

$$CO + H_2O \rightleftharpoons CO_2 + H_2 \text{ (water-gas shift)} \qquad \Delta H^0_{298K} = -41 \text{ kJ·mol}^{-1}$$

The last reaction, the water-gas shift reaction, can be set-up to occur at a reactor downstream of the reformer to adjust the CO to H_2 ratio in the reformed gas by producing more H_2 (forward water-gas shift) or more CO (reverse water-gas shift). This is done to match the requirements of the succeeding conversion of the syngas product. The Fischer-Tropsch process for example, requires a syngas feed with a CO to H_2 ratio of 2 to convert the syngas to heavy paraffins and liquid transportation fuels.[257]

Steam reforming is carried out in a reactor operating at 800–1000 °C and 15–30 atm, with an H_2O:CH_4 feed ratio of ca. 3.[257] The equilibrium methane conversion

under these conditions is ≥85%.[258] The catalyst used industrially is Ni nanoparticles supported on alumina (Ni/Al_2O_3).

1.3.3.2. Partial oxidation of methane to methanol

Controlled oxidation of methane can yield methanol:

$$CH_4 + ½\ O_2 \rightleftharpoons CH_3OH \qquad \Delta H^0_{298K} = -129\ kJ \cdot mol^{-1}$$

The reaction is exothermic and spontaneous even at room temperature. However, it is difficult to control the oxidation, because the reaction proceeds via a gas phase free radical mechanism, and because the more oxidized products, CO and CO_2 have higher stability than methanol. The non-catalytic conversion of methane to methanol has been reported with up to 83% selectivity at 12% conversion when carried out at 50 atm and 330 °C.[259] Reviews have noted, however, the poor reproducibility of results from non-catalytic methane to methanol conversions, including the promising results.[260,261] Zhang et al. cited methanol selectivities of 40–50% at 2–5% methane conversion as the more commonly reported literature values.[260]

A number of heterogenous catalysts have been tested for the reaction, but conversions and selectivities that are even lower than the non-catalytic system were observed.[262,263] Heterogeneous catalysts that showed activity in this gas phase conversion are Fe-sodalite[264] (25% selectivity and 5.8% methane conversion at 435 °C and 50 atm) and Ga_2O_3/MoO_3[265] (22% selectivity at 3.0% methane conversion at 455 °C and 15 atm).[262]

Currently, methanol is being produced industrially from natural gas through an indirect route via syngas. Syngas is converted to methanol with 99% selectivity using a

$Cu/Zn/Al_2O_3$ catalyst operated at 200-300 °C and 50-100 atm.[266,267] For the direct path of methanol production from methane oxidation to be competitive, a minimum selectivity of 90% at 7.5% methane conversion needs to be achieved.[268]

1.3.3.3. Oxidative coupling of methane

Ethylene can be obtained from the oxidative coupling of methane. The reaction involves the formation of methyl radicals on the surface of a catalyst, which desorb and couple in the gas phase. The initial product, ethane, undergoes oxidative dehydrogenation to form ethylene. Both C2 hydrocarbons, ethane and ethylene are primary products:[255,269]

$$2CH_4 + ½\ O_2 \rightleftharpoons C_2H_6 + H_2O \qquad \Delta H^0_{1073K} = -1465\ kJ\cdot mol^{-1}$$

$$2CH_4 + O_2 \rightleftharpoons C_2H_4 + 2H_2O \qquad \Delta H^0_{1073K} = -1163\ kJ\cdot mol^{-1}$$

Reaction selectivites are often reported as the combined C2 selectivity. Among the promising results are those from Thomas et al. who reported 47% C2 selectivity (ethylene to ethane ratio was 25) at 42% methane conversion using a bismuth oxychloride catalyst.[270] The reaction was carried out at 720 °C and with a diluted feed of 2:1 CH_4 to O_2.[270] Lundsford[269] in 2003 characterized oxidative coupling catalysts as generally having strong basicity (e.g., MgO), which was more recently supported by Zavyalova, et al.[271] from a statistical analysis of 421 publications from the last 30 years. Compositions with alkali and alkaline earth metal dopants have improved selectivity, while Mn, W, and Cl improve activity.[271]

1.3.3.4. Dehydrogenation of light alkanes

Olefins such as ethylene propylene can be obtained from the dehydrogenation of the corresponding alkane:

$$C_2H_6 \rightleftharpoons C_2H_4 + H_2 \qquad \Delta H^0_{298K} = 137\ kJ{\cdot}mol^{-1}$$

$$C_3H_8 \rightleftharpoons C_3H_6 + H_2 \qquad \Delta H^0_{298K} = 124\ kJ{\cdot}mol^{-1}$$

The dehydrogenation occurs above 500 °C, with the equilibrium conversion increasing at increasing temperatures and lower pressures (**Figure 1.13**). The reaction can also be coupled to the reverse water-gas shift reaction to remove the H_2 product and push the equilibrium forward.[272] Two industrial catalysts are being used today: CrO_x/Al_2O_3 (Catofin process) and Pt-Sn/Al_2O_3 (Oleflex process). The Catofin process operates at 575 °C and pressures of 0.2–0.5 atm.[174] The activity is attributed to coordinatively unsaturated Cr^{3+} sites generated on the catalyst surface during the reaction.[273] The Oleflex process operates at 525–705 °C and pressures of 1–3 atm.[274] Other catalysts with reported activity include GaO_x, VO_x, MoO_x, and carbon-based compositions such as carbides and nanotubes.[275]

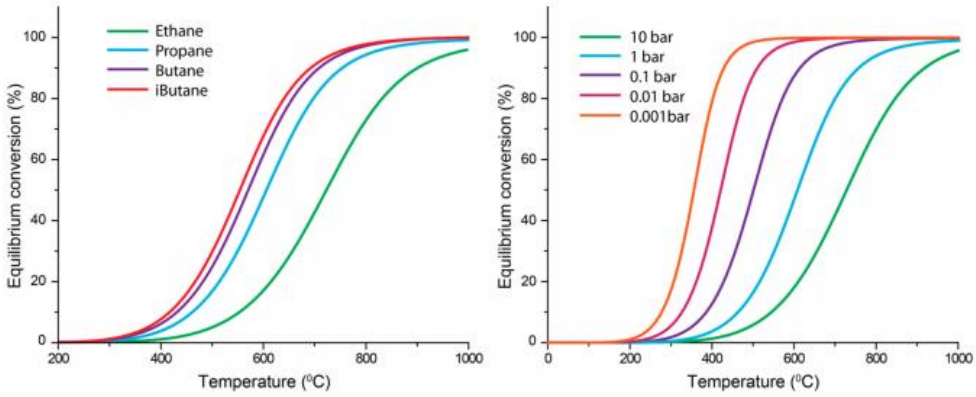

Figure 1.13. Temperature dependence of the equilibrium conversion of light alkanes at 1 bar (left) and the pressure and temperature dependence of the equilibrium conversion of propane. Reprinted with permission from Reference 174. Copyright © 2014 American Chemical Society.

1.3.4 Metal-Organic Frameworks in Natural Gas Conversion Catalysis

Recent reports[276-279] show the potential of MOF-based catalysts for the conversion of light alkanes. The MOF structure functions as host to a wide variety of catalytically active species. In the work by Xiao et al.,[277] these are Fe-oxo species, similar to those in metalloenzymes that carry out C–H functionalization like cytochrome P450.[280] The MOF is the mixed-metal $Fe_{0.1}Mg_{1.9}$(dobdc) (dobdc = 2,5-dioxido-1,4-benzenedicarboxylate), featuring terminal Fe-oxo groups that can activate the C-H bond of ethane and converts it to ethanol at 96% selectivity at 75 °C. Phan et al[278] reported two vanadium-containing MOFs, MIL-47 and MOF-48, that convert methane to acetic acid at 24% and 36% yield, respectively at 80°C. Ikuno et al[279] prepared Cu-oxo clusters supported on the MOF, NU-1000 which converts methane to methanol at 45–60% selectivity at 150 °C. The same MOF was used by Li et al[276] to support active Co^{2+} species, which is active in the oxidative dehydrogenation of propane to propene. While there are only a handful of examples that directly involve conversion of light alkanes so far, there are many others describing the manipulation of the C–H bond in higher alkanes and olefins using MOF-based catalysts.[281-287]

Notably, the reactions involving MOFs are carried out under mild conditions because of stability limitations as discussed in Section 1.1.2. This limits catalysis to those reactions that are exothermic, such as partial oxidation of alkanes, that can occur at low temperatures. Derivatization of MOFs to more stable forms should be done to catalyze reactions at high temperatures. An example is the work of Zhao et al.,[288] where a Cr MOF, MIL-101 was infiltrated with aluminum isopropoxide and calcined to make porous

Cr_2O_3/Al_2O_3 catalysts that was active for isobutane dehydrogenation at 600 °C (93% isobutene selectivity at 60% conversion).

1.4 Outline of the Remainder of the Thesis

The next sections of this thesis present work on the preparation and optimization of porous catalyst structures for application in solar thermochemical fuel production and high temperature natural gas conversion. The catalyst syntheses rely on sol-gel and templating techniques to create thermally stable porous structures and scaffolds made of metal oxides and silica.

Chapter 2 explores the use of wood as a hard template for the production of macroporous oxides for enhancing the kinetics of solar thermochemical cycling. Macroporous catalysts with large pore size and wall dimensions are desirable for this application because they can accommodate the large grain sizes formed at the high temperatures (> 1000 °C) used in cycling, making them resistant to structural collapse. The wood structure featuring macroporous channels was replicated into active metal oxide compositions and tested for thermal stability and activity in solar thermochemical CO production.

Chapters 3, 4 and 5 describe the work on the thermal stabilization of metal-organic framework-based catalytic metal sites for high temperature catalysis related to natural gas conversion. Chapter 3 presents the benchmark work on the development of a nanocasting method to incorporate a silica matrix in the pores of MOFs. The silica matrix serves as a secondary scaffold for the MOF-based metal sites, maintaining their site-

isolation at temperatures beyond the thermal stability limit of the parent MOF. The effectiveness of the nanocasting method in stabilizing MOF-based catalytic clusters was demonstrated in the Zr MOF, NU-1000. Chapter 4 depicts the extension of this silica nanocasting method to post-synthetically modified MOFs which have additional active metals installed onto the MOF nodes. Here, the nanocasting of bimetallated NU-1000 is reported. In Chapter 5, the generality in the applicability of the nanocasting technique to different MOF compositions is explored. Considerations associated with MOF stability under nanocasting conditions are discussed, and the method is tuned to enhance its compatibility with different MOFs. Finally, a summary and future outlook are given in Chapter 6.

Chapter 2

Thermochemical CO Production using Macroporous Oxides

This work was done in collaboration with Prof. Jane Davidson and Robert de Smith of the Solar Energy Laboratory, University of Minnesota, who carried out the thermochemical cycling experiments discussed herein.

2.1 Introduction

The use of concentrated solar energy to drive metal-oxide thermochemical cycles that split water and carbon dioxide is a potentially promising approach to reduce the global reliance on fossil fuels and to store solar energy, the earth's most abundant but intermittent source of renewable energy, in chemical form. The product gases, H_2 and CO, can be utilized directly for electricity generation or as valuable feedstocks for the production of liquid fuels including methanol, dimethyl ether, or Fischer-Tropsch products.[185-187,289,290]

Solar metal-oxide thermochemical cycles rely on the ability of select metal oxides to release and uptake oxygen in response to changes in temperature and oxygen partial pressure. One of the well-studied solar thermochemical cycles is the CeO_2 cycle:[203-206,291,292]

$$CeO_2 \rightarrow CeO_{2-\delta} + \frac{\delta}{2} O_2$$

$$CeO_{2-\delta} + \delta CO_2 \rightarrow CeO_2 + \delta CO$$

$$\text{Net reaction: } \delta CO_2 \rightarrow \delta CO + \frac{\delta}{2} O_2$$

CeO_2 is an attractive material for thermochemical CO_2 splitting because the rate of oxygen diffusion is high, and CeO_2 has the ability to accommodate substantial oxygen lattice vacancies while still maintaining a stable fluorite structure.[204] CeO_2 is currently the standard for comparing the performance of new materials for this application.[210-212]

In addition to the interest in identifying new metal oxide material compositions for solar thermochemical cycles, there is also a growing recognition that material

architecture is important.[291-295] Material structures that permit optimal solar penetration and absorption, rapid heat transfer, minimal pressure drop, high reactivity, and long-term stability for cycling at temperatures as high as 1500 °C are desired. The importance of material morphology on other attributes such as heat transfer, including solar absorption, and pressure drop will depend in large part on how the material is configured within a reactor. For example, in the case of a bed of particles, mass and heat transfer will be dominated by the bed structure rather than the individual particle morphology. High surface area is particularly crucial for reoxidation of the solid, in which the heterogeneous surface reaction has been found to be the rate-limiting step.[204,291,294,295]

Porous structures present a way of enhancing the kinetics by increasing the available surface area of the metal oxide.[294] Particularly high surface areas are obtained in nanoporous solids. However, pores tend to collapse at high temperatures as grain growth causes the pore walls to fuse together, reducing the active surface area.[296] A recent study by Rudisill et al. showed an enhancement of the kinetics of CO production from the CeO_2 cycle by molding the oxide into a three-dimensionally ordered macroporous (3DOM) structure, thereby increasing the specific surface area available for reaction.[293] Yet an instability of the pore structure was observed when the material was cycled at a reduction temperature of 1200 °C due to sintering. This structural instability at the high temperatures used was also observed with other porous structures studied for this application and led to the loss of surface area concomitant with the decline in kinetic performance of these materials.[203,206] A porous CeO_2 monolith made by Chueh et al. showed a decline in average oxidation rate from 3.2 to 1.3 mL min^{-1} g^{-1} over the first 100

cycles due to sintering when the material was reduced at 1500 °C and oxidized with steam at 800 °C.[203] Similarly, porous CeO_2 felt which has a surface area of 6.0 m^2 g^{-1} showed strong evidence of sintering after 10 cycles, with the highest reduction temperature attained during cycling being 1582 °C.[206] Thus, a more thermally stable porous structure is required for enhancing the kinetics at these high temperatures. So far, excellent sintering resistance in a porous structure has been achieved with CeO_2 reticulated porous ceramic (RPC).[291] Recently, Furler et al. reported the thermochemical CO_2 splitting by a CeO_2 RPC with dual-scale porosity, which exhibited only a slight decrease in oxidation rates from 2.01 to 1.76 mL min^{-1} g^{-1} over 20 cycles.[295]

In this work, the use of wood as a template to prepare porous structures for application in thermochemical CO_2 splitting was examined. Wood is a natural composite material consisting chiefly of the biomolecules cellulose, hemicellulose, and lignin.[297] It has a hierarchical cellular structure, and depending on the species and growth conditions, varying degrees of macro-, meso-, and microporosity can be found in different wood samples.[298] This open porosity makes wood accessible to infiltration, and thus it can function as a template to produce inorganic materials that are themselves porous. Biomorphic oxides and carbides,[49,50,299-301] carbon composites,[48,302,303] and zeolitic materials[304,305] have been synthesized using wood templates. While most of these templated materials are intended for low-temperature applications including photocatalysis, imaging, and gas sensing,[306,307] this work demonstrates that wood templates are also suitable for preparing materials for high-temperature applications. Micrometer-sized cellular channels make up the macroporous structure of wood. Also

present on the cell walls are circular openings called pits, which serve as interconnections between the individual cells. Using wood as a template allows the facile synthesis of a porous structure with pore sizes and wall thicknesses on the micrometer scale, i.e., larger dimensions than those in 3DOM CeO_2 and $Ce_xZr_{1-x}O_2$ structures that offer kinetic enhancement of CO_2 splitting up to only 1200 °C.[308] This study is based on the hypothesis that the walls of wood-templated CeO_2 (WT CeO_2), although yielding lower specific surface areas than 3DOM CeO_2, are thick enough to accommodate sintering of grains and maintain porosity when the material is exposed to high temperatures, so that the reduction temperature can be extended beyond 1200 °C. Here, WT CeO_2 is prepared via a modified Pechini method, and its structure, sintering behavior, and thermochemical cycling performance are studied at temperatures up to 1500 °C.

2.2 Experimental Methods

Cerium(III) chloride heptahydrate (99.9%) and citric acid monohydrate (≥99.0%) were purchased from Sigma-Aldrich, ethylene glycol (≥99.0%) from Macron Fine Chemicals, nonporous CeO_2 (3 mm pellets, 99.9%) from Alfa Aesar, nitrogen (10.6 ± 0.1 ppm of O2, balance N_2) and carbon dioxide (99.99%) from Airgas, and krypton (99.999%) from Matheson. The nonporous CeO_2 pellets were ground and sieved to sizes between 180 and 850 μm prior to use in the experiments. Eastern white pine (*P. strobus*) wood samples were obtained from a local wood supplier and used without further treatment. Deionized water produced on-site with minimum resistivity of 18.2 MΩ·cm was used in all experiments.

2.2.1 Material Synthesis

WT CeO_2 was synthesized via the Pechini process. A precursor solution was prepared using $CeCl_3 \cdot 7H_2O$, citric acid, ethylene glycol, and water in a 1:3:1:37 mole ratio. The templating process was carried out by immersing cut pine wood pieces of dimensions 0.5 cm × 0.5 cm × 4 cm into the precursor solution for 24 h. The soaked wood pieces were then removed from the solution and placed in an oven at 90 °C for 24 h to gel. To remove the wood template, the gelled wood samples were first calcined at 310 °C for 2 h and 450 °C for another 2 h under static air. A temperature ramp rate of 2 °C min^{-1} was used during the calcination. Subsequently, each sample was heated at the targeted reduction temperature (1200−1500 °C) for 4 h in a Carbolite high-temperature tube furnace, operated under static air, and using an 8 °C min^{-1} ramp rate.

2.2.2 Thermochemical Cycling

Thermochemical cycling experiments were carried out at the Solar Energy Laboratory, University of Minnesota by Prof. Jane Davidson and Robert De Smith. The cycling performance of WT CeO_2 samples, annealed at their targeted reduction temperatures, was evaluated for reduction temperatures from 1200 to 1500 °C and oxidation with CO_2 at 800 °C. The performance was compared with that of nonporous CeO_2 for reduction temperatures of 1400 and 1500 °C and to recently published data for electrospun fibers for reduction at 1400 °C under the same cycling conditions reported by Gibbons et al.[309] Nonporous CeO_2 provides a good baseline comparison for new materials for thermochemical cycling applications and has been used previously to assess

the degree of enhancement in CO productivity that can be achieved with these new systems.[211,212,293,308] Prior to cycling, the nonporous CeO_2 samples were also treated at 1400 and 1500 °C in the Carbolite furnace following the same heating procedure as WT CeO_2 .

The materials were thermochemically cycled in an infrared imaging furnace. **Figure 2.1** shows a sketch of the experimental setup. The WT and nonporous samples were sieved between 180 and 850 μm prior to cycling. Heat-treated CeO_2 samples (0.5 g) were loosely loaded into a 9.5 mm i.d. alumina tube, forming a bed of particles 4−10 mm long, which was held in place with a porous alumina disk. The alumina tube was placed horizontally in the infrared imaging furnace (ULVAC RIKO VHT-E44), and a Pt/Pt−Rh thermocouple (±3.8 °C at 1500 °C) was inserted in each end of the tube. The thermocouple positioned downstream of the bed was used to control the power of the furnace, and the second thermocouple was embedded in the CeO_2 sample to monitor its temperature. Inert and oxidizing gas flows were regulated with mass flow controllers (with an accuracy of ±1% of the flow) and pneumatic valves. The product gas stream exiting the furnace was monitored for O_2 and CO using a Raman laser gas analyzer (RLGA; Atmosphere Recovery, Inc., model RLGA-8800) with a sampling frequency of 1 Hz. The accuracy of the Raman laser gas analyzer is ±0.02 mol % based on calibration with bottled gases of known CO (5.056% CO, 10.08% CO_2, balance N_2) and O_2 concentrations. For a total gas flow rate of 250 mL min^{-1} and a ceria mass of 0.5 g, the measurement accuracy is ±0.1 mL min^{-1} g^{-1}. For our testing system and cycling approach, measurement of O_2 is much less accurate than measurement of CO because the

rates of O_2 release during reduction are low, yielding poor signal-to-noise ratios in the measurement of O_2 concentration by the Raman laser gas analyzer. This inaccuracy in the O_2 measurement causes the CO:O_2 ratio to deviate from 2:1 in experiments in which O_2 release rates are particularly slow, for example at reduction temperatures less than 1400 °C for WT and for all reduction temperatures for nonporous ceria. For this reason, we analyze the material based solely on CO concentration. The CO concentration data are used to calculate ceria nonstoichiometry, which is the basis of evaluation of the WT material. However, we report O_2 despite the low signal-to-noise ratio because the trends in the data are consistent with the more accurate CO data and provide qualitative information on the impact of changes in reduction temperature.

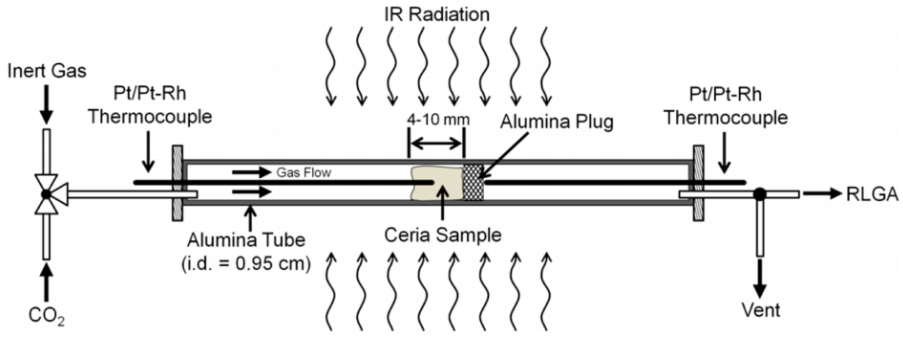

Figure 2.1. Experimental apparatus for thermochemical cycling, comprising a CeO_2 sample in an alumina tube which is placed in an IR imaging furnace, the gas flow control system, and gas analysis equipment. The CeO_2 sample is cycled at reduction temperatures from 1200 to 1500 °C and oxidized with CO_2 at 800 °C.

WT CeO_2 was first tested at reduction temperatures from 1200 to 1500 °C in 100 °C increments with a fixed oxidation temperature of 800 °C to investigate the rates of reduction and oxidation as well as the sintering resistance of the WT morphology.

Nonporous CeO_2 powder (**Figure 2.2** and **Figure 2.3**) was cycled at reduction temperatures of 1400 and 1500 °C for comparison.

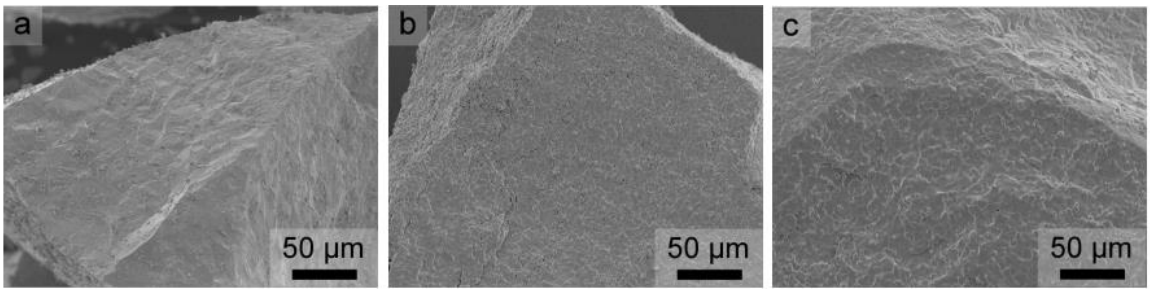

Figure 2.2. SEM images of nonporous commercial CeO_2 before (a) and after heat treatment at 1400 °C (b) and 1500 °C (c) for 4 h. The same heat-treated samples with particle sizes between 180 to 850 µm were used for the thermochemical cycling experiments.

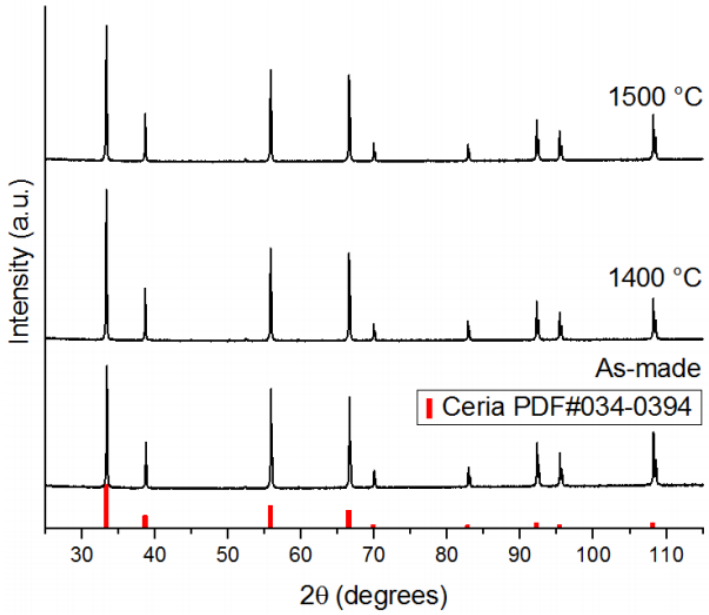

Figure 2.3. XRD patterns of nonporous commercial CeO_2 before (as-made) and after heat treatment at the indicated temperatures (1400 °C and 1500 °C) for 4 h. The patterns are consistent with the cubic fluorite structure of CeO_2.

Each experiment consisted of 21 cycles. The temperature and gas flow profile during a typical cycle is shown in **Figure 2.4**. During thermochemical cycling, CeO_2 was first reduced by ramping the temperature from 800 °C to the target reduction temperature at a rate of 200 °C min^{-1} while flowing 250 mL min^{-1} of inert gas (10.6 ppm of O_2 in N_2) through the ceria sample to maintain a low oxygen partial pressure. The temperature ramp rate was selected to ensure accurate measurement of temperature and control of the IR imaging furnace. It should be noted that the ramp rate is not a limitation of the WT CeO_2 samples being tested but rather of the response time of the thermocouples used in the reactor. Because the reduction rate follows the temperature ramp,[204,293,294] the measured rates of O_2 release are low and close to the detection limit of the RLGA. The reduction temperature was held for 5 min; at 1400 °C, the ceria reached approximately 40% of its equilibrium nonstoichiometry by the end of reduction. Longer reduction times would allow the samples to reach equilibrium and produce higher CO yield per cycle **Figure 2.5**. However, the long reduction periods required to reach equilibrium are not practical for implementation, because they yield low average rates of reduction and also require excessive amounts of inert gas and power input. After reduction, the temperature of the CeO_2 was lowered to 800 °C at a rate of 200 °C min^{-1}, and oxidation was initiated by switching from the flow of N_2 to a 250 mL min^{-1} flow of CO_2. Oxidation conditions proceeded until the CO signal was no longer detectable and oxidation reached completion.

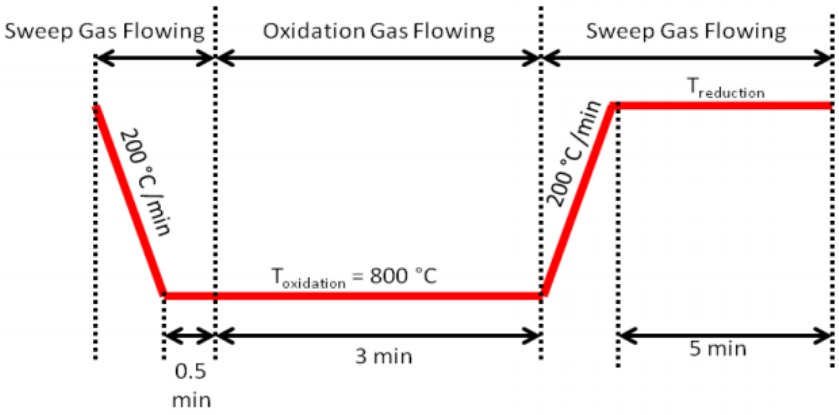

Figure 2.4. Temperature and gas flow profile during a thermochemical cycle of the CeO_2 samples. For WT CeO_2, thermochemical cycles were performed at $T_{reduction}$ from 1200 to 1500 °C. For comparison, nonporous CeO_2 samples were cycled at $T_{reduction}$ equal to 1400 °C.

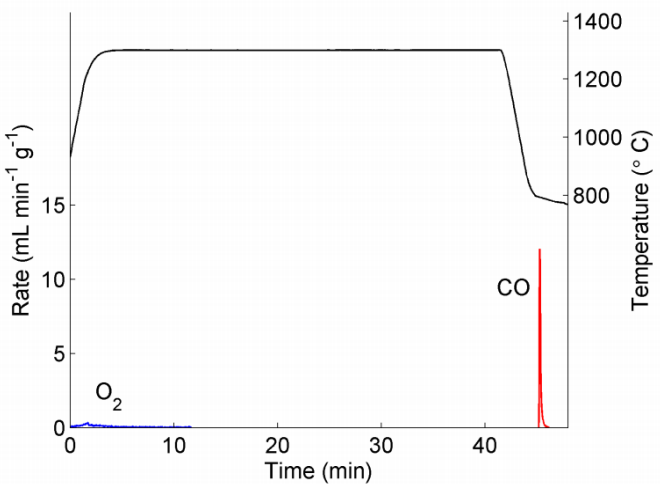

Figure 2.5. Temperature profile, O_2 production rate, and CO production rate from WT CeO_2 reduced at 1300 °C for a longer period (40 min instead of 5 min) and the same CO_2 splitting duration and temperature (3 min at 800 °C). The thermodynamic limit for CO production under these conditions is 1.7 mL g^{-1}. Actual CO production from the cycle is 1.5 mL g^{-1}. Note that the trace for O_2 is only qualitative.

To compare the WT CeO_2 and electrospun CeO_2 fibers, the test conditions reported by Gibbons et al.[309] were replicated at a reduction temperature of 1400 °C,

which is the high temperature limit for material stability for both morphologies. In each experiment, ~0.3 g of reactive material was used. Oxidation took place at ~750 °C and reduction at 1400 °C. The rising temperature ramp was at 100 °C min^{-1}, while the falling temperature ramp was at 200 °C min^{-1}. The gas flow rate during reduction was 300 mL min^{-1} of sweep gas (10 ppm of O_2 in N_2); during oxidation, 100 mL min^{-1} of CO_2 was added to the sweep gas flow, resulting in a stream of 25% CO_2. For all data, the transient rates of O_2 and CO production were calculated as

$$\dot{V}_i' = \frac{x_i \dot{V}_{total}}{m_{CeO_2}}$$

where $\dot{V}_i'$ is the volumetric rate of O_2 or CO production per unit mass of CeO_2 (evaluated at the reference conditions of 25 °C, 1 bar); x_i is the mole fraction of O_2 or CO in the product stream, measured by the RLGA; $\dot{V}_{total}$ is the total volumetric flow rate (also evaluated at the reference conditions); and m_{CeO_2} is the mass of the CeO_2 sample. Oxidation rates of the material structures are compared at the same values of δ calculated using CO concentration data. The less accurate O_2 data are qualitatively consistent with the more accurate CO data and provide qualitative information on the impact of changes in reduction temperature. The approach of comparing oxidation on the basis of nonstoichiometry, as opposed to the approach used in prior studies of comparing rates versus oxidation time,[203,204,291,293,294,308] provides an assessment of the effects of reduction temperature and material morphology on the rate of oxidation for situations in which oxidation is initiated at different nonstoichiometries. The CeO_2 nonstoichiometry during oxidation, δ, was evaluated using the CO production rate data:

$$\delta(t) - \delta_{eq} = \frac{M_{\mathrm{CeO_2}} P_{ref}}{R T_{ref}} \int_{t}^{t_{\mathrm{eq}}} \dot{V}_i'(\hat{t}) d\hat{t}\,,$$

where $M_{\mathrm{CeO_2}}$ is the molecular weight of CeO_2, P_{ref} and T_{ref} are the reference pressure (1 bar) and absolute temperature (298.15 K), t_{eq} is the time at which the CeO_2 reaches equilibrium at the end of the oxidation step, and δ_{eq} is the equilibrium nonstoichiometry at t_{eq} ($\delta_{\mathrm{eq}} \cong 0$ for oxidation at 800 °C with CO_2).

2.2.3 Characterization

The morphology of the wood template and the CeO_2 samples before and after cycling was probed using scanning electron microscopy (SEM). SEM measurements were performed on a JEOL 6500 scanning electron microscope operating at 5.0 kV accelerating potential. Prior to SEM analysis, all samples were sputter coated with a conductive thin film (50 Å) of Pt. Crystal structures were identified by X-ray diffraction (XRD) analysis using an X'Pert Pro diffractometer with an X'Celerator detector. A Co anode (Kα, λ = 1.789 Å) operated at 45 kV and 40 μA was used as the radiation source. Surface areas of the samples were determined by gas sorption analysis using a Quantachrome Autosorb iQ2 analyzer. Nitrogen was used as the adsorbate for the WT CeO_2 sample calcined at 450 °C, and krypton was the adsorbate for the samples treated at 1200−1500 °C. The samples were degassed at 200 °C and 1 mTorr for 8 h prior to the analysis. Brunauer−Emmett−Teller (BET) surface areas were evaluated from the adsorption isotherm within the 0.05−0.35 P/P0 range. A CHN analysis of WT CeO_2 (1200 °C) was performed by Atlantic Microlabs (Norcross, GA). The wood template was

analyzed by inductively coupled plasma−mass spectrometry using a Thermo Scientific XSERIES 2 ICP-MS with ESI PC3 Peltier cooled spray chamber, SC-FAST injection loop, and SC-4 autosampler by Dr. Rick Knurr at the Earth Science Department, University of Minnesota. Samples were diluted appropriately, and 40 ppb of indium internal standard was added. All elements were analyzed using He/H_2 collision reaction mode. Scanning electron microscopy-energy-dispersive X-ray spectroscopy (SEM-EDS) compositional analyses were acquired on a JEOL JXA-8900 electron microprobe operated at 15.0 kV accelerating potential. Samples were coated with a thin film (70 Å) of C prior to SEM-EDS measurements.

2.3 Results and Discussion

2.3.1 Replication of the Wood Structure

Softwood species like Eastern white pine (**Figure 2.6a**) have a cellular structure composed mainly of long parallel channels from the tracheid cells. These cells run along the direction of the tree trunk and branches. Softwoods also have ray cells, which are channels having thicker walls and smaller pore diameters than the tracheids. Ray cells occur between the tracheid cells and are oriented perpendicular to them (i.e., from the center of the tree to the bark). Shown in **Figure 2.6b** is an SEM image of the cross section of the tracheid cells of the Eastern white pine wood used as a template in this study. The channel diameters are approximately 20−50 μm, and the wall thicknesses are between 1 and 10 μm. Also visible in the image are the pits, which are the circular holes that line the channel walls, serving as interconnections between the channels. As a

template, the macroporous structure of wood allowed it to be easily infiltrated with an aqueous Pechini precursor solution containing Ce^{3+}−citrate complexes and ethylene glycol. The wood surface contains polar functional groups such as alcohols, esters, and carboxylic acids, allowing the aqueous precursor solution to wet this surface through hydrophilic interactions. Upon heat treatment, these functionalities serve as sites for condensation of the metal citrates and ethylene glycol, resulting in a gel coating on the wood surface (**Figure 2.6c**). During the calcination step, the Ce^{3+} Pechini gel on either side of the channel walls converts to the oxide form. As the wood burns off, a gap is created between these two solidifying Pechini gel layers. The layers then sinter and fuse together, closing the gap between them. As a result, pore diameters in the product structure approximately replicate the pore diameters in the original wood template. The wall thicknesses, on the other hand, are controlled by the template coating process and are not necessarily the same as those in the template. Thicker walls can be achieved by carrying out multiple infiltration and gelation steps during the synthesis. This coating process, followed by calcination, yielded porous CeO_2 as a positive replica of the wood template. An SEM image of WT CeO_2 after calcination at 450 °C is shown in **Figure 2.6d**. At this temperature, no significant shrinkage is observed compared to the original feature dimensions of the wood template. Typical pore diameters are in the 20−50 μm range, while wall thicknesses of 0.5−1 μm are common.

The XRD patterns of WT CeO_2 show a pure phase with peaks consistent with a cubic fluorite structure (**Figure 2.7**). The walls of the porous material are composed of nanocrystallites about 25 nm in diameter, estimated from XRD line broadening using the

Scherrer equation. This crystallite size is greater than that reported by Rudisill et al. for 3DOM CeO_2, which was calcined under the same heating profile during its synthesis.[293] The larger crystallite size obtained with the wood template could be attributed to increased local heating due to the exothermic combustion of the wood template compared to the polymer spheres used for the template to synthesize 3DOM CeO_2.

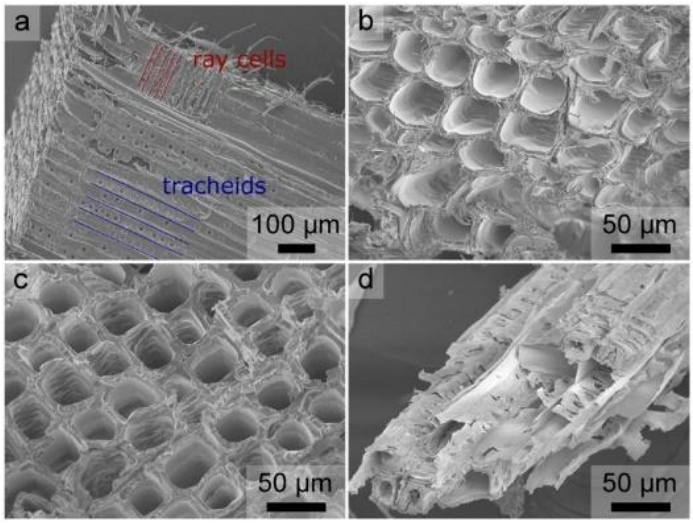

Figure 2.6. SEM images of (a) pristine Eastern white pine wood showing tracheid cells (elongated channels whose walls are lined with circular holes) and ray cells (smaller channels running perpendicular to the tracheids), (b) the cross section of tracheid cells, (c) the wood coated with a Ce^{3+} Pechini gel, and (d) the wood-templated CeO_2 product.

Further heat treatment was carried out to stabilize the wood-templated structure at the targeted reduction temperatures in the thermochemical cycles for CeO_2. Elemental analysis detected no residual carbon, hydrogen, or nitrogen from the wood template after thermal treatment at 1200 °C. Metals analysis of the wood template by ICP-MS (**Table 2.1**) indicates the metals that could be incorporated in the WT CeO_2 product from the template. Among the elements, Mg^{2+}, K^{+}, and Ca^{2+} are the ones present in highest

amounts in wood. SEM-EDS analysis was done on WT CeO_2 to detect these impurities but only Ca and Al were detected and at very low levels. (**Figure 2.8**). It is possible that Mg^{2+} and K^+ leached from the wood template during infiltration of the Pechini precursor which would explain why they were not detected by SEM-EDS. At these low levels, the impurities from the wood template should not affect the activity or thermal stability of WT CeO_2.

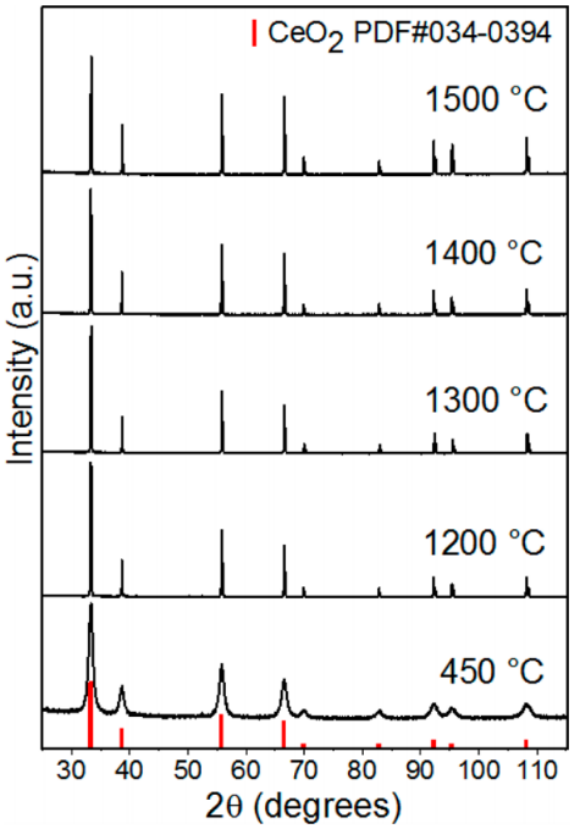

Figure 2.7. XRD patterns of WT CeO_2 samples labeled with the temperatures at which the samples were thermally treated: as-synthesized sample at 450 °C and further treatment at higher temperatures (1200 to 1400 °C) which are the targeted reduction temperatures for thermochemical cycling of WT CeO_2.

Table 2.1. ICP-MS analysis of the wood template identifying potential impurities in WT CeO_2.

element	content in wood (ppb)	element	content in wood (ppb)
^{24}Mg	98.32	^{75}As	0.07
^{31}P	25.35	^{85}Rb	1.92
^{39}K	1107.00	^{88}Sr	1.48
^{44}Ca	46.4	^{90}Zr	0.47
^{47}Ti	0.79	^{107}Ag	0.98
^{55}Mn	8.90	^{111}Cd	0.12
^{56}Fe	14.78	^{137}Ba	0.82
^{60}Ni	3.88	^{139}La	0.63
^{65}Cu	3.15	^{140}Ce	4.45
^{66}Zn	10.43	^{208}Pb	0.31

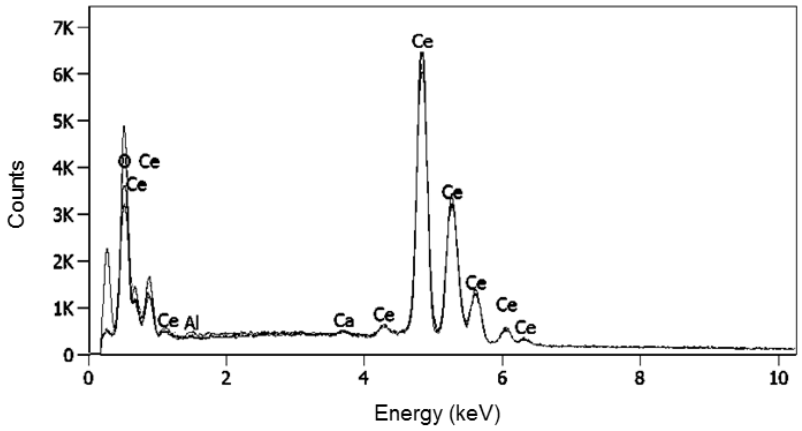

Figure 2.8. SEM-EDS analysis of WT CeO_2 treated at 1400 °C showing peaks for Ce, Ca, Al and O. Ca (10.2 ± 2.1 mmol per mol Ce) and Al (21.0 ± 10.0 mmol per mol Ce) are impurities from the wood template.

Grain growth occurred during heat treatment WT CeO_2 at the targeted reduction temperatures, as evidenced by the peak narrowing in the XRD patterns (**Figure 2.7**). Grain growth was accompanied by a reduction of surface area from 74.0 m^2 g^{-1} for WT CeO_2 calcined at 450 °C to values from 0.11 to 0.27 m^2 g^{-1} for the samples treated at 1200−1400 °C (**Figure 2.9**). The surface area values for the WT CeO_2 treated at 1200−1400 °C are comparable to those reported for a porous CeO_2 monolith and for RPC with dual-scale porosity, which also have micrometer-scale features in their porous structure but were prepared at higher temperatures than WT CeO_2 (see last row of **Table 2.2**).[203,295]

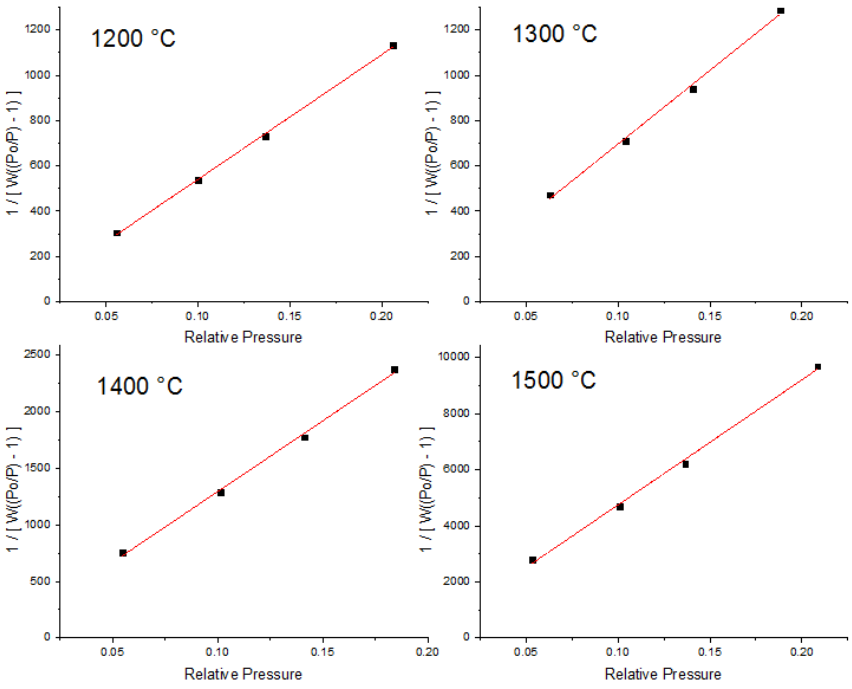

Figure 2.9. Linear BET plots from Kr sorption data of WT CeO_2 treated at the indicated temperatures. The BET surface areas evaluated from these plots are as follows: 0.27 m^2 g^{-1} at 1200 °C, 0.22 m^2 g^{-1} at 1300 °C, 0.12 m^2 g^{-1} at 1400 °C, and 0.03 m^2 g^{-1} at 1500 °C.

Table 2.2. Comparison of cycling conditions of several sets of CO_2 splitting data for CeO_2.

morphology	**wood-templated**	**Zr-doped electrospun fibers**	**dual-porosity RPC**	**3DOM**	**felt**	**porous monolith**
Reference	this study	Gibbons et al. 2014[309]	Furler et al. 2014[295]	Rudisill et al. 2013[293]	Furler et al. 2012[206]	Chueh et al. 2010[203]
Type of experiment	IR Furnace	IR Furnace	TG	IR Furnace	Solar Simulator	IR Furnace
Sample mass (g)	0.5	0.3	1.158	1.0	127	0.429
$T_{reduction}$ (°C)	1200-1500	1200-1500	1500	1200	1767-1855	1500
Reduction duration (min)	5	5	30	1	30	20
Sweep gas composition	10 ppm O_2 in N_2	10 ppm O_2 in N_2	180 ppm O_2 in Ar	10 ppm O_2 in N_2	< 2ppm O_2 in Ar	10 ppm O_2 in Ar
Sweep gas flow rate (mL min^{-1})	250	300	260	100	2000	1000
Mass-specific sweep gas flow rate (mL min^{-1} g^{-1})	500	1000	225	100	16	2300
$T_{oxidation}$ (°C)	800	800	1000	850	1200	800
Oxidation duration (min)	5-10	2	60	2	15	10
Oxidizer composition	100% CO_2	25% CO_2 in N_2	38% CO_2 in Ar	25% CO_2 in N_2	H_2O:CO_2 = 6:7 mole ratio	50% CO_2 in Ar
Oxidizer flow rate (mL min^{-1})	250	400	260	100	2500	500
Mass-specific oxidizer flow rate (mL min^{-1} g^{-1})	500	1333	225	100	20	1200
Rising temperature ramp rate (°C min^{-1})	200	100	20	800	400 (T < 1327 °C); 20 (T > 1327 °C)	1700
Falling temperature ramp rate (°C min^{-1})	200	200	20	800	125-135	1700
Peak CO production rate (mL min^{-1} g^{-1})	1200 °C: 1.3 1300 °C: 3.7 1400 °C: 10 1500 °C: 1.4	1200 °C: 7 1300 °C: 19 1400 °C: 3 1500 °C: 34 1400 °C (after 100+ cycles): 14	Not reported	6.3	0.48	10
Total CO produced (mL g^{-1})	1200 °C: 0.2 1300 °C: 0.8 1400 °C: 2.1 1500 °C: 2.5	1200 °C: 0.9 1300 °C: 1.6 1400 °C: 4.7 1500 °C: 7.0 1400 °C (after 100+ cycles): 3.9	2.1	0.9	3.15	6.9
Sintering Temperature (°C): Surface Area (m^2 g^{-1})	1200 °C: 0.27 1300 °C: 0.22 1400 °C: 0.12 1500 °C: 0.03	1200 °C: 3.17 1300 °C: 1.54 1400 °C: 0.60 1500 °C: 0.28 1400 °C (after 100+ cycles): 0.34	1600 °C: 0.095	1200 °C (after 50+ cycles): 3.95	Not reported: 6.0	1350: 0.1

While closing the smaller micropores and mesopores, thermal treatment did not eliminate the open pore network in the sintered materials. The effects of heating on the wood-templated structure are shown in **Figure 2.10**. The channels remained intact up to a temperature of 1400 °C, with some shrinkage in the pore network (typical pore diameters in the 15−25 μm range). At 1500 °C, the channels were no longer intact, but the structure remained open.

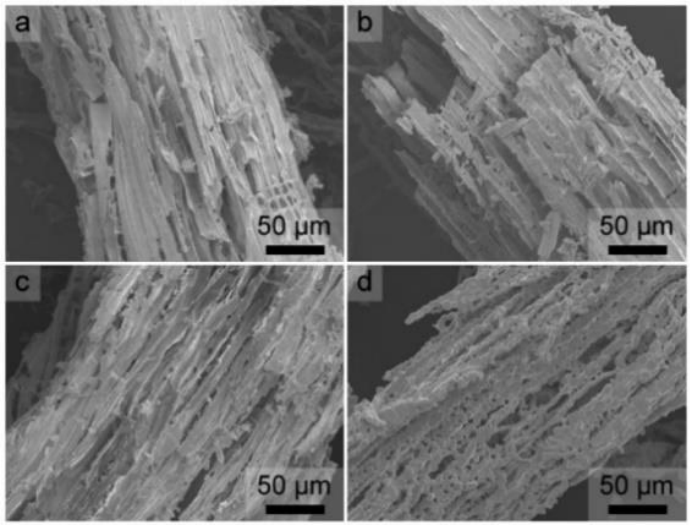

Figure 2.10. Structure of WT CeO_2 after treatment at (a) 1200, (b) 1300, (c) 1400, and (d) 1500 °C. Significant structural change due to extensive grain growth is observed between the samples treated at 1400 and 1500 °C. However, the structure remains open.

The open pore space and the wall thickness of WT CeO_2 play a significant role in the retention of its porous structure on exposure to high temperatures. The walls are thick enough to accommodate grain growth at these temperatures, while the space between opposing walls prevents these from fusing together. As a result, grain growth is restricted along the channel walls. Higher magnification SEM images of the sintered samples are

shown in **Figure 2.11**. Larger grains are formed at higher temperatures, with crystallite sizes as large as 5 μm observed in WT CeO_2 sintered at 1400 °C. The wood-templated structure is preserved up to this temperature, in which case the grains are still significantly smaller than the wall dimensions. At 1500 °C, the average grain size approaches the wall dimensions of WT CeO_2, resulting in significant changes in pore structure. The observed stability of the wood-templated structure at temperatures from 1200 to 1400 °C surpasses that of 3DOM CeO_2, which already showed extensive structural destabilization at 1200 °C.[293] Operating at higher temperatures favors the endothermic reduction of CeO_2 during the two-step conversion of CO_2 to CO and O_2, as illustrated in the following section.

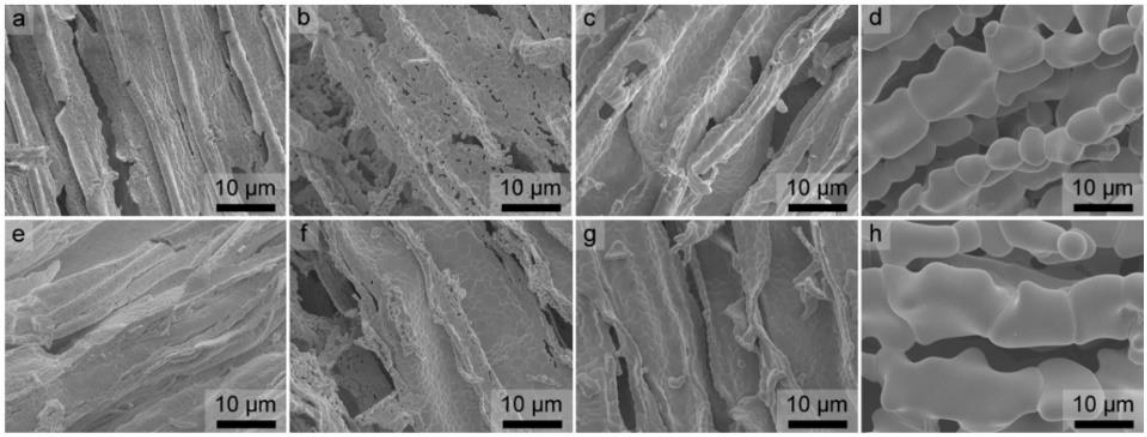

Figure 2.11. High resolution SEM images of WT CeO_2 showing the differences in grain size after heating at (a, e) 1200 °C, (b, f) 1300 °C, (c, g) 1400 °C and (d, h) 1500 °C. Images a–d correspond to the heat-treated materials, while images e–h are the same materials after the thermochemical cycling experiments described in the following section. No significant changes in grain size are observable in the pre- and post-cycled samples from 1200 °C to 1400 °C; grain sizes become slightly larger after cycling the sample at a reduction temperature of 1500 °C.

2.3.2 Thermochemical Cycling

The cycling behavior (CeO_2 reduction followed by CO production) of the presintered WT and nonporous ceria was steady over 21 reduction/oxidation cycles for all tests, without any observable changes in sample morphology of the heat-treated materials after cycling. The rates of O_2 and CO production are shown in **Figure 2.12**.

As mentioned in the Experimental Methods section, instrumental noise and the low gas production caused the $CO:O_2$ ratio to deviate from the expected value of 2:1. While relative O_2 production rates can be deduced, quantification of the total O_2 produced through integration of the O_2 production curves yields values that are lower than the actual amount of O_2 produced during reduction because, as discussed, the slow response rate of the thermocouples favored the use of slow ramp rates (200 °C min^{-1}) over faster ramp rates during the temperature swings between the reduction and oxidation temperatures. The rate of reduction followed the temperature ramps, indicating that the reduction is a heat-transfer-limited process consistent with other studies.[204,293,294] A consequence of this is the slow O_2 production, approaching the limit of detection of the Raman laser gas analyzer. For easier visualization of a cycle, **Figure 2.13** shows the temperature and gas production profiles during a typical thermochemical cycle for WT CeO_2 reduced at 1400 °C and reoxidized at 800 °C. CO was produced immediately after the temperature was lowered to 800 °C, and the gas flow was switched to CO_2. CO production quickly reached a peak rate of 9 mL min^{-1} g^{-1} and then decayed as the oxygen vacancies created during reduction were filled.

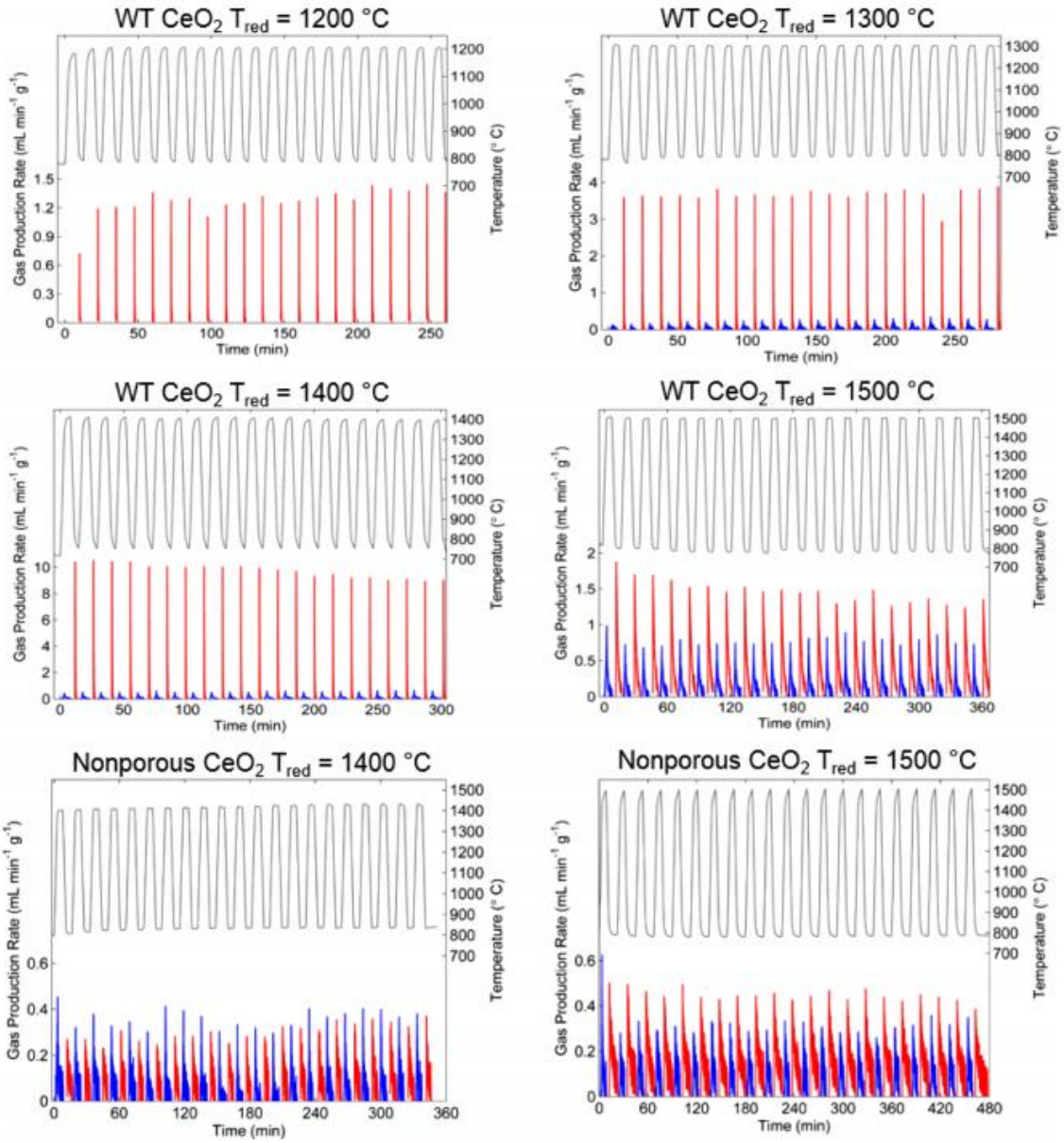

Figure 2.12. O_2 (blue) and CO (red) gas production rates from WT CeO_2 and nonporous CeO_2 for 21 cycles at the indicated reduction temperatures.

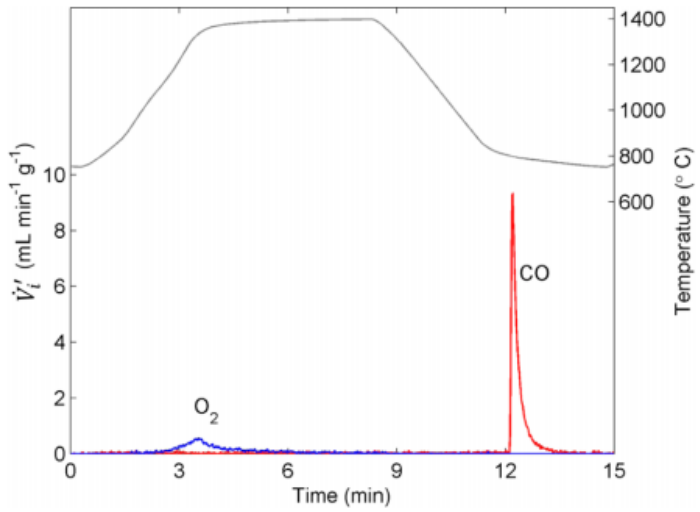

Figure 2.13. Temperature profile, O_2 production rate, and CO production rate during a typical thermochemical cycle, using a maximum WT CeO_2 reduction temperature of 1400 °C and a CO_2 splitting temperature of 800 °C.

Representative rates of CO production at 800 °C following reductions at 1200−1500 °C for WT CeO_2 and 1400−1500 °C for nonporous CeO_2 are compared in **Figure 2.14**. For WT CeO_2, peak CO production rates increased as the reduction temperature was raised from 1200 to 1400 °C because the improved reduction thermodynamics allowed the CeO_2 to reach higher nonstoichiometries, which are favorable for the oxidation reaction. However, after reduction at 1500 °C, the CO production rates decreased by a factor of 7 compared to oxidation after reduction at 1400 °C, from 9 to 1.3 mL min^{-1} g^{-1}. The decreased CO production rates following reduction at 1500 °C correlate with the decline in surface area from 0.11 to 0.03 m^2 g^{-1} as the maximum temperature during heat treatment was raised from 1400 to 1500 °C (**Figure 2.9**). The peak CO production rates for all WT CeO_2 samples were higher than those of the nonporous CeO_2 samples, which had specific surface areas of < 0.05 m^2 g^{-1}.

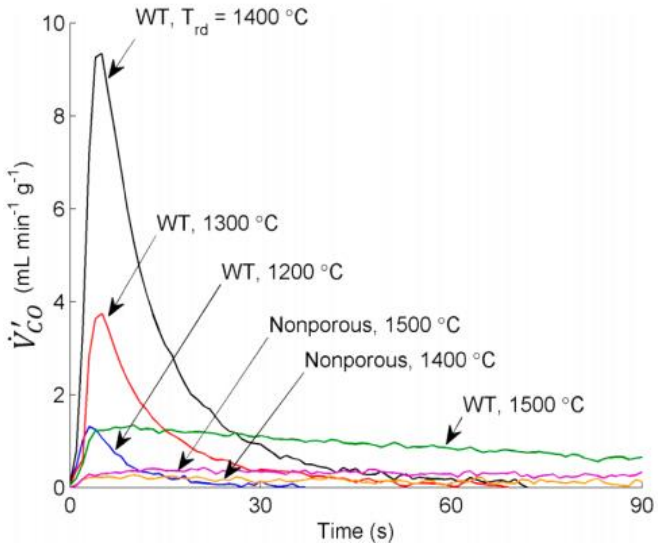

Figure 2.14. Transient CO production rate for WT CeO_2 at 800 °C following reduction at temperatures ranging from 1200 to 1500 °C and for nonporous CeO_2 powder at 800 °C following reduction at 1400−1500 °C. The WT CeO_2 sample reduced at 1500 °C, and both of the nonporous CeO_2 samples continued to produce measurable CO after 90 s (not shown).

Figure 2.15 shows oxidation rate versus CeO_2 nonstoichiometry for the two morphologies at each evaluated reduction temperature. This figure demonstrates the advantages of the WT material over nonporous CeO_2. Rates are plotted from the nonstoichiometry reached at the end of oxidation to the maximum nonstoichiometry attained during the preceding reduction. For each morphology, the maximum δ, which is consistent with the total amount of CO produced in a cycle, increased monotonically with reduction temperature, and for each reduction temperature, the rate of oxidation increased with increasing nonstoichiometry. The dependency of oxidation rate on δ is supported by kinetic models of CeO_2 oxidation.[310] At each reduction temperature, the WT CeO_2 reached a higher nonstoichiometry for the given time of reduction than the nonporous CeO_2. Furthermore, the WT CeO_2 produced CO faster at each δ. The rate of oxidation for

the WT material was 5−6 times faster than for the nonporous CeO_2 after reduction at 1400 °C and 2−3 times faster after reduction at 1500 °C.

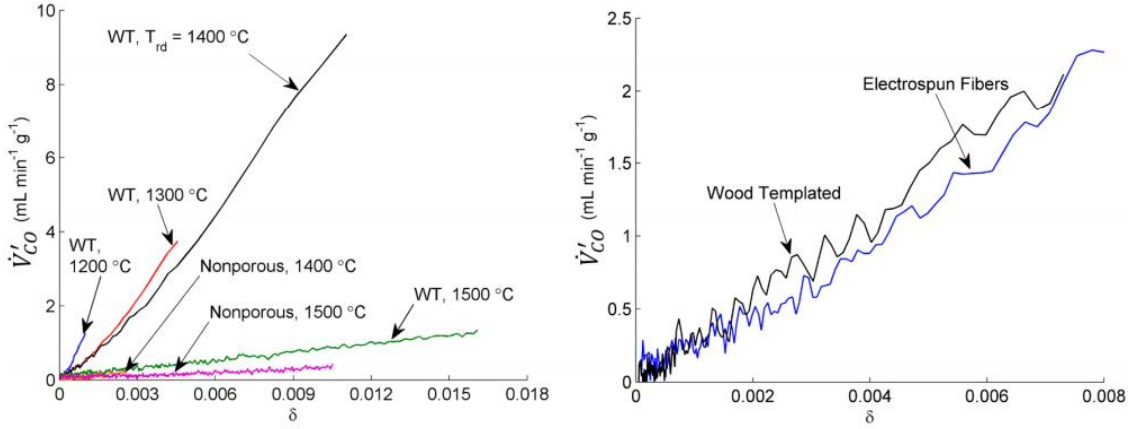

Figure 2.15. (left) CO production rate as a function of δ for WT CeO_2 at 800 °C following reduction at 1200−1500 °C and for nonporous CeO_2 at 800 °C following reduction at 1400−1500 °C. (right) CO production rate as a function of δ for WT CeO_2 and Zr-doped electrospun fibers (2.5 mol % dopant) at 800 °C following reduction at 1400 °C.[309]

The differences in the slopes of the curves for WT CeO_2 and nonporous CeO_2 in **Figure 2.15** (quantified in **Table 2.3**) are attributed primarily to the differences in specific surface area. The rate of increase of oxidation rate with nonstoichiometry is slowest for the nonporous material, for which the surface area is < 0.05 $m^2\ g^{-1}$, regardless of reduction temperature. For the WT material, from 1200 to 1400 °C, small reductions in the slope are consistent with modest changes in surface area as the reduction temperature was increased. In this temperature range, the benefit of improved reduction thermodynamics with increasing temperature outweighed the detrimental effect of reduced surface area, and as a result, the maximum δ increased with increasing reduction

temperature. From 1400 to 1500 °C, however, the loss in surface area was so pronounced that oxidation rates decreased significantly at all δ, reflected by the large change in slope of the curve at 1500 °C. Thus, for WT CeO_2, operating with a reduction temperature of 1400 °C offered the best balance of the benefit of improved reduction thermodynamics (achieving $\delta \cong 0.01$ for the cycling conditions used in this study) with the loss of surface area due to sintering (BET surface area = 0.11 $m^2\ g^{-1}$).

Table 2.3. Volumetric rate of CO production from nonporous and WT CeO_2

sample	$T_{reduction}$ (°C)	slope of $\dot{V}'_{CO}$ vs. δ in (mL mol_{CeO_2} min^{-1} g^{-1} $mol^{-1}_{vacancies}$)
WT CeO_2	450	-
	1200	1300
	1300	800
	1400	800
	1500	70
commercial CeO_2[b]	1400	70
	1500	30

[a]$\dot{V}'_{CO}$ is the volumetric rate of CO production per unit mass of CeO_2, evaluated at the reference conditions of 25 °C and 1 bar, and δ is the nonstoichiometry in $CeO_{2-\delta}$. [b]Particle sizes are between 180 and 850 μm.

A comparison of the total CO production from the WT and nonporous CeO_2 samples for each thermochemical cycle is shown in **Figure 2.16**. These data reflect the trends presented in **Figure 2.15** for maximum δ. Total CO production increased with reduction temperature as predicted by thermodynamics.[213] The representative CO

productivity for WT CeO_2 is 0.2 mL g^{-1} after reduction at 1200 °C, 0.8 mL g^{-1} after reduction at 1300 °C, 2.1 mL g^{-1} after reduction at 1400 °C, and 2.5 mL g^{-1} after reduction at 1500 °C. The total CO produced from WT CeO_2 reduced at 1400 °C is ~4 times higher than for nonporous CeO_2 (0.5 mL g^{-1}) cycled under the same conditions. The degree of enhancement is lower after reduction at 1500 °C, at which point CO production from WT CeO_2 is less than twice of nonporous CeO_2 (1.7 mL g^{-1}) as a result of the significant structural change in the wood-templated structure that occurred at this temperature. **Table 2.2** shows a comparison of the CO production of WT CeO_2 with some other materials in the literature, along with their respective cycling conditions. Direct comparison of the cycling behavior of the WT material with other porous architectures reported in the literature[203,206,293,295,309] is confounded by widely varying reported testing conditions. Total production as well as peak production rates of CO vary due to differences in the duration of reduction/oxidation cycles, flow rates and composition of the reducing and oxidizing gases, and test configuration, which ranges from TGA studies to evaluation of materials in a prototype solar thermochemical reactor. In addition, the rate of release of O_2 during reduction depends on the rate at which the temperature is ramped up. Differences in performance can therefore not be attributed directly to sample morphology.

In terms of total CO production per cycle, WT CeO_2 yielded a higher value (2.5 mL g^{-1}) than dual-porosity CeO_2 (2.1 mL g^{-1}),[295] when both are cycled at a reduction temperature of 1500 °C. This increase is despite the latter being cycled at longer reduction and oxidation times, which allows gas production to approach equilibrium and

thus produce more CO. Perhaps our best comparison of the WT CeO_2 is with 2.5 mol% Zr-doped CeO_2 electrospun fibers. This comparison is appropriate because even though the compositions are not identical, the $Ce_{0.975}Zr_{0.025}O_2$ fibers achieved similar CO production rates to undoped CeO_2 in the prior study, and the experimental conditions could be replicated in the test apparatus used in the present study. Lower peak CO production rates and total CO productivity are seen in WT CeO_2 as compared to Zr-doped electrospun fibers, monolith, and felt structures. However, it is important to note that the Zr dopant in the electrospun fibers inherently increases the amount of CO that can be produced from a thermochemical cycle as compared to pure CeO_2 and also increases the sintering resistance of porous CeO_2.[308] The same is true when using longer reduction and oxidation times as well as reduction temperatures during cycling. In this regard, we tested WT CeO_2 under the same cycling conditions (**Table 2.2**) as 2.5 mol % Zr-doped electrospun CeO_2 fibers. The two materials exhibited similar rate performance although the latter produced more CO, which could be due to the presence of the Zr dopant as mentioned above. A comparison of the CO production for WT CeO_2 and fiber materials over the range of nonstoichiometry for which data are available for both is shown in **Figure 2.15**. This demonstrates the viability of the wood-templated structure for thermochemical cycling applications, with further improvement in structural stability and performance expected by doping and choice of the wood template.

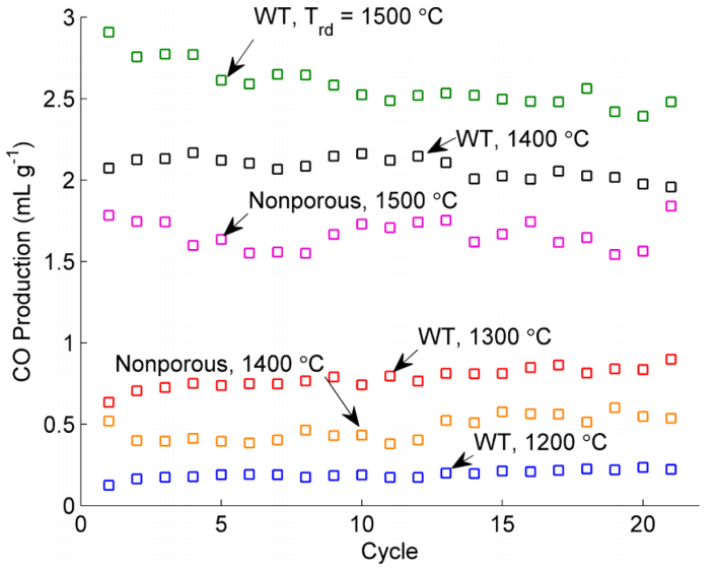

Figure 2.16. Total CO produced during the oxidation step in each thermochemical cycle of nonporous and WT CeO_2 after reduction at the indicated temperatures.

2.4 Conclusion

In this chapter, the viability of wood templating to produce porous CeO_2 with hierarchical pore structure and moderate surface areas is demonstrated. The oxide produced after calcination of infiltrated wood replicates the features of the wood with micrometer-thick walls and pores tens of micrometers in diameter that arise from the tracheids as well as smaller perpendicular pores from ray cells. This structure is maintained at elevated temperatures up to 1400 °C. While grain growth becomes extensive after heating to 1500 °C, an open pore structure is maintained even at that temperature. The Pechini-type synthesis used here is applicable to many different compositions, so that the wood templating approach lends itself also to other compositions for catalytic materials and to dopant addition.[64,308,311] Other attractive features of the wood templating method are that it is scalable and uses biomass as a template. In addition, the balance in feature size between structural stability and surface

area for enhancing cycling kinetics can be fine-tuned by the choice of the wood template as different wood species offer different macropore sizes in their cellular structure.[298]

The cycling performance of pre-sintered WT CeO_2 was studied in the thermochemical production of CO from CO_2. The material maintained a CO production rate up to 6 times that attained with nonporous CeO_2 when compared at the same nonstoichiometry and exhibited comparable CO production rates to electrospun fibers under similar cycling conditions. In the range from 1200 to 1400 °C for the reduction step, the structure of pre-sintered WT CeO_2 was maintained after 21 thermochemical cycles, and the peak CO production rate reached 10 mL min^{-1} g^{-1}; at 1500 °C, loss in surface area caused CO production rates to decrease. The ability of WT CeO_2 to maintain its structure at high temperatures surpasses that of 3DOM CeO_2 with thinner walls, where the original morphology is lost by sintering at much lower temperatures[293] and is similar to that of electrospun CeO_2 fibers.[309] Even though the WT CeO_2 was cycled at a lower reduction temperature (1400 °C) than porous CeO_2 monoliths reported in the literature (1500 °C),[203] the peak CO production rates were comparable but not as high as that of Zr-doped CeO_2 fibers.[309] On the other hand, the density of WT CeO_2 is greater than that of the fibers, allowing for a more compact reactor design. Considering these trade-offs between structural and performance parameters, WT CeO_2 is a complementary material among a range of attractive materials morphologies for thermochemical processes and other high-temperature applications. Continued efforts to improve its stability, such as via doping the CeO_2 (as demonstrated in Zr-doped 3DOM CeO_2), promise to further enhance the stability of this morphology.[308]

Chapter 3

Thermal Stabilization of Metal-Organic Framework-Based Catalytic Clusters through Nanocasting

Parts of this chapter was reprinted with permission from "Thermal Stabilization of Metal-Organic Framework Derived Single-Site Catalytic Clusters through Nanocasting" by Malonzo, C. D.; Shaker, S. M.; Ren, L.; Prinslow, S. D.; Platero-Prats, A. E.; Gallington, L. C.; Borycz, J.; Thompson, A. B.; Wang, T. C.; Farha, O. K.; Hupp, J. T.; Lu, C. C.; Chapman, K. W.; Myers, J. C.; Penn, R. L.; Gagliardi, L.; Tsapatsis, M.; and Stein, A. in the *Journal of the American Chemical Society*, **2016**, *138*, 2739-2748.

This work was done in collaboration with Prof. Omar Farha, Prof. Joseph Hupp, and Dr. Timothy Wang of Northwestern University (NU-1000 synthesis), Dr. Karena Chapman, Dr. Ana Platero-Prats and Dr. Leighanne Gallington of Argonne National Laboratory (PDF and DED analyses), Prof. Michael Tsapatsis and Dr. Limin Ren (catalyst testing for glucose isomerization), Prof. Lee Penn and Dr. Jason Myers (TEM analysis) and Prof. Laura Gagliardi and Dr. Joshua Borycz (computational catalytic reaction mechanism) of the University of Minnesota.

3.1 Introduction

In the pursuit of highly active heterogeneous catalysts, great emphasis has been placed on the catalyst surface, as mainly the surface atoms are involved in the catalytic reactions. The importance of this active surface has prompted efforts to convert bulk systems to nanoparticles and porous materials, where the reduced size and porosity work to increase the accessible surface area in these materials and thereby enhance reaction rates. Even with these systems, however, the ratio of surface to nonsurface atoms is still small. Structural defects and nonuniformity of the catalyst surface also exist, which can lead to poor selectivity in the reaction products. The need for a catalyst system that combines high catalytic activity and selectivity has thus sparked an interest in single catalytic sites—single atoms or small, well-defined clusters of atoms stabilized as discrete units on a support.[312] Single metal sites arguably maximize catalytic activity per metal compared to their nanoparticle counterparts.[313] Product selectivity can also be expected because these identical, structurally well-defined sites should have similar electronic and spatial interactions with reactant molecules.[314-317]

Recently, significant focus has been given to metal-organic frameworks (MOFs), which in comparison with zeolites, are a more diverse class of materials in terms of both structure and composition. MOFs are porous materials consisting of metal ions or clusters that are interconnected via organic linkers. The metal sites in the MOF themselves can be catalytic, and they can also be modified post-synthesis to install other single-site metals. Thus, a multitude of reactivities is possible by engineering these MOF-based catalytic metal sites, first with the choice of metal present in the framework itself, and then

similarly during post-synthetic modification. A key to promoting the catalytic activity of these single sites is to distribute them at high loadings in a heterogeneous system, which requires porous, high surface area supports. Microporous zeolites have been used as supports for these single sites and have become some of the most important catalyst systems in the industry.[318] Recently, significant focus has been directed to metal–organic frameworks (MOFs),[66,319-321] which in comparison with zeolites are a more diverse class of materials in terms of both structure and composition. MOFs are porous materials that consist of metal ions or clusters interconnected via organic linkers. The metal or cluster sites in the MOF themselves can be catalytic,[69,99,101,140,282,322] and these materials can be modified post-synthetically to install other single-site metals.[156,284,323-325] Thus, it is possible to tune the reactivity of a MOF-based catalyst by engineering the catalytic metal sites, first with the choice of metal present in the framework itself and then by post-synthetic modification.[73] In addition, larger pore sizes have been achieved in MOFs than in zeolites, providing easy reactant access to the catalytic sites present in the MOF structure.[91,326]

One drawback of MOFs, however, is their limited thermal stability. Most MOFs can only withstand temperatures of about 150–350 °C in air.[76,151-153,155,156,327] Above these temperatures, the organic linkers that connect the catalytic metal sites in the MOF structure decompose, leading to the aggregation of the metal sites and loss of their catalytic activity. For this reason, MOFs cannot be used to catalyze reactions that occur only at high temperatures, including a number of industrially important reactions, such as alkane dehydrogenation and water gas shift reactions.[174,328] Faster reaction rates are also

attained if catalysts can operate at high temperatures, which makes catalysts with high thermal stability desirable. To take advantage of the highly tunable catalytic metal sites in MOFs for high-temperature catalysis, it is therefore necessary to stabilize the sites so that they remain isolated from each other and accessible even after the linkers are lost at these high temperatures.

Inspired by nanocasting techniques developed extensively for mesoporous materials,[44] an approach was developed to stabilize the MOF cluster sites by supporting them in a secondary porous skeleton that is maintained at high temperatures. A few examples of nanocasting in MOFs exist in the literature, where the target structure is an inverse replica of the original MOF and all of the original material is removed.[75,329-333] In the product structures described here, only the organic linkers are eliminated, while the catalytic oxometal cluster sites are kept embedded in a thermally stable matrix where they remain isolated from each other and accessible to reactants. In this work, we report the preparation of a silica nanocast of NU-1000,[323] a MOF composed of hexanuclear oxozirconium clusters ($[Zr_6(\mu_3\text{-}O)_4(\mu_3\text{–}OH)_4(OH)_4(H_2O)_4]^{8+}$) and 1,3,6,8-tetrakis(*p*-benzoate)pyrene linkers ($TBAPy^{4-}$) (**Figure 3.1a**). When NU-1000 is heated to a temperature at which the oxozirconium clusters lose coordinated water (**Figure 3.1b**), it becomes a Lewis acid catalyst, showing superior activity, for example, in the catalytic breakdown of known chemical warfare agents.[99] The Lewis acid activity of the oxozirconium clusters was determined experimentally by measuring the catalytic activity and using theory by computing the reaction mechanism of glucose isomerization and analyzing the atomic charges in the clusters throughout the reaction. Nanocasting

NU-1000 maintains this activity after the organic linkers have been removed from the structure by high-temperature treatment. It is also shown in this work that through nanocasting with silica, aggregation of the oxozirconium clusters of NU-1000 is prevented after the linkers are removed. Thus, a high concentration of these well-dispersed catalytic sites is maintained in a thermally stable material that is now suitable for catalytic processes that may require high temperatures.

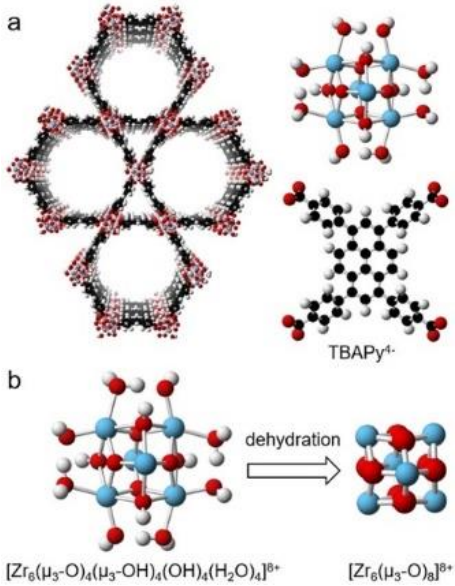

Figure 3.1. (a) Structure of NU-1000 showing the oxozirconium clusters ($[Zr_6(\mu_3\text{-}O)_4(\mu_3\text{-}OH)_4(OH)_4(H_2O)_4]^{8+}$) and organic linkers ($TBAPy^{4-}$) that make up the framework. (b) Dehydration of the oxozirconium clusters converts them to the Lewis acidic form ($[Zr_6(\mu_3\text{-}O)_8]^{8+}$). Color code: Zr (blue); O (red); C (black); H (white).

3.2 Experimental Methods

3.2.1 Materials

The following chemicals were used as received: tetramethyl orthosilicate (TMOS, 98%), methanol (≥99.8%), $ZrOCl_2 \cdot 8H_2O$ (98%), benzoic acid (99.5%), pyridine (99.8%),

and *d*-glucose (≥99.5%) from Sigma-Aldrich; acetone (98%) and N,N-dimethylformamide (DMF, 99.8%) from Macron Fine Chemicals; and hydrochloric acid (36.5–38.0%) from BDH Chemicals. The linker, 1,3,6,8-tetrakis(*p*-benzoic acid)pyrene (H_4TBAPy) was synthesized as previously described.[156] Deionized water produced on-site with a minimum resistivity of 18.2 MΩ·cm was used in all experiments.

3.2.2 Synthesis of NU-1000

NU-1000 was synthesized following a previously reported method.[92] Briefly, the benzoate-capped oxozirconium clusters were first prepared by sonicating $ZrOCl_2 \cdot 8H_2O$ (97 mg, 0.30 mmol) and a large excess of benzoic acid (2.7 g) in DMF (8 mL) until a colorless solution was obtained. This solution was then heated in a capped vial at 80 °C for 1 h. After this, the solution was allowed to cool down to room temperature, the H_4TBAPy ligand (40 mg, 0.059 mmol) was added to it, and the mixture was bath-sonicated for 10 min. The exchange between the benzoate capping groups and the ligand to form the NU-1000 framework was carried out by placing the recapped vial in an oven set at 100 °C for 24 h. After cooling to room temperature, the mother liquor was poured off, and the NU-1000 particles were washed three times with 10-mL portions of DMF. Between the washing steps, the sample was centrifuged (5 min, 7000 rpm) to separate the phases. The solid was then re-suspended in 12 mL DMF and 0.5 mL of 8 M HCl and treated at 100 °C for 24 h to remove the benzoate groups capping the clusters in the framework. After cooling down, the solid was washed twice with 6 mL DMF and then three times with 12 mL acetone, centrifuging between the washing steps (5 min,

7000 rpm) to separate the phases. The solid was then re-suspended in 12 mL acetone and allowed to soak for 24 h to allow complete solvent exchange to acetone. The sample was centrifuged (5 min, 7000 rpm) and acetone was decanted. The collected solids were dried under low vacuum (~0.2 mmHg) for 30 min at 50 °C. The NU-1000 was activated under dynamic vacuum at 120 °C until a vacuum level of ≤0.002 mmHg/min was reached.

3.2.3 Initial Attempt to Prepare a Silica Nanocast of NU-1000 (Method 1)

To prepare a silica nanocast of NU-1000, the infiltration of the MOF with a solution of tetramethylorthosilicate (TMOS), methanol and aqueous HCl was first attempted. In a vial, 1.5 g TMOS, 0.5 g methanol and 250 μL 8 M HCl were mixed to prepare a 68% v/v TMOS precursor solution. Then, 150 μL of this solution was used to suspend 30 mg of NU-1000. Infiltration of the solution into the NU-1000 particles was terminated after 5 h. At this point, the solution started to become cloudy, indicating that long silica chains began to form and, therefore, the formation of a silica coating on NU-1000 particles became more likely than infiltration. The infiltrated sample was then washed twice with methanol to remove the TMOS on the external surface of the NU-1000 particles, and dried under vacuum for 2 min at room temperature. This was followed by heat treatment in a closed vial at 60 °C for another 24 h to condense the TMOS to silica. This nanocast sample is denoted as SiO_2@NU-1000(Method1).

3.2.4 Optimized Method for Nanocasting NU-1000 with Silica

To prepare a silica nanocast of NU-1000, 300 μL of TMOS and 5 μL of H_2O were first sonicated in a vial for 10 min. The mixture was then added to 30 mg of activated NU-1000 and allowed to infiltrate the MOF particles for 24 h. The infiltrated sample was washed with methanol twice to remove the TMOS on the external surface of the NU-1000 particles and then heated at 50 °C for 5 min to dry. To induce polycondensation of TMOS within the sample, the sample was first exposed to HCl vapor for 24 h at room temperature. This was followed by heat treatment in a closed vial at 60 °C for another 24 h. The resulting nanocast material is referred to as SiO_2@NU-1000. This material was heated to 500 °C using a temperature ramp rate of 2 °C/min and maintained at that temperature in air for 1 h to remove the organic linkers from the structure. The resulting product is denoted as Zr_6@SiO_2. To determine the limits of thermal stabilization, SiO_2@NU-1000 was also independently calcined at 600 and 700 °C for 1 h using a ramp rate of 2 °C/min. The resulting samples are denoted as Zr_6@SiO_2 (600 °C) and Zr_6@SiO_2 (700 °C), respectively.

3.2.5 Pyridine Adsorption

The Lewis and Brønsted acid sites on Zr_6@SiO_2 were detected using pyridine as a probe molecule. The sample was placed under dynamic vacuum (<200 mTorr) at 200 °C for 1 h to remove surface-adsorbed water. After cooling to room temperature, the sample was placed under static vacuum, and excess pyridine was injected through a septum. The reaction with pyridine was allowed to proceed for 1 h. The sample was placed under

dynamic vacuum again at 200 °C for 1 h to remove any physisorbed pyridine and then cooled to room temperature. Pyridine adsorption was then analyzed by FT-IR spectroscopy.

3.2.6 Catalyst Testing: Glucose Isomerization

The catalytic performance of Zr_6@SiO_2 was tested using the Lewis-acid-catalyzed isomerization reaction of glucose to fructose as a model reaction. This reaction, carried out at a low temperature (90 °C), allows assessment of the retention of catalytic performance against the original NU-1000 structure, which is stable at this temperature. In a typical reaction, 0.03 g of D-glucose, 2.97 g of ethanol, and 0.012 g of the catalyst were added into a 20-mL thick-walled glass reactor and sealed with a crimp top (PTFE/silicone septum) from VWR. The reactor was placed in an oil bath at 90 °C at specific reaction times, and the reaction was quenched afterward by placing the reactor in an ice bath. The catalyst was then filtered out, and deionized H_2O (3.87 g) was added to the reaction solution to hydrolyze ethylated sugars at 90 °C for 2 days. All reactants and products were analyzed by HPLC. Aside from NU-1000, the catalytic performance of the nanocast material was tested against other samples including calcined NU-1000 and control samples of oxozirconium clusters in nontemplated silica prepared as follows:

dehyd-NU-1000. NU-1000 was heated at 300 °C for 8 h under vacuum (1 mTorr) to dehydrate the oxozirconium clusters in the structure, making them Lewis acidic.

cal-NU1000. NU-1000 was heated at the same temperature as $Zr_6@SiO_2$ (calcination in air at 500 °C for 1 h, 2 °C/min ramp rate) to remove the organic linkers from the structure.

Zr_6@n-t-SiO_2 and Zr_6@n-t-SiO_2(High Zr). Two control samples with different loadings of oxozirconium clusters dispersed in non-templated silica were synthesized. These samples were made by first preparing a DMF solution of benzoate-capped oxozirconium clusters (similar to the NU-1000 synthesis) by sonicating $ZrOCl_2 \cdot 8H_2O$ and benzoic acid in DMF until a clear solution was obtained. Two solutions of different concentrations were made. One contained 97 mg (0.30 mmol) $ZrOCl_2 \cdot 8H_2O$, 2.7 g benzoic acid and 8 mL DMF. The second solution had a higher concentration of Zr and was prepared using 485 mg $ZrOCl_2 \cdot 8H_2O$, 0.915 g benzoic acid and 2 mL DMF. For each case, the solutions were heated in a capped vial at 80 °C for 1 h. After cooling to room temperature, equal volumes of the solutions were added separately to mixtures of TMOS and H_2O (98 % v/v TMOS). The TMOS was then polycondensed (similar to NU-1000 nanocasting) by first exposing the samples to HCl vapor for 24 h at room temperature. This was followed by heat treatment in a closed vial at 60 °C for another 24 h. The samples were then calcined in air at 500 °C for 1 h at a 2 °C/min ramp rate to remove the organic components.

Zr_6@KIT-6. A control sample of KIT-6 (mesoporous silica) impregnated with oxozirconium clusters was also prepared. KIT-6 was first synthesized according to the method by Kleitz et al.[334] with slight modifications. Pluronic P123 (6 g) was dissolved in H_2O (217 g) and concentrated HCl (11.8 g). Butanol (6 g) was then added under stirring

at 35 °C. After 1 h, TEOS (12.9 g) was added and the mixture was kept stirring at 35 °C for 24 h. This was followed by hydrothermal treatment at 100 °C for 24 h. The product was then filtered and dried at 100 °C. The P123 template was removed by first pyrolyzing at 500 °C for 2 h under N_2 flow (700 mL/min) and then calcination at 550 °C for 2 h under air flow (700 mL/min). A 2 °C/min ramp was used for both pyrolysis and calcination steps. The KIT-6 sample was then infiltrated with the same DMF solution of benzoate-capped oxozirconium clusters used to prepare Zr_6@n-t-SiO_2(High Zr). After 24 h, the infiltrated KIT-6 was washed twice with acetone and dried at 80 °C for 12 h. The dried sample was then pyrolyzed (500 °C for 2 h at 2 °C/min ramp, under 700 mL min^{-1} N_2 flow) and calcined (550 °C for 2 h at 2 °C/min ramp, under 700 mL min^{-1} air flow) to remove the organic components.

3.2.7 Instrumentation

FT-IR spectra were collected on a Nicolet Magna-IR 760 spectrometer. Thermogravimetric analysis (TGA) was carried out using a Netzsch STA 409 PC Luxx instrument. Scanning electron microscopy (SEM) measurements were performed on a JEOL 6700 scanning electron microscope operated using a 3.0 kV accelerating voltage. Prior to SEM analysis, all samples were sputter coated with a conductive thin film (50 Å) of Pt. X-ray diffraction (XRD) patterns were collected using an X'Pert Pro diffractometer with an X'Celerator detector. A Co anode (Kα, λ = 1.789 Å) operated at 45 kV and 40 μA was used as the radiation source. Simulated XRD patterns of tetragonal ZrO_2 (PDF #50-1089) were generated using Mercury[335] based on Scherrer line widths for different

crystallite sizes. Inductively coupled plasma–optical emission spectrometry (ICP-OES) using a Thermo Scientific iCAP 6500 analyzer was employed for the determination of the Zr content in the samples. High-performance liquid chromatography (HPLC) with a Bio-Rad Aminex HPX87C (300 × 7.8 mm) column and refractive index detector was used for all reactant and product analyses during the catalytic tests. The mobile phase was ultrapure water (pH = 7), and the column temperature was 80 °C. The C, H, and N content in Zr_6@SiO_2 (500 °C) was determined to be 0.2, 1.1, and 0.0 wt %, respectively, using combustion analysis by Atlantic Microlab, Norcross, GA.

N_2 sorption analyses were conducted using a Quantachrome Autosorb iQ2. The NU-1000 and SiO_2@NU-1000 samples were degassed at 120 °C, and the Zr_6@SiO_2 and control samples were degassed at 200 °C, at 1 mTorr for 12 h prior to the analysis. Brunauer–Emmett–Teller (BET) surface areas were evaluated from the adsorption isotherms within the 0.08–0.28 P/P_o range. Pore size distributions and surface area histograms were obtained using DFT (Quantachrome, N_2at 77 K on carbon or silica, slit pore) methods.

Transmission electron microscopy (TEM) images were collected on an FEI Tecnai G^2 field-emission STEM operating at an accelerating voltage of 300 kV. High-angle annular dark field (HAADF) images were collected on an E. A. Fischione annular detector at a camera length of 120 mm, which yields an inner collection semiangle of 49.8 mrad. Energy-dispersive X-ray spectroscopy (EDS) spectra were collected using an EDAX RTEM thin-window detector. To provide sufficient X-ray intensity for the maps and line-scans, the sample was tilted to the detector takeoff angle of 15°. EDS line scans

and maps were collected using a pixel dwell time of 16 s, a beam convergence semiangle of 9.2 mrad, and a probe current of ~0.5 nA. Data were analyzed using FEI TIA software (version 4.5) and Gatan DigitalMicrograph software (version 1.84).

3.2.8 Synchrotron X-ray Structure Analysis

X-ray scattering data suitable for pair distribution function (PDF) and diffraction analysis were collected at beamline 11-ID-B at the Advanced Photon Source at Argonne National Laboratory. High-energy X-rays (wavelength 0.2114 Å, 58.6 keV) were used in combination with a large amorphous silicon-based area detector. For PDF analysis, total scattering data were collected using a short sample-to-detector distance (~18 cm) to Q_{max} = 23 Å^{-1}. For diffraction analysis, data with improved angular resolution were collected at longer sample-to-detector distance (~95 cm). The X-ray scattering images were reduced within QXRD and FIT2D.[336,337]

A difference envelope density (DED) analysis[338,339] was applied to diffraction data to evaluate the distribution of SiO_2 within the crystalline NU-1000 framework. The diffuse contributions to the background were removed by subtracting scattering measured for an empty sample capillary and amorphous SiO_2.[340-342] The Bragg peak intensities for pristine and nanocast NU-1000 were determined by performing Le Bail whole pattern fits to the diffraction data within the *P*6/*mmm*space group of the parent phase,[156] refining the hexagonal lattice parameters and pseudo-Voigt profile parameters. Structure envelopes were generated based on the low-index reflections, as described previously.[338,343] A difference envelope, reflecting the distribution of silica within the NU-1000 lattice, was

generated by taking the difference between the envelopes for SiO_2@NU-1000 and an unmodified NU-1000 sample.

Pair distribution functions (PDFs) were extracted from the total scattering data within PDFgetX2, correcting for background and Compton scattering.[344] Data were collected for pristine NU-1000, SiO_2@NU1000, Zr_6@SiO_2, TMOS-derived silica, and the control Zr_6@n-t-SiO_2. Differential analyses were applied to separate the contributions from silica from the oxozirconium clusters or NU-1000 lattice. Structure models were refined against the differential PDFs (dPDFs) within PDFgui to evaluate the particle size of the Zr-based clusters following thermal treatment.

3.3 Results and Discussion

3.3.1 Silica Nanocasting

Silica nanocasts of NU-1000 were prepared according to the scheme shown in **Figure 3.2**. The silica precursor, tetramethylorthosilicate (TMOS), is small enough to fit in the 3 nm pores of NU-1000, allowing the precursor to infiltrate these pores. Under hydrolytic conditions, TMOS can then be condensed in the presence of an acid catalyst to form silica within the NU-1000 framework.

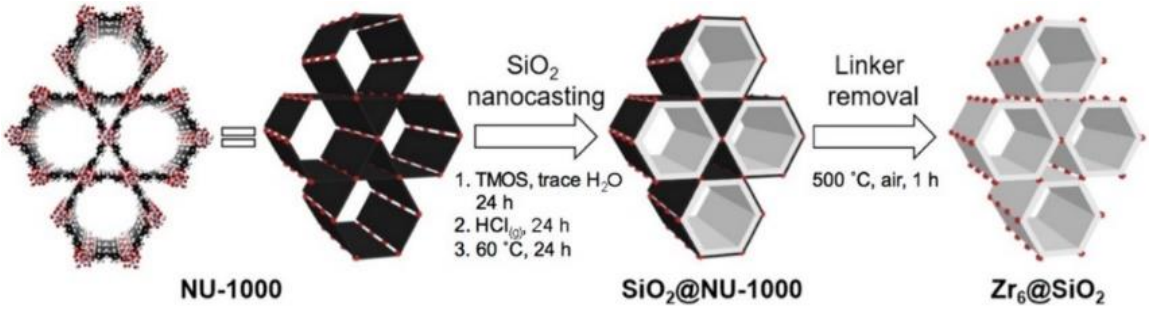

Figure 3.2. Scheme for the process of stabilizing the oxozirconium clusters in NU-1000 by nanocasting with silica. The image on the left represents the NU-1000 structure with cluster nodes (red) and linkers (black). The white layer in the middle image represents silica.

Our earlier attempts to nanocast NU-1000 with silica (Method 1) used a mixture of TMOS, aqueous HCl, and methanol as the casting fluid. The added methanol was necessary to slow down the silica formation during infiltration, which could otherwise lead to pore blockage, hindering percolation through the entire NU-1000 particle. However, that method yielded mainly extra-framework silica, with virtually no shift to lower pore size for the 3 nm channels in NU-1000, indicating that only a small amount of silica was present in these pores (**Figure 3.3**). This could be due to TMOS occupying only 68% of the precursor solution volume. Because both H_2O and HCl as an acid catalyst are present in the precursor solution, TMOS hydrolysis and oligomerization is also possible, yielding short silica chains that could already be too large to infiltrate into the NU-1000 pores. Multiple infiltration steps were carried out using this method, but this did not improve the silica loading in the pores (**Figure 3.3**).

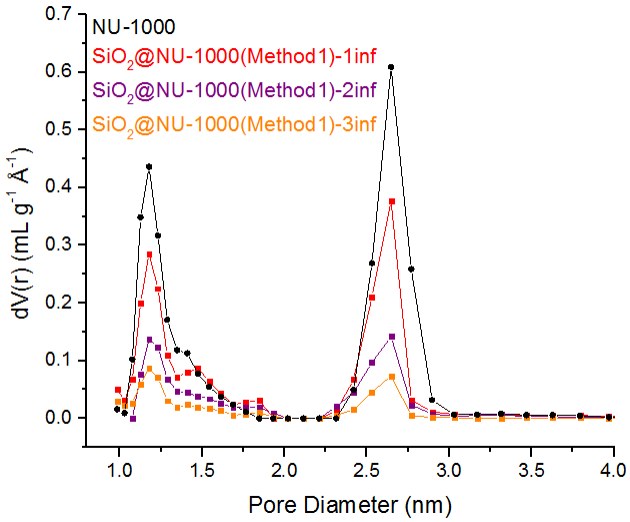

Figure 3.3. DFT pore size distribution of NU-1000 before and after nanocasting with silica using Method 1. The number of infiltration-gelation cycles used to prepare the nanocasts is indicated as 1, 2, and 3-inf for one, two and three cycles, respectively.

Instead, to raise the amount of silica in the pores of NU-1000, we increased the fraction of TMOS in the casting fluid to 98% v/v, the balance being water. As TMOS hydrolysis and condensation occur instantaneously when HCl is added to this mixture, the acid must be introduced (via vapor-phase HCl treatment) only after the mixture has percolated through the NU-1000 pores. The presence of silica in the product obtained after nanocasting was confirmed by the appearance of an intense absorption at 1090 cm^{-1} in the FT-IR spectrum (**Figure 3.4**) related to the Si–O–Si stretching vibration. While the total amount of silica in this nanocast product is approximately the same as in the sample from the original nanocasting method (TGA data, **Figure 3.5**), a larger proportion of it is present within the NU-1000 framework as shown by the greater shift in the DFT pore size distribution of the sample (**Figure 3.6a**). The pore radius decreased by

ca. 0.2 nm upon infiltration of the larger hexagonal channels in NU-1000, while the smaller trigonal channels maintained their original dimensions.

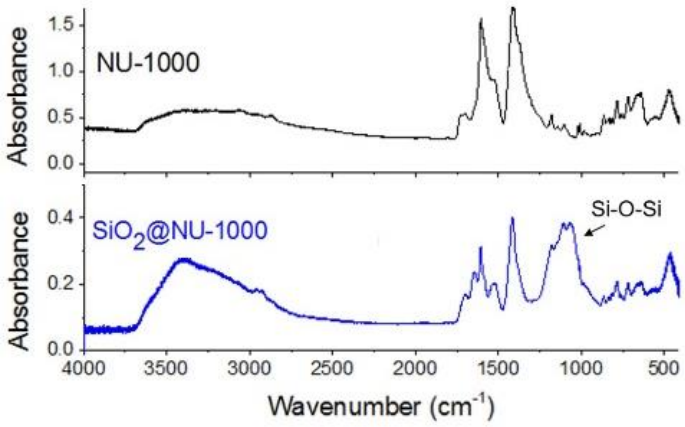

Figure 3.4. FT-IR spectra of NU-1000 and SiO_2@NU-1000. The presence of silica in the nanocast product is confirmed by the Si-O-Si absorption peak at 1090 cm^{-1}.

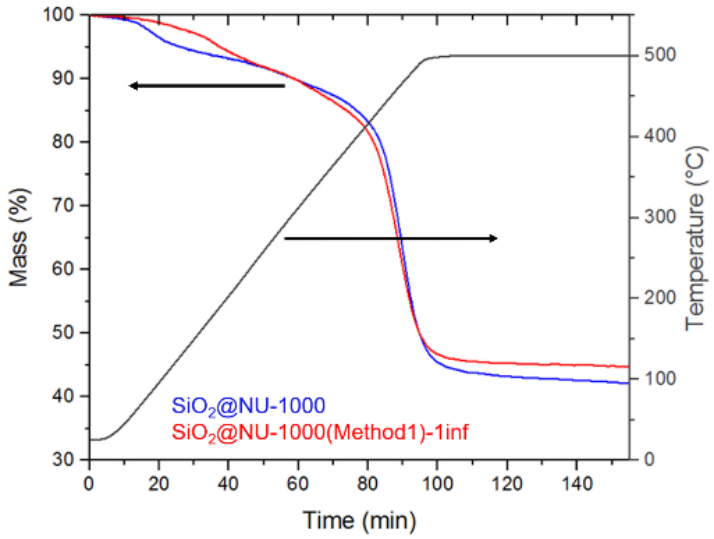

Figure 3.5. TGA curves showing similar mass loss for nanocast materials made by Method 1 (SiO_2@NU-1000(Method1)) and those made by the optimized nanocasting method described in the Experimental Methods section (SiO_2@NU-1000).

The diffraction and pair distribution function (PDF) data demonstrate that the NU-1000 framework structure is maintained through the nanocasting procedure. The presence of Bragg diffraction peaks indicates that the long-range crystalline ordering of the lattice is preserved (**Figure 3.7**). The differential PDF trace, subtracting the contributions from the new silica phase, shows the same local structures in the pristine and nanocast systems (**Figure 3.7**), characterized by a feature at ~1.4 Å associated with the C–C and C–O bonds in the $TBAPy^{4-}$ linker, and features at ~2.1 and 3.5 Å associated with the Zr–O and Zr···Zr′ atom–atom distances, respectively.

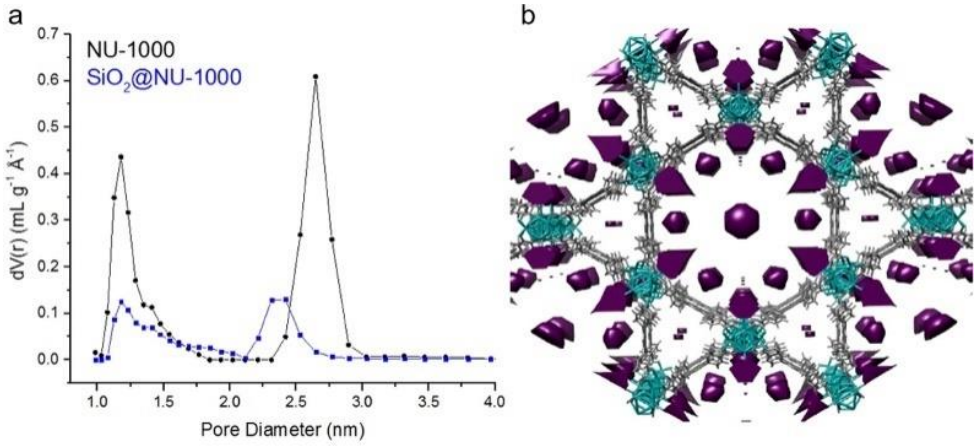

Figure 3.6. (a) DFT pore size distribution of NU-1000 (BET surface area = 2064 m^2g^{-1}, pore volume = 1.44 cm^3 g^{-1}) before and after nanocasting with SiO_2 (BET surface area = 901 m^2 g^{-1}, pore volume = 0.55 cm^3 g^{-1}). (b) Difference envelope density analysis data showing the new electron density (SiO_2, purple) after nanocasting NU-1000 (oxozirconium clusters in teal, organic linkers in gray).

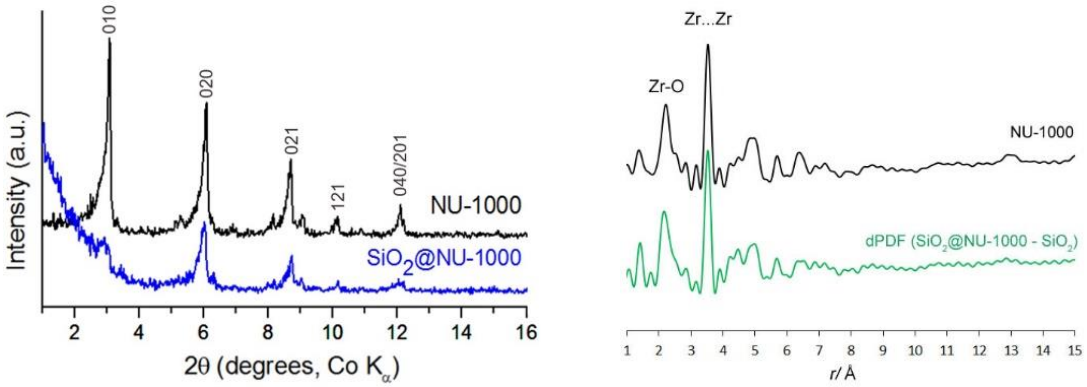

Figure 3.7. (left) XRD patterns of NU-1000 and SiO_2@NU-1000, showing a reduction in relative intensity of the (010) reflection, and (right) pairwise distribution function for NU-1000 and differential pairwise distribution function for SiO_2@NU-1000, showing features of the MOF framework structure in the nanocast product.

The difference envelope density (DED) analysis, based on the low-index Bragg reflections, provides a map of electron density added to the NU-1000 pores following the silica nanocasting (**Figure 3.6b**). This analysis shows that the silica is primarily deposited in a layer on the surface of the 3 nm hexagonal channels close to the oxozirconium nodes and organic linkers, with almost no silica in the smaller 1 nm trigonal pores. This is also reflected in the decrease in intensity of the 010 reflection following nanocasting (**Figure 3.7**)—this peak corresponds to the 3 nm channel spacing in NU-1000. The reduced electron contrast following silica incorporation into these channels leads to reduced intensity of this 010 peak. As suggested by the nitrogen sorption data (**Figure 3.6a**), there is no shift in the pore size for the trigonal pores indicating no significant silica electron density within these small pores. The distribution of the silica as a layer on the pore surface of the hexagonal channels provides a secondary skeleton or framework structure

that can serve as a scaffold for the oxozirconium clusters following removal of the organic linkers at high temperature.

3.3.2 Cluster Stabilization at High Temperatures

An ultimate aim is to use these nanocast products to catalyze reactions at high temperatures. To be useful for high-temperature catalysis, however, the silica backbone in the nanocast materials should be able to serve as a support for the Lewis acidic oxozirconium clusters in place of the organic linkers that are lost at these temperatures. Site isolation and accessibility of these clusters are necessary to maintain high Lewis acid catalytic activity. To determine whether this high-temperature cluster stabilization was achieved through nanocasting, we removed the organic linkers in the nanocast material (SiO_2@NU-1000) by calcination, which leaves only the oxozirconium clusters and the silica matrix (Zr_6@SiO_2).

The dPDF trace for Zr_6@SiO_2 (**Figure 3.8**, with 0–8 Å region highlighted) shows that the organic linkers were eliminated, with no peaks at ∼1.4 Å from C–C or C–O bonds within the linkers. This is consistent with chemical analysis that detected only 0.2 wt % of carbon in the sample. The dPDF is dominated by peaks at ∼2.14 and ∼3.47 Å associated with Zr–O and Zr···Zr correlations within oxozirconium clusters, respectively. Structural models, based on cubic ZrO_2, were refined against the dPDF data, using a spherical particle parameter to estimate the ZrO_2 particle size distribution. The nanocast Zr_6@SiO_2 was dominated by small ∼0.6 nm clusters ZrO_2 (∼95%, a = 4.88 Å) with a minor component of larger ∼3 nm nanoparticles, modeled as cubic ZrO_2 with

significant O disorder (~5%, *a* = 5.11 Å). The retention of such a large fraction of the small ~0.6 nm clusters suggests that the nanocasting approach is successful in improving the thermal stability of the clusters. While aggregation was not entirely eliminated in the nanocast system, it may be expected that oxozirconium clusters closer to the outer surface of the particles may be more susceptible to aggregation, and the larger nanoparticles observed in this case may be associated with clusters near the surface. Alternatively, small domains of NU-1000 not penetrated by the silica precursor could account for the minor phase of aggregated ZrO_2nanoparticles.

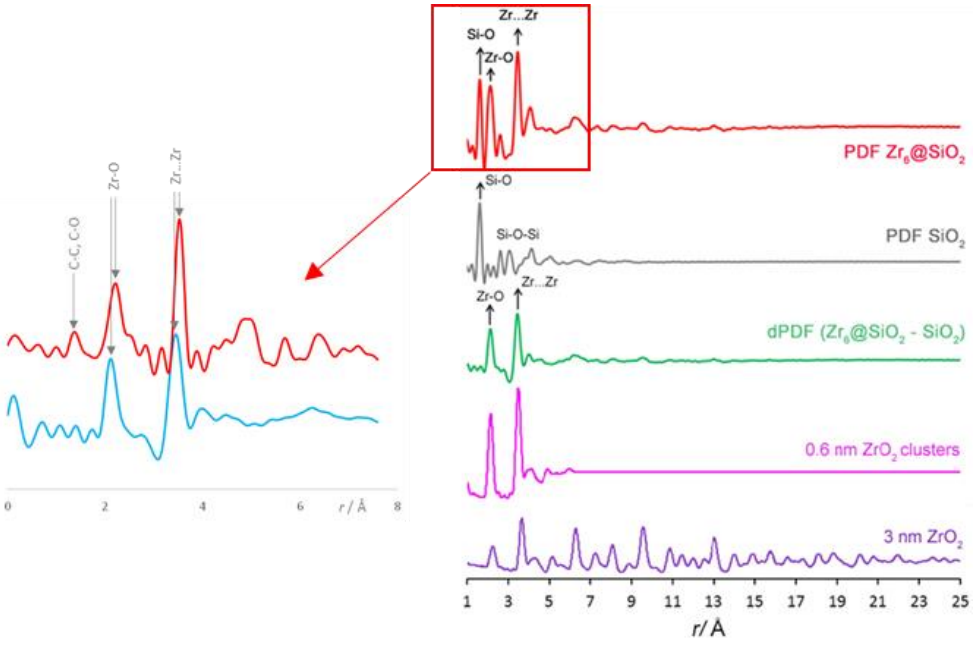

Figure 3.8. (left) PDFs for the pristine NU-1000 (red) and SiO_2-subtracted PDF of $Zr_6@SiO_2$ (blue). The feature at 1.35 Å, for the pristine NU-1000, associated with the C–C and C–O bonds within the organic ligand is not evident in the data for the calcined material, suggesting that the ligands have been successfully eliminated. (right) PDFs for $Zr_6@SiO_2$ and an amorphous silica sample, dPDF, for $Zr_6@SiO_2$ showing new Zr–O and Zr···Zr correlations and PDFs for the oxozirconium clusters (0.6 nm, $Fm\bar{3}m$, a = 4.88 Å) and larger cubic ZrO_2 particles (3 nm, $Fm\bar{3}m$, a = 4.88 Å).

Figure 3.9 shows electron micrographs tracking the progression from NU-1000 to the nanocast material SiO_2@NU-1000 and to the final product after removal of the linkers, Zr_6@SiO_2. There is no significant change in morphology after nanocasting (**Figure 3.9b**), and the lattice fringes from the 3 nm channels are still observable from the high magnification TEM image of the nanocast products (**Figure 3.9e**). This is consistent with the XRD data which shows a low angle peak at $2\theta = 3°$ that corresponds to structural features on the ∼3 nm scale (**Figure 3.7**). After the linkers are removed by heating the sample at 500 °C in air, the particles shrink, and the TEM image shows a more disordered structure (**Figure 3.9c**, **f**). This is accompanied by a decrease in BET surface area (from 944 to 444 $m^2\ g^{-1}$) and pore volume (from 0.55 to 0.46 $cm^3\ g^{-1}$) due to the loss of micropores in the structure. Of particular interest is the XRD pattern of this sample, which does not exhibit any notable diffraction peaks (**Figure 3.11**, Zr_6@SiO_2 (500 °C)). On the other hand, a noninfiltrated NU-1000 sample that was heated to the same temperature (cal-NU-1000) exhibits diffraction peaks that can be indexed to the tetragonal phase of ZrO_2 (**Figure 3.11**, cal-NU-1000 (500 °C)). This difference is also reflected in the selected area electron diffraction (SAED) patterns of the two samples (**Figure 3.10**), where cal-NU-1000 shows diffraction rings that index to tetragonal ZrO_2, which are absent in the SAED pattern of Zr_6@SiO_2. The presence of the diffraction patterns in the XRD and SAED data indicates that in cal-NU-1000, the oxozirconium clusters have aggregated at the high treatment temperatures to form larger ZrO_2 crystallites (ca. 18 nm calculated from the XRD line broadening using the Scherrer equation), which would cause a loss in catalytic activity because agglomeration reduces

the number of exposed Lewis acid sites. The absence of notable diffraction peaks in $Zr_6@SiO_2$ demonstrates that, by nanocasting with SiO_2, the oxozirconium clusters are prevented from aggregating after the linkers are removed at high temperatures, in agreement with the dPDF data.

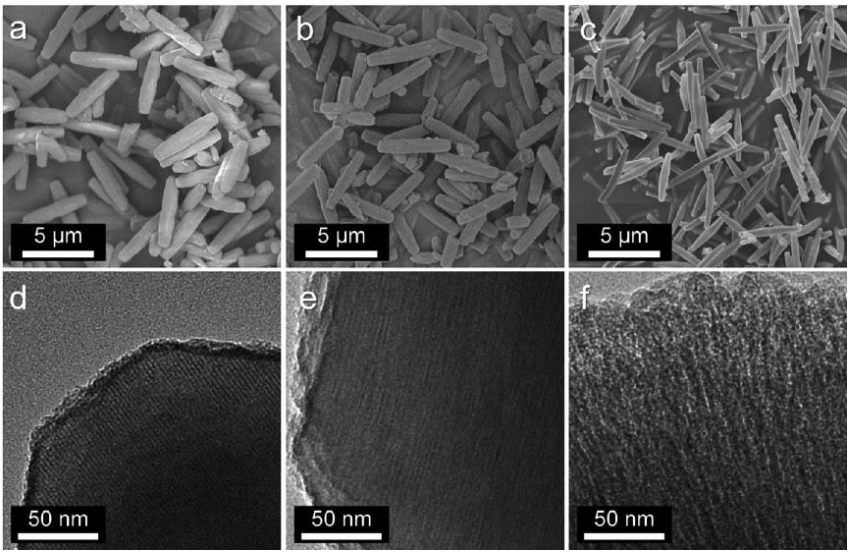

Figure 3.9. SEM (a–c) and TEM (d–f) images of NU-1000 (a, d), SiO_2@NU-1000 (b, e), and $Zr_6@SiO_2$ (c, f).

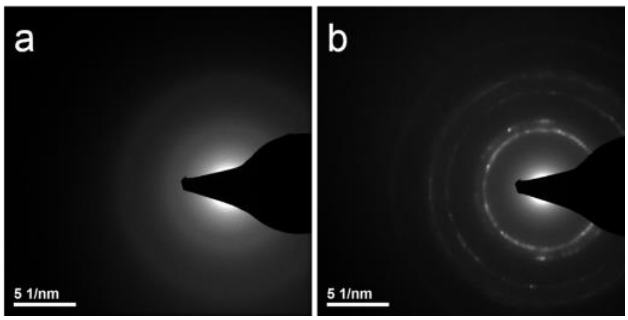

Figure 3.10. SAED patterns of (a) $Zr_6@SiO_2$ and (b) cal-NU-1000, both treated at 500 °C in air. The pattern of the calcined NU-1000 sample shows diffraction rings that can be indexed to ZrO_2. These are absent in the pattern of $Zr_6@SiO_2$.

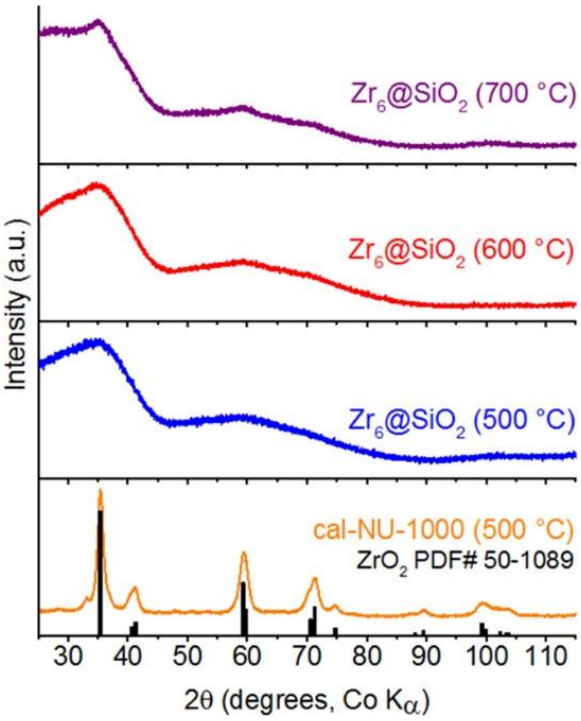

Figure 3.11. XRD patterns of Zr_6@SiO_2 after heat treatment at 500, 600, or 700 °C in air. For comparison, the XRD pattern of NU-1000 calcined at 500 °C in air is also shown. The line pattern corresponds to the published powder diffraction file pattern for tetragonal ZrO_2 (powder diffraction file #50–1089).

STEM-EDS elemental maps (**Figure 3.13**) of the nanocast products after linker removal show a homogeneous distribution of O, Si, and Zr throughout the material. For Si in particular, there is no Si-deficient core, which indicates that uniform infiltration was achieved during nanocasting. This presumably afforded the site isolation of the clusters, as the presence of silica throughout the particle can provide proximal anchor sites for these clusters. Additionally, the EDS map also shows only a very thin outer layer of silica on the sample surface, not a thick crust which would prevent access to the catalytic clusters within the particles.

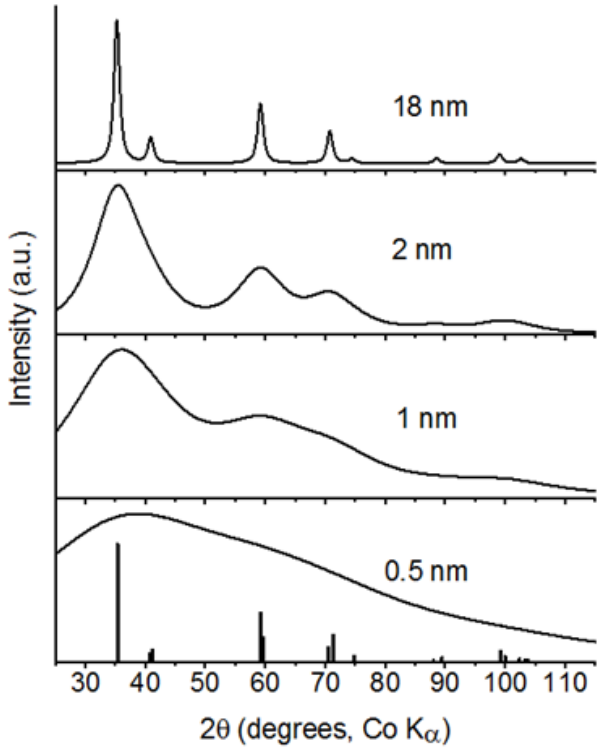

Figure 3.12. Stick pattern and simulated XRD diffraction patterns of tetragonal ZrO_2 (powder diffraction file #50-1089), corresponding to line broadening for the different crystallite sizes indicated in the figure.

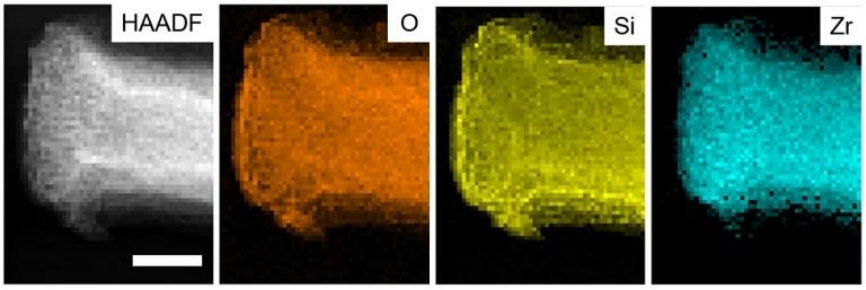

Figure 3.13. High-angle annular dark field (HAADF) image and STEM-EDS elemental maps of $Zr_6@SiO_2$. The scale bar corresponds to 200 nm.

3.3.3 Lewis Acidity and Catalytic Performance of Nanocast NU-1000

NU-1000 is an excellent Lewis acid catalyst owing to the high concentration of the Lewis acidic oxozirconium clusters in its structure, which are easily accessible through its mesoporous channels.[99] In particular, the Lewis acidity can be enhanced by dehydration of the clusters, which eliminates terminal aquo and hydroxo ligands and converts hydroxo bridges to oxo bridges, thereby reducing the number of oxide-based species that bind to the Zr(IV) centers.[99] Similar cluster dehydration processes are expected during the heat treatment at 500 °C to form Zr_6@SiO_2 and open up Zr(IV) sites.

To determine whether the Lewis acidic clusters in the nanocast materials remain accessible, we carried out a pyridine adsorption experiment on Zr_6@SiO_2. Pyridine is a common IR probe for detecting acidic sites in solid acid catalysts. The peaks for the ring vibrations of pyridine, which appear in the region between 1700 and 1400 cm^{-1}, shift depending on whether pyridine is coordinated to a Lewis acid site or is protonated by a Brønsted acid site.[345] After pyridine adsorption, the FT-IR spectrum of Zr_6@SiO_2 shows peaks for pyridine adsorbed on Lewis acid sites (**Figure 3.14**). These peaks correspond to the normal modes ν_{8a} and ν_{19a} of the ring-breathing (νCCN) vibrations of pyridine with A_1 symmetry (1607 and 1490 cm^{-1}, respectively) and the ν_{8b} and ν_{19b} modes with B_2 symmetry (1576 and 1445 cm^{-1}, respectively),[346] all in close agreement with those found for Lewis-site coordinated pyridine on ZrO_2.[347] Similar peaks are observed for pyridine adsorbed on dehydrated NU-1000. It is interesting to note that the pyridine peaks are less well resolved in the case of dehydrated NU-1000, possibly due to additional interactions of the probe molecule with linkers between oxozirconium clusters.

Evidence for some Brønsted acidity is also present in both the $Zr_6@SiO_2$ sample and the dehydrated NU-1000, as indicated by a vibrational band at 1545 cm^{-1} typical for pyridinium ions bonded to Brønsted sites.[347] Amorphous silica prepared from TMOS using the same treatment as for $Zr_6@SiO_2$ shows no corresponding absorption bands in the FT-IR spectrum. The pyridine adsorption data confirm that the clusters are accessible in the nanocast material.

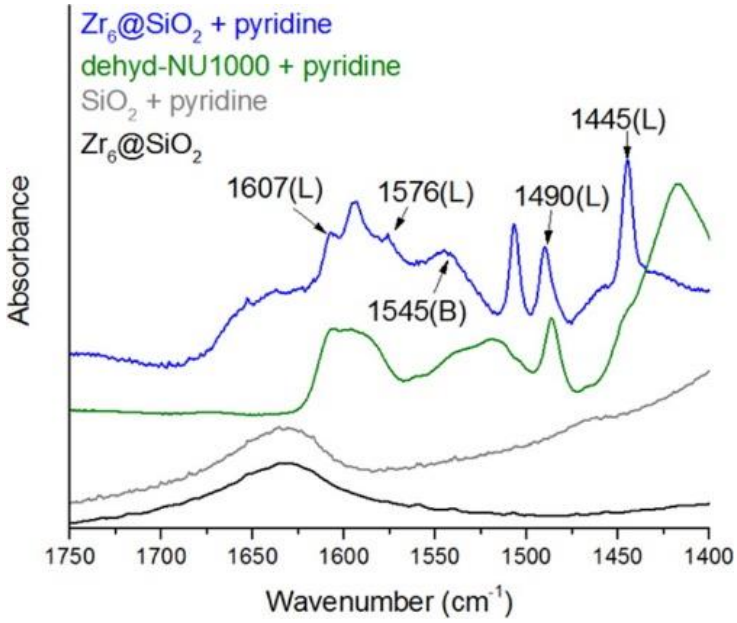

Figure 3.14. FT-IR spectra showing pyridine adsorption data for $Zr_6@SiO_2$ (500 °C) and dehyd-NU-1000. The peaks indicate the presence of accessible Lewis (L) and Brønsted (B) acid sites in the samples. The spectra of $Zr_6@SiO_2$ (500 °C) (before pyridine adsorption) and SiO_2 (after pyridine adsorption) are also shown for comparison.

We estimated the ratios of Lewis-to-Brønsted acid sites (L:B) in the $Zr_6@SiO_2$ (500 °C) and dehyd-NU-1000 samples by integrating the peaks at 1445 and 1545 cm^{-1} in **Figure 3.14** (see **Table 3.1** for the peak integration values). Absorption

coefficients from Rosenberg and Anderson[348] were used to estimate relative acid site concentrations from the peak areas. While the resulting L:B ratios of 0.46 for Zr_6@SiO_2 and 0.24 for dehyd-NU-1000 have some uncertainty due to peak fitting procedures, they show that the relative L:B content did not decrease after nanocasting and probably increased slightly, most likely because removal of the organic linkers exposed more Lewis acid sites on the clusters. More importantly, these data show that both materials contain appreciable amounts of Brønsted and Lewis acid sites, and both sites remain accessible to pyridine molecules.

Table 3.1. Lewis and Brønsted acid site ratios on Zr_6@SiO_2 and dehyd-NU-1000.

	Zr_6@SiO_2		**dehyd-NU-1000**	
	Lewis (L)	**Brønsted (B)**	**Lewis (L)**	**Brønsted (B)**
wavenumber (cm^{-1})[a]	1444	1542	1446	1540
peak area[a]	0.14	0.24	0.72	2.35
ε[b]	1.56	1.24	1.56	1.24
L:B site ratio[c]	~0.46		~0.24	

[a]Values determined by peak deconvolution of the spectra in Figure 3.14 using Origin software

[b]Average absorption coefficients, ε, values for the pyridinium ion and Lewis-bound pyridine obtained from Rosenberg and Anderson.[348] In that paper, the authors studied silica-zirconia mixed oxides and found that the absorption coefficients covered a relatively narrow range of values (1.16 to 1.32 at 1540 cm^{-1} for the pyridinium ion and 1.49 to 1.59 at 1450 cm^{-1} for the Lewis-bound pyridine)

[c]Estimated using Beer's Law: L:B = $(\text{peak area} \div \varepsilon)_{\text{Lewis}} \div (\text{peak area} \div \varepsilon)_{\text{Brønsted}}$.

The catalytic activity of the oxozirconium clusters was tested with the Lewis-acid-catalyzed isomerization of glucose to fructose. As this reaction occurs at low temperatures, the catalytic performance of the clusters in the nanocast Zr_6@SiO_2 and the

original NU-1000 structure can be compared. The glucose isomerization reaction was carried out in two steps (**Figure 3.15**), following the scheme of Saravanamurugan et al.[349,350] In the first step, glucose is isomerized to fructose in the presence of the catalyst. The fructose that is formed immediately reacts with the solvent, ethanol, to form ethyl fructoside. Water is then added in the second step to hydrolyze the fructoside back to fructose. Both steps are carried out at 90 °C. The catalytic performance of the nanocast material was tested against other samples (**Table 3.2**), including NU-1000, calcined NU-1000, and control samples of oxozirconium clusters in nontemplated silica and mesoporous silica (KIT-6) supports.

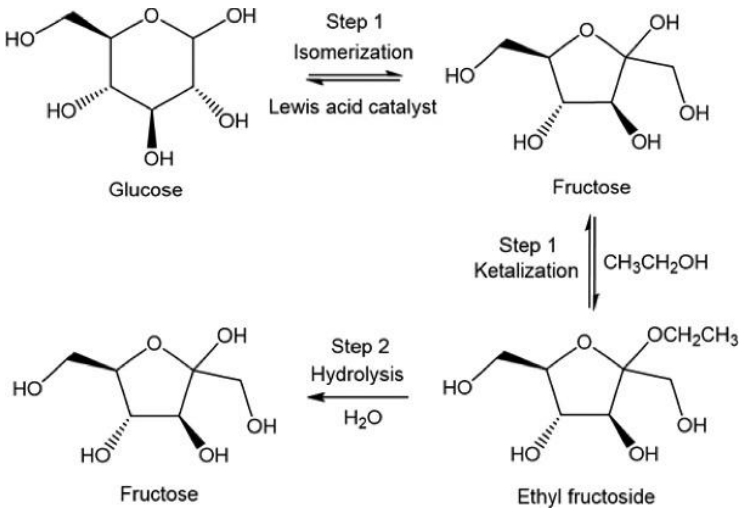

Figure 3.15. Reaction scheme for the isomerization of glucose to fructose. Adapted from Saravanamurugan et al.[350]

Table 3.2. Properties of catalysts tested for glucose isomerization.

sample	Zr content[a] (% w/w)	synthesis temperature (°C)	BET surface area[b] ($m^2\ g^{-1}$)	pore volume ($cm^3\ g^{-1}$)[b]
Zr_6@SiO_2	23	500	444	0.46
dehyd-NU-1000	30	300	2100	1.61
cal-NU-1000	74	500	52	0.13
Zr_6@n-t-SiO_2	0.7	500	371	0.32
Zr_6@n-t-SiO_2(High Zr)	9	500	173	0.12
Zr_6@KIT-6[c]	2	550	128	0.53

[a]The Zr content of dehyd-NU-1000 and cal-NU-1000 was estimated assuming the formulas $Zr(\mu_3\text{-}O)_8(HTBAPy)_2$ and ZrO_2, respectively. The Zr content of nanocast Zr_6@SiO_2 and the control samples, Zr_6@n-t-SiO_2, Zr_6@n-t-SiO_2(High Zr) and Zr_6@KIT-6 were determined by ICP-MS.
[b]The N_2 sorption isotherms and DFT surface area versus pore size histograms are shown in Figure 3.16 and Figure **3.17**.
[c]Additional characterization data for the support (KIT-6 mesoporous silica) are shown in Figure 3.18.

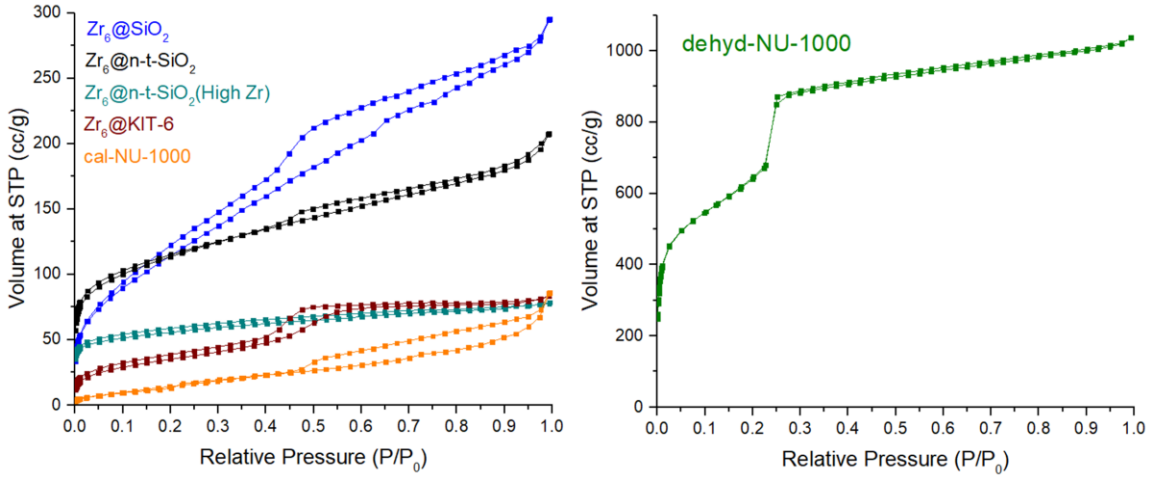

Figure 3.16. N_2 sorption isotherms of the nanocast Zr_6@SiO_2 and the control samples used for the catalytic tests for glucose isomerization.

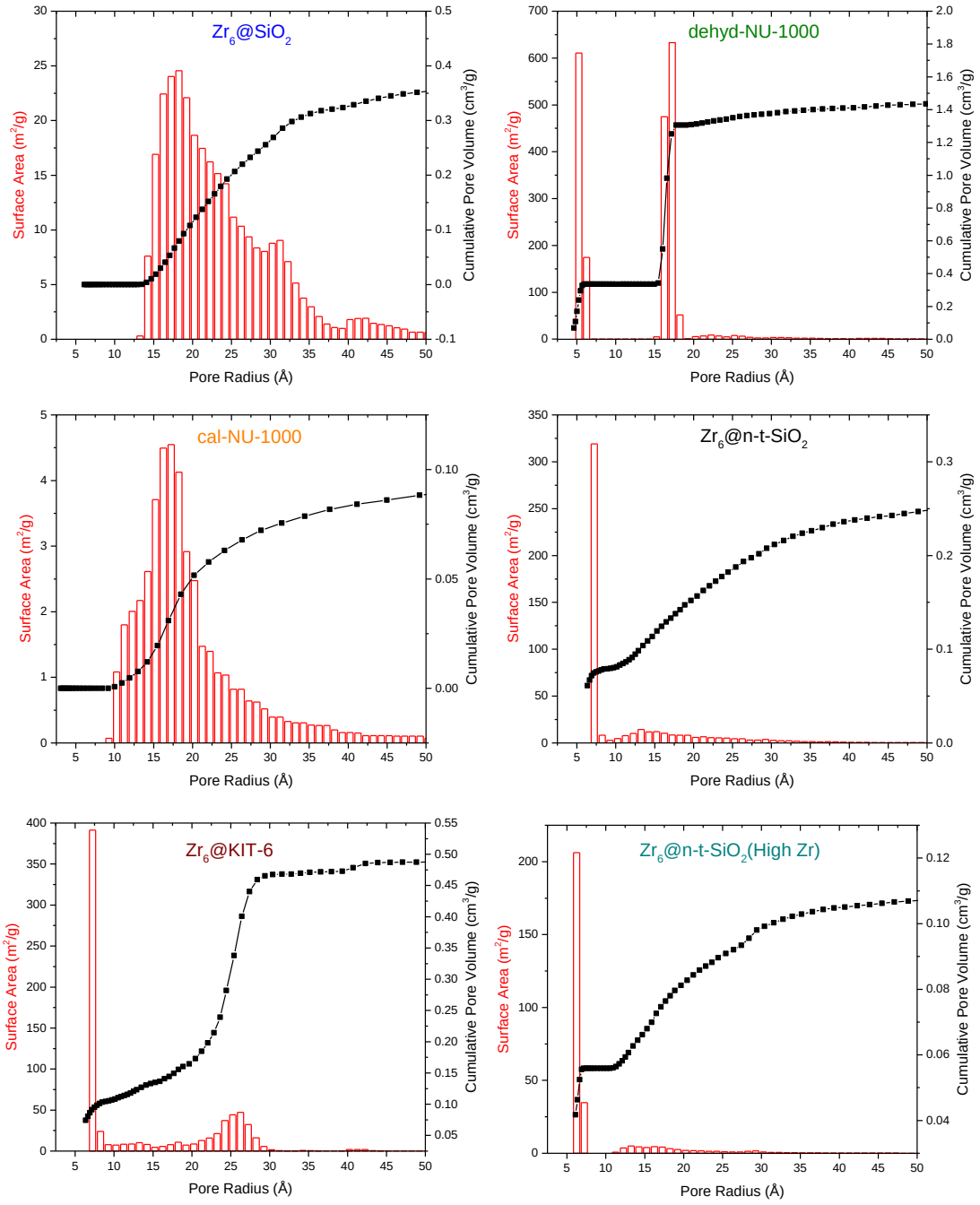

Figure 3.17. NLDFT (Quantachrome, N_2 adsorption at 77 K) area histograms evaluated from the N_2 sorption isotherms in Figure 3.16. A slit pore model with carbon as adsorbent was the model used to generate the area histogram for dehyd-NU-1000 and cal-NU-1000, whereas a cylindrical pore model with silica as adsorbent was used for the other samples.

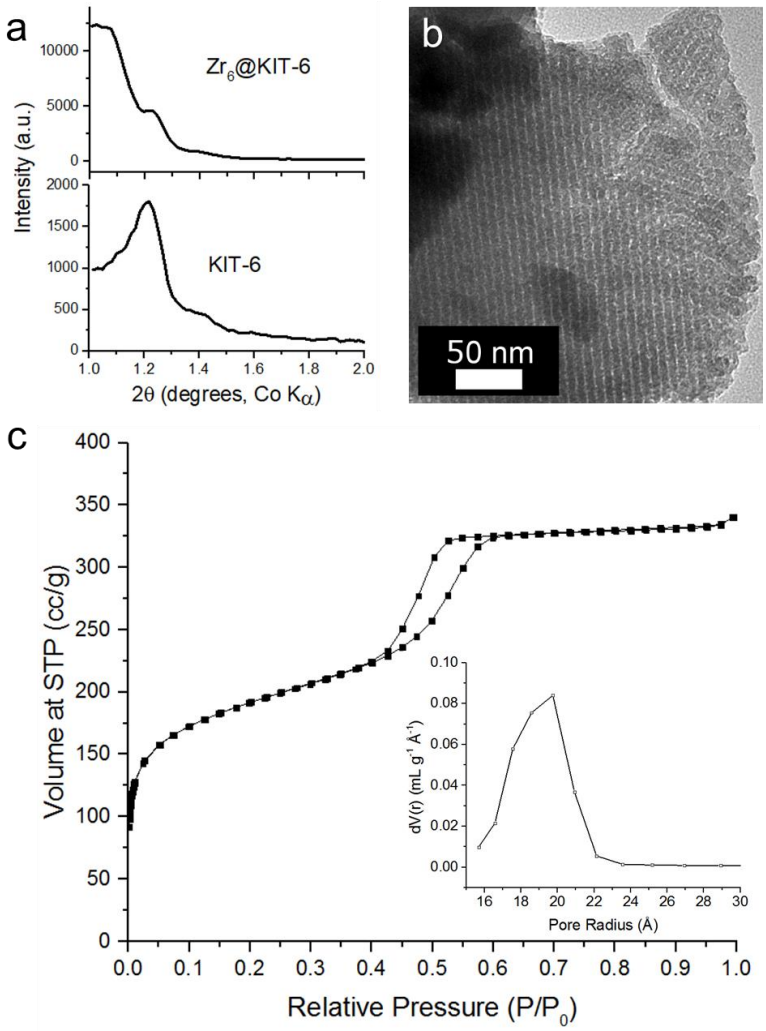

Figure 3.18. Characterization data for as-synthesized KIT-6, which is in good agreement with those reported by Kleitz et al.[334] (a) XRD pattern, (b) TEM image, and (c) N_2 sorption isotherm and (inset) BJH pore size distribution. The BET surface area of this KIT-6 material is 613 m^2/g.

The catalytic test results for glucose isomerization are shown in **Figure 3.19**. Both dehyd-NU-1000 (NU-1000 dehydrated at 300 °C under vacuum to make the oxozirconium clusters Lewis acidic) and the nanocast $Zr_6@SiO_2$ are active. The rate is slower for $Zr_6@SiO_2$ which could be due to some of the clusters becoming fully coated with SiO_2 during nanocasting or due to the silica scaffold providing some steric

hindrance. Despite this, significant catalytic activity was retained in the nanocast material even after it had been heated to 500 °C. In contrast, bare NU-1000 heated to the same temperature (cal-NU-1000) had very low activity. This shows the importance of maintaining the site isolation in the clusters in order to retain catalytic activity, which was made possible by nanocasting. An XRD pattern of the Zr_6@SiO_2 sample collected after the 72 h catalytic reaction (**Figure 3.20**) shows that the broad diffraction features seen for the original sample (**Figure 3.11**) are maintained, implying that the clusters remained isolated and did not aggregate during the catalytic reaction. Recycling experiments with Zr_6@SiO_2 show an average loss in glucose conversion of ~13% per cycle over five cycles (**Figure 3.21**). The loss in overall activity is more pronounced initially and appears to level off after the third cycle. Interestingly, the fructose yield loss is less pronounced, and as a result, the recycled catalysts become progressively more selective to fructose. It is possible that this is due to reduction of the Brønsted:Lewis acid site ratio with recycling, but further investigations are required to test this hypothesis. Despite these changes, higher catalyst activity is still maintained in recycled Zr_6@SiO_2 as compared to cal-NU-1000.

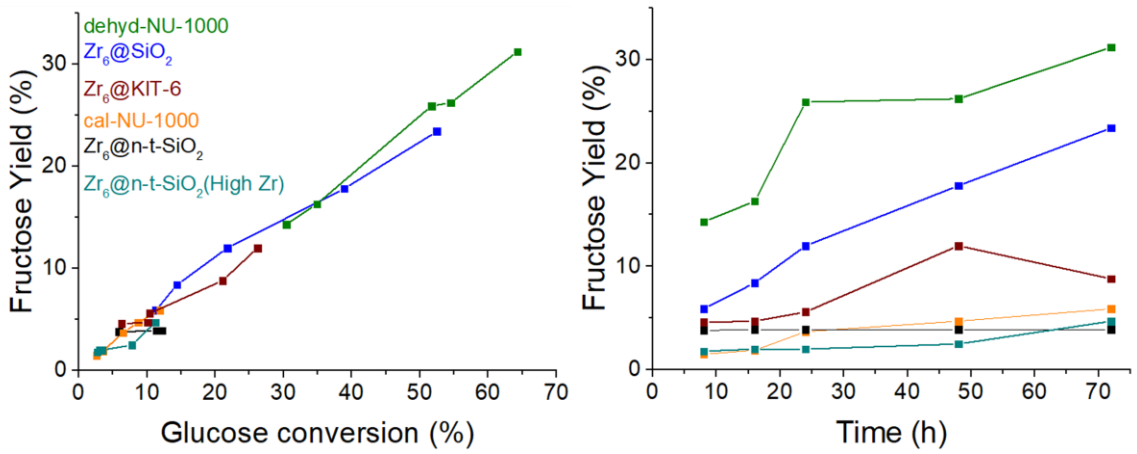

Figure 3.19. (left) Fructose yield versus glucose conversion and (right) fructose yield versus time over different catalysts.

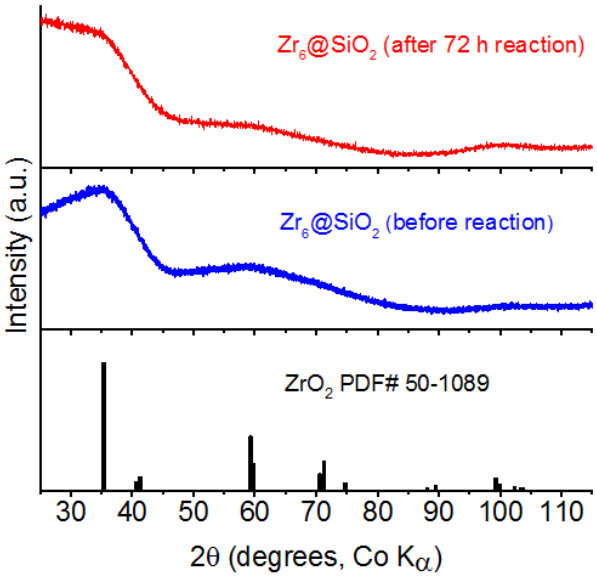

Figure 3.20. Powder XRD pattern of $Zr_6@SiO_2$ (500 ˚C) that had been subjected to the glucose isomerization reaction for 72 h. By comparing the pattern with simulated XRD diffraction patterns of tetragonal ZrO_2 (Figure 3.12), it can be concluded that this sample contains a distribution of crystalline ZrO_2 domains with grain sizes between 0.5 and 1 nm. This implies that minimal cluster aggregation has occurred during the catalytic reaction. It should be noted that even if only few 1 nm clusters have formed, they would predominate the intensity of the pattern compared to smaller clusters.

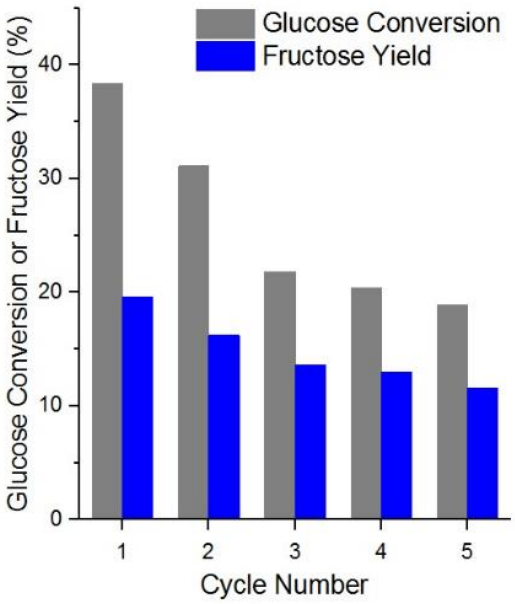

Figure 3.21. Glucose isomerization catalyst recycling experiments with Zr_6@SiO_2 catalyst. Cycle 1 refers to catalysis using fresh Zr_6@SiO_2 sample. The catalyst was regenerated by washing three times with methanol and calcining at 450°C for 1 h in air for the subsequent cycles. Reaction conditions were as indicated in the Experimental Methods section with a 24-h reaction time.

In addition, a higher loading of these site-isolated clusters is also obtained by the nanocasting method than by incorporating oxozirconium clusters in nontemplated or templated mesoporous silica (**Table 3.2**). The nontemplated samples Zr_6@n-t-SiO_2 and Zr_6@n-t-SiO_2(High Zr) exhibit cluster aggregation (**Figure 3.22**) despite having a lower Zr loading. Since only micropores are present in both nontemplated samples (**Figure 3.17**), the catalytic sites are also less accessible compared to those in the mesoporous nanocast material. This resulted in a significantly lower yield of fructose with Zr_6@n-t-SiO_2 and Zr_6@n-t-SiO_2(High Zr) samples as compared to Zr_6@SiO_2. Aside from maintaining site isolation of the clusters, the pore size is also an important factor for the catalytic activity, as the mesoporosity in the nanocast and Zr_6@KIT-6 afforded a

higher yield of fructose compared to the microporous non-templated control samples. The Zr_6@KIT-6 was less active than the nanocast Zr_6@SiO_2, possibly due to the lower loading of Zr in the former (**Table 3.2**). The ability to retain catalytic activity through site isolation and the templated porosity despite being heated to high temperatures makes nanocasting a useful technique for applying MOF-based catalytic clusters for catalytic processes that may require high temperatures.

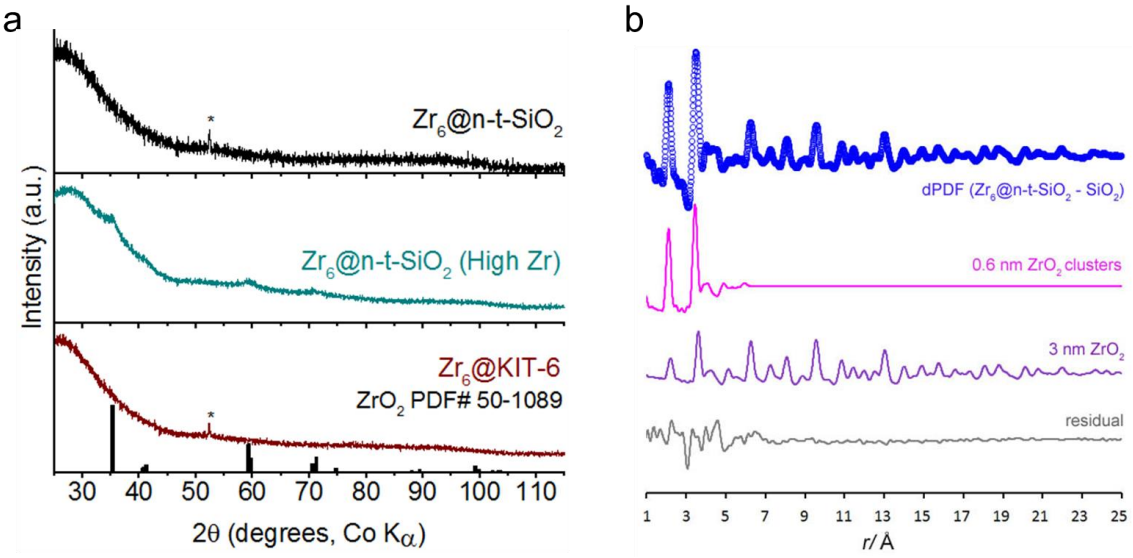

Figure 3.22. (a) XRD patterns of control samples made by incorporating the oxozirconium clusters in non-templated silica (Zr_6@n-t-SiO_2, Zr_6@n-t-SiO_2(High Zr) and mesoporous silica (Zr_6@KIT-6). The peak marked with an asterisk is from the Al sample holder. (b) dPDF trace of Zr_6@n-t-SiO_2 fitted with oxozirconium clusters (~80 wt%, Fm-3m, a = 4.88 Å) and cubic ZrO_2 (~20 wt%, Fm-3m, a = 5.11 Å). The dPDF trace of Zr_6@n-t-SiO_2, obtained using synchrotron X-rays, shows that there is aggregation of oxozirconium clusters in this sample, which was not detected by conventional XRD due to the low concentration of Zr (0.7 wt%) in this sample. The fit indicates that Zr_6@n-t-SiO_2 contained a significant fraction of larger 3 nm nanoparticles (20%) relative to small ~0.6 nm clusters. The size of the 0.6 nm ZrO_2 clusters matches the size of the oxozirconium clusters within NU-1000. The larger 3 nm nanoparticles correspond to 80 to 100 aggregated oxozirconium clusters.

3.4 Conclusion

This work demonstrated the effectiveness of nanocasting the MOF NU-1000 with silica as a strategy to maintain the catalytic activity of MOF-derived single-site catalytic clusters after high-temperature treatment. Silica coated the larger, 3 nm diameter mesopores, but the precursor did not infiltrate the smaller, 1 nm diameter micropores of NU-1000. Aggregation of oxozirconium clusters to form tetragonal ZrO_2 nanoparticles occurred when NU-1000 was heated to 500 °C in air, but in the nanocast materials no significant cluster agglomeration was observed even after heating to 600 °C in air. The clusters remained accessible to reagents such as pyridine or glucose after these high-temperature treatments. The Lewis acidity of these clusters was demonstrated through the isomerization of glucose to fructose, and the mechanism of this reaction was computed with DFT.

The nanocasting method should also be applicable to other large-pore MOF systems that can accommodate precursors like TMOS in the pores. In addition, other precursors could be used for infiltration to produce other secondary scaffold compositions like metal oxides (e.g., titanium dioxide)[329] or carbon by adapting existing nanocasting methods.[330] This affords another handle for optimizing the catalytic properties of the single-site metals or clusters in the nanocast materials. Multiple nanocasting cycles may be used to control the thickness and stability of the secondary scaffold. Nanocasting, combined with the exceptional tunability of MOFs, may pave the way toward a new generation of highly active and stable catalysts for many transformations.

Chapter 4

Thermal Stabilization of Catalytic Metal-Modified Clusters in Metal-Organic Frameworks through Nanocasting

Adapted with permission from "Assembly of Dicobalt and Cobalt-Aluminum Oxide Clusters on Metal-Organic Framework and Nanocast Silica Supports" by Desai, S. P.; Malonzo, C.; Webber, T.; Duan, J.; Thompson, A.; Tereniak, S.; DeStefano, M.; Buru, C.; Li, Z.; Penn. R. L.; Farha, O.; Hupp, J.; Stein, A.; and Lu, C. in *Faraday Discussions*, **2017**, Advance Article.

This work was done in collaboration with Prof. Connie Lu and Sai Desai (synthesis of bimetallated NU-1000), and Prof. Lee Penn and Thomas Webber (TEM analysis) of the University of Minnesota, and Prof. Omar Farha, Prof. Joseph Hupp, Dr. Zhanyong Li and Cassandra Buru of Northwestern University (NU-1000 synthesis, ICP-OES analysis).

4.1 Introduction

Metal–organic frameworks (MOFs), a class of crystalline material comprising metal or metal-cluster nodes connected by organic linkers, are promising as heterogeneous catalysts or as catalytic supports.[67,69,70,96,105,140,141,322,351,352] MOFs provide a highly tunable platform for integrating catalytically desirable properties, including high surface area, porosity, recyclability, and crystallinity.[66,91,320,321,353-356] Critical to the challenge in engineering single sites for heterogeneous catalysis,[19,357,358] the crystallinity of MOFs can enable synthetic access to metal active sites that are uniform, structurally well-defined, and site isolated.

Bimetallic active sites are of interest because they are capable of reactivities that are inaccessible in monometallic or non-noble metal catalysts, such as multi-electron redox chemistry[359] and asymmetric transformations.[360] The unique reactivity results from metal-metal cooperativity, as observed in bimetallic active sites in biological systems.[361-363] Thompson, et al. recently reported the selective installation of heterobimetallic Co–Al active sites in a single step on the MOF, NU-1000, by simply mixing the MOF with the organometallic precursor, (py_3tren)AlCoMe, where py_3tren is the triply deprotonated state of *N*,*N*,*N*-tris(2-(2-pyridylamino)ethyl)amine.[364] NU-1000, a MOF composed of hexazirconium nodes ($[Zr_6O_{16}H_{16}]^{8+}$, referred to as Zr_6-nodes) and 1,3,6,8-tetrakis(*p*-benzoate) pyrene linkers ($TBAPy^{4-}$), is an ideal crystalline support because of its mesoporosity and its high thermal stability compared to other MOFs.[92,102,108]

However, stabilization of active sites on an all-inorganic support, e.g., SiO_2, is also critical to broaden the potential catalytic applications to industrially relevant

conditions, such as high temperatures and/or oxidizing environments, which typically degrade MOFs.[76] This work addresses this challenge through silica nanocasting, a technique that was recently demonstrated for NU-1000.[365] In the nanocasting procedure, the NU-1000 template was cast with silica and subsequently calcined. In the resulting $Zr_6@SiO_2$ material, the silica framework imparts thermal stability and structural integrity, while the Zr_6 oxide clusters remain site isolated and accessible to substrates. In the present work, the nanocasting strategy has been extended to NU-1000 materials that have been functionalized with cobalt–aluminum and analogous dicobalt complexes, resulting in catalytic $AlCoZr_6$ and Co_2Zr_6 oxide clusters embedded in a nanostructured silica support (**Figure 4.1**).

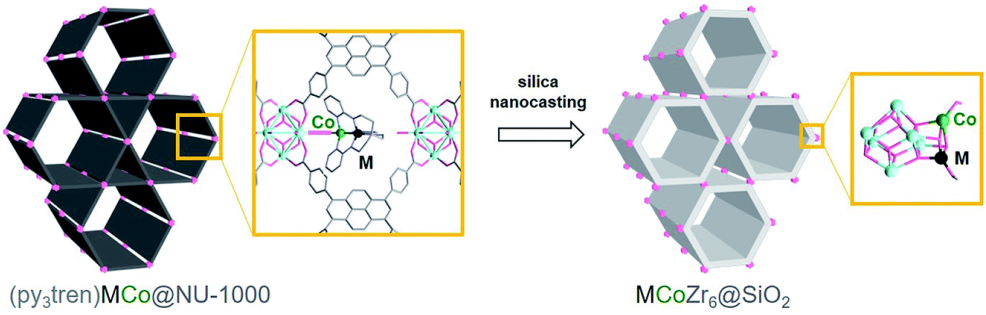

Figure 4.1. (left) Anchored Co–M bimetallic complexes on a NU-1000 support, where M = Al or Co; and (right) Co–M bimetallated Zr_6 oxide cluster on a nanocast silica support.

4.2 Experimental

4.2.1 General Considerations

Unless otherwise stated, all manipulations were performed using a glovebox or standard Schlenk techniques with an N_2 atmosphere. Standard solvents were deoxygenated by sparging with Ar and dried by passing though activated alumina

columns of an SG Water solvent purification system. Deuterated solvents were purchased from Cambridge Isotope Laboratories, degassed *via* freeze–pump–thaw cycles, dried over activated alumina, filtered, and stored over activated 4A molecular sieves. All reagents were purchased from Aldrich or Strem and used without further purification. NU-1000 was synthesized as previously described by solvothermally reacting 1,3,6,8-tetrakis(*p*-benzoic acid)-pyrene (abbreviated as H_4TBAPy), $ZrOCl_2 \cdot 8H_2O$, and benzoic acid.[108] *N*,*N*,*N*-Tris(2-(2-pyridylamino)ethyl)amine (abbreviated as H_3py_3tren), K[Co(py_3tren)] and (py_3tren)AlCo@NU-1000 were prepared using published procedures.[364,366]

4.2.2 Synthesis of (py_3tren)Co_2Br

A slurry of $CoBr_2$ (324 mg, 1.48 mmol) in 30 mL THF was added dropwise to 30 mL of a THF solution of K[Co(py_3tren)] (700 mg, 1.48 mmol) at room temperature. After stirring the reaction mixture for 12 h, the volatiles were removed *in vacuo*. The resulting powder was reconstituted in 80 mL CH_2Cl_2, filtered through Celite diatomaceous earth and layered with Et_2O to obtain olive-green crystals (613 mg, 72% crystalline yield). ^{1}H NMR (400 MHz, CD_2Cl_2): δ 22.5, 20.8, 11.4, 7.9, 6.8, −1.7. Anal. calcd for $C_{21}H_{24}N_7Co_2Br$: C: 44.08, H: 4.23, N: 17.13. Found C: 44.11, H: 4.18, N: 16.81.

4.2.3 Synthesis of (py_3tren)Co_2OPh

To a slurry of (py_3tren)Co_2Br (100 mg, 0.175 mmol) in 5 mL THF was added a 2 mL THF solution of NaOPh (20.3 mg, 0.175 mmol) at room temperature. The reaction

mixture was stirred vigorously for 1 h, and then filtered through Celite diatomaceous earth. The volatiles were removed *in vacuo* and the solids were extracted using 15 mL of benzene. The benzene solution was then layered with pentane to obtain single crystals (37 mg, 36% crystalline yield). ^{1}H NMR (400 MHz, C_6D_6): δ 25.3, 24.5, 12.5, 10.6, 4.4, 3.7, 3.6, 1.6, −1.9. Anal. calcd for $C_{27}H_{29}N_7OCo_2$: C: 55.37, H: 4.99, N: 16.75. Found C: 52.54, H: 4.27, N: 16.46.

4.2.4 Synthesis of (py_3tren)Co_2@NU-1000

Microcrystalline NU-1000 (29.2 mg, 0.014 mmol) was added to a 20 mL benzene solution of (py_3tren)Co_2OPh (20 mg, 0.034 mmol) at room temperature. After stirring for 12 h, the heterogeneous mixture was filtered using a fine porosity glass frit. The resulting solids were washed with copious amounts of benzene (∼20 mL). The solids were soaked overnight in 20 mL benzene and washed with fresh benzene (4 × 1 mL) and pentane (5 × 1 mL). The overnight soaking and rinsing procedure was repeated once more. Finally, the solids were dried under dynamic vacuum (<100 mTorr) for 5 h. ^{1}H NMR (500 MHz, D_2SO_4/DMSO-d_6): δ8.00 (d, $^{3}J_{H–H}$ = 8 Hz, 16H, 2 TBAPy), 7.93 (s, 2H*, 2 TBAPy), 7.77–7.84 (m, 6H, pyridyl), 7.70 (d, $^{3}J_{H–H}$ = 8 Hz, 16H, 2 TBAPy), 7.03 (d, $^{3}J_{H–H}$ = 8.5 Hz, 3H, pyridyl), 6.86 (t, $^{3}J_{H–H}$ = 7 Hz, 3H, pyridyl), 3.73 (br, 6H, tren CH_2), 3.49 (br, 6H, tren CH_2). *Note: not all pyrene-based protons were observed due to their exchange with the D_2SO_4 solvent. ICP-OES (wt%): 22.1 Zr, 5.01 Co (consistent with 2.10 Co per Zr_6).

4.2.5 Silica nanocasting

A casting solution composed of 300 μL of tetramethyl orthosilicate (TMOS), 5 μL of methanol and 5 μL H_2O was first mixed in a vial. It was then added to 30 mg of (py_3tren)Co_2@NU-1000 and allowed to infiltrate the MOF particles for 24 h. Afterwards, the sample was washed with methanol to remove the TMOS on the external surface of the particles, and heated at 40 °C for 5 min to dry. To induce hydrolysis and condensation of the TMOS in the sample, the sample was first exposed to HCl(g) for 24 h at room temperature, then heated in a closed vial at 60 °C for another 24 h, and finally, calcined at 500 °C for 1 h (with a temperature ramp rate of 2 °C min^{-1}). The silica nanocast of (py_3tren)AlCo@NU-1000 was prepared similarly. The resultant nanocast samples are referred to as Co_2Zr_6@SiO_2 and $AlCoZr_6$@SiO_2.

4.2.6 Catalytic studies

Each catalyst (1 μmol) was added to a vial charged with 2.5 mL CD_3CN, benzyl alcohol (0.92 mmol; 96 μL) and *t*-butyl hydroperoxide (TBHP) solution (5.5 M in decane; 1.84 mmol; 336 μL). The heterogeneous reaction mixture was stirred at 80 °C for 2 h. The contents of the vial were cooled to room temperature and filtered through glass fiber. The solutions were analyzed using ^{1}H NMR spectroscopy with 1,3,5-trimethoxybenzene (50 μL from a 0.7 M stock solution) as an internal standard. Catalytic runs were repeated in triplicate.

The filtered solids were washed with acetonitrile (3 × 5 mL) and dried *in vacuo* for 3 h (<100 mTorr). The recovered catalyst (1 μmol) was transferred into a vial,

to which 2.5 mL CD_3CN, benzyl alcohol (0.92 mmol; 96 μL) and TBHP solution (5.5 M in decane; 1.84 mmol; 336 μL) was added. The resultant mixture was stirred at 80 °C for 2 h and the aforementioned catalyst recovery/recycling procedure was repeated after each catalytic run.

4.2.7 Heterogeneity and Leaching Test

Leaching tests were conducted on two catalysts, $(py_3tren)Co_2$@NU-1000 and Co_2Zr_6@SiO_2. A mixture of benzyl alcohol (0.92 mmol; 96 μL), TBHP solution (5.5 M in decane; 1.84 mmol; 336 μL), catalyst (1 μmol of $(py_3tren)Co_2$@NU-1000 or $Co_2Zr_6SiO_2$) and CD_3CN (2.5 mL) were stirred in a scintillation vial at 80 °C. After 30 minutes, the solids were separated from the supernatant by filtration and the supernatant was analyzed using ^{1}H NMR spectroscopy.

A mixture of benzyl alcohol (0.92 mmol; 96 μL), TBHP solution (5.5 M in decane; 1.84 mmol; 336 μL), catalyst (1 μmol of $(py_3tren)Co_2$@NU-1000 or $Co_2Zr_6SiO_2$) and CD_3CN (2.5 mL) were stirred in a scintillation vial at 80 °C. After 30 minutes, the solids were separated from the supernatant by filtration and the supernatant was allowed to react at 80 °C for an additional 90 minutes. The contents of the vial were cooled to room temperature and the solutions were analyzed using ^{1}H NMR spectroscopy.

4.2.8 Instrumentation and measurements

^{1}H NMR spectra were recorded on Bruker Avance III 400 and 500 MHz spectrometers at room temperature. Elemental analyses were performed by Robertson

Microlit Laboratories, Inc. (Ledgewood, NJ). The metal content in (py_3tren)Co_2@NU-1000 was measured by inductively coupled plasma optical emission spectroscopy (ICP-OES) using a Varian Vista-MDX model spectrometer. (py_3tren)Co_2@NU-1000 (~2 mg) was digested in a mixture of conc. H_2SO_4 (0.75 mL) and 30% H_2O_2 (0.25 mL) by heating in a Biotage (Uppsala, Sweden) SPX microwave reactor (software version 2.3, build 6250) at 150 °C for 5 min. The solution was then diluted to a final volume of 15 mL with ultrapure deionized H_2O and analyzed for Co and Zr content. ICP-OES measurements for the nanocast samples were carried out by Galbraith Laboratories, Inc. (Knoxville, TN). Scanning electron microscopy-energy-dispersive X-ray spectroscopy (SEM-EDS) compositional analyses were acquired on a JEOL JXA-8900 electron microprobe operated at 15.0 kV accelerating potential. Samples were coated with a thin film (70 Å) of C prior to SEM-EDS measurements.

FT-IR spectra were collected on a Nicolet Magna-IR 760 spectrometer. Scanning electron microscopy (SEM) measurements were performed on a JEOL 6700 scanning electron microscope operated using a 3.0 kV accelerating voltage. Prior to SEM analysis, all samples were sputter coated with a conductive thin film (50 Å) of Pt. X-ray diffraction (XRD) patterns were collected using an X'Pert Pro diffractometer with an X'Celerator detector. A Co anode (Kα, λ = 1.789 Å) operated at 45 kV and 40 μA was used as the radiation source. N_2 sorption analyses were conducted using a Quantachrome Autosorb iQ2 instrument. Samples were degassed at 120 °C at 1 mTorr for 12 h prior to the analysis. Brunauer–Emmett–Teller (BET) surface areas were evaluated from the adsorption isotherms within the 0.08–0.28 P/P_o range. Pore size distributions and surface

area histograms were obtained using DFT (Quantachrome, N_2 at 77 K on carbon or silica, slit pore) methods.

Scanning transmission electron microscopy-energy dispersive X-ray spectroscopy (STEM-EDS) was performed using an FEI Tecnai G2 field-emission S/TEM operating at an accelerating voltage of 80 kV. The (py_3tren)Co_2@NU-1000 sample was loaded onto 300-mesh lacy carbon/Cu TEM grids by brief immersion of the grid into a dilute benzene suspension of the sample. The nanocast samples were loaded onto TEM grids from ethanol suspensions. High-angle annular dark field (HAADF) images were collected on an E. A. Fischione annular detector using an inner collection semiangle of 21.7 mrad. Energy-dispersive X-ray spectroscopy (EDS) spectra were obtained using the ChemiSTEM EDX spectrometer. EDS maps were collected while rastering the beam over the sample, which facilitated minimization of beam damage. A probe current of ~0.1 nA was used, and maps were collected over a minimum of 5 min. Data were analyzed using ESPRIT software (version 1.9.4).

4.3 Results and discussion

4.3.1 $AlCoZr_6$ and Co_2Zr_6 oxide clusters on nanocast silica supports

Previous work demonstrated the effectiveness of nanocasting MOFs with silica as a method to preserve the activity of MOF-based catalytic metal sites for high temperature reactions.[365] In nanocasting NU-1000, the MOF framework served as the template for a thermally stable silica scaffold, which then became the sole support for the catalytic zirconium oxide sites upon removal of the organic linkers at high temperatures. To

determine whether this stabilization can also be achieved with metal-modified MOFs, silica nanocasts of (py_3tren)AlCo@NU-1000 and (py_3tren)Co_2@NU-1000 were prepared by infiltrating the MOF particles with the silica precursor, tetramethyl orthosilicate (TMOS). Once inside the MOF pores, TMOS was condensed to silica under hydrolytic conditions in the presence of an acid catalyst, as shown in **Figure 4.2**. The resulting composite materials, where the bimetallated Zr_6 clusters are supported by both NU-1000 and SiO_2 supports, were then calcined to remove the organic groups, generating the desired bimetallated Zr_6 clusters on the nanocast SiO_2 support, Co_2Zr_6@SiO_2 and $AlCoZr_6$@SiO_2.

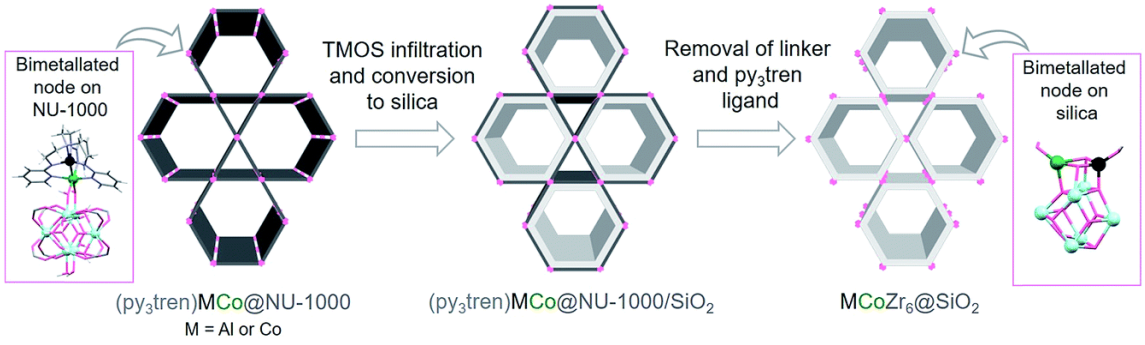

Figure 4.2. Synthetic methodology to generate bimetallated Zr_6 oxide clusters on a nanocast SiO_2 support, $AlCoZr_6$@SiO_2 and Co_2Zr_6@SiO_2.

Characterization data of the nanocast materials lend support to the generation of bimetallated Zr_6 oxide clusters within a nanocast SiO_2 matrix. The $AlCoZr_6$@SiO_2 and Co_2Zr_6@SiO_2 particles both share a rod-like morphology similar to the (py_3tren)MCo@NU-1000 precursors but are notably thinner (**Figure 4.3**). Particle shrinkage likely occurs during the calcination step (500 °C under air) of the nanocasting

process. The N_2 adsorption isotherms of $AlCoZr_6@SiO_2$ and $Co_2Zr_6@SiO_2$ indicate porosity, though the pore sizes cover a broad range, primarily between 2 and 5 nm (**Figure 4.4**). For $AlCoZr_6@SiO_2$ and $Co_2Zr_6@SiO_2$, the BET surface area (363 and 261 $m^2\ g^{-1}$, respectively) and pore volume (0.24 and 0.20 $cm^3\ g^{-1}$, respectively) are significantly reduced compared to the precursor materials before nanocasting, but they are similar in value to those previously reported for the nanocast NU-1000 material, $Zr_6@SiO_2$ (365 $m^2\ g^{-1}$ and 0.27 $cm^3\ g^{-1}$).

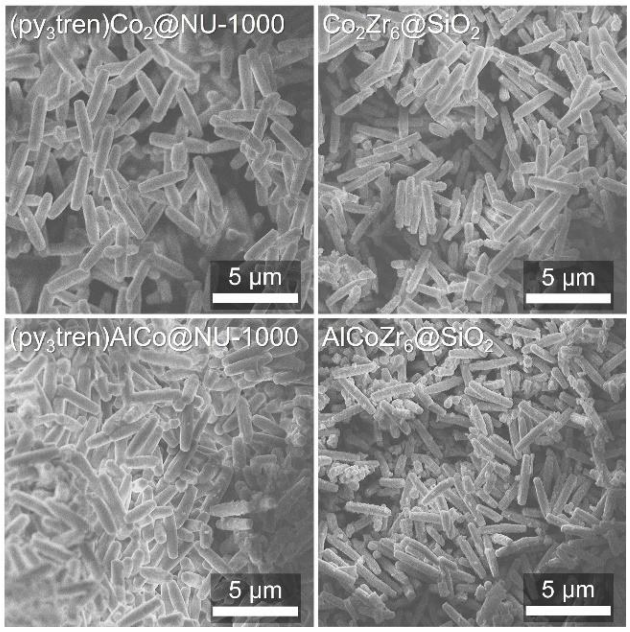

Figure 4.3. SEM images of the bimetallated NU-1000 samples, $(py_3tren)Co_2@NU\text{-}1000$ and $(py_3tren)AlCo@NU\text{-}1000$, and their corresponding silica nanocasts, $Co_2Zr_6@SiO_2$ and $AlCoZr_6@SiO_2$.

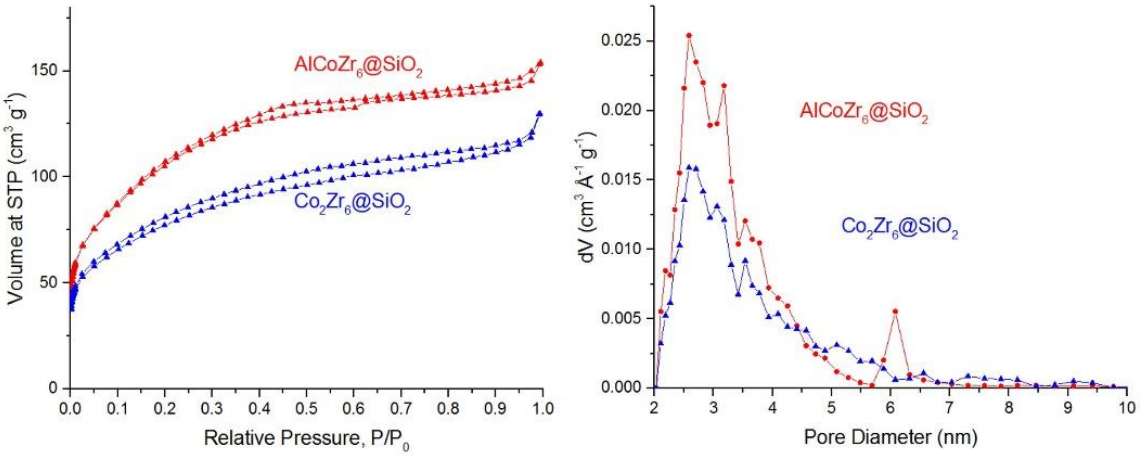

Figure 4.4. N_2 sorption isotherms (left) and DFT pore size distribution (right) of $Co_2Zr_6@SiO_2$ and $AlCoZr_6@SiO_2$, confirming the presence of mesopores in the amorphous silica matrices of these samples. The BET surface area and pore volume of $Co_2Zr_6@SiO_2$ are 261 m^2g^{-1} and 0.20 cm^3g^{-1}, respectively. The corresponding values for $AlCoZr_6@SiO_2$ are 363 m^2g^{-1} and 0.24 cm^3g^{-1}.

Figure 4.5 shows the HAADF images and STEM-EDS elemental maps of the nanocast materials, $AlCoZr_6@SiO_2$ and $Co_2Zr_6@SiO_2$. Elemental maps show a relatively dense silica matrix throughout the individual particles. Notably, the metals, Zr, Co, and/or Al, remain well-distributed throughout these particles. Silica formation was further confirmed by the intense absorption at 1090 cm^{-1} in the FT-IR spectra of these samples (**Figure 4.6**), which is assigned to the Si–O–Si stretching vibration.

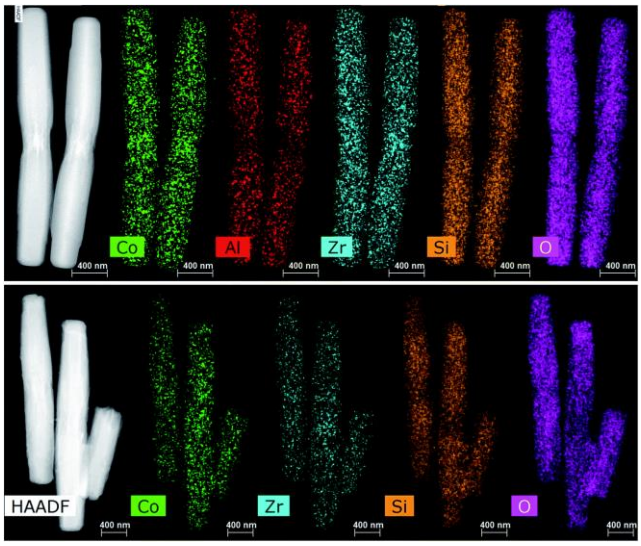

Figure 4.5. HAADF image of single particles of $AlCoZr_6@SiO_2$ (top) and $Co_2Zr_6@SiO_2$ (bottom) with the corresponding STEM-EDX elemental maps for Co, Al, Zr, Si, and O.

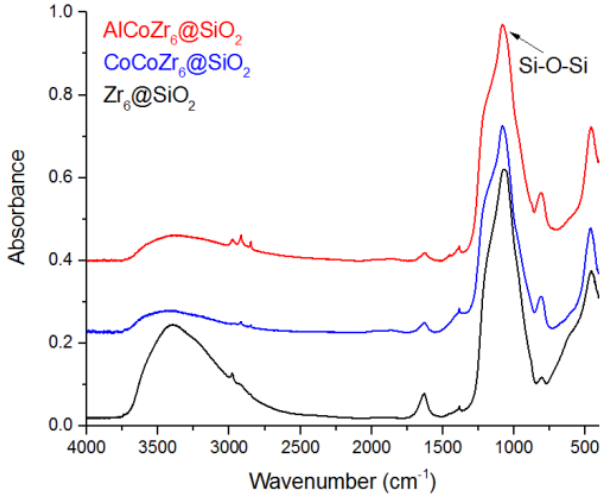

Figure 4.6. FT-IR spectra of $Co_2Zr_6@SiO_2$, $AlCoZr_6@SiO_2$, and $Zr_6@SiO_2$. The presence of silica in the nanocast samples is confirmed by the Si-O-Si absorption peak at 1090 cm^{-1}.

One critical challenge of the nanocasting process is to maintain the stoichiometry of the Co and/or Al metal centres per Zr_6 cluster. This is especially pertinent because high-spin Co complexes are labile and exchange ligands rapidly, which may lead to Co leaching out of the particles. Gratifyingly, the ratios of Co and/or Al per Zr_6 were unaffected by nanocasting. For $AlCoZr_6@SiO_2$, the Al : Co ratio per Zr_6 was determined by ICP-OES to be 1.4 : 1.2, while the ratio of Si was ~60 atoms per Zr_6. Analogously, for $Co_2Zr_6@SiO_2$, the ratio of Co and Si atoms per Zr_6 was 2.1 and ~50, respectively. Finally, the oxidation state of Co in both $AlCoZr_6@SiO_2$ and $Co_2Zr_6@SiO_2$ is Co(II), as determined by high resolution XPS data (**Figure 4.7**). The energy separation between the Co $2p_{1/2}$ and $2p_{3/2}$ peaks of $AlCo@Zr_6SiO_2$ (15.6 eV) and $Co_2Zr_6@SiO_2$ (15.5 eV) is similar to that observed for $(py_3tren)Co_2$@NU-1000 (15.4 eV). In addition, the presence of satellite peaks is consistent with divalent Co.[367,368] The absence of any nitrogen peaks in the XPS data for both $AlCoZr_6@SiO_2$ and $Co_2Zr_6@SiO_2$ further validates the removal of the py_3tren ligand during the nanocasting procedure.

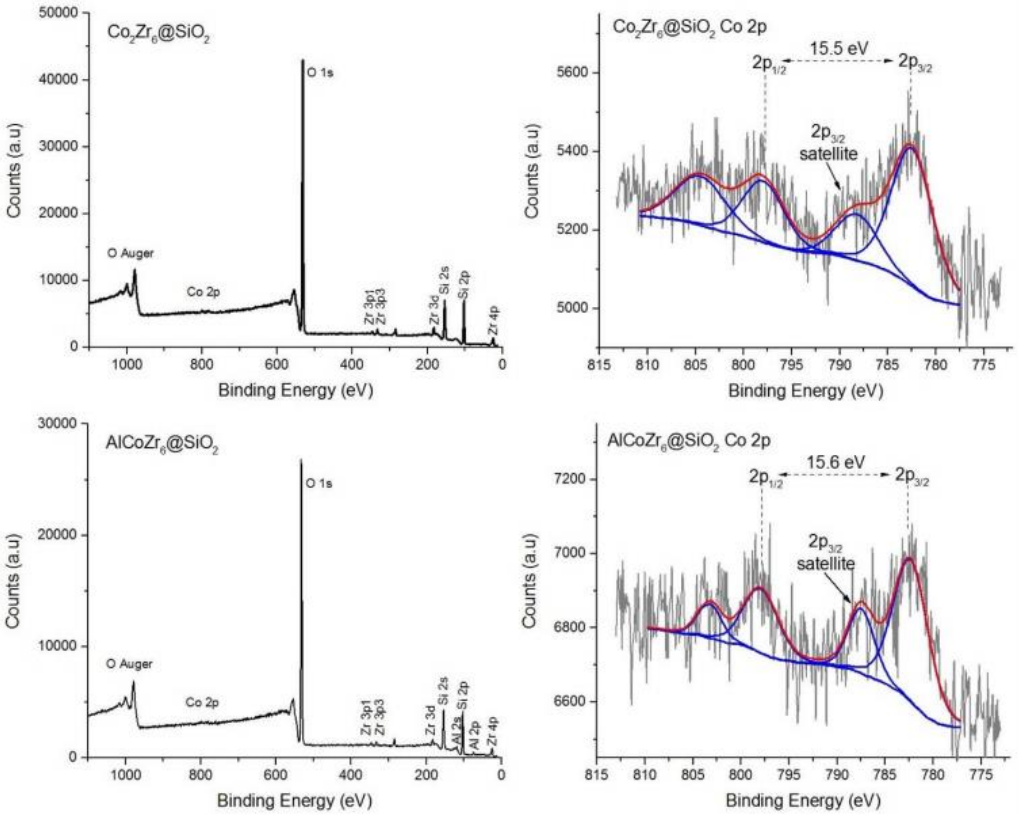

Figure 4.7. XPS survey (left column) and Co high resolution scans (right column) for $Co_2Zr_6@SiO_2$ and $AlCoZr_6@SiO_2$. The $2p_{1/2}$ and $2p_{3/2}$ peak separation and the presence of the $2p_{3/2}$ satellite peak indicate that the oxidation state of Co in the nanocast samples is +2, the same as in $(py_3tren)Co_2@NU\text{-}1000$.

X-ray diffraction (XRD) data of $AlCoZr_6@SiO_2$ and $Co_2Zr_6@SiO_2$ illustrate the importance of the silica matrix in stabilizing the bimetallated Zr_6 oxide clusters (**Figure 4.8**), which is critical for high-temperature catalytic applications. Without the nanocast silica backbone, heating NU-1000 at 500 °C resulted in agglomeration of the Zr_6 nodes to ZrO_2.[365] Large crystallites of ZrO_2 (*ca.* 18 nm, calculated by the Scherrer equation) were observed based on the sharp, characteristic peaks in the XRD pattern. By contrast, the XRD patterns of $AlCoZr_6@SiO_2$ and $Co_2Zr_6@SiO_2$ are devoid of any sharp peaks that

would indicate agglomerated metal oxides of Zr, Co, and/or Al. Hence, nanocasting with silica is highly effective at preventing the aggregation of metal sites even at temperatures as high as 500 °C. The notable lack of diffraction rings in the selected area electron diffraction (SAED) patterns of the nanocast materials (**Figure 4.9**), as opposed to calcined NU-1000, demonstrates that nanocasting effectively precludes aggregation of the bimetallated Zr_6 nodes.

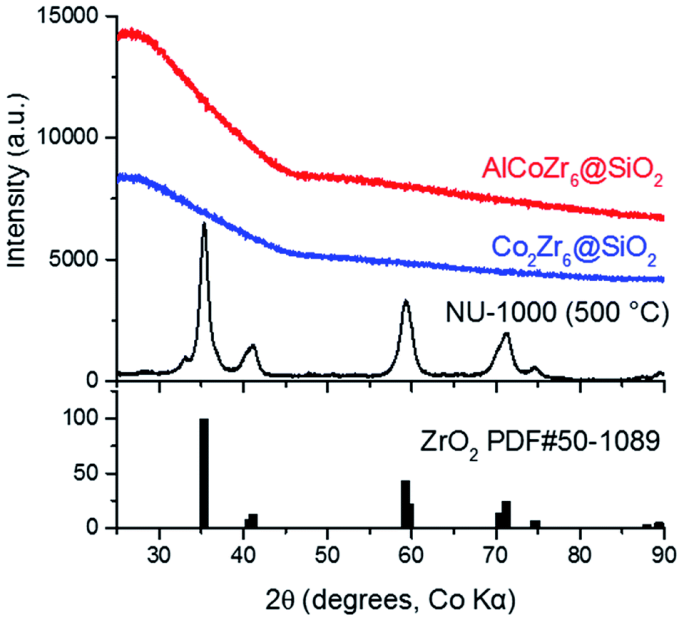

Figure 4.8. XRD patterns of the silica nanocasts, $AlCoZr_6@SiO_2$ and $Co_2Zr_6@SiO_2$, after heat treatment at 500 °C in air. For comparison, the XRD pattern of NU-1000 calcined at 500 °C in air is shown, which matches the published powder diffraction file pattern for tetragonal ZrO_2 (PDF#50-1089).

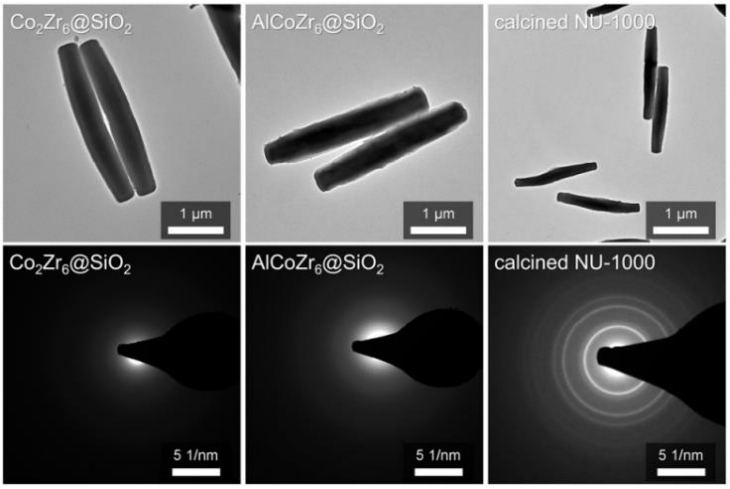

Figure 4.9. TEM images (top) and the corresponding SAED patterns (bottom) of $Co_2Zr_6@SiO_2$and $AlCoZr_6@SiO_2$ after linker removal at 500 °C in air. The absence of diffraction rings supports the hypothesis that no aggregation of the bimetallated Zr_6 nodes occurred in either sample. On the other hand, the SAED pattern of NU-1000 calcined at the same temperature shows diffraction rings that index to ZrO_2, indicating that the zirconium clusters in this sample have aggregated to form larger ZrO_2 crystallites.

4.3.2 Catalytic studies

To test whether the activity of the bimetallated Zr_6 nodes varies as a function of the support, e.g., NU-1000 or nanocast silica, we investigated a test catalytic reaction. Previously, (py_3tren)AlCo@NU-1000 was found to be a competent catalyst for the oxidation of benzyl alcohol;[364] however, *tert*-butyl hydroperoxide (TBHP) was needed as a stoichiometric oxidant, which is less desirable than H_2O_2.[369,370] The study concluded that Co centers were responsible for the catalytic activity because both NU-1000 and Al-functionalized NU-1000 gave low yields that were on par with the background reaction. Consistent with these findings, all materials containing Co were found to be competent catalysts (**Table 4.1**), with moderate conversions (42 to 56%) and turnover numbers

(TONs 330 to 490). On the other hand, NU-1000 and nanocast NU-1000, *i.e.* $Zr_6@SiO_2$, showed low conversions (6 to 7%).

Table 4.1. Properties of various materials and their catalytic activity in the oxidation of benzyl alcohol to benzaldehyde (Catalytic conditions: 0.1 mol% catalyst loading, 1.0 μmol catalyst, 0.92 mmol BnOH, 1.84 mmol TBHP (5.5 M in decane), 2.5 mL CD_3CN, 80 °C, 2 h).[a]

catalyst	Co: Zr_6[b]	Al: Zr_6[b]	Si: Zr_6[b]	BET surface area (m^2/g)	pore volume (cm^3/g)	conversion (%) of benzyl alcohol	TON of benzaldehyde per Zr_6 [c]
$(py_3tren)Co_2@NU\text{-}1000$	2.1	0	0	1352	0.89	56.0 ± 1.4	490 ± 20
$Co_2Zr_6@SiO_2$	2.1	0	50.7	261	0.20	52.8 ± 3.5	450 ± 5
$(py_3tren)AlCo@NU\text{-}1000$	1.2	1.2	0	1761	0.94	43.4 ± 3.6	350 ± 17
$AlCoZr_6@SiO_2$	1.2	1.4	59.9	363	0.24	42.2 ± 1.1	330 ± 5
NU-1000	0	0	0	1990	1.40	6.2 ± 0.7	45 ± 10
$Zr_6@SiO_2$	0	0	12.9	364	0.27	7.1 ± 1.9	50 ± 11

[a]Catalysis results are based on triplicate runs. [b]Atom ratios were calculated from ICP-OES data, except for $(py_3tren)AlCo@NU\text{-}1000$, for which ratios were calculated from SEM-EDS data. [c]TON = turnover number.

The materials $(py_3tren)Co_2@NU\text{-}1000$ and $Co_2Zr_6@SiO_2$, which have higher Co content, 2.1 Co per Zr_6, had conversions above 50% and similar TONs of 490 and 450, respectively. On the other hand, the TONs for $(py_3tren)AlCo@NU\text{-}1000$ and $AlCoZr_6@SiO_2$ were significantly lower at 350 and 330, respectively. However, the identity of the supporting matrix for the clusters, either the NU-1000 framework or the silica nanocast, did not influence catalytic activity significantly. This finding is consistent with the notion that the Co sites remain intact on the Zr_6 oxide clusters in both NU-1000 and the nanocast silica materials. Notably, the catalytic Co sites in the silica nanocasts

remain as accessible to small substrates compared to the bimetallated NU-1000 precursors, despite significant loss in both porosity and surface area of the silica nanocasts.

To test whether the catalytically active species is truly heterogeneous, leaching tests were conducted on two catalysts, (py_3tren)Co_2@NU-1000 and Co_2Zr_6@SiO_2.[371] After initiating catalysis for 30 minutes, the solids and supernatant were separated by filtration. SEM-EDS analysis of the solids showed that the post-catalysis material retained the same Co:Zr_6 ratio (~2 : 1, less than 2% loss, **Table 4.2**) as the material prior to catalysis. Furthermore, we subjected the supernatant to a second cycle of catalysis, during which the conversion of benzyl alcohol changed insignificantly from 2 to 3% (**Table 4.2** and **Table 4.3**). Finally, both (py_3tren)Co_2@NU-1000 and Co_2Zr_6@SiO_2 can be recycled and reused up to three times without any significant loss in catalytic activity (**Figure 4.10**). These observations collectively support the heterogeneous nature of the active catalyst, and rule out the possibility of leaching and/or the presence of soluble active species.

Table 4.2. Catalytic activity of (py_3tren)Co_2@NU-1000 and Co_2Zr_6@SiO_2 after 30 min. Co:Zr_6 obtained from SEM-EDS rule out the possibility of leaching of metals into the supernatant.

catalyst	**conversion (%) of benzyl alcohol**	**TON of benzaldehyde per Zr_6**	**Co:Zr_6 before catalysis**	**Co:Zr_6 after catalysis**
(py_3tren)Co_2@NU-1000	56.0 ± 1.4	490 ± 20	1.76	1.73
Co_2Zr_6@SiO_2	52.8 ± 3.5	450 ± 5	2.03	1.99

Table 4.3. Catalytic activity of $(py_3tren)Co_2$@NU-1000 and Co_2Zr_6@SiO_2 (testing of supernatant activity in the second cycle of catalysis). The conversion to benzaldehyde is essentially unchanged after the solids are removed from the reaction mixture, and the supernatant is subjected to further catalysis (based on a comparison of results to Table 4.2).

supernatant from	conversion (%) of benzyl alcohol	TON of benzaldehyde per Zr_6 [c]
$(py_3tren)Co_2$@NU-1000	15.6	127
Co_2Zr_6@SiO_2	13.8	104

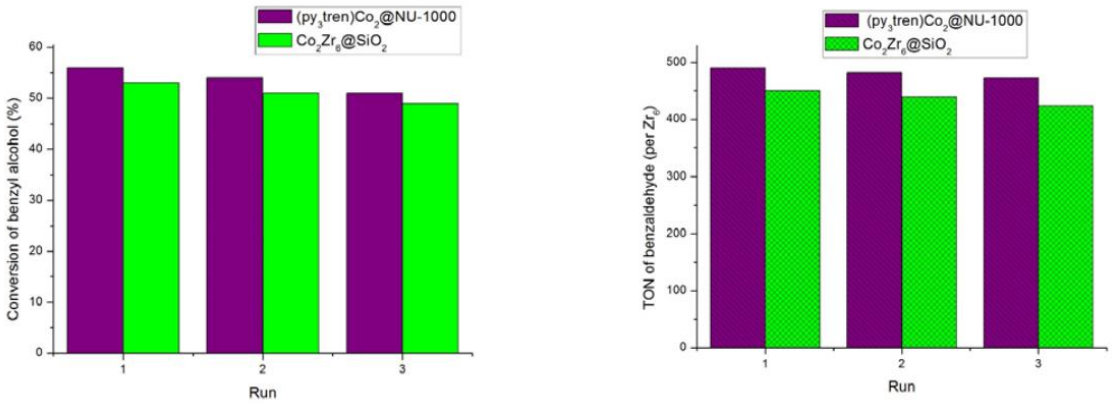

Figure 4.10. Recyclability and reuse of $(py_3tren)Co_2$@NU-1000 and Co_2Zr_6@SiO_2 as catalysts for the oxidation of benzyl alcohol to benzaldehyde. (left) Conversion of benzyl alcohol, and (right) TON of benzaldehyde per Zr_6.

4.4 Conclusion

A controlled loading of a single dicobalt synthon "$(py_3tren)Co_2$" per Zr_6 node was achieved using a simple solution-phase reaction involving a relatively stable metal–metal bonded complex, $(py_3tren)Co_2OPh$, and mesoporous NU-1000. The resulting material, $(py_3tren)Co_2$@NU-1000, along with the previously reported $(py_3tren)Co_2$@NU-1000,[364]

were nanocast with silica. $AlCoZr_6@SiO_2$ and $Co_2Zr_6@SiO_2$ materials were synthesized by this nanocasting method, demonstrating a new strategy to achieve site-isolated heterometallic sites in a porous, thermally stable silica matrix. Based on the characterization and catalytic data, the nanocasting procedure retains the site isolation and substrate accessibility of the bimetallated Zr_6 oxide clusters, as well as their catalytic activity.

Chapter 5

Application and Limitations of Nanocasting in Metal-Organic Frameworks for High Temperature Catalysis

This chapter describes investigations on nanocasting several other MOF systems with silica. I am extremely grateful to Jiaxin Duan, an undergraduate student at the University of Minnesota, for her help in the sunthesis and characterization of the MOFs and nanocast materials studied here. This work was done in collaboration with Prof. Lee Penn and Thomas Webber (TEM analysis), and Prof. Aditya Bhan and Dr. Praveen Bollini (dehydrogenation catalytic test) of the University of Minnesota, Prof. Omar Farha, Prof. Joseph Hupp, and Dr. Zhanyong Li of Northwestern University (Ni(SIM)-NU-1000 synthesis), and Dr. Alex Martinson and Dr. In Soo Kim of Argonne National Laboratory (In(AIM)-NU-1000 synthesis).

5.1 Introduction

Nanocasting is a method that allows the formation of nanostructured materials as direct or inverse replicas of a porous template. Combined with sol-gel techniques, it affords the synthesis of structurally tunable materials with tailorable compositions, including carbon, metal oxides, and other inorganic materials.[44,45] Nanocasting involves the infiltration of a precursor solution into a template, followed by the conversion of the precursor to a solid within the template. Removal of the template by methods such as etching or calcination yields the final nanocast material. The nanocasting method has been developed extensively for the preparation of nanostructured materials from mesoporous templates.[26,28,36,43]

Metal-organic frameworks (MOFs) form an emerging class of porous materials that is rapidly gaining interest for a variety of applications, including gas storage, separation, and catalysis.[66,372,373] MOFs consist of metal-based nodes that are interconnected via organic linkers, forming a porous, crystalline network. They have tunable pore morphology, and pore sizes of up to 98 Å have been achieved.[91] MOFs have been used as templates for nanocasting to make microporous and mesoporous materials, where the final nanocast material is void of the original MOF template, including microporous titania[329] and polyaniline[331] templated from the MOF HKUST-1, and other porous oxides, carbon and composites.[75]

While MOFs can be used as templates for other nanostructured materials, nanocasting of MOFs can be also done for a different purpose, particularly for stabilizing MOF-based catalysts. MOFs are of interest for catalysis because their structure

incorporates high loadings of well-defined metal sites that can be catalytically active.[73,74,98] The activity can also be tuned by the choice of metal during the synthesis and by post-synthetic metalation via atomic layer deposition, solution-phase deposition, or metal-exchange.[69,107,108,141,351,374] Catalysis with MOFs is, however, limited to low temperature reactions. At high temperatures and in oxidizing environments, degradation of the organic linkers occurs, along with the aggregation of the catalytic metal sites, which leads to loss of their catalytic activity. To address this, an approach was developed to stabilize the metal sites in MOFs by nanocasting with silica.[365] Nanocasting introduces a thermally stable silica layer in the pores of the MOF that can serve as a secondary support for the metal sites, keeping their site-isolation and catalytic activity even after the loss of organic linkers. Thus, through nanocasting, the highly tunable and well-defined metal sites in the MOFs can be used for high temperature catalysis.

This nanocasting method has been applied successfully to the mesoporous MOF, NU-1000,[365] as well as to bimetallated NU-1000 samples.[375] In both cases, the presence of silica in the MOF pores enabled maintenance of the site-isolation, accessibility and catalytic activity of the metal sites after high temperature treatment that removed the organic linkers from the structure. The current work describes the nanocasting experiments with other MOF systems with different pore sizes and metal node compositions (**Figure 5.1**).

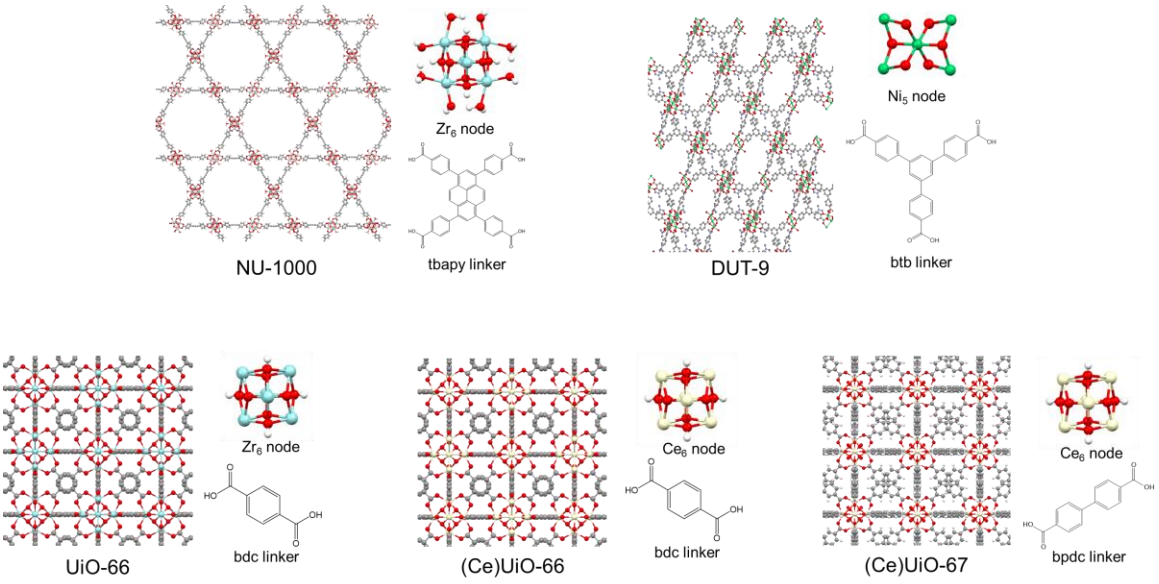

Figure 5.1. The framework structure and the secondary building units of the MOFs used for nanocasting.

Here, the MOFs UiO-66, (Ce)UiO-66, (Ce)UiO-67, DUT-9 and post-metalated NU-1000 MOFs were nanocast with silica. NU-1000, UiO-66, (Ce)UiO-66, and (Ce)UiO-67 feature isostructural hexazirconium (Zr_6) and hexacerium (Ce_6) oxide nodes. The Zr_6 node in UiO-66 is fully coordinated with 12 carboxylate groups (i.e., 12-connected) from the organic linkers, whereas in NU-1000, this cluster is only 8-connected and the rest of the coordination sites are occupied by –OH and $–H_2O$ groups (**Figure 5.1**). The Ce_6 nodes in (Ce)UiO-66, and (Ce)UiO-67 are also 12-connected, similar to UiO-66. In DUT-9, the Ni_5 nodes are 6-connected, with the four remaining coordination sites occupied by solvent molecules, e.g., DMF. This work demonstrates that the MOF nanocasting method can provide access to other catalytically interesting metal site compositions (e.g., Ni,[376-381] In,[382-384] and Ce,[385] for the high temperature catalytic manipulation of C–H and C–C bonds). Additionally, it is shown here that the

method is applicable to both microporous (e.g., UiO-66) and mesoporous MOFs (e.g., DUT-9). Considerations regarding the compatibility between the nanocasting conditions and MOF stability, and the associated method optimizations are also discussed.

5.2 Experimental Section

5.2.1 Materials

The following chemicals were used as received: $ZrOCl_2 \cdot 8H_2O$ (98%), $(NH_4)_2Ce(NO_3)_6$ (≥98.5%), $Ni(NO_3)_2 \cdot 6H_2O$ (≥97%), benzene-1,4-dicarboxylic acid (H_2BDC, 98%), benzene-1,3,5-tribenzoic acid (H_3BTB, (≥98%), tetramethyl orthosilicate (TMOS, 98%), and methanol (≥ 99.8%) from Sigma-Aldrich, biphenyl-4,4'-dicarboxylic acid (H_2BPDC, (≥97.0%) from TCI America, hydrochloric acid (36.5–38.0%) and formic acid (88–91%) from BDH Chemicals, *N*,*N*-dimethylformamide (DMF, 99.8%) from Macron Fine Chemicals, *N*,*N*-diethylformamide (DEF, 99%) from Acros Organics, dimethylsulfoxide (DMSO, 99.9%) from Fisher Chemical, and ethanol (100%) from Pharmco-Aaper. Deionized water produced on-site with a minimum resistivity of 18.2 MΩ·cm was used in all experiments.

5.2.2 Synthesis of MOFs

UiO-66. The procedure for the preparation of (Zr)UiO-66 was similar to the one described in the literature.[386] $ZrOCl_2 \cdot 8H_2O$ (125 mg, 0.54 mmol) was dissolved in a mixture of DMF (5 mL) and concentrated HCl (1 mL). In a separate vial, the linker, H_2BDC (123 mg, 0.75 mmol) was also dissolved in DMF (10 mL). The two solutions

were mixed and heated at 80 °C for 24 h. The product, (Zr)UiO-66, was washed twice with DMF and then twice with methanol prior to air-drying. The MOF was finally activated at 150 °C for 12 h.

(Ce)UiO-66 and (Ce)UiO-67. The procedure for the preparation of (Ce)UiO-66 and (Ce)UiO-67 was adapted from the literature.[387] To synthesize (Ce)UiO-66, H_2BDC (35.4 mg, 0.213 mmol) was dissolved in DMF (1.2 mL). In a separate vial, $(NH_4)_2Ce(NO_3)_6$ (117 mg, 0.21 mmol) was dissolved in deionized water (0.4 mL). The two solutions were mixed and heated at 100 °C for 15 min. The product, (Ce)UiO-66, was washed twice with DMF and then twice with methanol prior to air-drying. The MOF was finally activated at 130 °C for 12 h. (Ce)UiO-67 was prepared similarly, with the following exceptions: H_2BPDC (51.6 mg, 0.213 mmol) was used as the linker, the reaction time at 100 °C was increased from 15 min to 20 min, and the sample was washed twice with DMSO instead of DMF.

DUT-9. The procedure for the preparation of DUT-9 was adapted from the literature.[94] H_3BTB (90 mg, 0.20 mmol) and $Ni(NO_3)_2 \cdot 6H_2O$ (183 mg, 0.63 mmol) were dissolved in DEF (5.25 mL) in a vial. The solution was heated at 120 °C for 20 h. The product, DUT-9, was washed twice with DMF, which was then exchanged with 100% ethanol prior to supercritical CO_2 (sc-CO_2) drying.

Supercritical drying was performed on a Tousimis Samdri-780A critical point dryer. The sample was placed in fresh 100% ethanol immediately before placing it inside the dryer. The sample was purged with liquid CO_2 at 0–10 °C for 6 min and then soaked in it for 2 h. The CO_2 was then brought above the supercritical point (at 1100–1300 psi

and 33–41 °C) and released from the dryer. The sc-CO_2-dried DUT-9 was heated to 60 °C for 12 h to complete the activation.

5.2.3 Preparation of Metal-Modified MOFs

Ni(SIM)-NU-1000. Nickel-loaded NU-1000 was synthesized via solution deposition in MOFs (SIM). Nickel(II) acetate tetrahydrate (276.5 mg, 1.11 mmol) was suspended in 40 mL DMF in a 100-mL screw cap jar. It was subsequently incubated in an oven at 100 °C for 30 min or until the solution became clear. Next, NU-1000 (400 mg, 0.185 mmol) was added to the jar, and it was subjected to 5 min of sonication before incubation in an oven at 100 °C overnight. The suspension was centrifuged, and the mother liquor was decanted while hot after centrifugation. The solid residue was washed with hot DMF three times (3 × 50 mL) or until the DMF solution was colorless. The recovered solid material was immersed in acetone for one hour and then washed three times (30 min intervals) to remove the residual DMF by solvent exchange. After subsequent suspension in acetone for another 8 h, the yellow solid material was placed in a vacuum oven (< 100 mTorr, room temperature) for 2 h before it was thermally activated at 120 °C on a Smart VacPrep instrument for 24 h. The recovered material, denoted as Ni(SIM)-NU-1000, was kept in a vacuum desiccator for storage.

In(AIM)-NU-1000. Indium-loaded NU-1000 was synthesized via ALD in MOFs (AIM) using a modified procedure described previously.[388] In each experiment, 50 mg of NU-1000 powder was heated to 125 °C under suction with a continuous flow of 20 sccm nitrogen (N_2), resulting in 0.4 Torr – standard “purge” conditions. After 10 min of purge

conditions to remove any physisorbed water, the powder was reproducibly hydroxylated with a 60 s exposure to water vapor using a pulse sequence of t_1-t_2-t_3 (pulse length – exposure – purge), where t_1 = 1 s, t_2 = 59 s, t_3 = 300 s. Subsequently, the powder was purged for 5 min to remove physisorbed water and obtain a steady –OH and $–OH_2$ population. Trimethylindium ($InMe_3$) was then introduced into the reaction chamber using the same pulse sequence, but with standard pulse times of t_1 = 0.1 s, t_2 = 29.9 s, and t_3 = 30 s. Following 800 repeated exposures of $InMe_3$, the sample was left to purge for an additional 5 min to ensure a complete removal of any excess precursor and/or reaction by-products within the pores of NU-1000. The powder was then subjected to 80 doses of water vapor according to the previous dosing schedule, but with a shorter pulse length (0.1 s) in order to minimize the effects of MOF heating expected from the strongly exothermic heat of reaction.

5.2.4 Silica Nanocasting

Silica Nanocasting with Acid Catalyst. A casting solution composed of 300 μL of TMOS, 5 μL of methanol, and 5 μL H_2O was first mixed in a vial. The solution was then added to 30 mg of the MOF and allowed to infiltrate the MOF particles for 24 h. Afterwards, the sample was washed with methanol to remove any TMOS from the external surface of the particles and heated at 40 °C for 5 min to dry. To induce hydrolysis and condensation of the TMOS in the sample, the sample was first exposed to HCl(g) for 24 h at room temperature. The sample was then heated in a closed vial at 60 °C for another 24 h. Finally, the sample was calcined at 500 °C for 1 h in static air to

remove the organic linkers from the structure. A temperature ramp rate of 2 °C/min was used for calcination.

Silica Nanocasting without Acid Catalyst. A casting solution composed of 300 μL of TMOS, 75 μL of methanol, and 50 μL H_2O was first mixed in a vial. The solution was then added to 30 mg of the MOF and allowed to infiltrate the MOF particles for 24 h. The casting solution was removed by centrifugation and decantation. Afterwards, the sample was washed with methanol to remove any TMOS from the external surface of the particles, and heated at 40 °C for 5 min to dry. The sample was heated in a closed vial at 80 °C for 24 h to induce hydrolysis and condensation of the TMOS. Finally, the sample was calcined at 500 °C for 1 h to remove the organic linkers from the structure. A temperature ramp rate of 2 °C/min was used for calcination.

This procedure was used to prepare nanocast DUT-9 with slight modification. After the synthesized DUT-9 was washed twice with DMF, the DMF was replaced with the casting solution composed of 300 μL of TMOS, 75 μL of methanol, and 50 μL H_2O. The exchange was allowed to proceed for 3 days. The casting solution was removed by centrifugation and decantation, and the MOF particles were treated as described above to yield the final nanocast material.

Leaching Test for Ni(SIM)-NU-1000 and In(AIM)-NU-1000. After the infiltrated MOF particles were separated from the casting fluid, the latter was also exposed to HCl(g) for 24 h at room temperature. This was followed by heat treatment in a closed vial at 60 °C for another 24 h. Finally, the sample was calcined at 500 °C for 1 h. A temperature ramp rate of 2 °C/min was used for calcination. The presence of In or Ni in

the resulting sample was analyzed by SEM-EDS and XRD. Similar steps were taken for the methanol washings used to remove the TMOS on the external surface of the infiltrated particles.

5.2.5 Characterization

FT-IR spectra were collected on a Nicolet Magna-IR 760 spectrometer. Ground samples were placed between two KBr windows for FT-IR measurements. Scanning electron microscopy (SEM) measurements were performed on a JEOL 6700 scanning electron microscope operated using a 5.0 kV accelerating voltage. Prior to SEM analysis, all samples were sputter coated with a conductive thin film (70 Å) of Pt. X-ray diffraction (XRD) patterns were collected using an X'Pert Pro diffractometer with an X'Celerator detector. A Co anode (Kα, λ = 1.789 Å) operated at 45 kV and 40 μA was used as the radiation source. N_2 sorption analyses were conducted using a Quantachrome Autosorb iQ2. The MOF samples were degassed prior to the analysis at 1 mTorr for 12 h at the following temperatures: (Zr)UiO-66, (Ce)UiO-66, and (Ce)UiO-67 at 130 °C, DUT-9 at 60 °C, and Ni(SIM)-NU-1000 and In(AIM)-NU-1000 at 120 °C. Scanning electron microscopy-energy-dispersive X-ray spectroscopy (SEM-EDS) compositional analyses were acquired on a JEOL JXA-8900 electron microprobe operated at 15.0 kV accelerating potential. Samples were coated with a thin film (70 Å) of carbon prior to SEM-EDS measurements.

5.2.6 Catalyst Testing: Cyclohexane Dehydrogenation

Nanocast NU-1000 was prepared by silica nanocasting using the acid catalyst procedure described above and was tested as a cyclohexane dehydrogenation catalyst. The nanocast material (0.015 g, mesh 40-80) was heated in a flow reactor from room temperature to 610 °C under a flow of air (100 mL/min) for an hour and kept at temperature for another hour. The temperature was measured using a thermocouple probe in the middle of the catalyst bed. At this temperature, the reaction mixture consisting of a 1:8.31 molar ratio of cyclohexane and H_2 (0.95 kPa cyclohexane/7.90 kPa H_2/balance Ar and CH_4) was fed to the catalyst bed at a flow rate of 42 cm^3 min^{-1}.

5.3 Results and Discussion

5.3.1 General Considerations

Although some large pore MOFs have been prepared such as IRMOF-74-XI (pore size = 98 Å),[91] most MOFs have pores within a few nanometers in size,[66] composed of simpler linkers such as benzene-1,4-dicarboxylate (e.g., UiO-66)[386] and benzene-1,3,5-tricarboxylate (e.g., HKUST-1).[389] The small pore size in MOFs warrants the use of small precursors for casting to enable infiltration and to incorporate as much precursor as possible in the pores. For silica, tetramethyl orthosilicate (TMOS) is a good precursor because of its small size (~8 Å). TMOS is also a liquid, which eliminates the need for solvents that would reduce the maximum loading of the pores with silica. Based on the relative densities and molar masses of TMOS and silica and assuming that the MOF

pores are completely filled with TMOS after infiltration, up to ~18% of the total MOF pore volume could be occupied with silica when using TMOS as a precursor.

TMOS converts to silica by hydrolysis and condensation in the presence of water and an acid (or base) catalyst. Casting fluids typically consist of a solution of these three components. Methanol is also often added as a cosolvent and to slow down TMOS hydrolysis during template infiltration. For the MOFs investigated here, the small pore sizes necessitate that the silica precursor stays monomeric during infiltration, since even short condensed precursor units could already be too big to infiltrate the MOF pores. Thus, the presence of a catalyst in the casting fluid may not be ideal for MOFs. This was observed previously when NU-1000, a MOF with 3-nm pores, was cast using a solution of TMOS, $HCl_{(aq)}$, and methanol, where only a very small loading of silica in the MOF pores was achieved.[365] After the linkers were removed at high temperatures, the amount of silica incorporated in NU-1000 was not enough to provide sufficient anchoring sites for the hexazirconium oxide clusters of the MOF, leading to their aggregation. To keep TMOS monomeric during infiltration, the acid catalyst was removed from the precursor solution and was introduced afterwards via vapor phase HCl treatment of the infiltrated MOF particles. This yielded the desired silica loading in the MOF pores.

Successful incorporation of silica in the MOF pores can be evaluated by techniques such as infrared spectroscopy, gas physisorption analysis, and difference envelope density (DED) analysis.[338,339] Apart from the presence of silica however, other criteria must be met for nanocasting to be considered successful, especially for the purpose of stabilizing the metal clusters in MOFs for catalytic applications. One is that

the *site isolation of the clusters* must be maintained in the nanocast material after removal of the organic linkers, in the same way they are isolated in the original MOF. This ensures that the high loadings of catalytically active sites are maintained. Techniques such as X-ray diffraction (XRD), small area electron diffraction (SAED) and pair distribution function (PDF) analysis[344] can be used to differentiate between aggregated and site-isolated metal sites in the nanocast samples.

The second criterion is *accessibility*. The metal sites need to remain accessible to reactant molecules and not be fully coated with silica in the nanocast material. This is facilitated by removal of the organic linkers in the structure where the original points of attachment to the metal clusters are presumably open after linker removal. Four equivalents of methanol are also released from the hydrolysis of each TMOS unit, and can introduce additional porosity in the silica matrix formed in the nanocast samples. Gas physisorption can be used to determine the porosity of the nanocast material. However, it is also important to test the accessibility of the actual cluster using probe molecules, like pyridine, ammonia, or hydrogen, that can be chemisorbed onto these metal sites.

The last criterion, and the most important, is *catalytic activity*. The catalytic activity of the metal sites must be maintained as they are transferred from the MOF to the nanocast silica matrix. Comparison of activity with the original MOF can be done using low temperature model reactions. Notably, this activity is also reflective of the site isolation and accessibility of the metal sites in the nanocast sample.

Among the above methods, XRD is a convenient initial check to rule out the presence of large aggregated clusters in the material. When the metal sites in MOFs

aggregate into larger oxide crystallites, the XRD pattern of the samples consists of sharp peaks. In the case that the aggregated metal oxides are amorphous, transmission electron microscopy (TEM) can be used to see the aggregates, particularly for metal oxide compositions with high atomic number (Z) contrast with silicon.[390]

5.3.2 Nanocasting Different MOFs.

The previous work on nanocasting MOFs focused on NU-1000, which consists of four-coordinated hexazirconium oxide (Zr_6) clusters as nodes. The clusters are found to be active for low temperature Lewis acid-catalyzed reactions.[99,391] We showed that the catalytic activity of these clusters is retained after nanocasting, using glucose isomerization as a model Lewis acid-catalyzed reaction.[365] We attempted using the silica nanocast of NU-1000 for high temperature alkane dehydrogenation (610 °C), for which Lewis acidic oxides like Ga_2O_3 have been shown as active catalysts.[174] However, the clusters had very low activity for this reaction (**Figure 5.2**). Such low catalytic activity can be addressed by adding another catalytic metal to the clusters or by changing the clusters themselves.

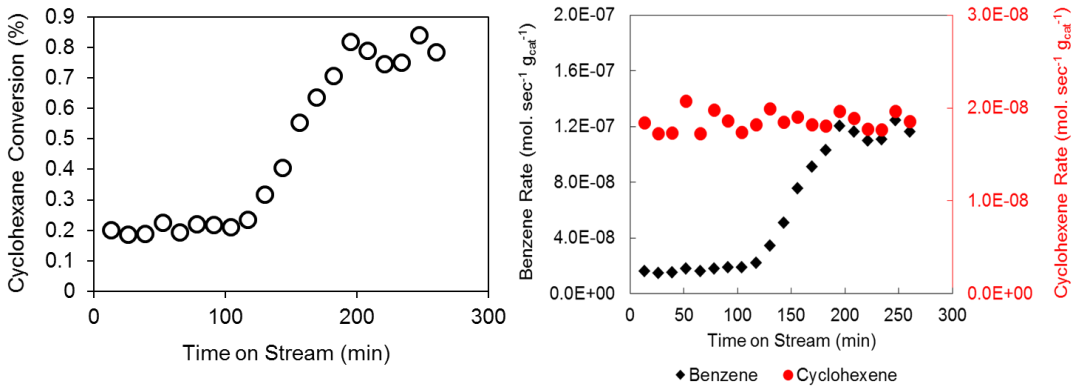

Figure 5.2. Catalytic activity of nanocast NU-1000 in cyclohexane dehydrogenation. Cyclohexane conversion is below 1%. The products are cyclohexene and benzene, with an induction period observed for benzene production.

To test the applicability of the nanocasting method to MOFs with smaller pore size and to access other catalytically active metal site compositions, four other MOFs were nanocast with silica: UiO-66, (Ce)UiO-66, (Ce)UiO-67 and DUT-9. **Table 5.1** summarizes some important compositional and structural information of each MOF.

The MOFs used for nanocasting in this work were prepared according to reported procedures.[94,386,387] The XRD patterns of the synthesized samples (**Figure 5.3**) are consistent with simulated patterns from published cif files of each MOF. For (Ce)UiO-66 and (Ce)UiO-67, the patterns are shifted to lower angles compared to their Zr counterparts, indicating larger *d*-spacing in these Ce MOFs. The SEM images and N_2 sorption isotherms **(Figure 5.4 and Figure 5.5**) are also consistent with literature data, proving the successful synthesis and activation of each MOF.

Table 5.1. Compositional and structural details of MOFs used for nanocasting

MOF	node	linker[a]	pore size (Å)	surface area[b, c] (m^2g^{-1})	pore volume[b] (cm^3g^{-1})
UiO-66	$[Zr_6(\mu_3\text{-}O)_4(\mu_3\text{-}OH)_4]^{+12}$	bdc^{2-}	11, 8	1580 (ref.[386]); 1357 (this work)	0.70 (this work)
(Ce)UiO-66	$[Ce_6(\mu_3\text{-}O)_4(\mu_3\text{-}OH)_4]^{+12}$	bdc^{2-}	11, 8[d]	1282 (ref.[387]); 1569 (this work)	0.50 (ref.[387]); 0.76 (this work)
(Ce)UiO-67	$[Ce_6(\mu_3\text{-}O)_4(\mu_3\text{-}OH)_4]^{+12}$	$bpdc^{2-}$	23, 11[d]	2064 (this work)	0.95 (this work)
DUT-9	$[Ni_5(\mu_3\text{-}O)_2]^{+6}$	btb^{3-}	25, 13	–	2.18 (ref.[94]); 1.21 (this work)

[a]bdc = benzene-1,4-dicarboxylate, bpdc = biphenyl-4,4'-dicarboxylate, btb = benzene-1,3,5-tribenzoate

[b]N_2 sorption isotherms of the MOFs used for the evaluation of BET surface area and pore volumes are shown in Figure 5.5.

[c](Ce)UiO-67 surface area not measured in ref.[387] due to decomposition at reduced pressure. DUT-9 does not have a linear range for evaluation of BET surface area.[94] BET surface areas in this work were evaluated according to the guidelines in ref.[78]. BET range: UiO-66 up to p/p_0 = 0.0746; (Ce)UiO-66 up to p/p_0 = 0.0739; (Ce)UiO-67 up to p/p_0 = 0.125.

[d]Indicated values are the pore sizes of the corresponding Zr MOFs: UiO-66 and UiO-67.[386]

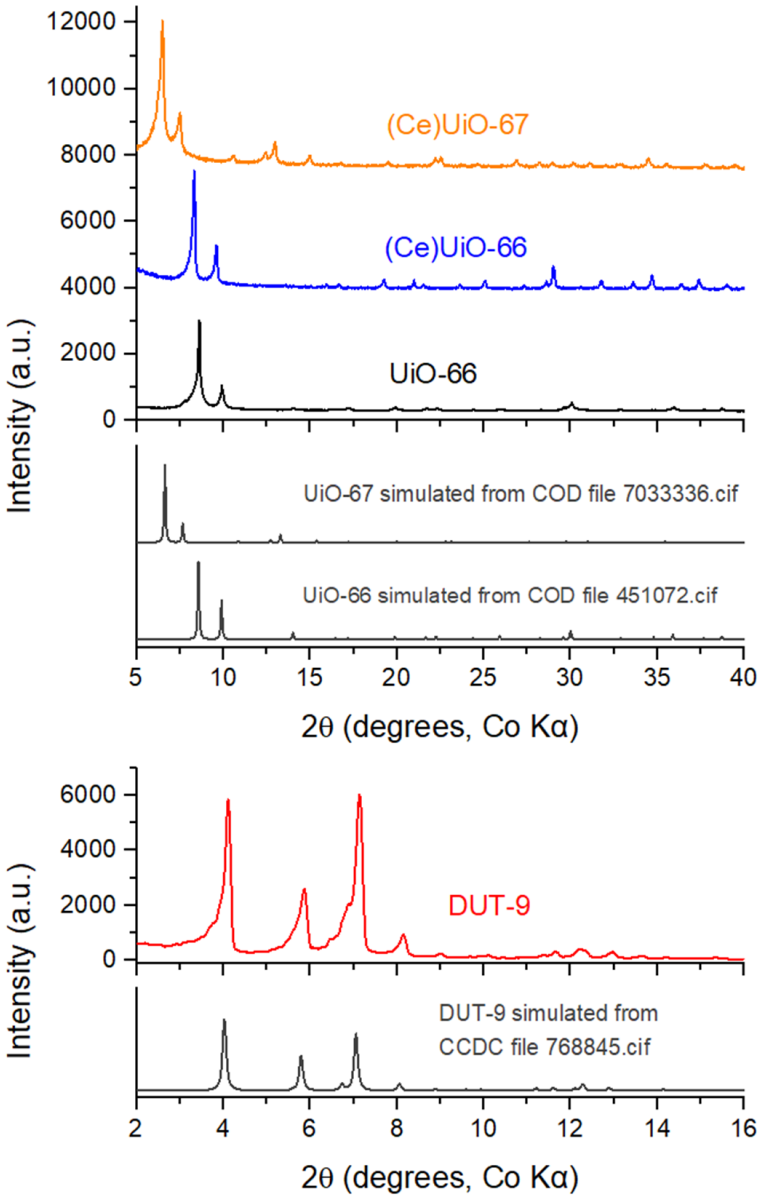

Figure 5.3. XRD patterns of the synthesized MOFs showing patterns consistent with published data of each MOF. Compared to UiO-66 (d = 1.18 nm), the highest d-spacing for (Ce)UiO-66 is 1.23 nm. Similarly, (Ce)UiO-67 the highest d-spacing is 1.58 nm, compared to UiO-67 at 1.54 nm.

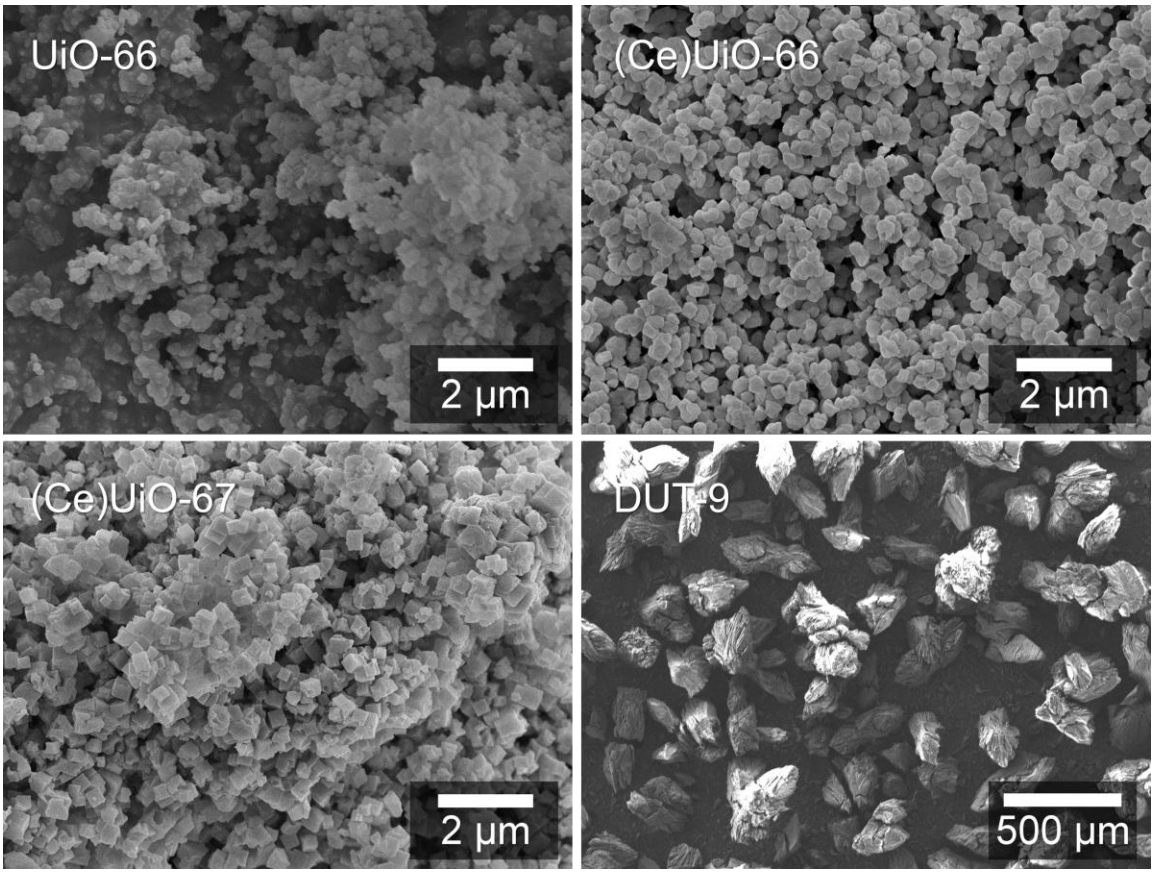

Figure 5.4. SEM images of the synthesized MOFs.

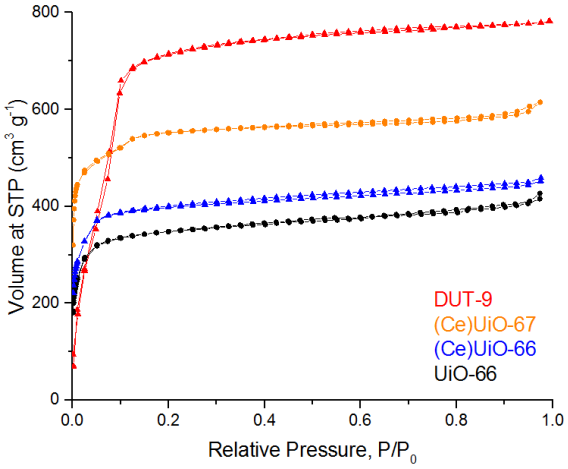

Figure 5.5. N_2 sorption isotherms of the synthesized MOFs.

Similar nanocasting conditions as we previously reported for NU-1000[365] were initially applied to all four MOFs. The casting fluid consisted of a TMOS mixture with water and methanol (97% by volume TMOS). Infiltration was followed by vapor phase HCl treatment, condensation at 60 °C, and lastly, linker removal by calcination. The XRD patterns of the nanocast samples are shown in **Figure 5.6**.

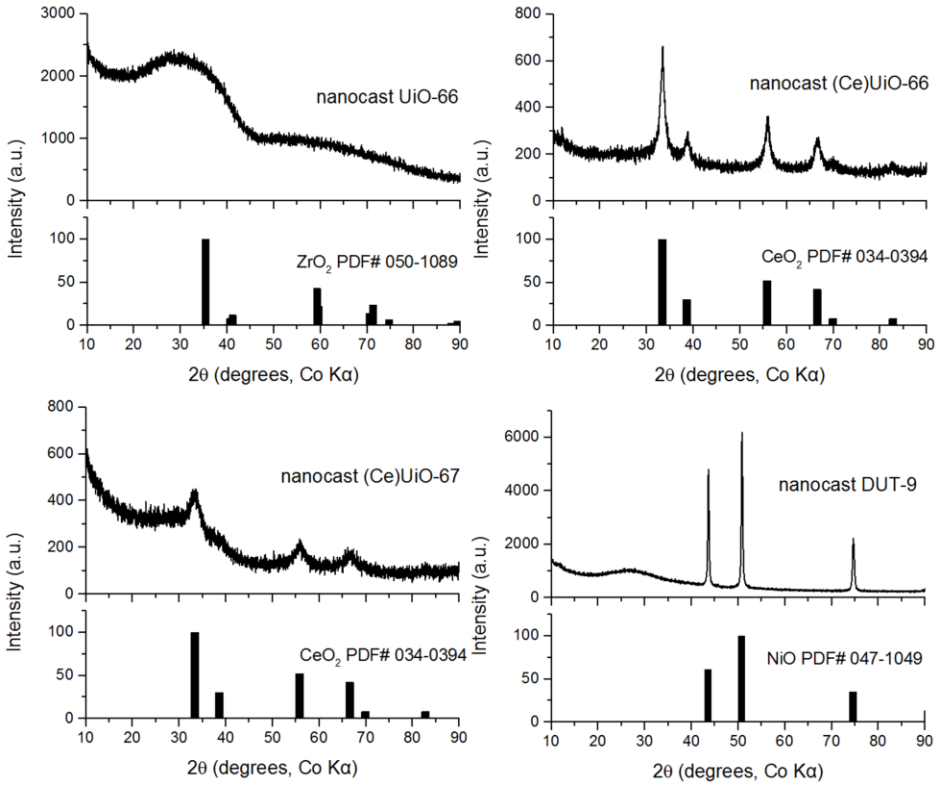

Figure 5.6. XRD patterns of nanocast MOFs prepared by nanocasting utilizing an acid catalyst. The XRD pattern was taken after the final calcination step at 500 °C in air.

Among the samples, only the nanocast UiO-66 has the broad features associated with amorphous silica in its XRD pattern, while the others exhibit sharp peaks indicative of aggregated clusters. TEM images (**Figure 5.7**) of the UiO-66 nanocast sample also do

not show large ZrO_2 aggregates, indicating that the clusters likely exist in individual, site-isolated form, similar to our previous study with NU-1000. We found that the clusters are also accessible and that the nanocast material was mesoporous by pyridine sorption and N_2 sorption analyses, respectively (**Figure 5.8**). This result of nanocasting UiO-66 shows that the reported method can be applied to MOFs with smaller pores.

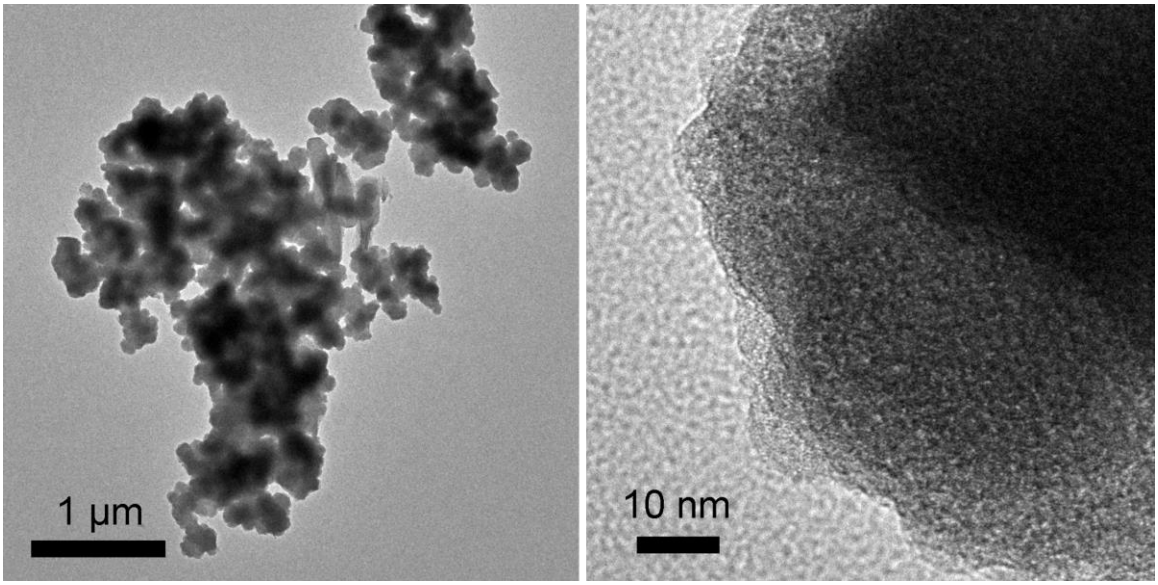

Figure 5.7. Low and high magnification TEM images of nanocast UiO-66. No large aggregates of ZrO_2 can discerned in the high magnification image.

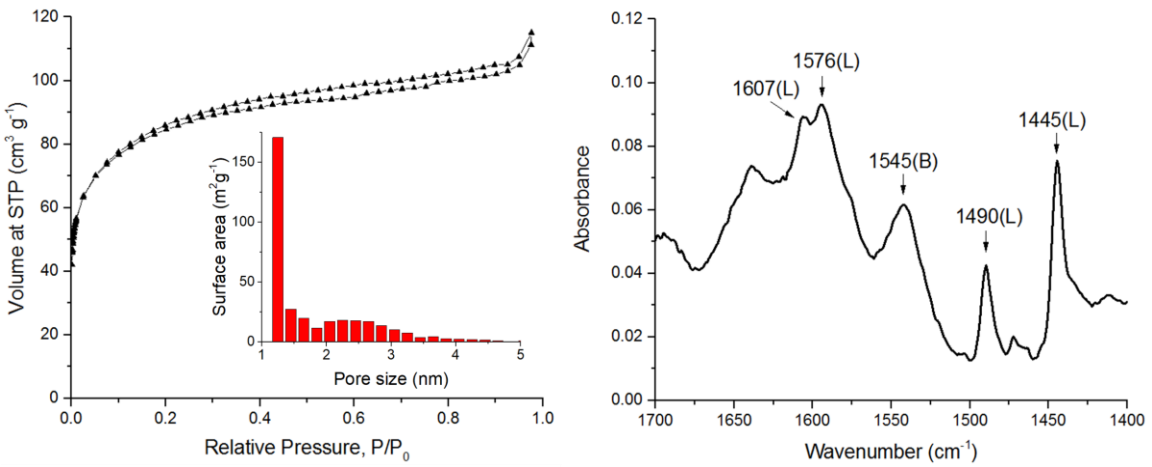

Figure 5.8. (a) N_2 sorption isotherm and surface area histogram (inset) of nanocast UiO-66 showing micro- and mesoporosity in the material, and (b) IR spectrum after pyridine adsorption on nanocast UiO-66. The peaks labeled L and B denote pyridine adsorbed on Lewis and Brønsted acid sites, respectively.

Unlike UiO-66, nanocasting DUT-9 resulted in aggregated NiO on silica (~90 nm grain size NiO, calculated from the peak broadening using the Scherrer equation). Some conditions in the nanocasting method are incompatible with DUT-9 and could have resulted in the loss of the MOF structure during nanocasting and the consequent aggregation of the pentanickel oxide nodes. For one, DUT-9 is unstable towards capillary forces associated with solvent removal. During its synthesis, DUT-9 cannot be dried from conventional solvents used in activation of MOFs. Drying DUT-9 from acetone (surface tension, γ, of 23 dynes cm^{-1}), for instance, leads to structural collapse of the MOF (**Figure 5.9**). Instead, DUT-9 must be supercritically dried (γ of supercritical CO_2 is 0.6 dynes cm^{-1}).[94] This instability toward capillary forces is also seen during infiltration where TMOS (γ = 23 dynes cm^{-1}) and other solvents cause structural collapse in the MOF (**Figure 5.9**).

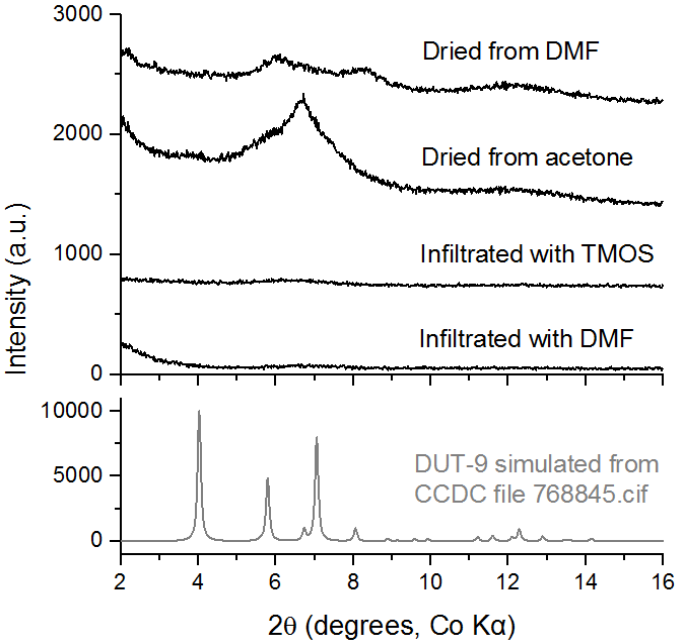

Figure 5.9. XRD patterns of DUT-9 showing effects of capillary forces on the MOF. Air-drying DUT-9 from DMF results in structural collapse indicated by the loss of the characteristic XRD pattern of the MOF. Conventional drying by exchanging the DMF with acetone followed by air-drying also results in a collapsed framework. Infiltration of an activated DUT-9 sample with TMOS or DMF yields the same result. The XRD patterns of the infiltrated samples were taken after 24 h of infiltration, and the samples were wetted with the corresponding solvent during XRD data collection.

One way to avoid this collapse during the infiltration step is through solvent exchange with the casting fluid. After DUT-9 is synthesized and washed with DMF, the DMF can be replaced with the casting fluid for exchange. However, modifying the infiltration step in this manner was not sufficient to prevent the aggregation of the clusters in the nanocast DUT-9 (**Figure 5.10**).

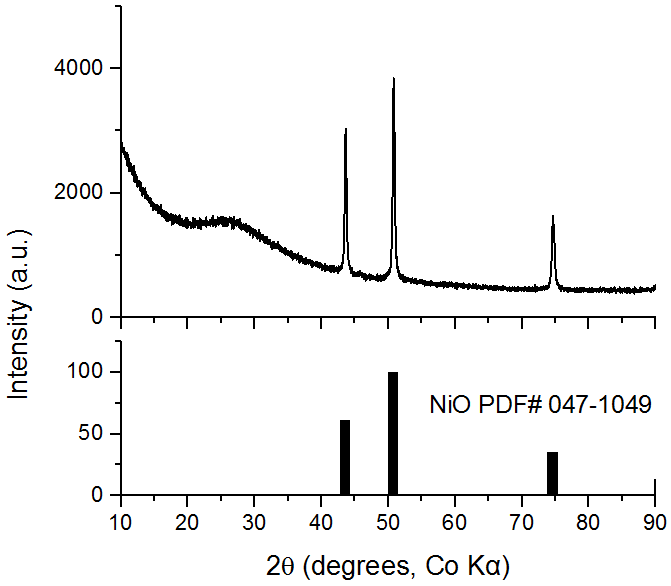

Figure 5.10. XRD pattern of nanocast DUT-9 prepared by a modified procedure where the casting fluid is introduced into the MOF pores by exchanging with the solvent (DMF) instead of infiltration of an activated sample. The rest of the procedure is the same as that outlined for silica nanocasting with an acid catalyst.

Apart from capillary forces, DUT-9 is also incompatible with the HCl catalyst, as shown by the loss of the characteristic XRD pattern of the MOF after exposure to the acid (**Figure 5.11**). Therefore, to cast DUT-9, casting should be done by solvent exchange and without using an acid catalyst. A modified casting method was therefore applied, consisting of solvent exchange with a solution of TMOS with water and methanol (70% by volume TMOS). Increasing the proportion of water in the mixture was necessary to achieve hydrolysis and condensation in a reasonable amount of time. After 24 h, the casting fluid was decanted and the solvent-exchanged particles were washed once with methanol. After gelation and linker removal, the sample shows no aggregation as indicated by the XRD pattern in **Figure 5.12**. The TEM image (**Figure 5.13**) also does not show large NiO domains, indicating that the modified casting procedure was

successful in stabilizing the pentanickel oxide clusters of the MOF. The nanocast material consists of these clusters supported on the silica matrix.

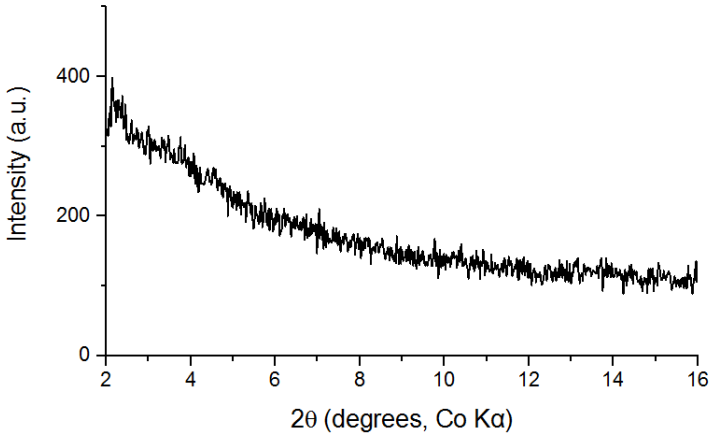

Figure 5.11. XRD pattern of DUT-9 after exposure to $HCl_{(g)}$ for 24 h.

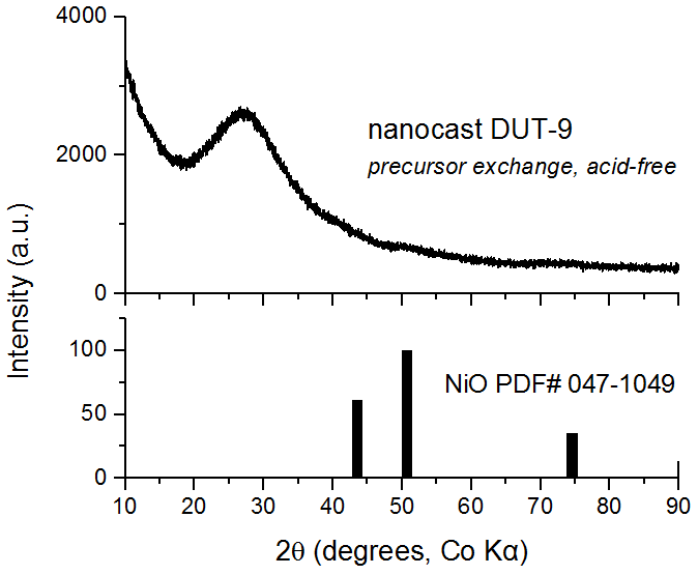

Figure 5.12. XRD pattern of nanocast DUT-9 prepared by the nanocasting without acid catalyst method. The silica precursor mixture was introduced by solvent-exchange instead of infiltration. The XRD pattern was taken after the final calcination step at 500 °C in air.

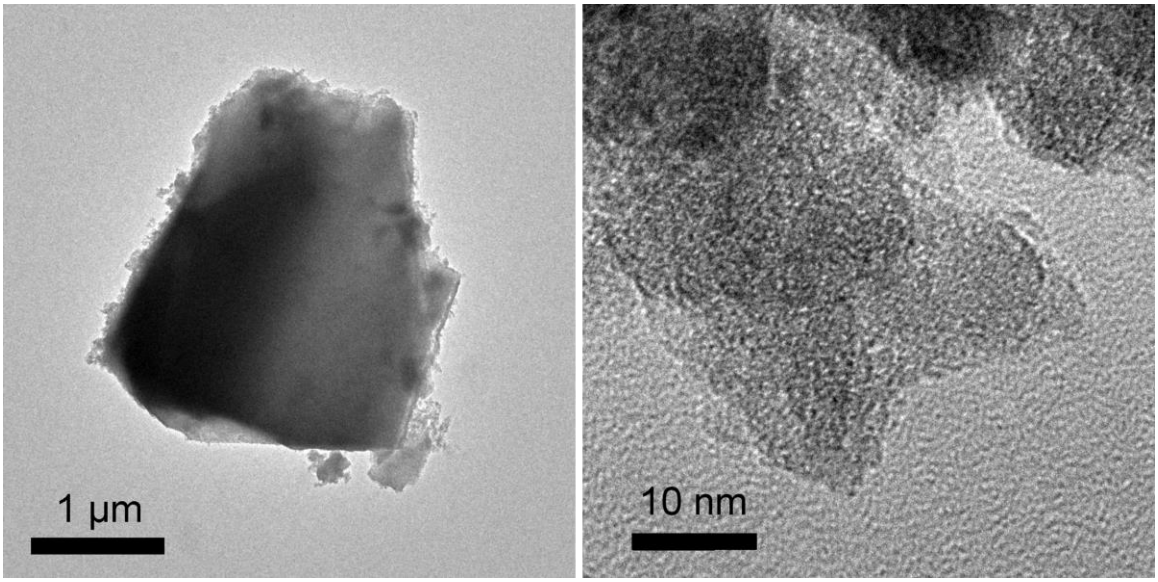

Figure 5.13. Low and high magnification TEM images of nanocast DUT-9. No large aggregated NiO can be seen in the high magnification image.

For (Ce)UiO-66 and (Ce)UiO-67, exposure to HCl also leads to loss of the MOF structure (**Figure 5.14**) due to the affinity of Ce^{4+} for Cl^-. This instability towards HCl could have resulted in the aggregated CeO_2 in the nanocast samples as seen in their XRD patterns in **Figure 5.6** Ce is also oxophilic, and so exposure of the MOFs to formic acid yielded the same structural destabilization (**Figure 5.14**). Thus, we also attempted using the acid catalyst-free casting procedure for these MOFs. With this method, however, the XRD patterns of the samples still show some aggregation, although not as much as in the case of the corresponding nanocast samples prepared with the use of an acid catalyst. TEM images (**Figure 5.16**) of the nanocast materials show aggregated CeO_2 particles ~2 nm in size.

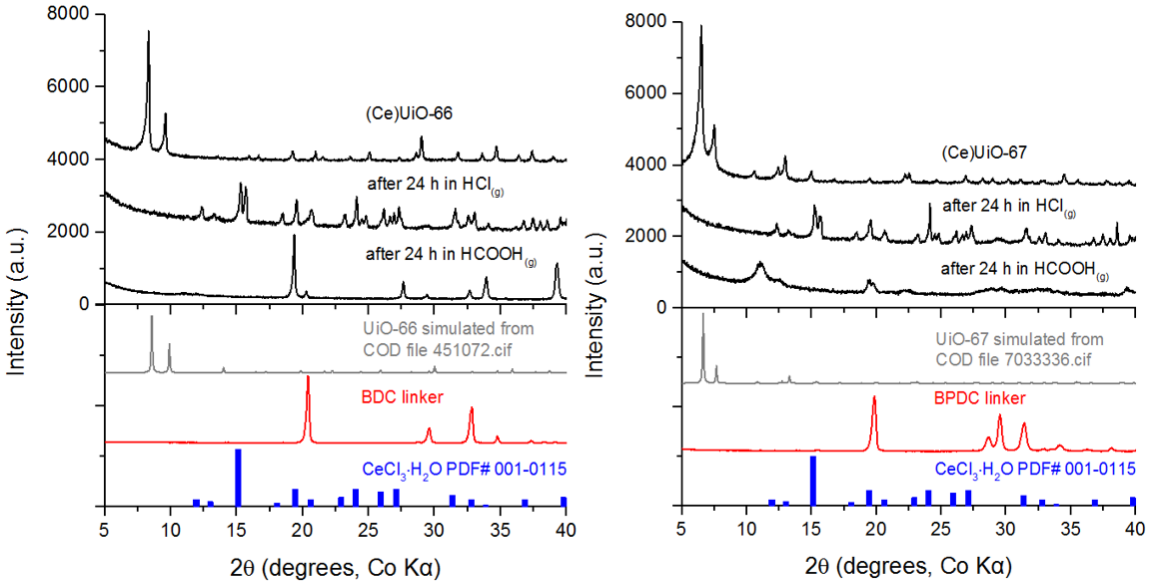

Figure 5.14. XRD patterns of (Ce)UiO-66 and (Ce)UiO-67 after exposure to $HCl_{(g)}$ and $HCOOH_{(g)}$ for 24 h. The pattern for the MOFs after exposure to $HCl_{(g)}$ corresponds to hydrated $CeCl_3$.

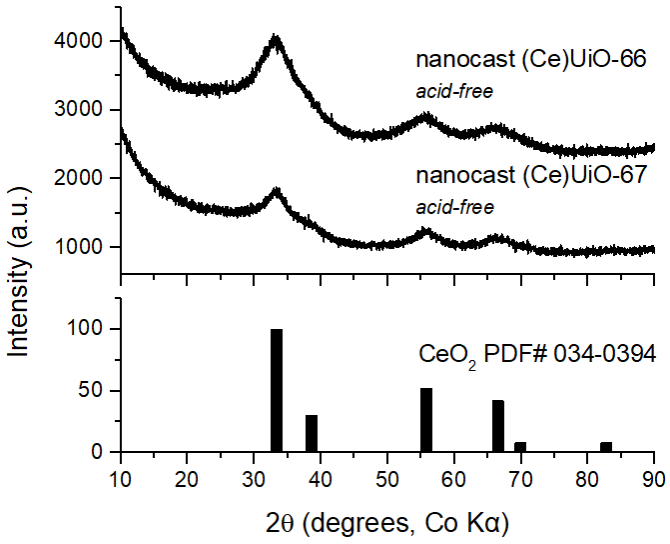

Figure 5.15. XRD pattern of nanocast (Ce)UiO-66 and (Ce)UiO-67 prepared by the nanocasting method without acid catalyst. The XRD pattern was taken after the final calcination step at 500 °C in air.

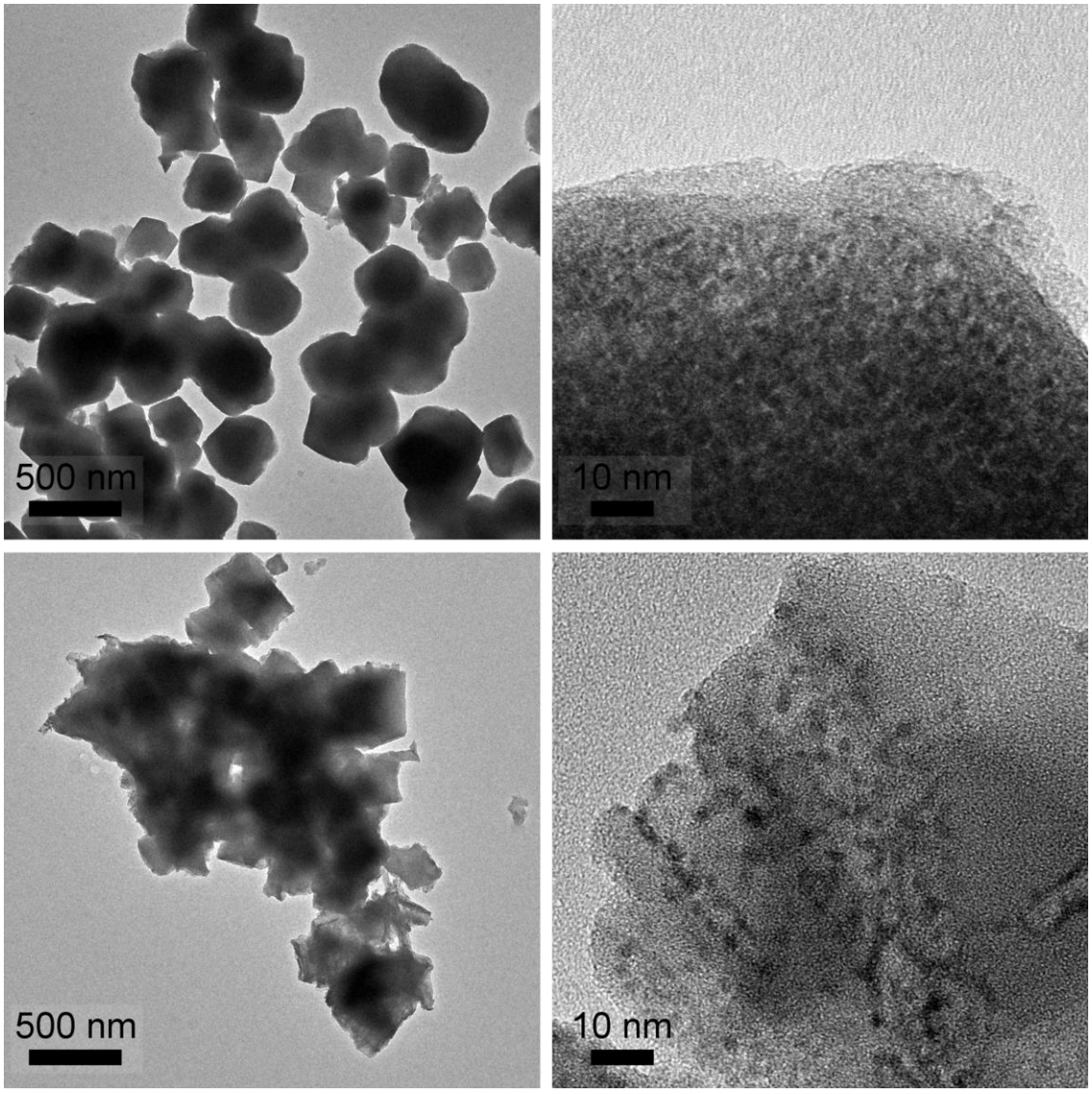

Figure 5.16. Low and high magnification TEM images of nanocast (Ce)UiO-66 (top images) and (Ce)UiO-67 (bottom images). In both materials, aggregated CeO_2 ~2 nm in size can be seen as dark spots in the high magnification images.

Table 5.2 compares the Si-to-node ratios in the different MOF nanocast samples measured experimentally by SEM-EDS to the expected ratios assuming complete infiltration of MOF particles during nanocasting. For both UiO-66 and DUT-9, the measured values significantly exceed the expected ratios. It is likely that an external silica

crust is present on the nanocast particles, which would explain the additional amount of silica in these samples. For the (Ce)UiO samples however, the measured values are similar to the expected ratios. It is possible that a significant fraction of this silica is present as an external crust as well. If this is the case, there might not be enough silica inside the MOF pores to stabilize the hexacerium oxide clusters, leading to their observed aggregation. Adjustment of nanocasting conditions, e.g., infiltration time, performing multiple nanocasting cycles, may be done to improve this silica loading and prevent the aggregation of the clusters.

Table 5.2. Expected Si-to-node ratios in the nanocast MOFs, assuming complete infiltration of the MOF particles during nanocasting. Experimental values from SEM-EDS are also shown for comparison.

MOF	mmol node per g MOF[a]	Volume (in cm^3) of TMOS in 1 g of infiltrated MOF[b]	mmol silica[c]	mol Si : mol node	mol Si:mol node from SEM-EDS
UiO-66	0.60	0.68	4.56	7.59	16.78
(Ce)UiO-66	0.51	0.53	3.58	7.00	8.13
(Ce)UiO-67	0.41	0.66	4.47	10.84	9.99
DUT-9	0.83	0.85	5.69	8.51	47.35

[a]The following formula masses (in g mol^{-1}) were used: UiO-66 = 1664.06, (Ce)UiO-66 = 1957.41, (Ce)UiO-67 = 2426.13, and DUT-9 = 1202.37
[b]Calculated by multiplying the experimental MOF pore volumes in Table 5.1 by the volume percentage of TMOS in the casting fluid.
[c]Calculated using the relative molar mass and densities of TMOS and amorphous silica.

Thus, in this work, the applicability of the nanocasting method was extended to other MOF structures and compositions. For the stable Zr MOFs (e.g., NU-1000 and

UiO-66), which have strong interactions between the metal node and carboxylate linkers, acids can be used to aid the hydrolysis and condensation of TMOS to silica during nanocasting. A modified method involving a casting solution composition that does not require this acid catalyst was also developed and is useful for MOFs that have either oxo- or halophilic metal sites. Finally, solvent exchange can be used to introduce the casting solution into MOF pores for MOFs that are unstable towards infiltration.

5.3.3 Nanocasting Metal-Modified MOFs

MOFs can be post-synthetically modified to install other metals on their nodes. For NU-1000, the sub-nm hexazirconium oxide (Zr_6) clusters have been used to support other catalytic metal sites including many first-row and noble transition metals.[105,108,136,156,284,325,364,378,388,392] This compositional tuning could translate to different catalytic properties in the resulting MOF samples. We have reported the nanocasting of NU-1000 that has bimetallic AlCo or Co_2 complexes installed on the node.[375] The catalytic activity of the nanocast materials was demonstrated to be similar to the corresponding bimetallated MOF. For metalated MOFs, retention of the metal loading after nanocasting is another important criterion for successful casting and was satisfied in the nanocast samples of these bimetallated NU-1000 systems.

Here, nanocasting was also applied to other metalated NU-1000 samples, namely, In- and Ni-loaded NU-1000. In-loaded NU-1000 was prepared by atomic layer deposition in MOFs (AIM), whereas the Ni-loaded NU-1000 was prepared by solution-deposition in MOFs (SIM). The samples will be referred to as In(AIM)-NU-1000 and

Ni(SIM)-NU-1000 for the remainder of this text. Computationally determined structures of the NU-1000 node with the deposited metals have been reported.[388] The XRD patterns of the samples show retention of the NU-1000 structure after metal deposition (**Figure 5.17**). Lower surface areas and pore volumes are consistent with metal loading (**Figure 5.17**). In(AIM)-NU-1000 had an In:Zr_6 ratio of 4.62, and for Ni(SIM)-NU-1000, the Ni:Zr_6 ratio was 3.86 on the basis of SEM-EDS measurements.

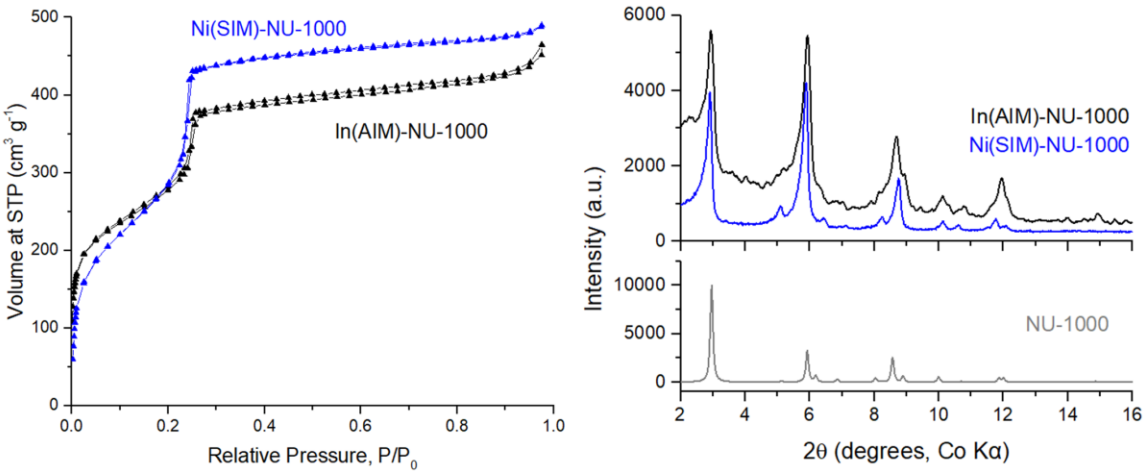

Figure 5.17. N_2 sorption isotherms (left) and XRD patterns (right) of Ni- and In-loaded NU-1000 (Ni(SIM)-NU-1000 and In(AIM)-NU-1000) prepared by solution deposition and atomic layer deposition, respectively. The BET surface area and pore volume of Ni(SIM)-NU-1000 are 1109 m^2g^{-1} and 0.75 cm^3g^{-1}, respectively. The corresponding values for In(AIM)-NU-1000 are 1028 m^2g^{-1} and 0.70 cm^3g^{-1}. BET surface areas were evaluated based on the guidelines in ref.[78] The BET range for Ni(SIM)-NU-1000 is at p/p_0 = 0.05 to 0.22. The range for In(AIM)-NU-1000 is at p/p_0 = 0.01 to 0.25.

After applying the original nanocasting method to these MOFs, the EDS data of the calcined nanocast material indicated that the metals were retained in the samples (**Figure 5.18**). However, the metals were present as aggregated NiO and In_2O_3 on silica (**Figure 5.19**). Notably, no aggregated ZrO_2 was detected in these samples by XRD. The

added metal seemed to detach from the node and aggregated to larger oxide crystallites during the nanocasting process. A leaching test was performed to determine whether the metals detached from the nodes during infiltration. However, neither the TMOS used for infiltration nor the methanol wash contained any detectable In or Ni by XRD or SEM-EDS (**Figure 5.18** and **Figure 5.19**).

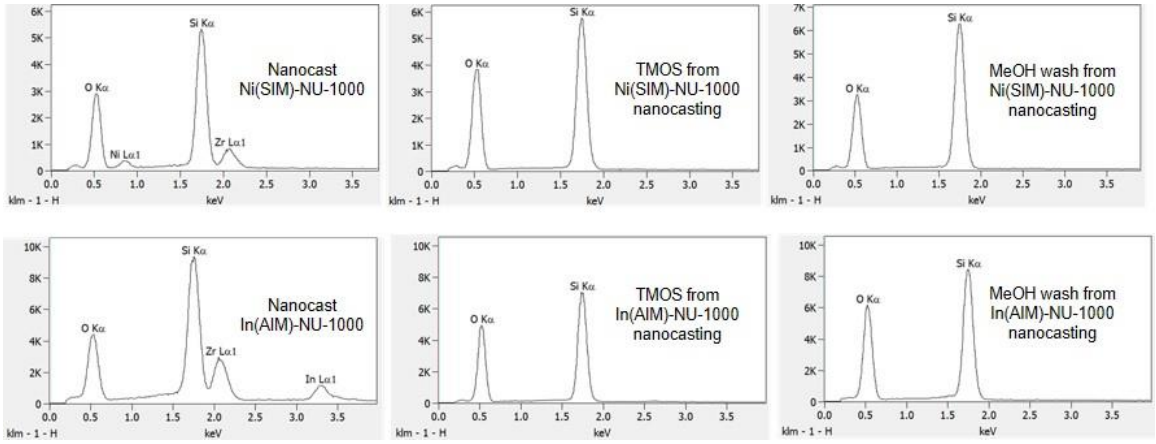

Figure 5.18. SEM-EDS data from the nanocasting and leaching test for Ni(SIM)-NU-1000 (top data) and In(AIM)-NU-1000 (bottom data) nanocasting. The data on the left are for the nanocast samples showing the presence of Ni (~4 Ni per Zr_6 node) and In (~5 In per Zr_6 node). No Ni or In was detected in the TMOS casting fluid or the methanol wash for both nanocasting samples.

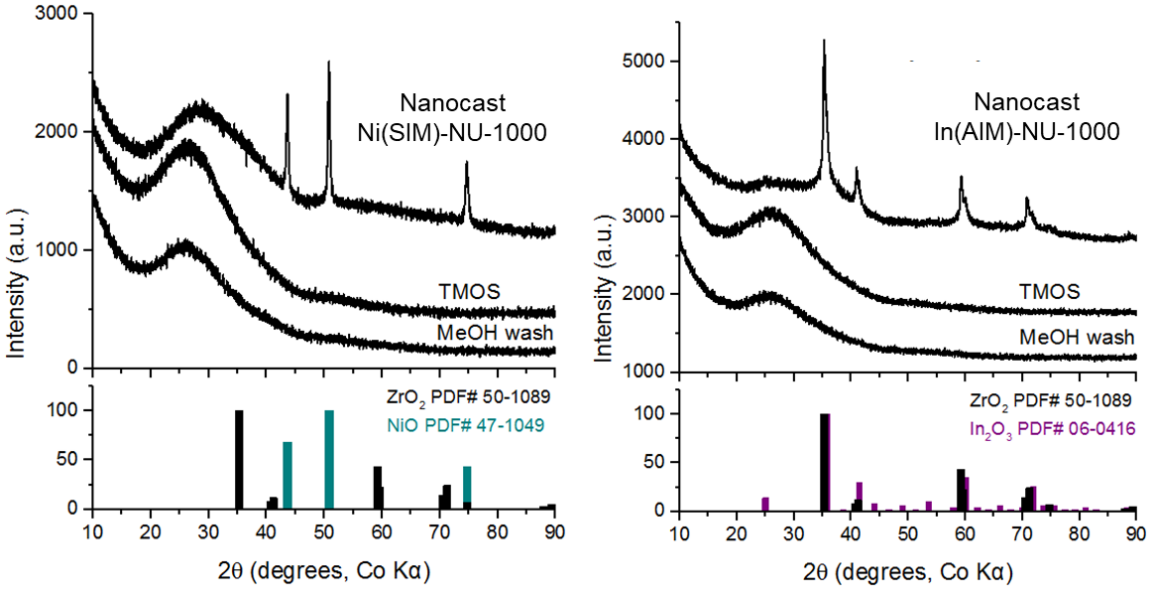

Figure 5.19. XRD patterns of nanocast In(AIM) and Ni(SIM) prepared by silica nanocasting with the use of an acid catalyst. The XRD pattern was taken after the final calcination step at 500 °C in air. Additional XRD patterns (labeled "TMOS" and "MeOH wash") were obtained from the leaching test during nanocasting in Ni(SIM)-NU-1000 and In(AIM)-NU-1000. No oxides of Ni or In was detected in the TMOS casting fluid ("TMOS") or the methanol wash ("MeOH wash") for both nanocasting samples.

The affinity of the metals to Cl^- from the HCl treatment could also have caused them to detach from the node and aggregate. Thus, nanocasting using the modified, acid catalyst-free method was attempted for Ni(SIM)-NU-1000. The XRD pattern of the nanocast sample (**Figure 5.20**) shows that the acid-free method was successful in maintaining the site isolation of the Ni-loaded Zr_6 nodes. The XRD pattern did not show any evidence for aggregated NiO. Large aggregated oxides are not observable from the TEM images (**Figure 5.21**) as well. SEM-EDS analysis of the nanocast Ni(SIM)-NU-1000 gave a Ni-to-Zr_6 ratio of 3.41, indicating only small loss of Ni during nanocasting.

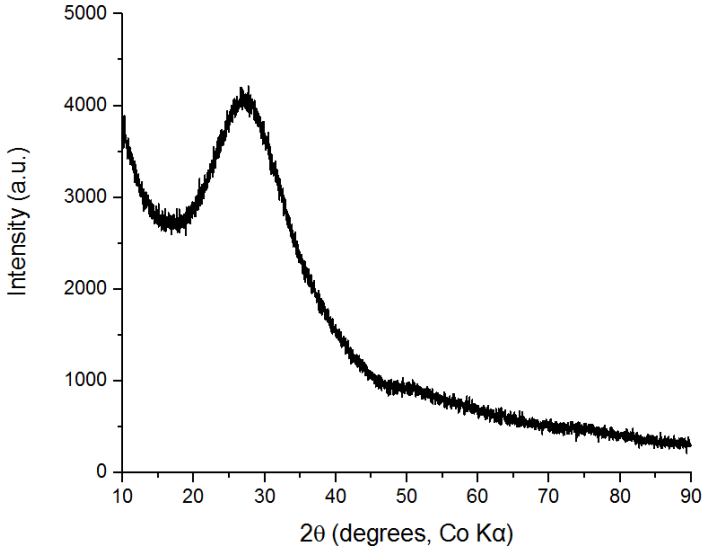

Figure 5.20. XRD pattern of nanocast Ni(SIM)-NU-1000 prepared using the modified nanocasting method without acid catalyst. The XRD pattern was taken after the final calcination step at 500 °C in air.

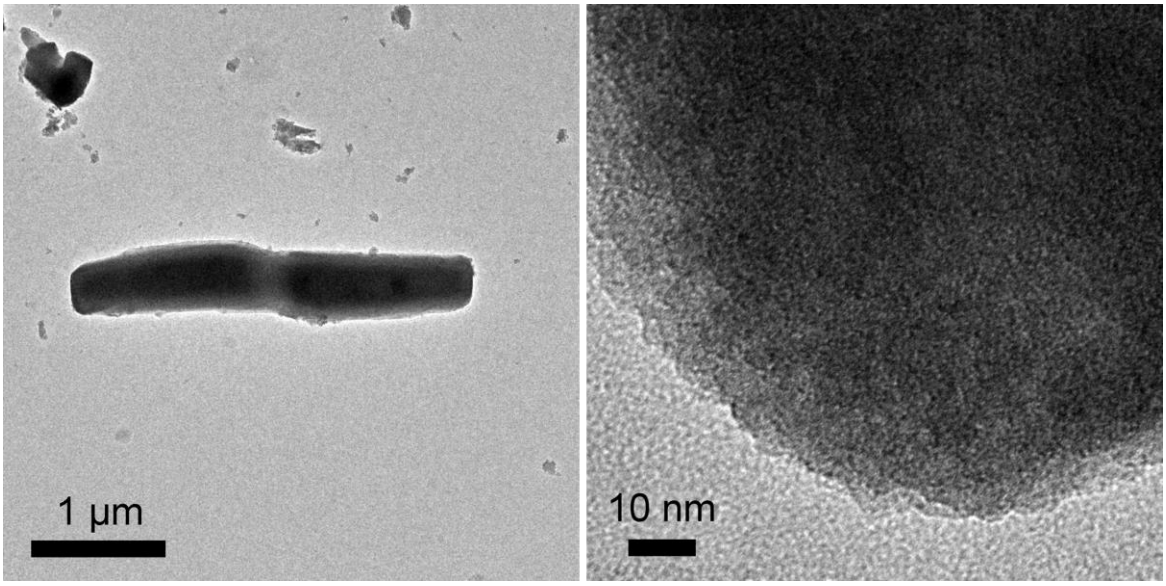

Figure 5.21. Low and high magnification TEM images of nanocast Ni(SIM)-NU-1000. No large aggregated metal oxides (NiO and/or ZrO_2) can be seen based on lack of contrast in the high magnification image.

5.4 Conclusion

This work demonstrated the applicability of silica nanocasting for stabilizing the metal clusters in different MOF systems at high temperatures. Nanocasting can be adapted to the restrictions imposed by the framework structure and chemistry of different MOFs. Due to their small pore size, the use of small precursors, as well as conditions that kept the precursors monomeric during infiltration were found necessary to achieve incorporation of silica in the MOF pores. For some MOFs, casting without the use of an acid or base catalyst was essential to maintain the pore structure of the MOF until silica was formed within the framework. In (Ce)UiO-66 and (Ce)UiO-67, both the protonation of the organic linker and the halophilicity of Ce can contribute to pore collapse when HCl is used as a catalyst for TMOS hydrolysis and condensation during casting. Instability towards HCl was also encountered when casting post-metalated MOFs, where detachment and aggregation of the installed metal from the MOF nodes was observed. This can also be prevented by doing acid-free casting in these samples. Structural instability in MOFs like DUT-9 that collapse under capillary forces can be overcome by carrying out a solvent exchange instead of infiltration.

Incorporation of silica in the MOF pore structure allowed retention of the site-isolation of the metal clusters in different MOF systems after linker removal at 500 °C. This work shows the adaptation and utility of nanocasting in extending the application of MOF-based catalytic clusters beyond the thermal stability limit of MOFs.

Chapter 6

Summary and Future Perspectives

6.1 Overall Summary

This thesis presents critical optimization methods to enhance the stability of catalytic systems for high temperature reactions. Two types of catalytic systems were the focus of this work, namely, porous metal oxides and metal-organic frameworks. In both cases, sol-gel and casting techniques are central in the formation of thermally stable structures, further manifesting the competence and flexibility of these methods in producing a wide variety of functional materials. First, I showed that macroporous metal oxides can be synthesized with structural stability up to 1400 °C, making them suitable as active material in thermochemical cycling applications. This was done via wood templating, using ceria as a representative active material. The work showed wood-templating as an approach to provide the crucial balance between accessible porosity for improving reaction kinetics and large feature sizes needed for stability under the high temperature cycling conditions. For MOF-supported catalytic metal and oxometal clusters, casting provided a means to transfer these well-defined active sites from the MOF to an all-inorganic support – silica. The resulting silica-supported clusters are stable up to at least 500 °C for the MOF compositions covered in this work. This allows the clusters to be utilized in a wider range of catalytic reactions, especially those requiring high temperatures. The remainder of this chapter outlines key findings and future perspectives for catalytic materials in the two applications described in this thesis – solar thermochemical fuel production and natural gas conversion.

6.2 Metal Oxides for Solar Thermochemical Fuel Production

6.2.1 Summary

In Chapter 2, I discussed the synthesis of porous CeO_2 via wood-templating, and its structural stability and activity as active material in the thermochemical production of CO from CO_2. Prior to this work, it was clear from the studies by Rudisill,[293] Chueh,[203,204] and Furler[206] that with respect to material structure, large feature sizes (e.g., large pores, thick walls) in the materials for this application are necessary, since sintering under the high temperature cycling conditions is significant and is the main detriment to catalyst activity even with macroporous structures (i.e., 3DOM,[293] felt,[206] and porous monolith[203,204]). In these studies, obvious morphological changes are seen when comparing the materials before and after cycling.

Here, I showed that a wood-templated structure has wall components with dimensions large enough to accommodate grain growth and allow the structure to be maintained up to 1400 °C. Wood-templated CeO_2 (WT CeO_2) was synthesized via the Pechini method and has a pore structure consisting of interconnected channels with pores tens of micrometers in diameter and micrometer-thick walls. The WT CeO_2 maintained its interconnected pore structure with surface areas of ~0.1 $m^2\ g^{-1}$ at temperatures up to 1400 °C, despite significant grain growth. The material showed CO production rates 6 times higher than nonporous CeO_2 compared at the same nonstoichiometry δ (for $CeO_{2-\delta}$) at 1400 °C.

From this work, it is clear that even larger feature sizes than those attained in the wood-templated structure would be necessary if cycling needs to be done above this

temperature. However, an appropriate balance between feature sizes and surface area must still be maintained. The advantage of templating techniques combined with Pechini method is the tunability in the composition and structure of the product, so that other active metal oxide compositions can be synthesized, and the balance between accessible porosity and stability can be adjusted based on the targeted cycling conditions for a specific active metal oxide. The diversity in wood structures, and the easy accessibility and structure replication of wood templates makes wood-templating a viable approach in preparing active materials for thermochemical cycling applications.

6.2.2 Outlook

Differences in the thermodynamic tendency of different metal oxides to form oxygen defects in their structure translate to variable conditions (e.g., temperature, oxygen partial pressure) at which each oxide composition should be cycled. Thus, thermal stability requirements are also expected to vary with active material composition. The ability to accommodate sintering effects under cycling conditions can be considered a basic requirement for oxide structures for this application. However, in addition to surface area and stability, considerations regarding heat transfer and gas flow through a structure are also necessary in the design of these materials. This is an avenue that still needs to be explored in the structure-based optimization of process efficiency for thermochemical cycles. This of course can be done experimentally, by fine tuning structures using synthetic methods that allow such versatility and control of structural features in product materials, coupled with cycling experiments. However, such work can

be tedious with a plethora of possible morphologies and variables such as wall thickness and tortuosity within each morphology to test.

Computational models that can predict optimal morphologies for kinetics, gas flow, and heat transfer based on intrinsic material properties (e.g., thermal conductivity, oxygen diffusion coefficient) as well as reactor properties (e.g., dimensions) could be key in the design of materials for thermochemical cycling applications. As mentioned, it can be expected that different morphologies will be suited for different oxides. In this case, a method that can build the morphology from a design would be ideal.

Three-dimensional (3-D) printing technologies (**Figure 6.1**) have seen enormous development in the past decade and have already been used to make oxide materials.[393] Nanometer-scale resolution have been achieved in certain printers[394] – and can therefore be applied to materials for thermochemical cycling that only require micron-scale resolution. The technology is largely developed for polymers that can then be used as templates to make other materials.[395] Developing this method for the direct fabrication of materials with tailorable compositions via sol-gel chemistry instead of polymer templates has great potential in revolutionizing the many applications of porous materials.

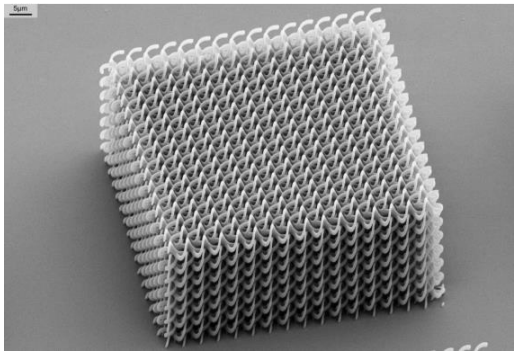

Figure 6.1. A 3D-printed epoxy photonic crystal. The scale bar on the top left is 5 μm. Reproduced with permission from Reference 396.

In terms of material composition, **Section 1.2.5** of this thesis already delved into the material requirements on the metal oxide used for thermochemical cycling that will optimize solar-to-fuel conversion efficiency, such as reduction and oxidation temperature limits, and practical pO_2 levels during reduction. The ideal metal oxide would have significant oxygen nonstoichiometry when cycling under these conditions. The vast literature on the oxygen defect formation in metal oxides is useful in identifying compositions that will be compatible with these process limits. Research on materials for oxygen ion conduction, e.g., in solid oxide fuel cells and in oxygen separation membranes, have identified metal oxides that can have large oxygen vacancy concentrations and high oxygen diffusion rates, the same properties that are desired for materials to be used in thermochemical H_2O and CO_2 splitting. These oxides commonly fall into three structure types, namely, the fluorites, the perovskites, and the K_2NiF_4 structures.[397] More recently, metal oxides with apatite structures have been reported to

have high oxygen excess nonstoichiometry and high conductivities from interstitial oxygen.[398,399]

The high-temperature thermodynamic data, i.e., pO_2–T–δ diagrams that are relevant to thermochemical CO_2 splitting, are available for many metal oxides. Primarily, the stability of oxides towards large concentrations of oxygen vacancies can be directly seen from their pO_2–T–δ diagrams, which thus presents a simple method of selecting materials with potentially high CO productivity. Screening of materials based on these literature data can be taken as a preliminary step in selecting active materials for H_2O and CO_2 splitting. A literature survey conducted so far has identified the following oxides with their respective attainable nonstoichiometries indicated in parentheses: the perovskites $La_{0.6}Sr_{0.4}Co_{1-y}Fe_yO_3$ (δ = 0.20, **Figure 6.2**),[227] $La_{0.7}Sr_{0.3}Cr_{0.9}Ti_{0.1}O_3$ (δ = 0.10) and $La_{0.75}Sr_{0.25}Cr_{0.5}Fe_{0.5}O_3$ (δ = 0.07),[223] and the K_2NiF_4-type oxide $La_{1.6}Sr_{0.4}NiO_4$ (δ = 0.08).[230] Values of δ greater than 0.05 are desired to surpass the fuel productivity that has been achieved for CeO_2 and CeO_2-based oxides.

In the absence of these pO_2–T–δ diagrams, especially for the recently studied nonstoichiometric oxides like the apatites, thermogravimetric analysis can be done to determine the cycling temperatures as described in literature. Also, the determination of active material compositions through computational methods has great potential for the systematic screening of materials for this application.

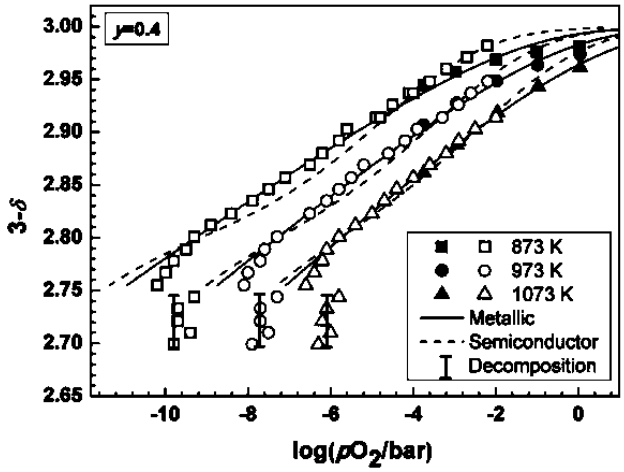

Figure 6.2. Thermodynamic diagram of oxygen defect formation in $La_{0.6}Sr_{0.4}Co_{0.6}Fe_{0.4}O_3$ showing high defect formation at T = 800 °C and $pO_2 = 10^{-6}$ bar. Determination of higher temperature isotherms can be done by extracting enthalpies and entropies of defect formation as described in Section 1.2.4. This would allow determination of a suitable reduction temperature at a more practical pO_2. Reprinted with permission from Reference 227. Copyright © 2013 The Electrochemical Society.

6.3 Stabilization of MOF-Based Catalysts through Nanocasting

6.3.1 Summary

In Chapters 3, 4 and 5, I presented the development of a silica nanocasting method for metal-organic frameworks. Prior to this work, MOF-based catalytic metal and oxo-metal sites could not be used for high temperature catalysis, as the decomposition of the organic linkers under these conditions causes the agglomeration of the metal sites, leading to loss of their catalytic activity. Some reported studies on the preparation of more thermally stable catalysts derived from MOFs involve conversion of these well-defined active sites into larger nanoparticles as new catalytic sites, which can be expected to have different activity and selectivity from the former.[161,162,288] A great advantage of MOFs as catalytic materials however, is the ability to engineer these well-defined active

sites in their structure. This would open new opportunities for high temperature catalysis if these active sites can maintain their site isolation under such conditions. Through the work I described in this thesis, MOF-based catalytic clusters can be transferred to a thermally stable, all-inorganic support while maintaining their site isolation, thereby providing a means to use the rich chemistry of MOF metal sites for high temperature catalysis.

Nanocasting has been employed for decades and has been used in the synthesis of a variety of materials from different templates.[44] The application of the technique in MOFs required optimization of process conditions to make it compatible with the MOF structure and stability. The methods described in this thesis take these factors into account, allowing the casting of MOFs with different pore sizes and including those with low mechanical stability and low resistance to acid attack. The final nanocast materials feature the site-isolated MOF-derived active sites in a porous, thermally stable silica matrix, suitable for catalysis at high temperatures.

6.3.2 Outlook

So far, catalytic tests conducted on the nanocast materials have been limited to low temperature reactions such as glucose isomerization and benzyl alcohol oxidation, which allow comparison of the activity of the nanocast material to the original MOF. Such tests are useful in assessing whether the catalytic activity of the metal sites is maintained when they are transferred from the MOF to the silica support. However, as these nanocast materials are targeted for high temperature catalysis, testing their activity,

particularly in those high temperature reactions involving natural gas conversion would be the next step in the study of these nanocast systems.

Critical to this application is the selection of MOFs to nanocast. The variety of metal node compositions reported in literature compounded by post-synthetic modification techniques provides many opportunities for the discovery of suitable active site compositions for particular reactions. Certain metal oxides, for example, have known activity in a reaction, e.g., Cr_2O_3 in alkane dehydrogenation,[174] making Cr-containing MOFs reasonable targets for nanocasting for the said reaction. One can also take inspiration from active sites in biological systems, as discussed in Section 1.3.4, and incorporate certain structural features in the MOF, e.g., adjacent metal sites, to achieve unique reactivities. Computational predictions can also be employed to complement these experimental observations relating active site composition and structure to reactivity. This is possible because of the crystallinity of MOFs, so that structural models can be used to predict reactivity, e.g., permutations of metals in a bimetallic active site.

Development of nanocasting processes for different support compositions aside from silica provide additional opportunities to tune catalytic activities and selectivities, especially with supports that have acid-base properties (e.g., Al_2O_3, MgO), redox properties (e.g., TiO_2) or conductivity (e.g., carbon, for electrocatalysis). Structured materials with these compositions have been made using sol-gel chemistry and templating.[44] Adaptation of the existing methods for the preparation of these materials can be investigated, as shown in this work for silica nanocasting. In this case, characterization of support effects on the catalytic reaction as well as on the active site

properties (e.g., electronic properties, sintering behavior) would also aid in the design of suitable nanocast systems for specific reactions.

Structural characterization is another area that needs further development in the study of these nanocast systems. Structural transitions can be expected to occur as the metal sites are transferred from the MOF to a silica support and heated at temperatures ≥ 500 °C. These transitions are seen even in the bare MOF,[102] such as when NU-1000 is heated to 350 °C, causing dehydration and distortions of the hexazirconium oxide node from cubic to a monoclinic-like structure (**Figure 6.3**). Pair distribution function (PDF) analysis, which provides the distribution of atom-atom distances in a sample, has been used to characterize nanocast NU-1000 and showed that the nodes are in their distorted form, and exist mostly as the individual (non-aggregated) clusters.[102,365] While PDF analysis presents a powerful method to characterize the active sites in nanocast materials, exploring the application of other techniques that have been traditionally used in the characterization of catalyst structures, such as X-ray absorption spectroscopy (XANES and EXAFS), solid-state NMR, vibrational spectroscopy (infrared and Raman), and UV-vis spectroscopy could provide important insights into the structure-activity relationships of the active sites in the nanocast systems.

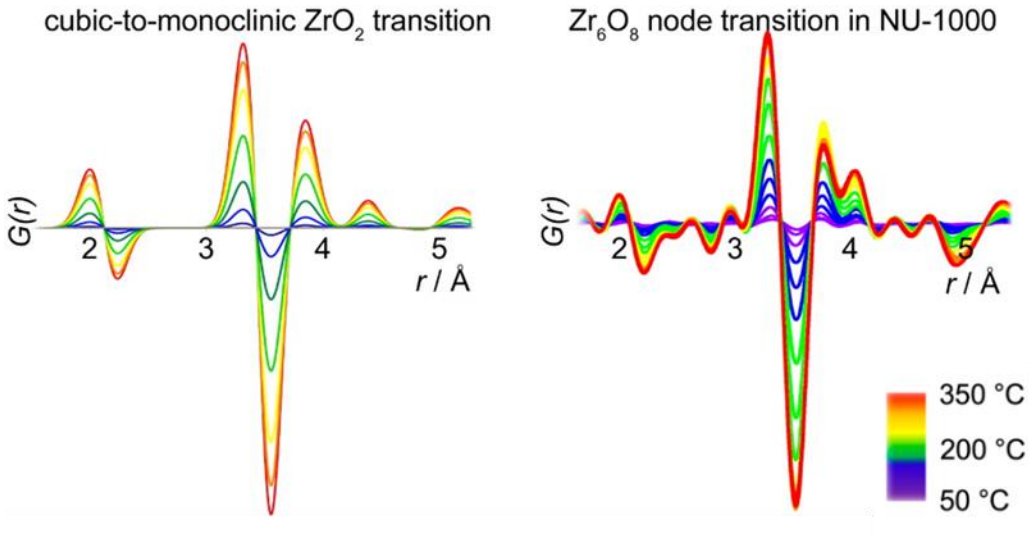

Figure 6.3. Differential pair distribution function analysis of the NU-1000 node (right) heated from 50 to 350 °C that correlate well with a cubic to monoclinic transition for ZrO_2 (left). Reprinted with permission from Reference 102. Copyright © 2016 American Chemical Society.

Bibliography

(1) Pal, N.; Bhaumik, A.: Mesoporous materials: versatile supports in heterogeneous catalysis for liquid phase catalytic transformations. *RSC Adv.* **2015**, *5*, 24363-24391.

(2) Wang, Y.; Arandiyan, H.; Scott, J.; Bagheri, A.; Dai, H.; Amal, R.: Recent advances in ordered meso/macroporous metal oxides for heterogeneous catalysis: a review. *J. Mater. Chem. A* **2017**, *5*, 8825-8846.

(3) Perego, C.; Millini, R.: Porous materials in catalysis: challenges for mesoporous materials. *Chem. Soc. Rev.* **2013**, *42*, 3956-3976.

(4) Corma, A.: From microporous to mesoporous molecular sieve materials and their use in catalysis. *Chem. Rev.* **1997**, *97*, 2373-2420.

(5) Everett, D. H.: Manual of Symbols and Terminology for Physicochemical Quantities and Units, Appendix II: Definitions, Terminology and Symbols in Colloid and Surface Chemistry. In *Pure and Applied Chemistry*, 1972; Vol. 31; pp 577.

(6) Yang, X.-Y.; Chen, L.-H.; Li, Y.; Rooke, J. C.; Sanchez, C.; Su, B.-L.: Hierarchically porous materials: synthesis strategies and structure design. *Chem. Soc. Rev.* **2017**, *46*, 481-558.

(7) Parlett, C. M.; Wilson, K.; Lee, A. F.: Hierarchical porous materials: catalytic applications. *Chem. Soc. Rev.* **2013**, *42*, 3876-93.

(8) Weitkamp, J.: Zeolites and catalysis. *Solid State Ion.* **2000**, *131*, 175-188.

(9) Abdo, S. F.; Wilson, S. T.: Zeolites in industrial catalysis. In *Zeolites in Catalysis: Properties and Applications*; The Royal Society of Chemistry, 2017; pp 310-350.

(10) Primo, A.; Garcia, H.: Zeolites as catalysts in oil refining. *Chem. Soc. Rev.* **2014**, *43*, 7548-7561.

(11) Vogt, E. T. C.; Whiting, G. T.; Dutta Chowdhury, A.; Weckhuysen, B. M.: Zeolites and zeotypes for oil and gas conversion. *Adv. Catal.* **2015**, *58*, 143-314.

(12) Corma, A.: Inorganic solid acids and their use in acid-catalyzed hydrocarbon reactions. *Chem. Rev.* **1995**, *95*, 559-614.

(13) Smit, B.; Maesen, T. L. M.: Towards a molecular understanding of shape selectivity. *Nature* **2008**, *451*, 671-678.

(14) Marcilly, C. R.: Where and how shape selectivity of molecular sieves operates in refining and petrochemistry catalytic processes. *Top. Catal.* **2000**, *13*, 357-366.

(15) Lopez-Orozco, S.; Inayat, A.; Schwab, A.; Selvam, T.; Schwieger, W.: Zeolitic materials with hierarchical porous structures. *Adv. Mater.* **2011**, *23*, 2602-2615.

(16) Egeblad, K.; Christensen, C. H.; Kustova, M.; Christensen, C. H.: Templating mesoporous zeolites. *Chem. Mater.* **2008**, *20*, 946-960.

(17) Perez-Ramirez, J.; Christensen, C. H.; Egeblad, K.; Christensen, C. H.; Groen, J. C.: Hierarchical zeolites: enhanced utilisation of microporous crystals in catalysis by advances in materials design. *Chem. Soc. Rev.* **2008**, *37*, 2530-2542.

(18) Sachse, A.; García-Martínez, J.: Surfactant-templating of zeolites: from design to application. *Chem. Mater.* **2017**, *29*, 3827-3853.

(19) Thomas, A.: Functional materials: from hard to soft porous frameworks. *Angew. Chem. Int. Ed.* **2010**, *49*, 8328-8344.

(20) Welbes, L. L.; Borovik, A. S.: Confinement of metal complexes within porous hosts: development of functional materials for gas binding and catalysis. *Acc. Chem. Res.* **2005**, *38*, 765-774.

(21) Wang, Y.; Angelatos, A. S.; Caruso, F.: Template synthesis of nanostructured materials via layer-by-layer assembly. *Chem. Mater.* **2008**, *20*, 848-858.

(22) Detavernier, C.; Dendooven, J.; Pulinthanathu Sree, S.; Ludwig, K. F.; Martens, J. A.: Tailoring nanoporous materials by atomic layer deposition. *Chem. Soc. Rev.* **2011**, *40*, 5242-5253.

(23) Luc, W.; Jiao, F.: Synthesis of nanoporous metals, oxides, carbides, and sulfides: beyond nanocasting. *Acc. Chem. Res.* **2016**, *49*, 1351-1358.

(24) Slater, A. G.; Cooper, A. I.: Function-led design of new porous materials. *Science* **2015**, *348*.

(25) Li, W.; Yue, Q.; Deng, Y.; Zhao, D.: Ordered mesoporous materials based on interfacial assembly and engineering. *Adv. Mater.* **2013**, *25*, 5129-5152.

(26) Gu, D.; Schüth, F.: Synthesis of non-siliceous mesoporous oxides. *Chem. Soc. Rev.* **2014**, *43*, 313-344.

(27) Carreon, M. A.; Guliants, V. V.: Ordered meso- and macroporous binary and mixed metal oxides. *Eur. J. Inorg. Chem.* **2005**, *2005*, 27-43.

(28) Ren, Y.; Ma, Z.; Bruce, P. G.: Ordered mesoporous metal oxides: synthesis and applications. *Chem. Soc. Rev.* **2012**, *41*, 4909-4927.

(29) Sun, L.-B.; Liu, X.-Q.; Zhou, H.-C.: Design and fabrication of mesoporous heterogeneous basic catalysts. *Chem. Soc. Rev.* **2015**, *44*, 5092-5147.

(30) Sun, M.-H.; Huang, S.-Z.; Chen, L.-H.; Li, Y.; Yang, X.-Y.; Yuan, Z.-Y.; Su, B.-L.: Applications of hierarchically structured porous materials from energy storage and conversion, catalysis, photocatalysis, adsorption, separation, and sensing to biomedicine. *Chem. Soc. Rev.* **2016**, *45*, 3479-3563.

(31) Frenzer, G.; Maier, W. F.: Amorphous porous mixed oxides: sol-gel ways to a highly versatile class of materials and catalysts. *Annu. Rev. Mater. Res.* **2006**, *36*, 281-331.

(32) Bravo-Suárez, J. J.; Chaudhari, R. V.; Subramaniam, B.: Design of heterogeneous catalysts for fuels and chemicals processing: an overview. In *Novel Materials for Catalysis and Fuels Processing*; American Chemical Society, 2013; Vol. 1132; pp 3-68.

(33) Post, J. E.: Manganese oxide minerals: crystal structures and economic and environmental significance. *Proc. Natl. Acad. Sci.* **1999**, *96*, 3447-3454.

(34) Pokhrel, R.; Goetz, M. K.; Shaner, S. E.; Wu, X.; Stahl, S. S.: The "best catalyst" for water oxidation depends on the oxidation method employed: a case study of manganese oxides. *J. Am. Chem. Soc.* **2015**, *137*, 8384-8387.

(35) Robinson, D. M.; Go, Y. B.; Mui, M.; Gardner, G.; Zhang, Z.; Mastrogiovanni, D.; Garfunkel, E.; Li, J.; Greenblatt, M.; Dismukes, G. C.:

Photochemical water oxidation by crystalline polymorphs of manganese oxides: structural requirements for catalysis. *J. Am. Chem. Soc.* **2013**, *135*, 3494-3501.

(36) Zhen, M.; Zhou, B.; Ren, Y.: Crystalline mesoporous transition metal oxides: hard-templating synthesis and application in environmental catalysis. *Fron. Environ. Sci. Eng.* **2013**, *7*, 341-355.

(37) Haber, J.: Catalysis by transition metal oxides. In *Solid State Chemistry in Catalysis*; American Chemical Society, 1985; Vol. 279; pp 3-21.

(38) Gervasini, A.: Characterization of acid–base sites in oxides. In *Calorimetry and Thermal Methods in Catalysis*; Auroux, A., Ed.; Springer Berlin Heidelberg: Berlin, Heidelberg, 2013; pp 319-352.

(39) Lloyd, L.: Handbook of Industrial Catalysts. Springer: New York, 2011; pp 1-490.

(40) Rase, H.: Handbook of commercial catalysts: heterogeneous catalysts. *CRC Press*: Boca Raton, FL, 2000; pp 1-488.

(41) Whitesides, G.; Mathias, J.; Seto, C.: Molecular self-assembly and nanochemistry: a chemical strategy for the synthesis of nanostructures. *Science* **1991**, *254*, 1312-1319.

(42) Wan, Y.; Shi, Y.; Zhao, D.: Designed synthesis of mesoporous solids via nonionic-surfactant-templating approach. *Chem. Commun.* **2007**, 897-926.

(43) Shi, Y.; Wan, Y.; Zhao, D.: Ordered mesoporous non-oxide materials. *Chem. Soc. Rev.* **2011**, *40*, 3854-3878.

(44) Lu, A. H.; Schüth, F.: Nanocasting: a versatile strategy for creating nanostructured porous materials. *Adv. Mater.* **2006**, *18*, 1793-1805.

(45) Yang, H.; Zhao, D.: Synthesis of replica mesostructures by the nanocasting strategy. *J. Mater. Chem.* **2005**, *15*, 1217-1231.

(46) Stein, A.; Wilson, B. E.; Rudisill, S. G.: Design and functionality of colloidal-crystal-templated materials-chemical applications of inverse opals. *Chem. Soc. Rev.* **2013**, *42*, 2763-2803.

(47) Stein, A.; Schroden, R. C.: Colloidal crystal templating of three-dimensionally ordered macroporous solids: materials for photonics and beyond. *Curr. Opin. Solid State Mater. Sci.* **2001**, *5*, 553-564.

(48) Bantsis, G.; Betsiou, M.; Bourliva, A.; Yioultsis, T.; Sikalidis, C.: Synthesis of porous iron oxide ceramics using Greek wooden templates and mill scale waste for EMI applications. *Ceram. Int.* **2012**, *38*, 721-729.

(49) Liu, Z.; Fan, T.; Zhang, W.; Zhang, D.: The synthesis of hierarchical porous iron oxide with wood templates. *Micropor. Mesopor. Mater.* **2005**, *85*, 82-88.

(50) Li, X.; Fan, T.; Liu, Z.; Ding, J.; Guo, Q.; Zhang, D.: Synthesis and hierarchical pore structure of biomorphic manganese oxide derived from woods. *J. Euro. Ceram. Soc.* **2006**, *26*, 3657-3664.

(51) Zhang, W.; Zhang, D.; Fan, T.; Ding, J.; Guo, Q.; Ogawa, H.: Morphosynthesis of hierarchical ZnO replica using butterfly wing scales as templates. *Micropor. Mesopor. Mater.* **2006**, *92*, 227-233.

(52) Dong, Q.; Su, H.; Song, F.; Zhang, D.; Wang, N.: Hierarchical metal oxides assembled by nanocrystallites via a simple bio-inspired route. *J. Am. Ceram. Soc.* **2007**, *90*, 376-380.

(53) Su, H.; Shi, Y.; Zhang, D.; Gao, J.; Wang, X.: Method for preparing multiple component porous hierarchical structure visible light catalyst comprising metal oxide substrate and semiconductor nanomaterial by using egg membrane as template. Shanghai Jiao Tong University, Peop. Rep. China . 2013; pp 7pp.

(54) Meldrum, F. C.; Seshadri, R.: Porous gold structures through templating by echinoid skeletal plates. *Chem. Commun.* **2000**, 29-30.

(55) Soitah, T. N.; Chunhui, Y.; Yong, Y.; Yinghua, N.; Liang, S.: Properties of Bi_2O_3 thin films prepared via a modified Pechini route. *Curr. Appl. Phys.* **2010**, *10*, 1372-1377.

(56) Wu, Y.; Wang, X.: Preparation and characterization of single-phase α-Fe_2O_3 nano-powders by Pechini sol–gel method. *Mater. Lett.* **2011**, *65*, 2062-2065.

(57) Wu, Y. T.; Wang, X. F.; Yu, C. L.; Li, E. Y.: Preparation and characterization of barium titanate ($BaTiO_3$) nano-powders by Pechini sol-gel method. *Mater. Manuf. Processes* **2012**, *27*, 1329-1333.

(58) Soisuwan, S.; Panpranot, J.; Trimm, D. L.; Praserthdam, P.: A study of alumina–zirconia mixed oxides prepared by the modified Pechini method as Co catalyst supports in CO hydrogenation. *Appl. Catal. A General* **2006**, *303*, 268-272.

(59) Sladkevich, S.; Kyi, N.; Gun, J.; Prikhodchenko, P.; Ischuk, S.; Lev, O.: Antimony doped tin oxide coating of muscovite clays by the Pechini route. *Thin Solid Films* **2011**, *520*, 152-158.

(60) Del Toro, R.; Hernández, P.; Díaz, Y.; Brito, J. L.: Synthesis of $La_{0.8}Sr_{0.2}FeO_3$ perovskites nanocrystals by Pechini sol–gel method. *Mater. Lett.* **2013**, *107*, 231-234.

(61) Lemos, F. C. D.; Melo, D. M. A.; da Silva, J. E. C.: Up-conversion luminescence in Er^{3+}/Yb^{3+}-codoped $PbTiO_3$ perovskite obtained via Pechini method. *Mater. Res. Bull.* **2005**, *40*, 187-192.

(62) Huízar-Félix, A. M.; Hernández, T.; de la Parra, S.; Ibarra, J.; Kharisov, B.: Sol–gel based Pechini method synthesis and characterization of $Sm_{1-x}Ca_xFeO_3$ perovskite $0.1 \leq x \leq 0.5$. *Powder Tech.* **2012**, *229*, 290-293.

(63) Pechini, M.: Method of preparing lead and alkaline earth titanates and niobates and coating method using the same to form a capacitor. Vol. U.S. Patent No. 3330697 A.

(64) Rudisill, S. G.; Hein, N. M.; Terzic, D.; Stein, A.: Controlling microstructural evolution in Pechini gels through the interplay between precursor complexation, step-growth polymerization, and template confinement. *Chem. Mater.* **2012**, *25*, 745-753.

(65) Danks, A. E.; Hall, S. R.; Schnepp, Z.: The evolution of 'sol-gel' chemistry as a technique for materials synthesis. *Mater. Horiz.* **2016**, *3*, 91-112.

(66) Furukawa, H.; Cordova, K. E.; O'Keeffe, M.; Yaghi, O. M.: The chemistry and applications of metal-organic frameworks. *Science* **2013**, *341*, 1230444.

(67) Huang, Y.-B.; Liang, J.; Wang, X.-S.; Cao, R.: Multifunctional metal-organic framework catalysts: synergistic catalysis and tandem reactions. *Chem. Soc. Rev.* **2017**, *46*, 126-157.

(68) Isaeva, V. I.; Kustov, L. M.: The application of metal-organic frameworks in catalysis (review). *Petrol. Chem.* **2010**, *50*, 167-180.

(69) Lee, J.; Farha, O. K.; Roberts, J.; Scheidt, K. A.; Nguyen, S. T.; Hupp, J. T.: Metal-organic framework materials as catalysts. *Chem. Soc. Rev.* **2009**, *38*, 1450-1459.

(70) Liu, J.; Chen, L.; Cui, H.; Zhang, J.; Zhang, L.; Su, C.-Y.: Applications of metal-organic frameworks in heterogeneous supramolecular catalysis. *Chem. Soc. Rev.* **2014**, *43*, 6011-6061.

(71) Loera-Serna, S.; Ortiz, E.: Catalytic applications of metal-organic frameworks. In *Advanced Catalytic Materials - Photocatalysis and Other Current Trends*; Norena, L. E., Wang, J.-A., Eds.; InTech: Rijeka, 2016; pp Ch. 04.

(72) Ma, L.; Lin, W.: Designing metal-organic frameworks for catalytic applications. In *Functional Metal-Organic Frameworks: Gas Storage, Separation and Catalysis*; Schröder, M., Ed.; Springer Berlin Heidelberg: Berlin, Heidelberg, 2010; pp 175-205.

(73) Ranocchiari, M.; Lothschütz, C.; Grolimund, D.; van Bokhoven, J. A.: Single-atom active sites on metal-organic frameworks. *Proc. R. Soc. London A* **2012**, *468*, 1985-1999.

(74) Rogge, S. M. J.; Bavykina, A.; Hajek, J.; Garcia, H.; Olivos-Suarez, A. I.; Sepulveda-Escribano, A.; Vimont, A.; Clet, G.; Bazin, P.; Kapteijn, F.; Daturi, M.; Ramos-Fernandez, E. V.; Llabres i Xamena, F. X.; Van Speybroeck, V.; Gascon, J.: Metal-organic and covalent organic frameworks as single-site catalysts. *Chem. Soc. Rev.* **2017**, *46*, 3134-3184.

(75) Sun, J.-K.; Xu, Q.: Functional materials derived from open framework templates/precursors: synthesis and applications. *Energy Environ. Sci.* **2014**, *7*, 2071-2100.

(76) Howarth, A. J.; Liu, Y.; Li, P.; Li, Z.; Wang, T. C.; Hupp, J. T.; Farha, O. K.: Chemical, thermal and mechanical stabilities of metal–organic frameworks. *Nat. Rev. Mater.* **2016**, *1*, 15018.

(77) Stock, N.; Biswas, S.: Synthesis of metal-organic frameworks (MOFs): routes to various MOF topologies, morphologies, and composites. *Chem. Rev.* **2012**, *112*, 933-969.

(78) Howarth, A. J.; Peters, A. W.; Vermeulen, N. A.; Wang, T. C.; Hupp, J. T.; Farha, O. K.: Best practices for the synthesis, activation, and characterization of metal–organic frameworks. *Chem. Mater.* **2017**, *29*, 26-39.

(79) Albuquerque, G. H.; Herman, G. S.: Chemically modulated microwave-assisted synthesis of MOF-74(Ni) and preparation of metal–organic framework-matrix based membranes for removal of metal ions from aqueous media. *Cryst. Growth Des.* **2017**, *17*, 156-162.

(80) Schaate, A.; Roy, P.; Godt, A.; Lippke, J.; Waltz, F.; Wiebcke, M.; Behrens, P.: Modulated synthesis of Zr-based metal–organic frameworks: from nano to single crystals. *Chem. Eur. J.* **2011**, *17*, 6643-6651.

(81) Xu, X.: Controllable synthesis of ultra-small metal-organic framework nanocrystals composed of copper(ii) carboxylates. *Nanoscale* **2016**, *8*, 16725-16732.

(82) Zhan, G.; Zeng, H. C.: Alternative synthetic approaches for metal-organic frameworks: transformation from solid matters. *Chem. Commun.* **2017**, *53*, 72-81.

(83) Maserati, L.; Meckler, S. M.; Li, C.; Helms, B. A.: Minute-MOFs: ultrafast synthesis of M_2(dobpdc) metal–organic frameworks from divalent metal oxide colloidal nanocrystals. *Chem. Mater.* **2016**, *28*, 1581-1588.

(84) Dunne, P. W.; Lester, E.; Walton, R. I.: Towards scalable and controlled synthesis of metal-organic framework materials using continuous flow reactors. *React. Chem. Eng.* **2016**, *1*, 352-360.

(85) McKinstry, C.; Cathcart, R. J.; Cussen, E. J.; Fletcher, A. J.; Patwardhan, S. V.; Sefcik, J.: Scalable continuous solvothermal synthesis of metal-organic framework (MOF-5) crystals. *Chem. Eng. J.* **2016**, *285*, 718-725.

(86) Rubio-Martinez, M.; Batten, M. P.; Polyzos, A.; Carey, K.-C.; Mardel, J. I.; Lim, K.-S.; Hill, M. R.: Versatile, high quality and scalable continuous flow production of metal-organic frameworks. *Sci. Rep.* **2014**, *4*, 5443.

(87) McCoy, M.: BASF makes MOFs on industrial scale. In *Chem. Eng. News*, 2010; Vol. 88; pp 18.

(88) Scott, A.: Round two for MOF commercialization. In *Chem. Eng. News*, 2017; Vol. 95; pp 18-19.

(89) Dhakshinamoorthy, A.; Alvaro, M.; Garcia, H.: Commercial metal-organic frameworks as heterogeneous catalysts. *Chem. Commun.* **2012**, *48*, 11275-11288.

(90) Chavan, S.; Vitillo, J. G.; Gianolio, D.; Zavorotynska, O.; Civalleri, B.; Jakobsen, S.; Nilsen, M. H.; Valenzano, L.; Lamberti, C.; Lillerud, K. P.; Bordiga, S.: H_2 storage in isostructural UiO-67 and UiO-66 MOFs. *Phys. Chem. Chem. Phys.* **2012**, *14*, 1614-1626.

(91) Deng, H.; Grunder, S.; Cordova, K. E.; Valente, C.; Furukawa, H.; Hmadeh, M.; Gándara, F.; Whalley, A. C.; Liu, Z.; Asahina, S.; Kazumori, H.; O'Keeffe, M.; Terasaki, O.; Stoddart, J. F.; Yaghi, O. M.: Large-pore apertures in a series of metal-organic frameworks. *Science* **2012**, *336*, 1018-1023.

(92) Planas, N.; Mondloch, J. E.; Tussupbayev, S.; Borycz, J.; Gagliardi, L.; Hupp, J. T.; Farha, O. K.; Cramer, C. J.: Defining the proton topology of the Zr_6-based metal-organic framework NU-1000. *J. Phys. Chem. Lett.* **2014**, *5*, 3716-3723.

(93) Guillerm, V.; Ragon, F.; Dan-Hardi, M.; Devic, T.; Vishnuvarthan, M.; Campo, B.; Vimont, A.; Clet, G.; Yang, Q.; Maurin, G.; Férey, G.; Vittadini, A.; Gross, S.; Serre, C.: A series of isoreticular, highly stable, porous zirconium oxide based metal–organic frameworks. *Angew. Chem. Int. Ed.* **2012**, *51*, 9267-9271.

(94) Gedrich, K.; Senkovska, I.; Klein, N.; Stoeck, U.; Henschel, A.; Lohe, M. R.; Baburin, I. A.; Mueller, U.; Kaskel, S.: A highly porous metal–organic framework with open nickel sites. *Angew. Chem. Int. Ed.* **2010**, *49*, 8489-8492.

(95) Ranocchiari, M.; Bokhoven, J. A. v.: Catalysis by metal-organic frameworks: fundamentals and opportunities. *Phys. Chem. Chem. Phys.* **2011**, *13*, 6388-6396.

(96) Gascon, J.; Corma, A.; Kapteijn, F.; Llabrés i Xamena, F. X.: Metal organic framework catalysis: quo vadis? *ACS Catal.* **2014**, *4*, 361-378.

(97) Easun, T. L.; Moreau, F.; Yan, Y.; Yang, S.; Schroder, M.: Structural and dynamic studies of substrate binding in porous metal-organic frameworks. *Chem. Soc. Rev.* **2017**, *46*, 239-274.

(98) Valvekens, P.; Vermoortele, F.; De Vos, D.: Metal-organic frameworks as catalysts: the role of metal active sites. *Catal. Sci. Tech.* **2013**, *3*, 1435-1445.

(99) Mondloch, J. E.; Katz, M. J.; Isley III, W. C.; Ghosh, P.; Liao, P.; Bury, W.; Wagner, G. W.; Hall, M. G.; DeCoste, J. B.; Peterson, G. W.; Snurr, R. Q.; Cramer, C. J.; Hupp, J. T.; Farha, O. K.: Destruction of chemical warfare agents using metal-organic frameworks. *Nat. Mater.* **2015**, *14*, 512-516.

(100) Duke, A. S.; Dolgopolova, E. A.; Galhenage, R. P.; Ammal, S. C.; Heyden, A.; Smith, M. D.; Chen, D. A.; Shustova, N. B.: Active sites in copper-based metal–organic frameworks: understanding substrate dynamics, redox processes, and valence-band structure. *J. Phys. Chem. C* **2015**, *119*, 27457-27466.

(101) Ren, H.-Y.; Yao, R.-X.; Zhang, X.-M.: Enhanced catalysis activity in a coordinatively unsaturated cobalt-MOF generated via single-crystal-to-single-crystal dehydration. *Inorg. Chem.* **2015**, *54*, 6312-6318.

(102) Platero-Prats, A. E.; Mavrandonakis, A.; Gallington, L. C.; Liu, Y.; Hupp, J. T.; Farha, O. K.; Cramer, C. J.; Chapman, K. W.: Structural transitions of the metal-oxide nodes within metal–organic frameworks: on the local structures of NU-1000 and UiO-66. *J. Am. Chem. Soc.* **2016**, *138*, 4178-4185.

(103) Kumar, S.; Mandal, S. K.: Capturing the structural diversification upon thermal desolvation of a robust metal organic framework via a single-crystal-to-single-crystal transformation. *CrystEngComm* **2015**, *17*, 8801-8806.

(104) Metzger, E. D.; Comito, R. J.; Hendon, C. H.; Dincă, M.: Mechanism of single-site molecule-like catalytic ethylene dimerization in Ni-MFU-4l. *J. Am. Chem. Soc.* **2017**, *139*, 757-762.

(105) Manna, K.; Ji, P.; Lin, Z.; Greene, F. X.; Urban, A.; Thacker, N. C.; Lin, W.: Chemoselective single-site earth-abundant metal catalysts at metal–organic framework nodes. *Nat. Comm.* **2016**, *7*, 12610.

(106) Canivet, J.; Aguado, S.; Schuurman, Y.; Farrusseng, D.: MOF-supported selective ethylene dimerization single-site catalysts through one-pot postsynthetic modification. *J. Am. Chem. Soc.* **2013**, *135*, 4195-4198.

(107) Wu, C.-D.; Zhao, M.: Incorporation of molecular catalysts in metal–organic frameworks for highly efficient heterogeneous catalysis. *Adv. Mater.* **2017**, *29*, 1605446-n/a.

(108) Wang, T. C.; Vermeulen, N. A.; Kim, I. S.; Martinson, A. B. F.; Stoddart, J. F.; Hupp, J. T.; Farha, O. K.: Scalable synthesis and post-modification of a mesoporous metal-organic framework called NU-1000. *Nat. Protoc.* **2016**, *11*, 149-162.

(109) Kim, M.; Cahill, J. F.; Fei, H.; Prather, K. A.; Cohen, S. M.: Postsynthetic ligand and cation exchange in robust metal–organic frameworks. *J. Am. Chem. Soc.* **2012**, *134*, 18082-18088.

(110) Feng, D.; Gu, Z.-Y.; Li, J.-R.; Jiang, H.-L.; Wei, Z.; Zhou, H.-C.: Zirconium-metalloporphyrin PCN-222: mesoporous metal–organic frameworks with ultrahigh stability as biomimetic catalysts. *Angew. Chem. Int. Ed.* **2012**, *51*, 10307-10310.

(111) Huh, S.; Kim, S.-J.; Kim, Y.: Porphyrinic metal-organic frameworks from custom-designed porphyrins. *CrystEngComm* **2016**, *18*, 345-368.

(112) Li, J.; Ren, Y.; Qi, C.; Jiang, H.: A chiral salen-based MOF catalytic material with high thermal, aqueous and chemical stabilities. *Dalton Trans.* **2017**, *46*, 7821-7832.

(113) Liu, Y.; Li, Z.; Yuan, G.; Xia, Q.; Yuan, C.; Cui, Y.: Chiral Cu(salen)-based metal–organic framework for heterogeneously catalyzed aziridination and amination of olefins. *Inorg. Chem.* **2016**, *55*, 12500-12503.

(114) Xia, Q.; Liu, Y.; Li, Z.; Gong, W.; Cui, Y.: A Cr(salen)-based metal-organic framework as a versatile catalyst for efficient asymmetric transformations. *Chem. Commun.* **2016**, *52*, 13167-13170.

(115) Zhu, C.; Xia, Q.; Chen, X.; Liu, Y.; Du, X.; Cui, Y.: Chiral metal–organic framework as a platform for cooperative catalysis in asymmetric cyanosilylation of aldehydes. *ACS Catal.* **2016**, *6*, 7590-7596.

(116) Fei, H.; Shin, J.; Meng, Y. S.; Adelhardt, M.; Sutter, J.; Meyer, K.; Cohen, S. M.: Reusable oxidation catalysis using metal-monocatecholato species in a robust metal–organic framework. *J. Am. Chem. Soc.* **2014**, *136*, 4965-4973.

(117) Chen, G.-J.; Ma, H.-C.; Xin, W.-L.; Li, X.-B.; Jin, F.-Z.; Wang, J.-S.; Liu, M.-Y.; Dong, Y.-B.: Dual heterogeneous catalyst Pd–Au@Mn(II)-MOF for one-pot tandem synthesis of imines from alcohols and amines. *Inorg. Chem.* **2017**, *56*, 654-660.

(118) Chen, G.-J.; Wang, J.-S.; Jin, F.-Z.; Liu, M.-Y.; Zhao, C.-W.; Li, Y.-A.; Dong, Y.-B.: Pd@Cu(II)-MOF-catalyzed aerobic oxidation of benzylic alcohols in air with high conversion and selectivity. *Inorg. Chem.* **2016**, *55*, 3058-3064.

(119) Falcaro, P.; Ricco, R.; Yazdi, A.; Imaz, I.; Furukawa, S.; Maspoch, D.; Ameloot, R.; Evans, J. D.; Doonan, C. J.: Application of metal and metal oxide nanoparticles@MOFs. *Coord. Chem. Rev.* **2016**, *307*, 237-254.

(120) Song, J.; Luo, Z.; Britt, D. K.; Furukawa, H.; Yaghi, O. M.; Hardcastle, K. I.; Hill, C. L.: A multiunit catalyst with synergistic stability and reactivity: a polyoxometalate–metal organic framework for aerobic decontamination. *J. Am. Chem. Soc.* **2011**, *133*, 16839-16846.

(121) Sun, J.-W.; Yan, P.-F.; An, G.-H.; Sha, J.-Q.; Li, G.-M.; Yang, G.-Y.: Immobilization of Polyoxometalate in the Metal-Organic Framework rht-MOF-1: Towards a Highly Effective Heterogeneous Catalyst and Dye Scavenger. *Sci. Rep.* **2016**, *6*, 25595.

(122) Mali, G.: Looking into metal-organic frameworks with solid-state NMR spectroscopy. In *Metal-Organic Frameworks*; Zafar, F., Sharmin, E., Eds.; InTech: Rijeka, 2016; pp Ch. 03.

(123) Volkringer, C.; Popov, D.; Loiseau, T.; Guillou, N.; Ferey, G.; Haouas, M.; Taulelle, F.; Mellot-Draznieks, C.; Burghammer, M.; Riekel, C.: A microdiffraction set-up for nanoporous metal-organic-framework-type solids. *Nat. Mater.* **2007**, *6*, 760-764.

(124) Gandara, F.; Bennett, T. D.: Crystallography of metal-organic frameworks. *IUCrJ* **2014**, *1*, 563-570.

(125) Borfecchia, E.; Gianolio, D.; Agostini, G.; Bordiga, S.; Lamberti, C.: Characterization of MOFs: long and local range order structural determination of MOFs by combining EXAFS and diffraction techniques. In *Metal Organic Frameworks as Heterogeneous Catalysts*; The Royal Society of Chemistry, 2013; pp 143-208.

(126) Gonzalez, M. I.; Bloch, E. D.; Mason, J. A.; Teat, S. J.; Long, J. R.: Single-crystal-to-single-crystal metalation of a metal–organic framework: a route toward structurally well-defined catalysts. *Inorg. Chem.* **2015**, *54*, 2995-3005.

(127) Coudert, F.-X.; Fuchs, A. H.: Computational characterization and prediction of metal–organic framework properties. *Coord. Chem. Rev.* **2016**, *307*, 211-236.

(128) Witman, M.; Ling, S.; Anderson, S.; Tong, L.; Stylianou, K. C.; Slater, B.; Smit, B.; Haranczyk, M.: In silico design and screening of hypothetical MOF-74 analogs and their experimental synthesis. *Chem. Sci.* **2016**, *7*, 6263-6272.

(129) Kulkarni, A. R.; Sholl, D. S.: Screening of copper open metal site MOFs for olefin/paraffin separations using DFT-derived force fields. *J. Phys. Chem. C* **2016**, *120*, 23044-23054.

(130) Gomez-Gualdron, D. A.; Gutov, O. V.; Krungleviciute, V.; Borah, B.; Mondloch, J. E.; Hupp, J. T.; Yildirim, T.; Farha, O. K.; Snurr, R. Q.: Computational design of metal–organic frameworks based on stable zirconium building units for storage and delivery of methane. *Chem. Mater.* **2014**, *26*, 5632-5639.

(131) Lee, J. S.; Vlaisavljevich, B.; Britt, D. K.; Brown, C. M.; Haranczyk, M.; Neaton, J. B.; Smit, B.; Long, J. R.; Queen, W. L.: Understanding small-molecule interactions in metal–organic frameworks: coupling experiment with theory. *Adv. Mater.* **2015**, *27*, 5785-5796.

(132) Watanabe, T.; Sholl, D. S.: Accelerating applications of metal–organic frameworks for gas adsorption and separation by computational screening of materials. *Langmuir* **2012**, *28*, 14114-14128.

(133) Pidko, E. A.; Hensen, E. J. M.: Computational approach to chemical reactivity of MOFs. In *Metal Organic Frameworks as Heterogeneous Catalysts*; The Royal Society of Chemistry, 2013; pp 209-234.

(134) Odoh, S. O.; Cramer, C. J.; Truhlar, D. G.; Gagliardi, L.: Quantum-chemical characterization of the properties and reactivities of metal–organic frameworks. *Chem. Rev.* **2015**, *115*, 6051-6111.

(135) Vogiatzis, K. D.; Haldoupis, E.; Xiao, D. J.; Long, J. R.; Siepmann, J. I.; Gagliardi, L.: Accelerated computational analysis of metal–organic frameworks for oxidation catalysis. *J. Phys. Chem. C* **2016**, *120*, 18707-18712.

(136) Bernales, V.; League, A. B.; Li, Z.; Schweitzer, N. M.; Peters, A. W.; Carlson, R. K.; Hupp, J. T.; Cramer, C. J.; Farha, O. K.; Gagliardi, L.: Computationally

guided discovery of a catalytic cobalt-decorated metal–organic framework for ethylene dimerization. *J. Phys. Chem. C* **2016**, *120*, 23576-23583.

(137) Ortuño, M. A.; Bernales, V.; Gagliardi, L.; Cramer, C. J.: Computational study of first-row transition metals supported on MOF NU-1000 for catalytic acceptorless alcohol dehydrogenation. *J. Phys. Chem. C* **2016**, *120*, 24697-24705.

(138) Wang, W.; Xu, X.; Zhou, W.; Shao, Z.: Recent progress in metal-organic frameworks for applications in electrocatalytic and photocatalytic water splitting. *Adv. Sci.* **2017**, *4*, 1600371-n/a.

(139) Zeng, L.; Guo, X.; He, C.; Duan, C.: Metal–organic frameworks: versatile materials for heterogeneous photocatalysis. *ACS Catal.* **2016**, *6*, 7935-7947.

(140) Zhang, T.; Lin, W.: Metal-organic frameworks for artificial photosynthesis and photocatalysis. *Chem. Soc. Rev.* **2014**, *43*, 5982-5993.

(141) Corma, A.; García, H.; Llabrés i Xamena, F. X.: Engineering metal-organic frameworks for heterogeneous catalysis. *Chem. Rev.* **2010**, *110*, 4606-4655.

(142) Zhu, L.; Liu, X.-Q.; Jiang, H.-L.; Sun, L.-B.: Metal–organic frameworks for heterogeneous basic catalysis. *Chem. Rev.* **2017**, *117*, 8129-8176.

(143) Wang, C.; Liu, X.; Keser Demir, N.; Chen, J. P.; Li, K.: Applications of water stable metal-organic frameworks. *Chem. Soc. Rev.* **2016**, *45*, 5107-5134.

(144) Burtch, N. C.; Jasuja, H.; Walton, K. S.: Water stability and adsorption in metal–organic frameworks. *Chem. Rev.* **2014**, *114*, 10575-10612.

(145) Banerjee, R.; Phan, A.; Wang, B.; Knobler, C.; Furukawa, H.; O'Keeffe, M.; Yaghi, O. M.: High-throughput synthesis of zeolitic imidazolate frameworks and application to CO_2 Capture. *Science* **2008**, *319*, 939-943.

(146) Yang, C.; Kaipa, U.; Mather, Q. Z.; Wang, X.; Nesterov, V.; Venero, A. F.; Omary, M. A.: Fluorous metal–organic frameworks with superior adsorption and hydrophobic properties toward oil spill cleanup and hydrocarbon storage. *J. Am. Chem. Soc.* **2011**, *133*, 18094-18097.

(147) Nguyen, J. G.; Cohen, S. M.: Moisture-resistant and Ssuperhydrophobic metal−organic frameworks obtained via postsynthetic modification. *J. Am. Chem. Soc.* **2010**, *132*, 4560-4561.

(148) Nijem, N.; Canepa, P.; Kaipa, U.; Tan, K.; Roodenko, K.; Tekarli, S.; Halbert, J.; Oswald, I. W. H.; Arvapally, R. K.; Yang, C.; Thonhauser, T.; Omary, M. A.; Chabal, Y. J.: Water cluster confinement and methane adsorption in the hydrophobic cavities of a fluorinated metal–organic framework. *J. Am. Chem. Soc.* **2013**, *135*, 12615-12626.

(149) Wu, H.; Yildirim, T.; Zhou, W.: Exceptional mechanical stability of highly porous zirconium metal–organic framework UiO-66 and its important implications. *J. Phys. Chem. Lett.* **2013**, *4*, 925-930.

(150) Van de Voorde, B.; Stassen, I.; Bueken, B.; Vermoortele, F.; De Vos, D.; Ameloot, R.; Tan, J.-C.; Bennett, T. D.: Improving the mechanical stability of zirconium-based metal-organic frameworks by incorporation of acidic modulators. *J. Mater. Chem. A* **2015**, *3*, 1737-1742.

(151) Zhang, L.; Hu, Y. H.: A systematic investigation of decomposition of nano $Zn_4O(C_8H_4O_4)_3$ metal−organic framework. *J. Phys. Chem. C* **2010**, *114*, 2566-2572.

(152) Kang, I. J.; Khan, N. A.; Haque, E.; Jhung, S. H.: Chemical and thermal stability of isotypic metal-organic frameworks: effect of metal ions. *Chem. Eur. J.* **2011**, *17*, 6437-6442.

(153) Ma, S.; Wang, X.-S.; Yuan, D.; Zhou, H.-C.: A coordinatively linked Yb metal-organic framework demonstrates high thermal stability and uncommon gas-adsorption selectivity. *Angew. Chem. Int. Ed.* **2008**, *47*, 4130-4133.

(154) DeCoste, J. B.; Peterson, G. W.; Jasuja, H.; Glover, T. G.; Huang, Y.-g.; Walton, K. S.: Stability and degradation mechanisms of metal-organic frameworks containing the $Zr_6O_4(OH)_4$ secondary building unit. *J. Mater. Chem. A* **2013**, *1*, 5642-5650.

(155) Cavka, J. H.; Jakobsen, S.; Olsbye, U.; Guillou, N.; Lamberti, C.; Bordiga, S.; Lillerud, K. P.: A new zirconium inorganic building brick forming metal-organic frameworks with exceptional stability. *J. Am. Chem. Soc.* **2008**, *130*, 13850-13851.

(156) Mondloch, J. E.; Bury, W.; Fairen-Jimenez, D.; Kwon, S.; DeMarco, E. J.; Weston, M. H.; Sarjeant, A. A.; Nguyen, S. T.; Stair, P. C.; Snurr, R. Q.; Farha, O. K.; Hupp, J. T.: Vapor-phase metalation by atomic layer deposition in a metal-organic framework. *J. Am. Chem. Soc.* **2013**, *135*, 10294-10297.

(157) Valenzano, L.; Civalleri, B.; Chavan, S.; Bordiga, S.; Nilsen, M. H.; Jakobsen, S.; Lillerud, K. P.; Lamberti, C.: Disclosing the complex structure of UiO-66 metal-organic framework: a synergic combination of experiment and theory. *Chem. Mater.* **2011**, *23*, 1700-1718.

(158) Bennett, T. D.; Goodwin, A. L.; Dove, M. T.; Keen, D. A.; Tucker, M. G.; Barney, E. R.; Soper, A. K.; Bithell, E. G.; Tan, J.-C.; Cheetham, A. K.: Structure and Properties of an Amorphous Metal-Organic Framework. *Physical Review Letters* **2010**, *104*, 115503.

(159) Umeyama, D.; Horike, S.; Inukai, M.; Itakura, T.; Kitagawa, S.: Reversible solid-to-liquid phase transition of coordination polymer crystals. *J. Am. Chem. Soc.* **2015**, *137*, 864-870.

(160) Rudisill, S. G.; Wang, Z.; Stein, A.: Maintaining the structure of templated porous materials for reactive and high-temperature applications. *Langmuir* **2012**, *28*, 7310-7324.

(161) An, B.; Cheng, K.; Wang, C.; Wang, Y.; Lin, W.: Pyrolysis of metal–organic frameworks to Fe_3O_4@Fe_5C_2 core–shell nanoparticles for Fischer–Tropsch synthesis. *ACS Catal.* **2016**, *6*, 3610-3618.

(162) Shen, K.; Chen, X.; Chen, J.; Li, Y.: Development of MOF-derived carbon-based nanomaterials for efficient catalysis. *ACS Catal.* **2016**, *6*, 5887-5903.

(163) Besler, R.; Rossetti da Silva, M.; do Rosario, J. J.; Dosta, M.; Heinrich, S.; Janssen, R.: Sintering simulation of periodic macroporous alumina. *J. Am. Ceram. Soc.* **2015**, *98*, 3496-3502.

(164) Aboav, D. A.: The stability of grains in a polycrystal. *Metallography* **1971**, *4*, 425-441.

(165) Whittemore, O. J.; Sipe, J. J.: Pore growth during the initial stages of sintering ceramics. *Powder Tech.* **1974**, *9*, 159-164.

(166) Olevsky, E. A.; Tikare, V.; Garino, T.: Multi-scale study of sintering: a review. *J. Am. Ceram. Soc.* **2006**, *89*, 1914-1922.

(167) Casillas, D. C.; Wilkinson, D. C.; Lai, C.-H.; Wilke, S. K.; Ignatowich, M. J.; Haile, S. M.; Dunn, B. S.: High-temperature structural stability of ceria-based inverse opals. *J. Am. Ceram. Soc.* **2017**, *100*, 2659-2668.

(168) Forzatti, P.; Lietti, L.: Catalyst deactivation. *Catal. Today* **1999**, *52*, 165-181.

(169) Bartholomew, C. H.: Mechanisms of catalyst deactivation. *Appl. Catal. A Gen.* **2001**, *212*, 17-60.

(170) Arai, H.; Machida, M.: Thermal stabilization of catalyst supports and their application to high-temperature catalytic combustion. *Appl. Catal. A Gen.* **1996**, *138*, 161-176.

(171) Eastman, P. F.; Cutler, I. B.: Effect of water vapor on initial sintering of magnesia. *J. Am. Ceram. Soc.* **1966**, *49*, 526-530.

(172) Petersen, R. O.; Cutler, I. B.: Effects of water vapor on the initial sintering of calcia. *J. Am. Ceram. Soc.* **1968**, *51*, 21-22.

(173) Verissimo, C.; Alves, O. L.: Microstructural modifications in macroporous oxides prepared via latex templating: synthesis and thermal stability of porous microstructure. *J. Am. Ceram. Soc.* **2006**, *89*, 2226-2231.

(174) Sattler, J. J. H. B.; Ruiz-Martinez, J.; Santillan-Jimenez, E.; Weckhuysen, B. M.: Catalytic dehydrogenation of light alkanes on metals and metal oxides. *Chem. Rev.* **2014**, *114*, 10613-10653.

(175) Miller, J. "Initial case for splitting carbon dioxide to carbon monoxide and oxygen," Sandia National Laboratories, 2007.

(176) Graves, C.; Ebbesen, S. D.; Mogensen, M.; Lackner, K. S.: Sustainable hydrocarbon fuels by recycling CO_2 and H_2O with renewable or nuclear energy. *Renew. Sustainable Energy Rev.* **2011**, *15*, 1-23.

(177) Thevenin, P. O.; Ersson, A. G.; Kušar, H. M. J.; Menon, P. G.; Järås, S. G.: Deactivation of high temperature combustion catalysts. *Appl. Catal. A Gen.* **2001**, *212*, 189-197.

(178) Goswami, D. Y.: Solar energy. In *2010 Survey of Energy Resources* Judy, T., Alan, C., Eds.; World Energy Council: London, 2010; pp 408-452.

(179) Villafán-Vidales, H. I.; Arancibia-Bulnes, C. A.; Riveros-Rosas, D.; Romero-Paredes, H.; Estrada, C. A.: An overview of the solar thermochemical processes for hydrogen and syngas production: reactors, and facilities. *Renew. Sustainable Energy Rev.* **2017**, *75*, 894-908.

(180) Peng, X.; Root, T. W.; Maravelias, C. T.: Storing solar energy with chemistry: the role of thermochemical storage in concentrating solar power. *Green Chem.* **2017**, *19*, 2427-2438.

(181) Romero, M.; Steinfeld, A.: Concentrating solar thermal power and thermochemical fuels. *Energy Environ. Sci.* **2012**, *5*, 9234-9245.

(182) Muller-Steinhagen, H.: Concentrating solar power: a review of technology. *Ingenia* **2004**, 43-50.

(183) Fletcher, E. A.: Solarthermal processing: a review. *J. Sol. Energy Eng.* **2000**, *123*, 63-74.

(184) Hou, Y.; Vidu, R.; Stroeve, P.: Solar energy storage methods. *Ind. Eng. Chem. Res.* **2011**, *50*, 8954-8964.

(185) Dry, M. E.: High quality diesel via the Fischer-Tropsch process - a review. *J. Chem. Technol. Biotechnol.* **2002**, *77*, 43-50.

(186) Dry, M. E.: Chemicals produced in a commercial Fischer-Tropsch process. *ACS Symp. Ser.* **1987**, *328*, 18-33.

(187) Lee, S.: *Methanol synthesis technology*; CRC Press: Boca Raton, FL, 1990.

(188) Züttel, A.; Remhof, A.; Borgschulte, A.; Friedrichs, O.: Hydrogen: the future energy carrier. *Philos. Trans. Royal Soc. A Math. Phys. Eng. Sci.* **2010**, *368*, 3329-3342.

(189) Olah, G. A.; Goeppert, A.; Prakash, G. K. S.: The "methanol economy": general aspects. In *Beyond Oil and Gas: The Methanol Economy*; Wiley-VCH Verlag GmbH & Co. KGaA, 2009; pp 179-184.

(190) Kogan, A.: Direct solar thermal splitting of water and on-site separation of the products II. Experimental feasibility study. *Int. J. Hydrogen Energy* **1998**, *23*, 89-98.

(191) Etiévant, C.: Solar high-temperature direct water splitting — a review of experiments in France. *Sol. Energ. Mater.* **1991**, *24*, 413-440.

(192) Kodama, T.; Gokon, N.: Thermochemical cycles for high-temperature solar hydrogen production. *Chem. Rev.* **2007**, *107*, 4048-4077.

(193) Gálvez, M. E.; Loutzenhiser, P. G.; Hischier, I.; Steinfeld, A.: CO_2 splitting via two-step solar thermochemical cycles with Zn/ZnO and FeO/Fe_3O_4 redox reactions: thermodynamic analysis. *Energy Fuels* **2008**, *22*, 3544-3550.

(194) Stamatiou, A.; Loutzenhiser, P. G.; Steinfeld, A.: Solar syngas production via H_2O/CO_2-splitting thermochemical cycles with Zn/ZnO and FeO/Fe_3O_4 redox reactions. *Chem. Mater.* **2010**, *22*, 851-859.

(195) Loutzenhiser, P. G.; Meier, A.; Steinfeld, A.: Review of the two-Step H_2O/CO_2-splitting solar thermochemical cycle based on Zn/ZnO redox reactions. *Materials* **2010**, *3*.

(196) Steinfeld, A.: Solar hydrogen production via a two-step water-splitting thermochemical cycle based on Zn/ZnO redox reactions. *Int. J. Hydrogen Energy* **2002**, *27*, 611-619.

(197) Pacchioni, G.: Oxygen vacancy: the invisible agent on oxide surfaces. *ChemPhysChem* **2003**, *4*, 1041-1047.

(198) Sudakar, C.; Singh, S.; Rao, M. S. R.; Lawes, G.: The role of defects in functional oxide nanostructures. In *Functional Metal Oxide Nanostructures*; Wu, J., Cao, J., Han, W.-Q., Janotti, A., Kim, H.-C., Eds.; Springer New York: New York, NY, 2012; pp 37-68.

(199) Kalinin, S. V.; Spaldin, N. A.: Functional ion defects in transition metal oxides. *Science* **2013**, *341*, 858-9.

(200) Patrakeev, M. V.; Leonidov, I. A.; Kozhevnikov, V. L.: Applications of coulometric titration for studies of oxygen non-stoichiometry in oxides. *J. Solid State Electrochem.* **2010**, *15*, 931-954.

(201) Gradassi, M. J.; Wayne Green, N.: Economics of natural gas conversion processes. *Fuel Process. Technol.* **1995**, *42*, 65-83.

(202) Ling, Y.; Wang, F.; Budiman, R. A.; Nakamura, T.; Amezawa, K.: Oxygen nonstoichiometry, the defect equilibrium model and thermodynamic quantities of the Ruddlesden-Popper oxide Sr3Fe2O7-[small delta]. *Phys. Chem. Chem. Phys.* **2015**, *17*, 7489-7497.

(203) Chueh, W. C.; Falter, C.; Abbott, M.; Scipio, D.; Furler, P.; Haile, S. M.; Steinfeld, A.: High-flux solar-driven thermochemical dissociation of CO_2 and H_2O using nonstoichiometric ceria. *Science* **2010**, *330*, 1797-1801.

(204) Chueh, W. C.; Haile, S. M.: A thermochemical study of ceria: exploiting an old material for new modes of energy conversion and CO_2 mitigation. *Philos. Trans. Royal Soc. A Math. Phys. Eng. Sci.* **2010**, *368*, 3269-3294.

(205) Furler, P.; Scheffe, J.; Steinfeld, A.: Two-step solar thermochemical cycle for splitting H_2O and CO_2 via ceria redox reactions: Experimental investigation with a 3 kW solar reactor. *Abstr. Pap. Am. Chem. Soc.* **2011**, *241*.

(206) Furler, P.; Scheffe, J. R.; Steinfeld, A.: Syngas production by simultaneous splitting of H_2O and CO_2 via ceria redox reactions in a high-temperature solar reactor. *Energy Environ. Sci.* **2012**, *5*, 6098-6103.

(207) Rager, T.: Re-evaluation of the efficiency of a ceria-based thermochemical cycle for solar fuel generation. *Chem. Commun.* **2012**, *48*, 10520-10522.

(208) Chueh, W. C.; Haile, S. M.: Ceria as a thermochemical reaction medium for selectively generating syngas or methane from H_2O and CO_2. *ChemSusChem* **2009**, *2*, 735-739.

(209) Abanades, S.; Flamant, G.: Thermochemical hydrogen production from a two-step solar-driven water-splitting cycle based on cerium oxides. *Sol. Energ.* **2006**, *80*, 1611-1623.

(210) Arifin, D.; Aston, V. J.; Liang, X.; McDaniel, A. H.; Weimer, A. W.: $CoFe_2O_4$ on a porous Al_2O_3 nanostructure for solar thermochemical CO_2 splitting. *Energy Environ. Sci.* **2012**, *5*, 9438-9443.

(211) McDaniel, A. H.; Miller, E. C.; Arifin, D.; Ambrosini, A.; Coker, E. N.; O'Hayre, R.; Chueh, W. C.; Tong, J.: Sr- and Mn-doped $LaAlO_{3-\delta}$ for solar thermochemical H_2 and CO production. *Energy Environ. Sci.* **2013**, *6*, 2424-2428.

(212) Scheffe, J. R.; Weibel, D.; Steinfeld, A.: Lanthanum–strontium–manganese perovskites as redox materials for solar thermochemical splitting of H_2O and CO_2. *Energy Fuels* **2013**, *27*, 4250-4257.

(213) Panlener, R. J.; Blumenthal, R. N.; Garnier, J. E.: A thermodynamic study of nonstoichiometric cerium dioxide. *J. Phys. Chem. Solids* **1975**, *36*, 1213-1222.

(214) Ahn, K.; Chung, Y.-C.; Yoon, K.; Son, J.-W.; Kim, B.-K.; Lee, H.-W.; Lee, J.-H.: Lattice-strain effect on oxygen vacancy formation in gadolinium-doped ceria. *J. Electroceram.* **2013**, 1-6.

(215) Lu, Z.; Yang, Z.; He, B.; Castleton, C.; Hermansson, K.: Cu-doped ceria: oxygen vacancy formation made easy. *Chem. Phys. Lett.* **2011**, *510*, 60-66.

(216) Nolan, M.: Enhanced oxygen vacancy formation in ceria (111) and (110) surfaces doped with divalent cations. *J. Mater. Chem.* **2011**, *21*, 9160-9168.

(217) Suresh, B.; Ranjith, T.; Talgat, I.; Richard, D.; Artëm, E. M.; Alfons, S.; Sudipta, S.: Dopant-mediated oxygen vacancy tuning in ceria nanoparticles. *Nanotechnology* **2009**, *20*, 085713.

(218) Le Gal, A.; Abanades, S.: Catalytic investigation of ceria-zirconia solid solutions for solar hydrogen production. *Int. J. Hydrogen Energy* **2011**, *36*, 4739-4748.

(219) Le Gal, A.; Abanades, S.: Dopant incorporation in ceria for enhanced water-splitting activity during solar thermochemical hydrogen generation. *J. Phys. Chem. C* **2012**, *116*, 13516-13523.

(220) Mulmi, S.; Chen, H.; Hassan, A.; Marco, J. F.; Berry, F. J.; Sharif, F.; Slater, P. R.; Roberts, E. P. L.; Adams, S.; Thangadurai, V.: Thermochemical CO_2 splitting using double perovskite-type $Ba_2Ca_{0.66}Nb_{1.34-x}Fe_xO_{6-\delta}$. *J. Mater. Chem. A* **2017**, *5*, 6874-6883.

(221) Rao, C. N. R.; Lingampalli, S. R.; Dey, S.; Roy, A.: Solar photochemical and thermochemical splitting of water. *Philos. Trans. Royal Soc. A Math. Phys. Eng. Sci.* **2016**, *374*.

(222) Peña, M. A.; Fierro, J. L. G.: Chemical structures and performance of perovskite oxides. *Chem. Rev.* **2001**, *101*, 1981-2018.

(223) Oishi, M.; Yashiro, K.; Sato, K.; Mizusaki, J.; Kawada, T.: Oxygen nonstoichiometry and defect structure analysis of B-site mixed perovskite-type oxide (La, Sr)(Cr, M)$O_{3-\delta}$ (M=Ti, Mn and Fe). *J. Solid State Chem.* **2008**, *181*, 3177-3184.

(224) Kuhn, M.; Hashimoto, S.; Sato, K.; Yashiro, K.; Mizusaki, J.: Oxygen nonstoichiometry, thermo-chemical stability and lattice expansion of $La_{0.6}Sr_{0.4}FeO_{3-\delta}$. *Solid State Ion.* **2011**, *195*, 7-15.

(225) Mizusaki, J.; Mori, N.; Takai, H.; Yonemura, Y.; Minamiue, H.; Tagawa, H.; Dokiya, M.; Inaba, H.; Naraya, K.; Sasamoto, T.; Hashimoto, T.: Oxygen nonstoichiometry and defect equilibrium in the perovskite-type oxides $La_{1-x}Sr_xMnO_{3+\delta}$. *Solid State Ion.* **2000**, *129*, 163-177.

(226) Onuma, S.; Yashiro, K.; Miyoshi, S.; Kaimai, A.; Matsumoto, H.; Nigara, Y.; Kawada, T.; Mizusaki, J.; Kawamura, K.; Sakai, N.; Yokokawa, H.: Oxygen nonstoichiometry of the perovskite-type oxide $La_{1-x}Ca_xCrO_{3-\delta}$ (x=0.1, 0.2, 0.3). *Solid State Ion.* **2004**, *174*, 287-293.

(227) Kuhn, M.; Fukuda, Y.; Hashimoto, S.; Sato, K.; Yashiro, K.; Mizusaki, J.: Oxygen nonstoichiometry and thermo-chemical stability of perovskite-type $La_{0.6}Sr_{0.4}Co_{1-y}Fe_yO_{3-\delta}$ (y = 0, 0.2, 0.4, 0.5, 0.6, 0.8, 1) materials. *J. Electrochem. Soc.* **2013**, *160*, F34-F42.

(228) Kanai, H.; Mizusaki, J.; Tagawa, H.; Hoshiyama, S.; Hirano, K.; Fujita, K.; Tezuka, M.; Hashimoto, T.: Defect chemistry of $La_{2-x}Sr_xCuO_{4-\delta}$: Oxygen nonstoichiometry and thermodynamic stability. *J. Solid State Chem.* **1997**, *131*, 150-159.

(229) Nakamura, T.; Yashiro, K.; Sato, K.; Mizusaki, J.: Oxygen nonstoichiometry and chemical stability of $Nd_{2-x}Sr_xNiO_{4+\delta}$. *J. Solid State Chem.* **2009**, *182*, 1533-1537.

(230) Nakamura, T.; Yashiro, K.; Sato, K.; Mizusaki, J.: Oxygen nonstoichiometry and defect equilibrium in $La_{2-x}Sr_xNiO_{4+\delta}$. *Solid State Ion.* **2009**, *180*, 368-376.

(231) Jiang, S.: Development of lanthanum strontium manganite perovskite cathode materials of solid oxide fuel cells: a review. *J. Mater. Sci.* **2008**, *43*, 6799-6833.

(232) Siegel, N. P.; Miller, J. E.; Ermanoski, I.; Diver, R. B.; Stechel, E. B.: Factors affecting the efficiency of solar driven metal oxide thermochemical cycles. *Ind. Eng. Chem. Res.* **2013**, *52*, 3276-3286.

(233) Ivy, J. "Summary of electrolytic hydrogen production," National Renewable Energy Laboratory, 2004.

(234) Kolb, G. J. H., C. K.
Mancini, T. R.
Gary, J. A. "Screening analysis of solar thermochemical hydrogen concepts," Sandia National Laboratories, 2011.

(235) Miller, J. E.; McDaniel, A. H.; Allendorf, M. D.: Considerations in the design of materials for solar-driven fuel production using metal-oxide thermochemical cycles. *Adv. Energy Mater.* **2014**, *4*, 1300469-n/a.

(236) Allendorf, M. D.; Miller, J. E.; McDaniel, A.: Design of materials for solar-driven fuel production by metal-oxide thermochemical cycles. *Electrochem. Soc. Interface* **2013**, *22*, 63-68.

(237) Perret, R. "Solar thermochemical hydrogen production research: thermochemical cycle selection and investment priority," Sandia National Laboratories, 2011.

(238) "Short-Term Energy Outlook," US Energy Information Administration, 2017.

(239) "Annual Energy Outlook 2017," US Energy Information Administration, 2017.

(240) Saha, D.; Grappe, H. A.; Chakraborty, A.; Orkoulas, G.: Postextraction separation, on-board storage, and catalytic conversion of methane in natural gas: a review. *Chem. Rev.* **2016**, *116*, 11436-11499.

(241) Schwach, P.; Pan, X.; Bao, X.: Direct conversion of methane to value-added chemicals over heterogeneous catalysts: challenges and prospects. *Chem. Rev.* **2017**, *117*, 8497-8520.

(242) Appl, M.: Ammonia, 2. Production Processes. In *Ullmann's Encyclopedia of Industrial Chemistry*; Wiley-VCH Verlag GmbH & Co. KGaA, 2000.

(243) Franke, R.; Selent, D.; Börner, A.: Applied hydroformylation. *Chem. Rev.* **2012**, *112*, 5675-5732.

(244) Zhen, X.; Wang, Y.: An overview of methanol as an internal combustion engine fuel. *Renew. Sustainable Energy Rev.* **2015**, *52*, 477-493.

(245) Hader, R. N.; Wallace, R. D.; McKinney, R. W.: Formaldehyde from methanol. *Ind. Eng. Chem.* **1952**, *44*, 1508-1518.

(246) Maitlis, P. M.; Haynes, A.; Sunley, G. J.; Howard, M. J.: Methanol carbonylation revisited: thirty years on. *J. Chem. Soc. Dalton Trans.* **1996**, 2187-2196.

(247) Keil, F. J.: Methanol-to-hydrocarbons: process technology. *Micropor. Mesopor. Mater.* **1999**, *29*, 49-66.

(248) Tian, P.; Wei, Y.; Ye, M.; Liu, Z.: Methanol to olefins (MTO): from fundamentals to commercialization. *ACS Catal.* **2015**, *5*, 1922-1938.

(249) Nicholas, C. P.: Applications of light olefin oligomerization to the production of fuels and chemicals. *Appl. Catal. A Gen.* **2017**, *543*, 82-97.

(250) Kwapien, K.; Paier, J.; Sauer, J.; Geske, M.; Zavyalova, U.; Horn, R.; Schwach, P.; Trunschke, A.; Schlögl, R.: Sites for methane activation on lithium-doped magnesium oxide surfaces. *Angew. Chem. Int. Ed.* **2014**, *53*, 8774-8778.

(251) Labinger, J. A.; Bercaw, J. E.: Understanding and exploiting C-H bond activation. *Nature* **2002**, *417*, 507-514.

(252) Stahl, S. S.; Labinger, J. A.; Bercaw, J. E.: Homogeneous oxidation of alkanes by electrophilic late transition metals. *Angew. Chem. Int. Ed.* **1998**, *37*, 2180-2192.

(253) Janowicz, A. H.; Bergman, R. G.: Carbon-hydrogen activation in completely saturated hydrocarbons: direct observation of M + R-H → M(R)(H). *J. Am. Chem. Soc.* **1982**, *104*, 352-354.

(254) Caballero, A.; Perez, P. J.: Methane as raw material in synthetic chemistry: the final frontier. *Chem. Soc. Rev.* **2013**, *42*, 8809-8820.

(255) Olivos-Suarez, A. I.; Szécsényi, À.; Hensen, E. J. M.; Ruiz-Martinez, J.; Pidko, E. A.; Gascon, J.: Strategies for the direct catalytic valorization of methane using heterogeneous catalysis: challenges and opportunities. *ACS Catal.* **2016**, *6*, 2965-2981.

(256) Rostrup-Nielsen, J. R.: Production of synthesis gas. *Catal. Today* **1993**, *18*, 305-324.

(257) Baltrusaitis, J.; Luyben, W. L.: Methane conversion to syngas for gas-to-liquids (GTL): Is sustainable CO_2 reuse via dry methane reforming (DMR) cost competitive with SMR and ATR processes? *ACS Sustainable Chem. Eng.* **2015**, *3*, 2100-2111.

(258) Aasberg-Petersen, K.; Dybkjær, I.; Ovesen, C. V.; Schjødt, N. C.; Sehested, J.; Thomsen, S. G.: Natural gas to synthesis gas – catalysts and catalytic processes. *J. Nat. Gas Sci. Eng.* **2011**, *3*, 423-459.

(259) Feng, W.; Knopf, F. C.; Dooley, K. M.: Effects of pressure, third bodies, and temperature profiling on the noncatalytic partial oxidation of methane. *Energy Fuels* **1994**, *8*, 815-822.

(260) Zhang, Q.; He, D.; Zhu, Q.: Recent progress in direct partial oxidation of methane to methanol. *J. Nat. Gas Chem.* **2003**, *12*, 81-89.

(261) Rasmussen, C. L.; Glarborg, P.: Direct partial oxidation of natural gas to liquid chemicals: chemical kinetic modeling and global optimization. *Ind. Eng. Chem. Res.* **2008**, *47*, 6579-6588.

(262) Otsuka, K.; Wang, Y.: Direct conversion of methane into oxygenates. *Appl. Catal. A Gen.* **2001**, *222*, 145-161.

(263) Hunter, N. R.; Gesser, H. D.; Morton, L. A.; Yarlagadda, P. S.; Fung, D. P. C.: Methanol formation at high pressure by the catalyzed oxidation of natural gas and by the sensitized oxidation of methane. *Appl. Catal.* **1990**, *57*, 45-54.

(264) Lyons, J. E.; Ellis, P. E.; Durante, V. A.: Active iron oxo centers for the selective catalytic oxidation of alkanes. *Stud. Surf. Sci. Catal.* **1991**, *67*, 99-116.

(265) Hargreaves, J. S. J.; Hutchings, G. J.; Joyner, R. W.; Taylor, S. H.: Methane partial oxidation to methanol over Ga_2O_3-based catalysts: use of the CH_4/D_2 exchange reaction as a design tool. *Chem. Commun.* **1996**, 523-524.

(266) Stiles, A. B.; Chen, F.; Harrison, J. B.; Hu, X.; Storm, D. A.; Yang, H. X.: Catalytic conversion of synthesis gas to methanol and other oxygenated products. *Ind. Eng. Chem. Res.* **1991**, *30*, 811-821.

(267) Da Silva, M. J.: Synthesis of methanol from methane: challenges and advances on the multi-step (syngas) and one-step routes (DMTM). *Fuel Process. Technol.* **2016**, *145*, 42-61.

(268) Kuo, J. C. W.; Kresge, C. T.; Palermo, R. E.: Evaluation of direct methane conversion to higher hydrocarbons and oxygenates. *Catal. Today* **1989**, *4*, 463-470.

(269) Lunsford, J. H.: The catalytic oxidative coupling of methane. *Angew. Chem. Int. Ed.* **1995**, *34*, 970-980.

(270) Thomas, J. M.; Ueda, W.; Williams, J.; Harris, K. D. M.: New families of catalysts for the selective oxidation of methane. *Faraday Discuss. Chem. Soc.* **1989**, *87*, 33-45.

(271) Zavyalova, U.; Holena, M.; Schlögl, R.; Baerns, M.: Statistical analysis of past catalytic data on oxidative methane coupling for new insights into the composition of high-performance catalysts. *ChemCatChem* **2011**, *3*, 1935-1947.

(272) Michorczyk, P.; Ogonowski, J.; Zeńczak, K.: Activity of chromium oxide deposited on different silica supports in the dehydrogenation of propane with CO_2 – a comparative study. *J. Mol. Catal. A Chem.* **2011**, *349*, 1-12.

(273) Weckhuysen, B. M.; Verberckmoes, A. A.; Debaere, J.; Ooms, K.; Langhans, I.; Schoonheydt, R. A.: In situ UV–vis diffuse reflectance spectroscopy — on line activity measurements of supported chromium oxide catalysts: relating isobutane dehydrogenation activity with Cr-speciation via experimental design. *J. Mol. Catal. A Chem.* **2000**, *151*, 115-131.

(274) Agrafiotis, C.; Block, T.; Senholdt, M.; Tescari, S.; Roeb, M.; Sattler, C.: Exploitation of thermochemical cycles based on solid oxide redox systems for thermochemical storage of solar heat. Part 6: testing of Mn-based combined oxides and porous structures. *Sol. Energ.* **2017**, *149*, 227-244.

(275) Nawaz, Z.: Light alkane dehydrogenation to light olefin technologies: a comprehensive review. In *Rev. Chem. Eng.*, 2015; Vol. 31; pp 413.

(276) Li, Z.; Peters, A. W.; Bernales, V.; Ortuño, M. A.; Schweitzer, N. M.; DeStefano, M. R.; Gallington, L. C.; Platero-Prats, A. E.; Chapman, K. W.; Cramer, C. J.; Gagliardi, L.; Hupp, J. T.; Farha, O. K.: Metal–organic framework supported cobalt catalysts for the oxidative dehydrogenation of propane at low temperature. *ACS Cent. Sci.* **2017**, *3*, 31-38.

(277) Xiao, D. J.; Bloch, E. D.; Mason, J. A.; Queen, W. L.; Hudson, M. R.; Planas, N.; Borycz, J.; Dzubak, A. L.; Verma, P.; Lee, K.; Bonino, F.; Crocellà, V.; Yano, J.; Bordiga, S.; Truhlar, D. G.; Gagliardi, L.; Brown, C. M.; Long, J. R.: Oxidation of ethane to ethanol by N_2O in a metal–organic framework with coordinatively unsaturated iron(II) sites. *Nat. Chem.* **2014**, *6*, 590-595.

(278) Phan, A.; Czaja, A. U.; Gándara, F.; Knobler, C. B.; Yaghi, O. M.: Metal–organic frameworks of vanadium as catalysts for conversion of methane to acetic acid. *Inorg. Chem.* **2011**, *50*, 7388-7390.

(279) Ikuno, T.; Zheng, J.; Vjunov, A.; Sanchez-Sanchez, M.; Ortuño, M. A.; Pahls, D. R.; Fulton, J. L.; Camaioni, D. M.; Li, Z.; Ray, D.; Mehdi, B. L.; Browning, N. D.; Farha, O. K.; Hupp, J. T.; Cramer, C. J.; Gagliardi, L.; Lercher, J. A.: Methane oxidation to methanol catalyzed by Cu-oxo clusters stabilized in NU-1000 metal–organic framework. *J. Am. Chem. Soc.* **2017**.

(280) Meunier, B.; de Visser, S. P.; Shaik, S.: Mechanism of oxidation reactions catalyzed by cytochrome P450 enzymes. *Chem. Rev.* **2004**, *104*, 3947-3980.

(281) Comito, R. J.; Fritzsching, K. J.; Sundell, B. J.; Schmidt-Rohr, K.; Dincă, M.: Single-site heterogeneous catalysts for olefin polymerization enabled by cation exchange in a metal-organic framework. *J. Am. Chem. Soc.* **2016**, *138*, 10232-10237.

(282) Junghans, U.; Suttkus, C.; Lincke, J.; Lassig, D.; Krautscheid, H.; Glaser, R.: Selective oxidation of cyclooctene over copper-containing metal-organic frameworks. *Micropor. Mesopor. Mater.* **2015**, *216*, 151-160.

(283) Li, Z.; Peters, A. W.; Liu, J.; Zhang, X.; Schweitzer, N. M.; Hupp, J. T.; Farha, O. K.: Size effect of the active sites in UiO-66-supported nickel catalysts synthesized via atomic layer deposition for ethylene hydrogenation. *Inorg. Chem. Front.* **2017**, *4*, 820-824.

(284) Yang, D.; Odoh, S. O.; Wang, T. C.; Farha, O. K.; Hupp, J. T.; Cramer, C. J.; Gagliardi, L.; Gates, B. C.: Metal-organic framework nodes as nearly ideal supports for molecular catalysts: NU-1000- and UiO-66-supported iridium complexes. *J. Am. Chem. Soc.* **2015**, *137*, 7391-7396.

(285) Dhakshinamoorthy, A.; Asiri, A. M.; Garcia, H.: Metal-organic frameworks catalyzed C-C and C-heteroatom coupling reactions. *Chem. Soc. Rev.* **2015**, *44*, 1922-1947.

(286) Stephenson, C. J.; Hupp, J. T.; Farha, O. K.: Pt@ZIF-8 composite for the regioselective hydrogenation of terminal unsaturations in 1,3-dienes and alkynes. *Inorg. Chem. Front.* **2015**, *2*, 448-452.

(287) Van Vu, T.; Kosslick, H.; Schulz, A.; Harloff, J.; Paetzold, E.; Schneider, M.; Radnik, J.; Steinfeldt, N.; Fulda, G.; Kragl, U.: Selective hydroformylation of olefins over the rhodium supported large porous metal–organic framework MIL-101. *Appl. Catal. A Gen.* **2013**, *468*, 410-417.

(288) Zhao, H.; Song, H.; Xu, L.; Chou, L.: Isobutane dehydrogenation over the mesoporous Cr_2O_3/Al_2O_3 catalysts synthesized from a metal-organic framework MIL-101. *Appl. Catal. A Gen.* **2013**, *456*, 188-196.

(289) Havran, V.; Duduković, M. P.; Lo, C. S.: Conversion of methane and carbon dioxide to higher value products. *Ind. Eng. Chem. Res.* **2011**, *50*, 7089-7100.

(290) Nguyen, V. N.; Blum, L.: Syngas and synfuels from H_2O and CO_2: current status. *Chem. Ing. Tech.* **2015**, *87*, 354-375.

(291) Furler, P.; Scheffe, J.; Gorbar, M.; Moes, L.; Vogt, U.; Steinfeld, A.: Solar thermochemical CO_2 splitting utilizing a reticulated porous ceria redox system. *Energy Fuels* **2012**, *26*, 7051-7059.

(292) Le Gal, A.; Abanades, S.; Flamant, G.: CO_2 and H_2O splitting for thermochemical production of solar fuels using nonstoichiometric ceria and ceria/zirconia solid solutions. *Energy Fuels* **2011**, *25*, 4836-4845.

(293) Rudisill, S. G.; Venstrom, L. J.; Petkovich, N. D.; Quan, T.; Hein, N.; Boman, D. B.; Davidson, J. H.; Stein, A.: Enhanced oxidation kinetics in thermochemical cycling of CeO_2 through templated porosity. *J. Phys. Chem. C* **2012**, *117*, 1692-1700.

(294) Venstrom, L. J.; Petkovich, N.; Rudisill, S.; Stein, A.; Davidson, J. H.: The effects of morphology on the oxidation of ceria by water and carbon dioxide. *J. Solar Energy Eng.* **2011**, *134*, 011005-011005.

(295) Furler, P.; Scheffe, J.; Marxer, D.; Gorbar, M.; Bonk, A.; Vogt, U.; Steinfeld, A.: Thermochemical CO_2 splitting via redox cycling of ceria reticulated foam structures with dual-scale porosities. *Phys. Chem. Chem. Phys.* **2014**, *16*, 10503-10511.

(296) Lu, K.; Li, W.; Chen, B.: Sintering of porous materials. In *Sintering*; Castro, R., Benthem, K., Eds.; Springer Berlin Heidelberg, 2013; Vol. 35; pp 115-136.

(297) Nakano, J.: *Recent progress in wood chemistry - fundamentals and applications*. Horwood, 1987; pp 499-512.

(298) Plötze, M.; Niemz, P.: Porosity and pore size distribution of different wood types as determined by mercury intrusion porosimetry. *Eur. J. Wood Wood Prod.* **2011**, *69*, 649-657.

(299) Sun, B.; Fan, T.; Zhang, D.: Porous TiC ceramics derived from wood template. *J. Porous Mater.* **2002**, *9*, 275-277.

(300) Esposito, L.; Sciti, D.; Piancastelli, A.; Bellosi, A.: Microstructure and properties of porous ß-SiC templated from soft woods. *J. Euro. Ceram. Soc.* **2004**, *24*, 533-540.

(301) Wang, L.-Q.; Shin, Y.; Samuels, W. D.; Exarhos, G. J.; Moudrakovski, I. L.; Terskikh, V. V.; Ripmeester, J. A.: Magnetic resonance studies of hierarchically ordered replicas of wood cellular structures prepared by surfactant-mediated mineralization. *J. Phys. Chem. B* **2003**, *107*, 13793-13802.

(302) Wang, T.-C.; Fan, T.-X.; Zhang, D.; Zhang, G.-D.; Xiong, D.-S.: Thermal conductivity and thermal expansions of aluminum/carbon composites based on wood templates. *Mater. Lett.* **2007**, *61*, 1849-1854.

(303) Zhu, Y.; Zhu, Z.; Chen, Y.; Yang, F.; Qin, H.; Xie, L.: Kinetics and thermodynamics of sorption for As(V) on the porous biomorph-genetic composite of α-Fe_2O_3/Fe_3O_4/C with eucalyptus wood hierarchical microstructure. *Water Air Soil Pollut.* **2013**, *224*, 1-19.

(304) Onyestyak, G.: Pinewood char templated mordenite/carbon honeycomb composite. *New J. Chem.* **2006**, *30*, 1058-1064.

(305) Dong, A.; Wang, Y.; Tang, Y.; Ren, N.; Zhang, Y.; Yue, Y.; Gao, Z.: Zeolitic tissue through wood cell templating. *Adv. Mater.* **2002**, *14*, 926-929.

(306) Fan, T.; Li, X.; Liu, Z.; Gu, J.; Zhang, D.; Guo, Q.: Microstructure and infrared absorption of biomorphic chromium oxides templated by wood tissues. *J. Am. Ceram. Soc.* **2006**, *89*, 3511-3515.

(307) Liu, Z.; Fan, T.; Zhang, D.; Gong, X.; Xu, J.: Hierarchically porous ZnO with high sensitivity and selectivity to H_2S derived from biotemplates. *Sens. Actuators B Chem.* **2009**, *136*, 499-509.

(308) Petkovich, N. D.; Rudisill, S. G.; Venstrom, L. J.; Boman, D. B.; Davidson, J. H.; Stein, A.: Control of heterogeneity in nanostructured $Ce_{1-x}Zr_xO_2$ binary oxides for enhanced thermal stability and water splitting activity. *J. Phys. Chem. C* **2011**, *115*, 21022-21033.

(309) Gibbons, W. T.; Venstrom, L. J.; De Smith, R. M.; Davidson, J. H.; Jackson, G. S.: Ceria-based electrospun fibers for renewable fuel production via two-step thermal redox cycles for carbon dioxide splitting. *Phys. Chem. Chem. Phys.* **2014**, *16*, 14271-14280.

(310) Bulfin, B.; Lowe, A. J.; Keogh, K. A.; Murphy, B. E.; Lübben, O.; Krasnikov, S. A.; Shvets, I. V.: Analytical model of CeO_2 oxidation and reduction. *J. Phys. Chem. C* **2013**, *117*, 24129-24137.

(311) Lin, J.; Yu, M.; Lin, C.; Liu, X.: Multiform oxide optical materials via the versatile Pechini-type sol−gel process: Synthesis and characteristics. *J. Phys. Chem. C* **2007**, *111*, 5835-5845.

(312) Thomas, J. M.; Raja, R.; Lewis, D. W.: Single-site heterogeneous catalysts. *Angew. Chem. Int. Ed.* **2005**, *44*, 6456-6482.

(313) Liang, S.; Hao, C.; Shi, Y.: The power of single-atom catalysis. *ChemCatChem* **2015**, *7*, 2559-2567.

(314) Vilé, G.; Albani, D.; Nachtegaal, M.; Chen, Z.; Dontsova, D.; Antonietti, M.; López, N.; Pérez-Ramírez, J.: A stable single-site palladium catalyst for hydrogenations. *Angew. Chem. Int. Ed.* **2015**, *54*, 11265-11269.

(315) Hu, B.; Schweitzer, N. M.; Zhang, G.; Kraft, S. J.; Childers, D. J.; Lanci, M. P.; Miller, J. T.; Hock, A. S.: Isolated Fe^{II} on silica as a selective propane dehydrogenation catalyst. *ACS Catal.* **2015**, *5*, 3494-3503.

(316) Dal Santo, V.; Guidotti, M.; Psaro, R.; Marchese, L.; Carniato, F.; Bisio, C.: Rational Design of Single-Site Heterogeneous Catalysts: Towards High Chemo-, Regio- and Stereoselectivity. *Proc. R. Soc. London A* **2012**, *468*, 1904-1926.

(317) Guo, X.; Fang, G.; Li, G.; Ma, H.; Fan, H.; Yu, L.; Ma, C.; Wu, X.; Deng, D.; Wei, M.; Tan, D.; Si, R.; Zhang, S.; Li, J.; Sun, L.; Tang, Z.; Pan, X.; Bao, X.: Direct, Non-oxidative Conversion of Methane to Ethylene, Aromatics, and Hydrogen. *Science* **2014**, *344*, 616-619.

(318) Yilmaz, B.; Müller, U.: Catalytic applications of zeolites in chemical industry. *Top. Catal.* **2009**, *52*, 888-895.

(319) Ferey, G.: Hybrid porous solids: past, present, future. *Chem. Soc. Rev.* **2008**, *37*, 191-214.

(320) Horike, S.; Shimomura, S.; Kitagawa, S.: Soft porous crystals. *Nat. Chem.* **2009**, *1*, 695-704.

(321) Farha, O. K.; Hupp, J. T.: Rational design, synthesis, purification, and activation of metal−organic framework materials. *Acc. Chem. Res.* **2010**, *43*, 1166-1175.

(322) Zhao, M.; Ou, S.; Wu, C.-D.: Porous metal–organic frameworks for heterogeneous biomimetic catalysis. *Acc. Chem. Res.* **2014**, *47*, 1199-1207.

(323) Deria, P.; Mondloch, J. E.; Karagiaridi, O.; Bury, W.; Hupp, J. T.; Farha, O. K.: Beyond post-synthesis modification: evolution of metal-organic frameworks via building block replacement. *Chem. Soc. Rev.* **2014**, *43*, 5896-5912.

(324) Gotthardt, M. A.; Schoch, R.; Brunner, T. S.; Bauer, M.; Kleist, W.: Design of highly porous single-site catalysts through two-step postsynthetic modification of mixed-linker MIL-53(Al). *ChemPlusChem* **2015**, *80*, 188-195.

(325) Kim, I. S.; Farha, O. K.; Hupp, J. T.; Gagliardi, L.; Chapman, K. W.; Cramer, C.; Martinson, A. B. F.: A precise and scalable post-modification of mesoporous metal-organic framework NU-1000 via atomic layer deposition. *ECS Trans.* **2016**, *75*, 93-99.

(326) Liu, J.; Lukose, B.; Shekhah, O.; Arslan, H. K.; Weidler, P.; Gliemann, H.; Bräse, S.; Grosjean, S.; Godt, A.; Feng, X.; Müllen, K.; Magdau, I.-B.; Heine, T.; Wöll, C.: A Novel Series of Isoreticular Metal-Organic Frameworks: Realizing Metastable Structures by Liquid Phase Epitaxy. *Sci. Rep.* **2012**, *2*, 921.

(327) Alaerts, L.; Séguin, E.; Poelman, H.; Thibault-Starzyk, F.; Jacobs, P. A.; De Vos, D. E.: Probing the Lewis acidity and catalytic activity of the metal–organic framework $[Cu_3(btc)_2]$ (BTC=benzene-1,3,5-tricarboxylate). *Chem. Eur. J.* **2006**, *12*, 7353-7363.

(328) LeValley, T. L.; Richard, A. R.; Fan, M.: The progress in water gas shift and steam reforming hydrogen production technologies – a review. *Int. J. Hydrogen Energy* **2014**, *39*, 16983-17000.

(329) Hall, A. S.; Kondo, A.; Maeda, K.; Mallouk, T. E.: Microporous brookite-phase titania made by replication of a metal–organic framework. *J. Am. Chem. Soc.* **2013**, *135*, 16276-16279.

(330) Leong, K.; Foster, M. E.; Wong, B. M.; Spoerke, E. D.; Van Gough, D.; Deaton, J. C.; Allendorf, M. D.: Energy and charge transfer by donor-acceptor pairs confined in a metal-organic framework: a spectroscopic and computational investigation. *J. Mater. Chem. A* **2014**, *2*, 3389-3398.

(331) Lu, C.; Ben, T.; Xu, S.; Qiu, S.: Electrochemical synthesis of a microporous conductive polymer based on a metal-organic framework thin film. *Angew. Chem. Int. Ed.* **2014**, *53*, 6454-6458.

(332) Sabo, M.; Henschel, A.; Frode, H.; Klemm, E.; Kaskel, S.: Solution infiltration of palladium into MOF-5: synthesis, physisorption and catalytic properties. *J. Mater. Chem.* **2007**, *17*, 3827-3832.

(333) Talin, A. A.; Centrone, A.; Ford, A. C.; Foster, M. E.; Stavila, V.; Haney, P.; Kinney, R. A.; Szalai, V.; El Gabaly, F.; Yoon, H. P.; Léonard, F.; Allendorf, M. D.: Tunable Electrical Conductivity in Metal-Organic Framework Thin-Film Devices. *Science* **2014**, *343*, 66-69.

(334) Kleitz, F.; Hei Choi, S.; Ryoo, R.: Cubic Ia3d large mesoporous silica: synthesis and replication to platinum nanowires, carbon nanorods and carbon nanotubes. *Chem. Commun.* **2003**, 2136-2137.

(335) Macrae, C. F.; Edgington, P. R.; McCabe, P.; Pidcock, E.; Shields, G. P.; Taylor, R.; Towler, M.; van de Streek, J.: Mercury: visualization and analysis of crystal structures. *J. Appl. Crystallogr.* **2006**, *39*, 453-457.

(336) Jennings, G.: *QXRD*. 0.11.10 ed.: Argonne National Laboratory.

(337) Hammersley, A. P.; Svensson, S. O.; Hanfland, M.; Fitch, A. N.; Hausermann, D.: Two-dimensional detector software: from real detector to idealised image or two-theta scan. *High Pressure Res.* **1996**, *14*, 235-248.

(338) Yakovenko, A. A.; Reibenspies, J. H.; Bhuvanesh, N.; Zhou, H.-C.: Generation and applications of structure envelopes for porous metal-organic frameworks. *J. Appl. Crystallogr.* **2013**, *46*, 346-353.

(339) Yakovenko, A. A.; Wei, Z.; Wriedt, M.; Li, J.-R.; Halder, G. J.; Zhou, H.-C.: Study of guest molecules in metal–organic frameworks by powder X-ray diffraction: analysis of difference envelope density. *Cryst. Growth Des.* **2014**, *14*, 5397-5407.

(340) Le Bail, A.: Modelling the silica glass structure by the Rietveld method. *J. Non-Cryst. Solids* **1995**, *183*, 39-42.

(341) Petříček, V.; Dušek, M.; Palatinus, L.: Crystallographic computing system JANA2006: general features. *Z. Kristallogr.* **2014**, *229*, 345-352.

(342) Wojdyr, M.: Fityk: a general-purpose peak fitting program. *J. App. Crystallogr.* **2010**, *43*, 1126-1128.

(343) McCusker, L. B.; Baerlocher, C.: Using electron microscopy to complement X-ray powder diffraction data to solve complex crystal structures. *Chem. Commun.* **2009**, 1439-1451.

(344) Qiu, X.; Thompson, J. W.; Billinge, S. J. L.: PDFgetX2: a GUI-driven program to obtain the pair distribution function from X-ray powder diffraction data. *J. Appl. Crystallogr.* **2004**, *37*, 678.

(345) Zaki, M. I.; Hasan, M. A.; Al-Sagheer, F. A.; Pasupulety, L.: In situ FTIR spectra of pyridine adsorbed on SiO_2–Al_2O_3, TiO_2, ZrO_2 and CeO_2: general considerations for the identification of acid sites on surfaces of finely divided metal oxides. *Colloid Surf. A* **2001**, *190*, 261-274.

(346) Kline, C. H.; Turkevich, J.: The vibrational spectrum of pyridine and the thermodynamic properties of pyridine vapors. *J. Chem. Phys.* **1944**, *12*, 300-309.

(347) Bagshaw, S. A.; Cooney, R. P.: FTIR surface site analysis of pillared clays using pyridine probe species. *Chem. Mater.* **1993**, *5*, 1101-1109.

(348) Rosenberg, D. J.; Anderson, J. A.: On determination of acid site densities on sulfated oxides. *Catal. Lett.*, *83*, 59-63.

(349) Ren, L.; Guo, Q.; Kumar, P.; Orazov, M.; Xu, D.; Alhassan, S. M.; Mkhoyan, K. A.; Davis, M. E.; Tsapatsis, M.: Self-pillared, single-unit-cell Sn-MFI zeolite nanosheets and their use for glucose and lactose isomerization. *Angew. Chem. Int. Ed.* **2015**, *54*, 10848-10851.

(350) Saravanamurugan, S.; Paniagua, M.; Melero, J. A.; Riisager, A.: Efficient isomerization of glucose to fructose over zeolites in consecutive reactions in alcohol and aqueous media. *J. Am. Chem. Soc.* **2013**, *135*, 5246-5249.

(351) Farrusseng, D.; Aguado, S.; Pinel, C.: Metal–organic frameworks: opportunities for catalysis. *Angew. Chem. Int. Ed.* **2009**, *48*, 7502-7513.

(352) Chughtai, A. H.; Ahmad, N.; Younus, H. A.; Laypkov, A.; Verpoort, F.: Metal-organic frameworks: versatile heterogeneous catalysts for efficient catalytic organic transformations. *Chem. Soc. Rev.* **2015**, *44*, 6804-6849.

(353) Farha, O. K.; Eryazici, I.; Jeong, N. C.; Hauser, B. G.; Wilmer, C. E.; Sarjeant, A. A.; Snurr, R. Q.; Nguyen, S. T.; Yazaydın, A. Ö.; Hupp, J. T.: Metal–organic framework materials with ultrahigh surface areas: Is the sky the limit? *J. Am. Chem. Soc.* **2012**, *134*, 15016-15021.

(354) Furukawa, H.; Ko, N.; Go, Y. B.; Aratani, N.; Choi, S. B.; Choi, E.; Yazaydin, A. Ö.; Snurr, R. Q.; O'Keeffe, M.; Kim, J.; Yaghi, O. M.: Ultrahigh Porosity in Metal-Organic Frameworks. *Science* **2010**, *329*, 424-428.

(355) Kitagawa, S.; Kitaura, R.; Noro, S.-i.: Functional porous coordination polymers. *Angew. Chem. Int. Ed.* **2004**, *43*, 2334-2375.

(356) Zhou, H.-C.; Long, J. R.; Yaghi, O. M.: Introduction to metal–organic frameworks. *Chem. Rev.* **2012**, *112*, 673-674.

(357) Rimoldi, M.; Bernales, V.; Borycz, J.; Vjunov, A.; Gallington, L. C.; Platero-Prats, A. E.; Kim, I. S.; Fulton, J. L.; Martinson, A. B. F.; Lercher, J. A.; Chapman, K. W.; Cramer, C. J.; Gagliardi, L.; Hupp, J. T.; Farha, O. K.: Atomic layer deposition in a metal–organic framework: synthesis, characterization, and performance of a solid acid. *Chem. Mater.* **2017**.

(358) Hlatky, G. G.: Heterogeneous single-site catalysts for olefin polymerization. *Chem. Rev.* **2000**, *100*, 1347-1376.

(359) Mazzacano, T. J.; Mankad, N. P.: Base metal catalysts for photochemical C–H borylation that utilize metal–metal cooperativity. *J. Am. Chem. Soc.* **2013**, *135*, 17258-17261.

(360) Park, J.; Hong, S.: Cooperative bimetallic catalysis in asymmetric transformations. *Chem. Soc. Rev.* **2012**, *41*, 6931-6943.

(361) Serrano-Plana, J.; Garcia-Bosch, I.; Company, A.; Costas, M.: Structural and reactivity models for copper oxygenases: cooperative effects and novel reactivities. *Acc. Chem. Res.* **2015**, *48*, 2397-2406.

(362) Carboni, M.; Latour, J.-M.: Enzymes with an heterodinuclear iron–manganese active site: curiosity or necessity? *Coord. Chem. Rev.* **2011**, *255*, 186-202.

(363) Bender, G.; Pierce, E.; Hill, J. A.; Darty, J. E.; Ragsdale, S. W.: Metal centers in the anaerobic microbial metabolism of CO and CO2. *Metallomics* **2011**, *3*, 797-815.

(364) Thompson, A. B.; Pahls, D. R.; Bernales, V.; Gallington, L. C.; Malonzo, C. D.; Webber, T.; Tereniak, S. J.; Wang, T. C.; Desai, S. P.; Li, Z.; Kim, I. S.; Gagliardi, L.; Penn, R. L.; Chapman, K. W.; Stein, A.; Farha, O. K.; Hupp, J. T.; Martinson, A. B. F.; Lu, C. C.: Installing heterobimetallic cobalt–aluminum single sites on a metal-organic framework support. *Chem. Mater.* **2016**, *28*, 6753-6762.

(365) Malonzo, C. D.; Shaker, S. M.; Ren, L.; Prinslow, S. D.; Platero-Prats, A. E.; Gallington, L. C.; Borycz, J.; Thompson, A. B.; Wang, T. C.; Farha, O. K.; Hupp, J. T.; Lu, C. C.; Chapman, K. W.; Myers, J. C.; Penn, R. L.; Gagliardi, L.; Tsapatsis, M.; Stein, A.: Thermal stabilization of metal–organic framework-derived single-site catalytic clusters through nanocasting. *J. Am. Chem. Soc.* **2016**, *138*, 2739-2748.

(366) Tereniak, S. J.; Carlson, R. K.; Clouston, L. J.; Young, V. G.; Bill, E.; Maurice, R.; Chen, Y.-S.; Kim, H. J.; Gagliardi, L.; Lu, C. C.: Role of the metal in the bonding and properties of bimetallic complexes involving manganese, iron, and cobalt. *J. Am. Chem. Soc.* **2014**, *136*, 1842-1855.

(367) Frost, D. C.; McDowell, C. A.; Woolsey, I. S.: Evidence for multiplet splitting of 2p photoelectron lines of transition metal complexes. *Chem. Phys. Lett.* **1972**, *17*, 320-323.

(368) Frost, D. C.; McDowell, C. A.; Woolsey, I. S.: X-ray photoelectron spectra of cobalt compounds. *Mol. Phys.* **1974**, *27*, 1473-1489.

(369) Jia, A.; Lou, L.-L.; Zhang, C.; Zhang, Y.; Liu, S.: Selective oxidation of benzyl alcohol to benzaldehyde with hydrogen peroxide over alkali-treated ZSM-5 zeolite catalysts. *J. Mol. Catal. A Chem.* **2009**, *306*, 123-129.

(370) Ming-Lin, G.; Hui-Zhen, L.: Selective oxidation of benzyl alcohol to benzaldehyde with hydrogen peroxide over tetra-alkylpyridinium octamolybdate catalysts. *Green Chem.* **2007**, *9*, 421-423.

(371) Widegren, J. A.; Finke, R. G.: A review of the problem of distinguishing true homogeneous catalysis from soluble or other metal-particle heterogeneous catalysis under reducing conditions. *J. Mol. Catal. A Chem.* **2003**, *198*, 317-341.

(372) Pettinari, C.; Marchetti, F.; Mosca, N.; Tosi, G.; Drozdov, A.: Application of metal − organic frameworks. *Polymer Int.* **2017**, *66*, 731-744.

(373) Ricco, R.; Pfeiffer, C.; Sumida, K.; Sumby, C. J.; Falcaro, P.; Furukawa, S.; Champness, N. R.; Doonan, C. J.: Emerging applications of metal-organic frameworks. *CrystEngComm* **2016**, *18*, 6532-6542.

(374) Evans, J. D.; Sumby, C. J.; Doonan, C. J.: Post-synthetic metalation of metal-organic frameworks. *Chem. Soc. Rev.* **2014**, *43*, 5933-5951.

(375) Desai, S. P.; Malonzo, C. D.; Webber, T.; Duan, J.; Thompson, A. B.; Tereniak, S. J.; DeStefano, M. R.; Buru, C. T.; Li, Z.; Penn, R. L.; Farha, O. K.; Hupp, J. T.; Stein, A.; Lu, C. C.: Assembly of dicobalt and cobalt-aluminum oxide clusters on metal-organic framework and nanocast silica supports. *Faraday Discuss.* **2017**.

(376) U.S. Energy Information Administration, What are Greenhouse Gases?, http://www.eia.gov/oiaf/1605/ggccebro/chapter1.html, April 2, 2004.

(377) Finiels, A.; Fajula, F.; Hulea, V.: Nickel-based solid catalysts for ethylene oligomerization - a review. *Catalysis Science & Technology* **2014**, *4*, 2412-2426.

(378) Li, Z.; Schweitzer, N. M.; League, A. B.; Bernales, V.; Peters, A. W.; Getsoian, A. B.; Wang, T. C.; Miller, J. T.; Vjunov, A.; Fulton, J. L.; Lercher, J. A.; Cramer, C. J.; Gagliardi, L.; Hupp, J. T.; Farha, O. K.: Sintering-resistant single-site nickel catalyst supported by metal–organic framework. *J. Am. Chem. Soc.* **2016**, *138*, 1977-1982.

(379) Resasco, D. E.; Marcus, B. K.; Huang, C. S.; Durante, V. A.: Isobutane dehydrogenation over sulfided nickel catalysts. *J. Catal.* **1994**, *146*, 40-55.

(380) Xu, X.; Liu, X.; Xu, B.: A survey of nickel-based catalysts and monolithic reformers of the onboard fuel reforming system for fuel cell APU applications. *Int. J. Energy Res.* **2016**, *40*, 1157-1177.

(381) Ragsdale, S. W.: Nickel-based Enzyme Systems. *J. Biol. Chem.* **2009**, *284*, 18571-18575.

(382) Chen, M.; Xu, J.; Liu, Y.-M.; Cao, Y.; He, H.-Y.; Zhuang, J.-H.: Supported indium oxide as novel efficient catalysts for dehydrogenation of propane with carbon dioxide. *Applied Catalysis A: General* **2010**, *377*, 35-41.

(383) Halász, J.; Kónya, Z.; Fudala, Á.; Béres, A.; Kiricsi, I.: Indium and gallium containing ZSM-5 zeolites: acidity and catalytic activity in propane transformation. *Catal. Today* **1996**, *31*, 293-304.

(384) Schneider, U.; Kobayashi, S.: Low-oxidation state indium-catalyzed C–C bond formation. *Acc. Chem. Res.* **2012**, *45*, 1331-1344.

(385) Beckers, J.; Rothenberg, G.: Sustainable selective oxidations using ceria-based materials. *Green Chem.* **2010**, *12*, 939-948.

(386) Katz, M. J.; Brown, Z. J.; Colon, Y. J.; Siu, P. W.; Scheidt, K. A.; Snurr, R. Q.; Hupp, J. T.; Farha, O. K.: A facile synthesis of UiO-66, UiO-67 and their derivatives. *Chem. Commun.* **2013**, *49*, 9449-9451.

(387) Lammert, M.; Wharmby, M. T.; Smolders, S.; Bueken, B.; Lieb, A.; Lomachenko, K. A.; Vos, D. D.; Stock, N.: Cerium-based metal organic frameworks with UiO-66 architecture: synthesis, properties and redox catalytic activity. *Chem. Commun.* **2015**, *51*, 12578-12581.

(388) Kim, I. S.; Borycz, J.; Platero-Prats, A. E.; Tussupbayev, S.; Wang, T. C.; Farha, O. K.; Hupp, J. T.; Gagliardi, L.; Chapman, K. W.; Cramer, C. J.; Martinson, A. B. F.: Targeted single-site MOF node modification: trivalent metal loading via atomic layer deposition. *Chem. Mater.* **2015**, *27*, 4772-4778.

(389) Zhuang, J.-L.; Ceglarek, D.; Pethuraj, S.; Terfort, A.: Rapid room-temperature synthesis of metal–organic framework HKUST-1 crystals in bulk and as oriented and patterned thin films. *Adv. Funct. Mater.* **2011**, *21*, 1442-1447.

(390) Jiao, F.; Frei, H.: Nanostructured cobalt oxide clusters in mesoporous silica as efficient oxygen-evolving catalysts. *Angew. Chem. Int. Ed.* **2009**, *48*, 1841-1844.

(391) Yabushita, M.; Li, P.; Islamoglu, T.; Kobayashi, H.; Fukuoka, A.; Farha, O. K.; Katz, A.: Selective metal–organic framework catalysis of glucose to 5-hydroxymethylfurfural using phosphate-modified NU-1000. *Ind. Eng. Chem. Res.* **2017**, *56*, 7141-7148.

(392) Nguyen, H. G. T.; Schweitzer, N. M.; Chang, C.-Y.; Drake, T. L.; So, M. C.; Stair, P. C.; Farha, O. K.; Hupp, J. T.; Nguyen, S. T.: Vanadium-Node-Functionalized UiO-66: A Thermally Stable MOF-Supported Catalyst for the Gas-Phase Oxidative Dehydrogenation of Cyclohexene. *ACS Catalysis* **2014**, *4*, 2496-2500.

(393) Zhang, M.; Yang, L.: Ceramic product forming technologies research based on 3D printing. *IEEE Access* **2016**, *4*, 9345-9349.

(394) Barner-Kowollik, C.; Bastemeyer, M.; Blasco, E.; Patrick, M.; Delaittre, G.; Richter, B.; Wegener, M.: 3D laser micro- and nano-printing: challenges for chemistry. *Angew. Chem. Int. Ed.*, Accepted Author Manuscript. doi:10.1002/ange.201704695.

(395) Hermatschweiler, M.; Werner, A.; Lindenmann, N.; Bückmann, T.; Bauer, J.; Bastmeyer, M.; Chanda, D.; Zhang, L.; Marino, A.; Tanguy, Y.; Niesler, F.; Frölich, A.; Thieme, K.: *Spectrum of applications*. Nanoscribe, Ed.: Eggenstein-Leopoldshafen, Germany, 2017.

(396) Thiel, M.; Rill, M. S.; von Freymann, G.; Wegener, M.: Three-dimensional bi-chiral photonic crystals. *Adv. Mater.* **2009**, *21*, 4680-4682.

(397) Skinner, S. J.; Kilner, J. A.: Oxygen ion conductors. *Mater. Today* **2003**, *6*, 30-37.

(398) Slater, P. R.; Sansom, J. E. H.; Tolchard, J. R.: Development of apatite-type oxide ion conductors. *Chem. Rec.* **2004**, *4*, 373-384.

(399) Orera, A.; Baikie, T.; Panchmatia, P.; White, T. J.; Hanna, J.; Smith, M. E.; Islam, M. S.; Kendrick, E.; Slater, P. R.: Strategies for the Optimisation of the Oxide Ion Conductivities of Apatite-Type Germanates. *Fuel Cells* **2011**, *11*, 10-16.